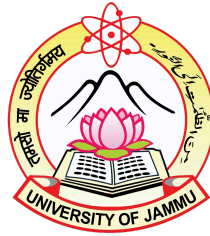


An event-by-event study of local fluctuations in multiparticle production at ultra-relativistic energies



THESIS

SUBMITTED TO THE UNIVERSITY OF JAMMU
FOR
THE AWARD OF DEGREE
OF

DOCTOR OF PHILOSOPHY
IN
PHYSICS

BY

Salman Khurshid Malik

UNDER THE SUPERVISION
OF

Prof. Ramni Gupta

Department of Physics
University of Jammu, Jammu
Jammu and Kashmir—180006 (India)

December, 2024


**DEPARTMENT OF PHYSICS
UNIVERSITY OF JAMMU
JAMMU-180006**



CERTIFICATE

It is certified that **Mr. Salman Khurshid Malik** worked under my supervision and the work is worthy of consideration for the award of Ph.D. degree in Physics. It is further certified that:

- i. the thesis embodies the work of the candidate himself. It is original and not copied from any other source.
- ii. the candidate worked under my supervision for the prescribed period required under statutes.
- iii. the candidate has put in the required attendance in the Department of Physics, University of Jammu, Jammu during the period of research.
- iv. the candidate fulfils all the requirements of the UGC-MSP-2016 regulations.
- v. the candidate has fulfilled the statutory conditions as laid down in Section 18 of the statutes governing the degree of Doctor of Philosophy.


24/12/2024

(Prof. Arun Bharti)
Head of the Department
P. G. Department of Physics,
University of Jammu,
Jammu


24.12.2024

(Prof. Ramni Gupta)
Research Supervisor
Department of Physics
University of Jammu,
Jammu

PLAGIARISM CERTIFICATE

I, **Salman Khurshid Malik**, S/O Mr. Khurshid Ahmad Malik, hereby declare that the work reported in this thesis entitled "**An event-by-event study of local fluctuations in multiparticle production at ultra-relativistic energies**" has been entirely done by me under the supervision of **Prof. Ramni Gupta**, Department of Physics, University of Jammu. The work undertaken by me in this thesis is original and has not been copied from other sources without due acknowledgement. I also ascertain that no part of this thesis is presented elsewhere for the award of any degree or diploma of any University or Institution. Moreover, this thesis is having **3%** degree of plagiarism as per the **DrillBit plagiarism detection software** analysis report.

Dated: 24-12-2024

Salman

(Salman Khurshid Malik)

Countersigned by:

Arun
24/12/2024

(Prof. Arun Bharti)
Head of the Department
P. G. Department of Physics,
University of Jammu, Jammu.
Jammu

Ramni Gupta
24.12.2024
(Prof. Ramni Gupta)
Research Supervisor
Department of Physics
University of Jammu
Jammu


DECLARATION


I, **Salman Khurshid Malik**, S/O Mr. Khurshid Ahmad Malik, hereby declare that the work reported in this thesis entitled "**An event-by-event study of local fluctuations in multiparticle production at ultra-relativistic energies**" has been entirely done by me under the supervision of **Prof. Ramni Gupta**, Department of Physics, University of Jammu. The work undertaken by me in this thesis is original and has not been copied from other sources without due acknowledgements. It has not been submitted fully or partially elsewhere for the award of any degree, diploma, fellowship or other similar titles of recognition to the best of my knowledge to anybody else in any other University or Institution.

Dated: 24-12-2024


(Salman Khurshid Malik)

Countersigned by:


(Prof. Arun Bharti)
Head of the Department
Department of Physics,
University of Jammu,
Jammu


24.12.2024
(Prof. Ramni Gupta)
Research Supervisor
Department of Physics
University of Jammu,
Jammu

ACKNOWLEDGEMENT

First and foremost, I would like to express my gratitude to **The Almighty Allah**, whose grace and guidance have been the unwavering pillars of strength throughout this journey. This endeavor would not have been possible without His infinite blessings, which have sustained me through countless challenges and given me strength to overcome every obstacle possible.

Secondly, with all due respect I want to forward my greatest thanks to **Prof. Ramni Gupta**, my esteemed supervisor, for her unfailing support, invaluable guidance, and belief in my abilities. Her knowledge, insightful feedback, and encouragement have been instrumental in shaping the direction and quality of this research. It has been an honor to learn from her expertise and a privilege to have had the opportunity to work under her mentorship. I am particularly indebted to her supportive attitude which helped me to come forward and face the challenging phases of my research, providing me with the motivation and encouragement necessary to persevere and achieve my research goals. I would also like to thank her for taking the time, putting in the effort to read the thesis multiple times and provide me with useful comments.

My sincere thanks to **Prof. Arun Bharti**, Head of the Department of Physics, for providing the necessary facilities for this work. I extend my sincerest appreciation to **Prof. Anju Bhasin**, whose support and guidance throughout this time helped me a lot. I am deeply grateful for her consistent support, which extended beyond academic guidance to include securing project funding. Her efforts in securing financial support through “Indian Participation in ALICE experiment at CERN” as a Project Associate, provided me with the necessary financial stability to dedicate myself fully to this research. I am deeply indebted to **Er. Anik Gupta**, for his indispensable assistance during my work. His technical expertise and prompt support helped me to learn a lot of new things. I would also like to thank the other members of the high-energy group group in Jammu: **Prof. Sanjeev Singh Sambyal, Dr. Renu Bala, Dr. Rajendra Nath Patra, Er. Sanjay Mahajan and Dr. Saroj Nayak**. It has been a pleasant working atmosphere while

working in the high-energy group. I extend my sincere gratitude to all the teaching and non-teaching staff of this department.

I would like to express my sincere gratitude to **Mesut Arslandok**, whose guidance during the data analysis phase of my work was invaluable. He taught me about analysis, and was always ready to answer questions, even when busy. Whenever I felt lost he always showed a way, and motivated me throughout my work. I am also grateful to work with the members of PWG (Physics Working Group) and PAG (Physics Analysis Group): **Igor Altsybeev**, **Dr. Tapan Nayak**, **Ante Bilandzic**, **Sumit Basu** for their valuable suggestions, comments and helpful physics discussions to proceed with this work. Thank you, **Ole Schmidt**, for your support in completing the service work and for always being ready to discuss the challenges I encountered.

My heartfelt thanks to **Pratibha Bhagat** for always being there and bearing with me the good and bad times during this time. Thanks to **Aamir Ahmed**, **Tariq Mustafa** for supporting me and reminding me to take breaks in stressful times. Thanks to **Balwan Singh** for proofreading this thesis. I would like to acknowledge the camaraderie and support of my lab mates, **Vikash Sumberia**, **Sheetal Sharma**, **Binti Sharma**, **Nasir Mehdi Malik**, **Zarina Banoo**, **Ashish Jalotra**, **Mahima Sharma**, **Upasana Sharma**, **Fakhar Ul Haider** and **Mokshi Vaid** whose collaboration and encouragement created a dynamic and productive research environment. The memories of working together and exchanging ideas will forever hold a special place in my heart. I wish all of them best of luck for their future. I would also like to thank my friends, **Rahul Uttam**, **Anshiv Sharma**, **Sameer Ahmed**, **Haq Nawaz** for their support and encouragement during this time.

Thanks to my parents, **Mr. Khurshid Ahmad** and **Mrs. Zahida Begum** for for patiently tolerating my behaviour in this long journey of research. I am grateful to my parents for their unwavering mental and financial support. I am also thankful to my siblings, **Rafiya Tabassum**, **Roziya Tabassum**, **Zaid Malik** who have always been there for me, providing me with the necessary emotional support and encouragement to keep going.

(Salman Khurshid Malik)

ABSTRACT

The exploration of the Quark-Gluon Plasma (QGP) is one of the central challenge in high-energy heavy-ion physics. This state of matter, where quarks and gluons—the fundamental constituents of protons and neutrons—are no longer confined within hadrons, is believed to have existed during the first few microseconds after the Big Bang. Under extremely hot and dense conditions, quarks and gluons moved freely before cooling to form the hadrons that make up all visible matter today. Understanding the properties and evolution of the QGP is crucial for gaining insights into the early Universe and the fundamental nature of the strong interactions, the force governing interactions between quarks and gluons.

To study QGP, Quantum Chromodynamics (QCD), the fundamental theory governing the strong interactions predicts that at sufficiently high temperatures or baryon densities, matter undergoes a phase transition from a hadronic phase to a deconfined phase, known as the QGP. Mapping QCD phase diagram, which describes the behaviour of matter under varying conditions of temperature (T) and baryon chemical potential (μ_B), is a key objective of the field. A particularly intriguing feature of this diagram is the hypothesized critical point (CP), where the first-order phase transition line ends and a crossover region begins. Discovering and characterising CP would offer profound insights into the nature of the QCD and the behaviour of strongly interacting matter during phase transition. Information about the properties of the system at critical point would lead to significant additions to our knowledge, such as on evolution of the early Universe, formation of compact stellar objects, etc..

Lattice QCD plays an important role in these investigations by providing a non-perturbative approach to solve QCD on a discrete spacetime lattice. This allows the exploration of the QCD phase diagram at finite temperatures and densities, enabling to make predictions on the behaviour of matter under various conditions. Through extensive computational efforts, lattice QCD calculations predict a crossover transition from hadronic matter to QGP at low baryon chemical potentials and high temperatures. Whereas, at higher baryon densities, these calculations suggest presence of first-order phase transition, which is believed to

culminate at a critical point as one move towards low μ_B . Insights gained from lattice QCD are instrumental in guiding experimental exploration for the CP and understanding associated phase transition.

Experimental efforts to locate critical point are carried out through high-energy heavy-ion collisions, such as those at the Relativistic Heavy Ion Collider (RHIC) at BNL (USA), Large Hadron Collider (LHC) at Geneva, the upcoming Nuclotron-based Ion Collider fAcility (NICA) at Russia and Compressed Baryonic Matter (CBM) experiment at Germany. These experiments aim to recreate the extreme conditions required to form QGP, thus facilitating the study of properties of the resulting matter. One promising approach for identifying the CP is the analysis of fluctuations in the particle number density in kinematic phase space. These fluctuations can reveal signatures of phase transition expected near critical point. Based on the Ising-QCD calculations, the density-density correlation function has a power-law, or self-similar, structure which gives rise to large density fluctuations in the multiparticle production in heavy-ion collisions. These fluctuations can be probed using intermittency analysis wherein the normalized factorial moments (NFM) of particle density distributions are calculated. Fluctuations in the multiplicity distributions arising because of phase-transition gives scaling behaviour of NFM with decreasing resolution of phase space which is termed as intermittency. Intermittency analysis to investigate fluctuations in the particle number density is thus a tool in this context as it can identify non-random correlations in the particle distributions, indicating underlying critical phenomena.

Large amount of data collected by recent collider experiments such as LHC and RHIC, are suitable to carry detailed statistical analysis of particle multiplicity fluctuations as intermittency study requires high particle densities per bin. Intermittency signify “big bursts from small region (cells) of the phase space”, that appears as a power-law (scaling) behaviour of NFM (F_q). The observation of power-law scaling of these moments suggests that the fluctuations are not random but are correlated over different scales, reflecting a fractal structure of the produced matter. This connection to fractal structures is significant, as it helps characterise the self-similarity in particle production. The strength of intermittency is quantified by the intermittency index (ϕ_q) extracted from the power-law behaviour of F_q on the number of partitioned cells (M) in the phase space. As per the studies performed using the Ginzburg-Landau theory, the scaling exponent (ν) obtained from the power-law behaviour of higher-order NFM (F_q , $q > 2$) with the second-order NFM (F_2) is predicted to give information about the critical nature of the system. The fractal observable, often denoted as D_q , measures how the density fluctuations behave under rescaling, providing insights into the critical nature of the system. CERN based experiments – NA49, NA61/SHINE,

and recently STAR experiment at RHIC have actively investigated phase transition and searched for the critical point using the intermittency analysis of data by colliding of various systems and at different energies. Meanwhile, heavy-ion collision events from the Toy model, the AMPT, EPOS3 and UrQMD model have also been investigated using the intermittency methodology to get a baseline behaviour of the normalized factorial moments for the systems and energies under investigation at the various collider experiments.

This doctoral thesis, presents the intermittency analysis performed on charged particles recorded in the two dimensional (η, φ) phase space by the ALICE experiment at LHC. The data presented here has mainly been obtained from Pb–Pb collisions at $\sqrt{s_{\text{NN}}} = 5.02$ TeV, recorded by the ALICE detector during 2015 to 2018. Analysis performed on the events generated using PYTHIA8/Angantyr is also presented.

The whole work is compiled in a thesis with 5 chapters, structured as follows:

Chapter 1: This chapter introduces the fundamental physics of heavy-ion collisions, focusing on the key concepts. An overview of the Standard Model of particle physics, which describes elementary particles and their interactions is presented followed by discussion on the quantum chromodynamics (QCD). A brief historical perspective on the discovery of the Quark-Gluon Plasma (QGP) is given, highlighting its significance in the studies of the high-energy collisions, outlining key stages such as pre-equilibrium, the QGP phase, and freeze-out. Kinematic parameters to describe the geometry and dynamics of the collisions are briefly introduced. The chapter also discusses experimental observables, used in general, to probe the creation of QGP formation and provide insight into the properties of the QGP, helping to understand the complex behaviour of matter under extreme conditions. An introduction to multiplicity fluctuations as a tool to characterise the system formed during heavy-ion collisions is also discussed.

Chapter 2: Details of the physics observables and methodology to determine these observables, studied in this thesis, for understanding the charged particle production and to characterise the medium formed in Pb–Pb collisions during RunII of the LHC operation are given in this chapter. Before that, a discussion on the QCD phase diagram and related concepts, with perspective to the observables under study is given. An overview of the QCD phase diagram, with a focus on the region of relatively high temperature and low chemical potential, where the QCD phase transition and the critical point are expected is given along with a review of different order parameters used to understand the quark-hadron phase transition. A system undergoing second order phase transition at the critical point exhibits

scale invariance, fractal structures and self-similarity, due to long-range correlations. This behaviour can be described through scaling laws characterised by a handful of critical exponents, dictated by the universality class to which the phase transition belongs. An elaborate discussion on this is given followed by details on the intermittency analysis and analysis methodology for two dimensional study. Observables – NFM ($F_q(M)$), fractal parameter (D_q), intermittency indices (ϕ_q), and scaling exponent (ν) are all defined and the procedure to obtain these is also presented. Results and observations from the intermittency analysis of a few models and experiments (NA61, STAR) are also given.

Chapter 3: This chapter gives a brief introduction to the LHC and some of its main experiments. It introduces a few important beam parameters and the ALICE detector setup. An overview of the detectors of the ALICE experiment, data from which is used for the physics analysis in this thesis, viz: ITS (Inner Tracking System), TPC (Time Projection Chamber) and V0 detector is given. Chapter further gives an introduction to the set of C++ libraries built on top of ROOT analysis software that is used by ALICE – the AliPhysics and AliROOT. AliRoot is the base framework, written in C++, that handles the core modules for detector simulation, event generation, reconstruction, and analysis of data from ALICE. AliPhysics as an extension focusses only on the online/offline analysis. Various data formats and the method for centrality determination used in ALICE experiment are also given.

Chapter 4: This chapter gives a detailed discussion on the analysis performed on the experimental data and event samples from the Monte Carlo event generators. At the outset, description of the datasets, event selection, filterbit cuts on tracks and techniques used to extract the clean data from the raw data is given. The intermittency analysis as described in Chapter 2 is performed on the generated and reconstructed Monte Carlo events from the HIJING and the Monte Carlo closure test so performed is discussed. Analysis results from various steps and cut study are given. M-scaling behaviour of the NFM (F_q), i.e., $\ln F_q$ vs $\ln M^2$ behaviour, for the charged particles produced in the mid rapidity region in the full azimuth for different soft p_T (transverse momentum) intervals is also studied. Scaling exponent (ν), a parameter to quantify fluctuations of charged particle density in the spatial phase space extracted from the scaling of $\ln F_q$ with $\ln F_2$ is studied for its dependence on the p_T bin, p_T bin width and centrality. Observations and results from this study are found to be in agreement with some models and theoretical predictions. Cut studies performed on data for its comparison with results from RunI (Pb–Pb, 2.76 TeV) are discussed in detail. Observations and results obtained from data are compared with that from HIJING event samples and PYTHIA8/Angantyr for Pb–Pb collisions at $\sqrt{s_{NN}} = 2.76$ and 5.02 TeV.

Chapter 5: This chapter provides a summary of the research conducted and the key conclusions derived from the analysis of data collected by the ALICE experiment. It also outlines potential future directions for investigating the QCD phase transition using intermittency analysis in heavy-ion collision experiments.

LIST OF FIGURES

Figure 1.1: Elementary particles described by the Standard Model.	4
Figure 1.2: A quark-antiquark pair gets created as potential between two quarks increases with increasing separation.	5
Figure 1.3: Schematic description of the evolution of the system created by two heavy-ion colliding beams.	11
Figure 1.4: Sketch of the coordinate system at ALICE, which is visualised as a cylinder, with its center aligned at the interaction point (IP _z).	12
Figure 1.5: Illustration depicting impact parameter in a heavy-ion collision. .	14
Figure 1.6: Strangeness enhancement reported by ALICE.	15
Figure 1.7: Schematic representation of Jet quenching wherein the jet that goes in up direction is more or less unaffected whereas the one going in down direction is quenched in the QGP medium.	16
Figure 1.8: Illustration showing quenched and unquenched jet.	16
Figure 1.9: A comparison of nuclear modification factor, R_{AA} for $J/\Psi \rightarrow \mu^+ \mu^-$ production between Pb–Pb collisions at $\sqrt{s_{NN}} = 5.02$ TeV and $\sqrt{s_{NN}} = 2.76$ TeV. ALICE measurements of R_{AA} for Pb–Pb $\sqrt{s_{NN}} = 2.76$ TeV compared to PHENIX for Au–Au collisions $\sqrt{s_{NN}} = 200$ GeV are also shown.	18
Figure 1.10: Transverse momentum spectra of π^\pm (left), K^\pm (middle) and $p(\bar{p})$ (right) measured for different centrality classes in p–p and Pb–Pb collisions at $\sqrt{s_{NN}} = 5.02$ TeV (ALICE)	20
Figure 1.11: Schematic depicting a heavy ion collision illustrating development of flow.	20
Figure 1.12: ALICE integrated flow measurements for the flow coefficients $v_n\{m\}$	22
Figure 1.13: Mean ($\langle N_{ch} \rangle$), standard deviation (σ_{ch}^2), and scaled variance (ω_{ch}) of charged-particle multiplicity distributions at ALICE.	24
Figure 1.14: ALICE mean p_T event-by-event fluctuations measurements. ...	25
 Figure 2.1: Schematic phase diagram of nuclear dense matter with boundaries outlining various states of QCD matter.	 29
Figure 2.2: Characteristic points on the QCD phase diagram.	32

Figure 2.3: Depiction of a heavy-ion collision event showing local density fluctuations in $\eta - \varphi$ phase space.	42
Figure 2.4: Schematic representation of two dimensional (η, φ) phase space partitioned into $M \times M$ bins (where $M = 5$ in figure is shown) to calculate factorial moments.	45
Figure 2.5: $\ln F_q$ vs bin size, x and $\ln F_q$ vs $\ln F_2$ as per GL description of critical systems.	49
Figure 2.6: β_q as a function q determined within GL theory (solid line) is shown along with nuclear data results from KLM and EMU01 experiments.	50
Figure 2.7: Temperature dependence of scaling exponent, $\nu(T)$ from Ising model (black line), GL theory (red dashed line) and SCR model (blue line).	51
Figure 2.8: D_i as a function of i for different (a) sources and (b) for different collision systems.	53
Figure 2.9: Intermittency analysis results for proton number from the NA61/SHINE experiment for Ar+Sc collision energies summarised.	54
Figure 2.10: NA61/SHINE diagram showing chemical freeze-out temperature as a function of baryon-chemical potential. The values calculated from p+p interactions are shown by the dashed line, while the dotted line is for central Pb+Pb collisions. Colored points highlight reactions (Ar+Sc and Pb+Pb) where the search of the critical point was done.	55
Figure 2.11: $\Delta F_q(M)$ as a function of bin numbers, M^2 in 0–5% central Au+Au collisions at $\sqrt{s_{NN}} = 19.6, 27$ GeV.	56
Figure 2.12: The measured $\Delta F_q(M)$ ($q=3-6$) as a function of $\Delta F_2(M)$ in 0–5% Au+Au collisions at $\sqrt{s_{NN}} = 19.6$ GeV on a logarithmic scale.	56
Figure 2.13: Energy dependence of scaling exponent, ν , of charged hadrons in Au+Au collisions at $\sqrt{s_{NN}} = 7.7-200$ GeV. Red stars and blue circles represent ν in most central collisions (0-5%) and central collisions (10–40%), respectively.	57
Figure 3.1: Illustration visualising LHC accelerator complex with it's four main experiments and additional access points.	60
Figure 3.2: Schematics of ALICE Detector showing subsystems.	66
Figure 3.3: Sketch of the Inner Tracking System (ITS).	68
Figure 3.4: Sketch of the Time Projection Chamber (TPC).	70
Figure 3.5: Sketch of V0 scintillators: V0–A and V0–C.	71
Figure 3.6: Transverse momentum resolution for TPC and ITS–TPC matched tracks.	74
Figure 3.7: Visualisation of the workflow from event generation to the final data format.	77
Figure 3.8: V0M (V0–A + V0–C) amplitude for Pb–Pb, $\sqrt{s_{NN}} = 5.02$ TeV.	79

Figure 4.1: <i>Observables</i> : Normalized factorial moments (NFM) of order q as function of number of bins, M in the D dimensional phase space and the scaling behaviours of NFM.	81
Figure 4.2: Centrality resolution of various centrality estimators used in ALICE during Pb–Pb collisions at $\sqrt{s_{\text{NN}}} = 2.76$ TeV.	87
Figure 4.3: <i>ALICE</i> : Multiplicity vs V0M percentile before (left) and after (right) the cuts.	89
Figure 4.4: <i>ALICE</i> : CL0 vs V0M percentile before (left) and after (right) the cuts.	89
Figure 4.5: <i>HIJING</i> : Centrality and vertex- z (v_z) distributions of raw and selected tracks.	94
Figure 4.6: <i>HIJING</i> : Number of events obtained after applying various event selection cuts on the HIJING event sample.	94
Figure 4.7: <i>HIJING</i> : p_T , η and φ distributions comparing “reconstructed level” and “generator level” tracks.	95
Figure 4.8: <i>HIJING</i> : $\ln F_q(M)$ vs $\ln M^2$ (M –scaling) plots for reconstructed and generated level tracks for moment order $q = 2, 3, 4, 5$	97
Figure 4.9: <i>HIJING</i> : MC closure for $F_q(M)$ ($F_q(M)^{\text{reco}}/F_q(M)^{\text{gen}}$) as function of $\ln M^2$ in $0.4 \leq p_T \leq 1.0$ (GeV/c) for $q = 2, 3, 4, 5$	98
Figure 4.10: <i>HIJING</i> : Ratio of shared clusters to crossed rows and crossed rows to findable clusters as a function of shared clusters to total clusters.	99
Figure 4.11: <i>HIJING</i> : Shared clusters/Crossed rows vs p_T (on the left). On the right, $F_q(M)^{\text{reco}}/F_q(M)^{\text{gen}}$ plot with respect to $\ln M^2$ showing the effect of various cuts.	101
Figure 4.12: <i>HIJING</i> : $F_q(M)$ vs $\ln M^2$ plots for $q = 2, 3, 4, 5$ in case of reconstructed and generated level tracks. $F_q(M)^{\text{reco}}/F_q(M)^{\text{gen}}$ as function of $\ln M^2$ to check the MC closure achieved.	102
Figure 4.13: <i>HIJING</i> : $\ln F_q(M)$ vs $\ln M^2$ (M –scaling) plot for charged particles in $0.4 \leq p_T \leq 1.0$ (GeV/c) for reconstructed (on the left) and generator (on the right) level tracks.	103
Figure 4.14: <i>HIJING</i> : $\ln F_q(M)$ vs $\ln F_2(M)$ (F –scaling) plot for reconstructed (on the left) and generated (on the right) level tracks respectively.	103
Figure 4.15: <i>HIJING</i> : $\ln F_q(M)$ vs $\ln F_2(M)$ (F –scaling) plot with line fits and value of scaling exponent calculated for both simulations levels.	104
Figure 4.16: <i>HIJING</i> : D_q vs q plot for reconstructed (left) and generated (right) simulation events.	105
Figure 4.17: <i>ALICE</i> : Percentage of events obtained after applying various event selection cuts on the data.	106
Figure 4.18: <i>ALICE</i> : Centrality (left) and vertex- z (v_z) distributions (right) of data before and after applying event selection cuts.	106
Figure 4.19: <i>ALICE</i> : η and φ distributions of the charged particle tracks before	

and after applying track selection cuts on 0–5% centrality events.	107
Figure 4.20: <i>ALICE</i> : Number of clusters and number of crossed rows in TPC distributions for charged particle tracks in TPC before and after applying track selection cuts.	107
Figure 4.21: <i>ALICE</i> : χ^2 distributions of charged particle tracks in ITS and TPC before and after applying track selection cuts.	108
Figure 4.22: <i>ALICE</i> : DCA of tracks to primary vertex in xy , z plane and as a function of p_T for raw tracks and selected tracks.	109
Figure 4.23: <i>ALICE</i> : Charged particle multiplicity distributions in narrow p_T bins (left) and wide (right) p_T bins within $ \eta \leq 0.8$ and $0 \leq \varphi \leq 2\pi$ in 0–5% central events.	110
Figure 4.24: <i>ALICE</i> : Average bin content as a function of number of phase space bins ($\ln M^2$) for the narrow (left) and wide (right) p_T bins.	110
Figure 4.25: <i>ALICE</i> : $f_q^e(M)$ distributions for $q = 2, 3, 4, 5$ of charged particles in (η, φ) phase space partitioned into $M = 20, 34, 50, 60$ bins in $0.4 \leq p_T \leq 1.0$ GeV/ c	111
Figure 4.26: <i>ALICE</i> : $\ln(F_q(M))$ vs $\ln M^2$ plot, (M -scaling) for all orders $q = 2, 3, 4, 5$	112
Figure 4.27: <i>ALICE</i> : M -scaling plot for higher M values with straight line fits (on the left) to calculate intermittency index ϕ_q as a function of q (right). ..	112
Figure 4.28: <i>ALICE</i> : $\ln F_q(M)$ vs $\ln F_2(M)$ plot, (F -scaling) for all orders $q = 3, 4, 5$	114
Figure 4.29: <i>ALICE</i> : $\ln F_q(M)$ vs $\ln F_2(M)$ plot, (F -scaling) for $q = 3, 4, 5$ with the line fits in the higher M region where acceptable MC closure was obtained with HIJING.	114
Figure 4.30: <i>ALICE</i> : $\ln \beta_q$ as a function for $\ln(q - 1)$ in the most central (0–5%) Pb–Pb collision events.	115
Figure 4.31: <i>ALICE</i> : D_q as a function of q for the most central (0–5%) events from Pb–Pb collisions at $\sqrt{s_{NN}} = 5.02$ TeV.	116
Figure 4.32: <i>ALICE</i> : Dependence of $\ln F_q(M)$ on $\ln M^2$ (M -scaling) for $q = 2, 3, 4, 5$ in the central Pb–Pb collisions at $\sqrt{s_{NN}} = 5.02$ TeV for ALICE data, HIJING and EPOS–LHC.	118
Figure 4.33: <i>ALICE</i> : D_q as a function of moment order q for $0.4 \leq p_T \leq 1.0$ GeV/ c range compared with HIJING and EPOS–LHC.	119
Figure 4.34: <i>ALICE</i> : $\ln F_q(M)$ vs $\ln M^2$ plot (M -scaling) ($q = 2, 3, 4, 5$) for charged particles produced in narrow p_T bins.	120
Figure 4.35: <i>ALICE</i> : $\ln F_q(M)$ vs $\ln M^2$ plot (M -scaling) ($q = 2, 3, 4, 5$) for charged particle produced in wide p_T bins.	121
Figure 4.36: <i>ALICE</i> : $\ln F_q(M)$ vs $\ln F_2(M)$ plot (F -scaling) for $q = 3, 4, 5$ for the charged particle produced in narrow p_T bins.	123

Figure 4.37: <i>ALICE</i> : $\ln F_q(M)$ vs $\ln F_2(M)$ plot (F -scaling) for $q = 3, 4, 5$ for the charged particle produced in wide p_T bins.	123
Figure 4.38: <i>ALICE</i> : Scaling exponent (ν) as a function of p_T in the wide/non-overlapping p_T bins.	124
Figure 4.39: <i>ALICE</i> : Scaling exponent (ν) as a function of p_T in the narrow/overlapping p_T bins.	125
Figure 4.40: <i>ALICE</i> : D_q as a function of moment order q comparison for various p_T bins.	126
Figure 4.41: <i>ALICE</i> : $\ln F_q(M)$ vs $\ln M^2$ (M -scaling) for $q = 2, 3, 4, 5$ in $0.4 \leq p_T \leq 1.0$ GeV/c for different centralities.	127
Figure 4.42: <i>ALICE</i> : $\ln F_q(M)$ vs $\ln F_2(M)$ (F -scaling) ($q = 3, 4, 5$) in $0.4 \leq p_T \leq 1.0$ GeV/c for different centralities.	128
Figure 4.43: <i>ALICE</i> : Dependence of scaling exponent, ν on centrality.	129
Figure 4.44: <i>ALICE</i> : Relative uncertainties (default value/variation value) from sources in case of M -scaling ($\ln F_q(M)$ vs $\ln M^2$) for $q = 2, 3, 4, 5$	131
Figure 4.45: <i>ALICE</i> : Relative uncertainties (default value/variation value) for scaling exponent (ν).	132
Figure 4.46: <i>PYTHIA8/Angantyr</i> : Charged particle pseudorapidity distribution using Angantyr compared with that from ALICE at 2.76 TeV and 5.02 TeV.	134
Figure 4.47: <i>PYTHIA8/Angantyr</i> : $\ln F_q(M)$ vs $\ln M^2$ (M -scaling) and $F_q(M)$ vs $\ln F_2(M)$ (F -scaling) for charged particles within 0–5% centrality of Pb–Pb collisions at 2.76 TeV.	137
Figure 4.48: <i>PYTHIA8/Angantyr</i> : $\ln F_q(M)$ vs $\ln M^2$ (M -scaling) and $F_q(M)$ vs $\ln F_2(M)$ (F -scaling) for charged particles within generated 0–5% centrality of Pb–Pb collisions at 5.02 TeV.	138
Figure 4.49: <i>PYTHIA8/Angantyr</i> : Centrality dependence of scaling exponent, ν for different centralities in Pb–Pb collisions at $\sqrt{s_{NN}} = 2.76, 5.02$ TeV.	139
 Figure A.1: Schematic cross-section of the ALICE detector in the LHC beam direction.	168
Figure A.2: Left: Illustration of generated ionization along the path of electrons and pions through a TRD chamber. Right: Measured average puls height distribution as a function of the signal arrival time.	169
Figure A.3: <i>TRD QC</i> : Number of matched TRD tracks and number of tracklets per matched TRD track.	171
Figure A.4: <i>TRD QC</i> : p_T , η , φ distributions for TRD matched tracks.	172
Figure A.5: <i>TRD QC</i> : Average pulse height vs. drift time plot (top), pulse height for each chamber vs. drift time plot (bottom) for matched TRD tracks.	173
Figure A.6: <i>TRD QC</i> : η , φ distribution for all matched TRD tracks giving chamber wise view of TRD.	174
Figure A.7: <i>TRD QC</i> : η , φ distribution for positive charged matched TRD tracks	

giving chamber wise view for the six layers of TRD.	175
Figure A.8: <i>TRD QC</i> : η, φ distribution for negative charged matched TRD tracks giving chamber wise view for the six layers of TRD.	176
Figure A.9: <i>TRD QC</i> : η, φ distribution giving chamber wise view of the average number of tracklets for matched TRD tracks.	177
Figure A.10: <i>TRD QC</i> : η, φ distribution giving chamber wise view of the average number of tracklets for matched negative and positive charged TRD tracks.	177
Figure C.1: <i>HIJING</i> : MC closure for $0.4 \leq p_T \leq 0.6$ (GeV/c).	185
Figure C.2: <i>HIJING</i> : MC closure for $F_q(M)$ ($F_q(M)^{\text{reco}}/F_q(M)^{\text{gen}}$) of charged particles in $0.4 \leq p_T \leq 0.6$ (GeV/c) for $q = 2, 3, 4, 5$	185
Figure C.3: <i>HIJING</i> : $\ln F_q(M)$ vs $\ln M^2$ (M -scaling) plot and $\ln F_q(M)$ vs $\ln F_2(M)$ (F -scaling) plots for $0.4 \leq p_T \leq 0.6$ (GeV/c) for reconstructed level (left) and generated level (right) tracks.	186
Figure C.4: <i>HIJING</i> : F -scaling line-fit in higher M region for $0.4 \leq p_T \leq 0.6$ (GeV/c) to calculate β_q and ν for reconstructed level (top) and generated level (bottom) tracks.	186
Figure C.5: <i>HIJING</i> : MC closure ratios ($F_q(M)^{\text{reco}}/F_q(M)^{\text{gen}}$) comparison for different track selection cuts for $0.4 \leq p_T \leq 1.0$ (GeV/c).	187
Figure C.6: <i>PYTHIA8/Angantyr</i> : $\ln F_q(M)$ vs $\ln M^2$, M -scaling and $F_q(M)$ vs $\ln F_2(M)$, F -scaling for $q = 2, 3, 4, 5$ for 5–10% centrality of Pb–Pb 2.76 TeV.	188
Figure C.7: <i>PYTHIA8/Angantyr</i> : $\ln F_q(M)$ vs $\ln M^2$, M -scaling and $F_q(M)$ vs $\ln F_2(M)$, F -scaling for $q = 2, 3, 4, 5$ for 5–10% centrality of Pb–Pb 5.02 TeV.	189

LIST OF TABLES

Table 2.1: Value of scaling exponent (ν) summarised for some of the theoretical and experimental studies.	51
Table 4.1: Data samples of heavy-ions collected over the span of different years during Run I and II of LHC operation are tabulated giving collision system, center of mass energy per nucleon pair, statistics etc. Datasets used in the present work from specific periods are in bold. “Events” column lists the count of events triggered by minimum bias trigger criteria. The total event counts from the 2011 and 2018 data samples include a combination of minimum bias, central, and semi-central triggered events.	82
Table 4.2: Monte Carlo event samples simulated as per the detector settings in the ALICE Run II.	84
Table 4.3: The track selection parameters used in the present analysis. These cuts are combined together in ALICE as a standard and are termed as <i>Filterbit 768</i> track cuts.	91
Table 4.4: Kinematic cuts and p_T intervals studied in this analysis. Different momentum ranges are used to check the dependence of analysis observables on the momentum, p_T bin width.	91
Table 4.5: Cuts on the TPC tracks used in the analysis for selection of tracks in addition to the cuts used for getting better closure at all M	98
Table 4.6: Intermittency indices (ϕ_q) summarised for $0.4 \leq p_T \leq 0.6$ GeV/ c (narrow) and $0.4 \leq p_T \leq 1.0$ GeV/ c (wide) p_T bins.	111
Table 4.7: Summary of parameters for systematic uncertainty estimations. .	130
Table 4.8: Selection cuts as a standard used for the track selection. These are termed as <i>Filterbit 128</i>	130

CONTENTS

ACKNOWLEDGEMENT	(i)
ABSTRACT	(iii)
LIST OF FIGURES	(ix)
LIST OF TABLES	(xv)

1 INTRODUCTION	1
1.1 Elementary particles	3
1.2 Theory of strong interactions: QCD	4
1.2.1 Femtoscopic to cosmological scales	6
1.3 Quark-Gluon plasma and its evolution	7
1.4 Collision geometry and kinematic observables	10
1.5 Centrality of the collisions	13
1.6 Signatures of QGP formation	13
1.6.1 Strangeness enhancement	13
1.6.2 Jet quenching and high p_T suppression	15
1.6.3 J/ψ suppression	17
1.6.4 Flow	19
1.6.5 Fluctuations	22
1.7 Outline of thesis	26
2 ANALYSIS METHODOLOGY	27
2.1 QCD phase structure	28
2.1.1 Deconfinement	28

2.1.2 Chiral restoration	30
2.2 Phase diagram	31
2.3 Order parameters	34
2.3.1 Breaking of chiral symmetry	34
2.3.2 Polyakov loop	35
2.4 Phase transition and universality	36
2.5 Lattice QCD simulations	38
2.5.1 Critical exponents	39
2.5.2 Scale invariance	41
2.6 Local density fluctuations	41
2.7 Factorial moments and intermittency	43
2.7.1 M -scaling	47
2.7.2 F -scaling and scaling exponent (ν)	48
2.7.3 Fractal observables	52
2.7.4 Recent experimental review	54
3 EXPERIMENTAL SETUP	59
3.1 LHC	59
3.1.1 Main experiments	60
3.1.2 Parameters of heavy-ion beams	62
3.2 ALICE experiment	64
3.2.1 Inner Tracking System (ITS)	68
3.2.2 Time Projection Chamber (TPC)	69
3.2.3 V0 Scintillators	70
3.2.4 Triggering	71
3.3 ALICE: Particle reconstruction and data formats	72
3.3.1 Vertex determination	72
3.3.2 Track reconstruction	73
3.3.3 Data formats and software	75
3.3.4 Centrality determination	77
4 INTERMITTENCY ANALYSIS	81
4.1 Data samples	82
4.2 Monte Carlo simulation samples	83
4.3 Event selection	83
4.3.1 Physics selection	84
4.3.2 Centrality estimators	86

4.3.3 Pileup rejection	87
4.4 Track selection	90
4.5 Observations and results	93
4.5.1 HIJING events analysis	93
4.5.1.1 Closure study	96
4.5.1.2 Fraction of shared TPC clusters	97
4.5.1.3 Observables	100
4.5.2 ALICE data analysis	104
4.5.2.1 Bin content and event factorial moments	105
4.5.2.2 Scaling behaviour of normalized factorial moments	108
4.5.2.3 Scaling exponent (ν)	113
4.5.2.4 Fractal dimension (D_q)	113
4.5.2.5 Comparison of data and Monte Carlo	116
4.5.2.6 Transverse momentum (p_T) dependence	120
4.5.2.7 Centrality dependence	123
4.5.3 Estimation of uncertainties	125
4.5.3.1 Statistical uncertainties	126
4.5.3.2 Systematic uncertainties	128
4.6 PYTHIA8/Angantyr event analysis	130
5 SUMMARY AND CONCLUSIONS	141
BIBLIOGRAPHY	145
SERVICE WORK IN TRD	167
ANALYSIS CODES AND DATA LISTS	179
SUPPLEMENTARY FIGURES	184
 LIST OF PRESENTATIONS	 191
LIST OF PUBLICATIONS	193

INTRODUCTION

The quest to understand the fundamental nature of the matter has spanned centuries, evolving from ancient philosophical notions to sophisticated modern theories. In ancient Greece, matter was initially conceived as being composed of four fundamental elements: water, earth, fire, and air. This early framework eventually gave way to a more nuanced philosophical concept involving indivisible particles, termed as *atoma* and now termed as “atom”. The first scientific revival of atomic theory in the early 19th century was marked by english school teacher, John Dalton’s postulates given in 1808, which redefined matter as composed of discrete units.

Early 20th century saw significant advancements in the atomic theory paving way for nuclear physics and eventually later to the high-energy physics. This can be said to begin in 1897 with the discovery of electron by J. J. Thomson, a negatively charged subatomic particle and discovery of radioactivity by Henri Becquerel and by Marie Curie. Going beyond Becquerel’s work, she gave a crucial hypothesis: “the emission of rays by the uranium compound could be an atomic property of the elements – something built into the very structure of its atoms”. This was followed by the pioneering work of Ernest Rutherford, Hans Geiger, and Ernest Marsden, who, through their experiments, identified the positively charged nucleus at the center of the atom. Niels Bohr expanded atomic theory by introducing the planetary atomic model in 1913, integrating quantum mechanics to explain the structure of the atom [1,2]. The understanding of atomic structure was further advanced by the discovery of proton in 1919 followed by the discovery of neutron by James Chadwick in 1932, which established that the nucleus of an atom includes protons and neutrons. This was the beginning of

nuclear physics. Later with discovery of more particles like pions, muons, new areas of research began like high energy physics, particle physics etc. As high-energy experiments progressed, the discovery of numerous short-lived particles highlighted the need for a more comprehensive classification system. Murray Gell-Mann's introduction of the quark model provided a framework for categorizing these particles with their constituents named *quarks* [3], based on the SU(3) group symmetry. Although initially a theoretical construct, existence of quarks was experimentally confirmed in the 1970s through deep inelastic scattering experiments at the Stanford Linear Accelerator Center (SLAC) [4]. The force that keeps the neutrons, protons and their constituents inside the nucleus is the strong nuclear force. The validation of quantum chromodynamics (QCD), the theory of strong interactions, was achieved in 1979 with the discovery of gluons through three-jet events, confirming the role of gluons in mediating the strong force between quarks [5]. This marked a significant milestone in our understanding of fundamental particles and their interactions, leading to the intricate and dynamic field of particle physics that focuses to explore the elementary constituents of matter and the interactions between them.

Particle physics delves into this study by trying to answer: What are the elementary constituents of matter? How do these particles interact, and what insights can they provide about the origins and structure of the cosmos? Direct observation of theoretical and experimental particles at subatomic scale is beyond the capabilities of the conventional microscopy. Replicating the conditions of the early universe to take out studies at these scales and energies presents significant challenges. To overcome these limitations, particle accelerators and colliders, such as Relativistic Heavy Ion Collider (RHIC), USA and Large Hadron Collider (LHC) [6] at CERN, are employed to simulate the extreme conditions of the primordial universe. By accelerating particles to velocities approaching the speed of light and inducing high-energy collisions, scientists aim to recreate the conditions that existed just a few microseconds after the Big Bang. These collisions produce a state of matter known as the quark-gluon plasma (QGP) [7–10], where quarks and gluons, the fundamental constituents of protons and neutrons, are liberated from their usual confinement and move freely.

The quark-gluon plasma, though ephemeral, leaves behind discernible signatures that can be studied experimentally. For example, the ALICE (A Large Ion Collider Experiment) [11] experiment at the LHC, equipped with a comprehensive array of detectors, is instrumental in analysing these signatures. By scrutinising the particles (and their distributions) that result from the quark-gluon

plasma's transition back to ordinary matter, valuable insights into the properties and behaviour of the QGP can be gained. Among the various observables used to characterise the strongly interacting matter produced in these collisions [7,12], fluctuations in the number of particles (multiplicity) produced are of particular significance. These fluctuations, that pertain to variations in the particle production and their various distributions across different collision events, offer an understanding of the formed system dynamics.

The measurement central to this research work is the analysis of multiplicity fluctuations using the technique of intermittency. This chapter briefly introduces the field of high-energy physics, and concludes with an outline of the whole thesis..

1.1 Elementary particles

The four known forces in the nature are gravity, electromagnetic, strong and the weak nuclear forces. *Standard Model* is a successful model that describes the interaction among three of these forces (except gravity) and the elementary particles. Elementary particles are the fundamental building blocks of matter in the universe. There are three main groups of fundamental particles within the Standard Model: leptons, quarks and bosons (summarised in **Figure 1.1**) [13]. Leptons include charged particles like electrons and chargeless neutrinos, while quarks are further divided into six types (up, down, charm, strange, top, bottom) which combine to form hadrons. Hadrons are composite particles categorized into baryons (which consist of three quarks) and mesons (which consist of a quark-antiquark pair). These leptons and quarks are classified into three generations. The higher generation particle correspond directly to higher particle mass but to a lower particle stability. This instability is responsible for the decay of higher-generation particles into their lower-generation counterparts. As a consequence, the predominant composition of matter in the universe comprises primarily of (*u*) and (*d*) quarks, alongside electrons.

Bosons, which include gluons, W^\pm , Z^0 bosons, and the Higgs boson, are force carriers that mediate interactions among particles. Gluons mediate interactions among quarks through the strong force by exchanging the strong charge, commonly referred to as *colour*. Quarks (*q*) and gluons (*g*) exhibit colour charges – red, green, and blue. When forming a hadron, quarks must combine in a way that ensures a colour sum of zero, such as red + green + blue = 0 or blue + anti-blue = 0. Under normal conditions, of temperature and density, quarks only exist in bound state called hadron – either as baryons, (qqq or $\bar{q}\bar{q}\bar{q}$) or mesons, ($q\bar{q}$) [14].

Alongside baryons and mesons, experimental evidence of tetraquarks made of $qq\bar{q}\bar{q}$ was confirmed in 2003 by the Belle collaboration [15] while pentaquarks made of $q\bar{q}qqq$ were discovered in 2015 at the LHCb experiment [16]. While quarks can have a single colour charge, gluons exhibit a linear combination of both colour and anti-colour charges. There exist eight gluons, associated with the eight possible colour charges carrying a combination of colour and anti-colour charge. The theory that describes strong interactions by explicating interactions between quarks and gluons is known as Quantum Chromodynamics (QCD)*.

1.2 Theory of strong interactions: QCD

QCD is a well established theoretical framework has been built in the realm of QFT (Quantum Field Theory). The basic equations of QCD are elegant and simple which are derived from a few basic principles. These are symmetric (invariant) under local gauge transformations. However, applying this theory to real-world situations and solving its fundamental equations is a challenge. The main difficulty arises because QCD is a non-abelian theory, meaning that the mediating bosons (gluons) carrying charge also interact and intertwine with each

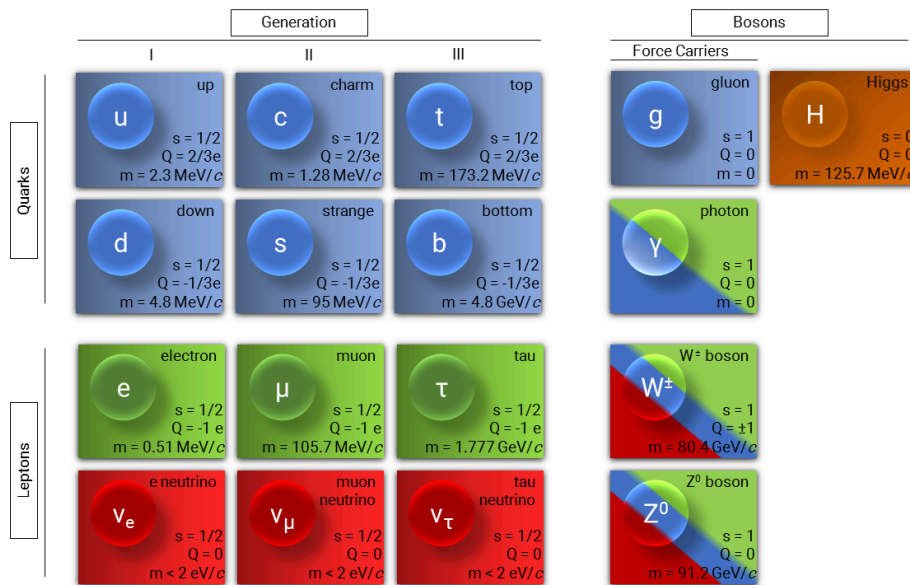


FIGURE 1.1:

Elementary particles described by the Standard Model. The assigned colours in the illustration signify the potential interactions between particles. To illustrate, the gluon, which interacts with quarks, shares a common colour code. Photons can interact with both charged leptons and quarks. W^{\pm} and Z^0 bosons, responsible for particle decays, interact with both leptons and quarks. The Higgs particle interacts with quarks, leptons, and bosons.

*Derived from the Greek word “chromos” = colour

other, distinguishing it from Quantum Electrodynamics (QED) [17]. Despite numerous symmetries present in the (classical) QCD Lagrangian, many of these seem to be broken in the actual physical world. The most noticeable difference between theory and observation lies in the fact that the fundamental particles such as quarks and gluons are not found freely. They are rather confined within hadrons. Under high temperature and pressure, matter organises into colour-singlet resonances. The theoretical understanding of this quark confinement is not yet complete; however, lattice QCD calculations [18] have confirmed its existence. This phenomenon is known as *colour confinement*. When an effort is made to separate, for example, Figure 1.2 depicts two closely bound quarks, the energy in the field between them becomes sufficient to produce a quark-antiquark pair.

The unique nature of gluons, possessing colour charges, enables them to interact freely with one another by radiating additional gluons. This stands in contrast to the behaviour of photons, which do not exhibit self-interactions in the electromagnetic force. The phenomenon of anti-screening manifests itself as particles with colour charges, such as quarks and gluons, are enveloped by a dynamic colour field [19]. This field is a consequence of gluon self-interactions, leading to the qualitative observation that the colour field surrounding particles with colour charges strengthens with increasing distance, opposing the behaviour seen in the electromagnetic force. Unlike QED, where charges experience screening effects at short distances, in QCD, quarks and gluons experience a decrease in interaction strength as they come closer together. This phenomenon is known as *asymptotic freedom* [19,20].

The potential of strong interactions between quarks and gluons can be approximated as [14]:

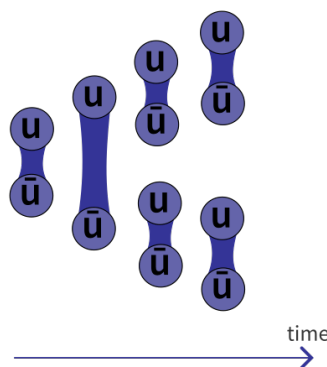


FIGURE 1.2:

A quark-antiquark pair gets created as potential between two quarks increases with increasing separation.

$$V = -\frac{4}{3} \frac{\alpha_s}{r} + kr. \quad 1.1$$

where r is the distance between two quarks, α_s is the coupling constant of strong interactions, k is the strength of the linear term and the second term (kr) represents the linear (or confinement) part of the potential, which increases linearly with the distance r . At small distances, the strong potential behaves akin to the Coulomb potential, resembling a quasi-free interaction. However, as the distance increases, the potential intensifies, leading to the strong confinement of quarks into hadrons. Remarkably, the closer the quarks are to each other, the weaker the confining force becomes. This transition from strong confinement to quasi-free behaviour is what characterises asymptotic freedom in the context of QCD. It suggests that at high momenta, or equivalently at short distances, a particle can effectively penetrate the strengthening colour field. In the early universe, where energy scales were massive and corresponding length scales were small, particles with colour charges moved with relatively little constraint due to the weakening of the colour field at high energies.

1.2.1 Femtoscopic to cosmological scales

According to the most acceptable theory, the Big Bang theory [21], about the creation of the universe, at the very beginning, the universe existed in an extremely small and highly energetic state. Other leading scientific theories such as Grand Unified Theory (GUT) propose that all fundamental forces—gravity, electromagnetism, strong nuclear, and weak nuclear forces were unified at this initial moment. As the universe expanded, gravity decoupled from this unification first, approximately after 10^{-36} seconds [22,23]. It was followed by the separation of strong and electroweak force, leading to a significant expansion that caused the universe's size to increase. Fast forward to around 10^{-33} seconds after the Big Bang, quarks began to emerge. In this early universe, shortly following the Big Bang, conditions were extremely hot and dense, characterized by a phase referred to as the Quark-Gluon Plasma (QGP). Quarks and the exchange bosons (gluons), the fundamental constituents of matter, are thought to be asymptotically free in QGP [24], meaning they were not bound together as they typically are at lower temperatures. After about 10^{-6} seconds, the universe started to cool down. Once temperatures fell below 10^{12} K, most of these particles decayed or annihilated, leaving a residual collection of protons and neutrons. This transition marks a critical juncture in the evolution of the universe, as it began its journey from an intensely hot and dense state to the diverse and expansive cosmos that we observe today [25].

Following this transitory period, universe remained in an extremely hot state, with temperatures high enough to produce electron-positron pairs. However, as the universe rapidly expanded and cooled, temperatures dropped below 10^{10} K, reducing the frequency of electron-positron pair production. Despite this, a slight excess of electrons over positrons persisted due to a small imbalance between matter and antimatter. As the universe continued to cool, quarks began to combine, forming hadrons such as protons and neutrons. Approximately 10 seconds after the Big Bang [21], these hadrons combine to form light nuclei, such as deuterons and helium, through a process known as *nucleosynthesis*. The relative abundances of protons, deuterons, and helium observed in the universe today provide insight into the conditions during this nucleosynthesis phase [26].

As the universe cooled further, with temperature dropping below 3000 K around 400,000 years post-Big Bang, neutral atoms were formed from the combination of electrons and nuclei. This process, termed as recombination allowed the free moment of photons, resulting in the separation of matter and radiation. This event resulted in cosmic microwave background radiation, a remnant of this epoch, providing a snapshot of the universe at that time [21]. The Big Bang theory aligns well with contemporary observations of the universe. However, several critical details about the early universe, particularly the dynamics of the quark-gluon plasma phase, remains enigmatic. Understanding these processes not only sheds light on the fundamental forces at play during the universe's infancy but also bridges the gap between femtoscopic scales – where quarks and gluons interact – and cosmological scales, where the large-scale structure of the universe is shaped [23,27].

1.3 Quark-Gluon plasma and its evolution

Quark-Gluon Plasma (QGP) is a state of matter characterized by the deconfinement of quarks and gluons, which are the fundamental constituents of protons and neutrons. In this state, these particles are no longer bound together by the strong force, allowing them to move freely in a hot and dense medium. The concept of QGP emerged in the context of extremely high energy densities. Experimental searches for the QGP began at BNL's (Brookhaven National Laboratory, USA) AGS (Alternating Gradient Synchrotron) and CERN's (European Organisation for Nuclear Research) SPS (Super Proton Synchrotron), leading to a claimed discovery in 2000 [28]. This discovery was confirmed by four main experiments at the Relativistic Heavy Ion Collider (RHIC) in BNL [29–32] in

2005. ALICE (A Large Ion Collider Experiment), at CERN joined the quest in 2010, adding more insights into QGP properties [33,34].

Exploring the creation and evolution of the QGP in experiments like at LHC or RHIC involves studies that rely on combining various accurate measurements to glean insights into the plasma. Asserting QGP creation in an experimental setting necessitates the study of multiple observables [35]. Key information available for exploring the QGP in ultra-relativistic heavy-ion collisions [36], key observables and some related theories are discussed below.

As a state of matter where quarks and gluons are not confined within the hadrons, the QGP provides crucial insights into the conditions of the early universe and the properties of strong interactions. Studying QGP's evolution in the laboratory involves analysing how this state of matter evolves during heavy-ion collisions [14,37,38], which helps elucidate the dynamics of quark-gluon interactions and the underlying physics of the strong force. QGP expands and cools rapidly, typically within time scales on the order of 1 fm/c, thus it is not observed directly. However, its creation and evolution impact the final distributions of the particles observed in the experiments [39].

The QGP formation requires extreme conditions of high energy density and temperature, which can only be achieved in the laboratory through relativistic heavy-ion (A-A) collisions. High energy densities exceeding 12 GeV/fm³ are attained for $\sqrt{s_{NN}} = 2.76$ TeV within 1 fm (or 3×10^{-23} s) approximately after the collision. This energy density is more than 20 times that of a proton's density (450 MeV/fm³) [24]. These conditions are consistent with the values predicted by the lattice QCD over 300 MeV. The number of particles produced at these energies in these collisions is immense, resulting in a significant increase in entropy [40]. While the entropy of the nuclei colliding initially is zero, the collision produces a large number of particles, thereby increasing the entropy significantly. At $\tau = 0$, the instantaneous positions of the nucleons is described by the transverse structure of the nuclei, whereas high nuclei contraction leads to the maximum value of energy density. A low momentum transfer is experienced by most of the participating quarks and gluons (soft collisions). These are primarily dominated by gluon interactions. Only a few constituents experience hard collisions and most of the entropy production occurs during this initial moment.

Figure 1.3 gives a visual representation of the QGP evolution during a relativistic heavy-ion collision. It is shown that collision of nuclei takes place at $(t, z) = (0, 0)$, and z, t denote the space and time dimensions. By employing parameters that are invariant under Lorentz transformations, a clearer picture of

the dynamics can be achieved. The proper time, for example, serves as a key variable to track the evolution of the QGP in a consistent manner across different reference frames. **Figure 1.3** shows the evolution of the system formed after the collision of two heavy ions at high energies. A neat way to do this is to use proper time of these particles, which is given as:

$$\tau = \sqrt{t^2 - z^2}. \quad 1.2$$

In **Figure 1.3**, $t^2 - z^2 > 0$ is called time-like region and $t^2 - z^2 < 0$ is referred to as the spacelike region. After the collision, particles are produced in phases that include:

1. **Pre-equilibrium** ($0 < \tau < \tau_0$) : During the pre-equilibrium stage, the system is characterised by rapid fluctuations and strong interactions among the constituent quarks and gluons. τ_0 represents the proper time at which significant thermalization begins in the system after the initial collision. It marks the transition from rapid fluctuations to a more stable state where interactions among particles start to align with thermal equilibrium. This stage is crucial for understanding how the system transitions from a state of high energy density and low temperature to one where quarks and gluons become deconfined. The dynamics of this phase can be modelled using various approaches, for example the Color Glass Condensate (CGC) [41], which accounts for the high density of gluons and the non-linear dynamics that arise from their interactions. At extremely small distances and high energies, the number of gluons becomes so large that traditional methods, like perturbative QCD, becomes less effective. The CGC model considers a saturated state where the gluon density is so high that additional gluons do not significantly alter the dynamics. The colour fields generated in CGC when highly saturated gluons collide play a crucial role in the early stages of a collision [41]. The initial state resulting from the collision, characterised by these strong color fields and high gluon densities, is referred to as *glasma*. Glasma is considered to be out of equilibrium and represents a state of hot, dense, and strongly interacting matter that precedes the QGP formation [42].
2. **QGP phase and phase transition** ($\tau_0 < \tau < \tau_{ch}$) : As the system evolves under extreme conditions, quarks and gluons undergo deconfinement, forming the QGP. Simultaneously, thermalisation occurs, aligning particle energies and momenta with a thermal equilibrium state at high temperatures. The QGP phase also exhibits properties such as collective flow [43], which are indicative of its fluid-like behaviour [24,44]. Theoretical models, such as lattice QCD, are used to study this transition and predict the properties of the QGP,

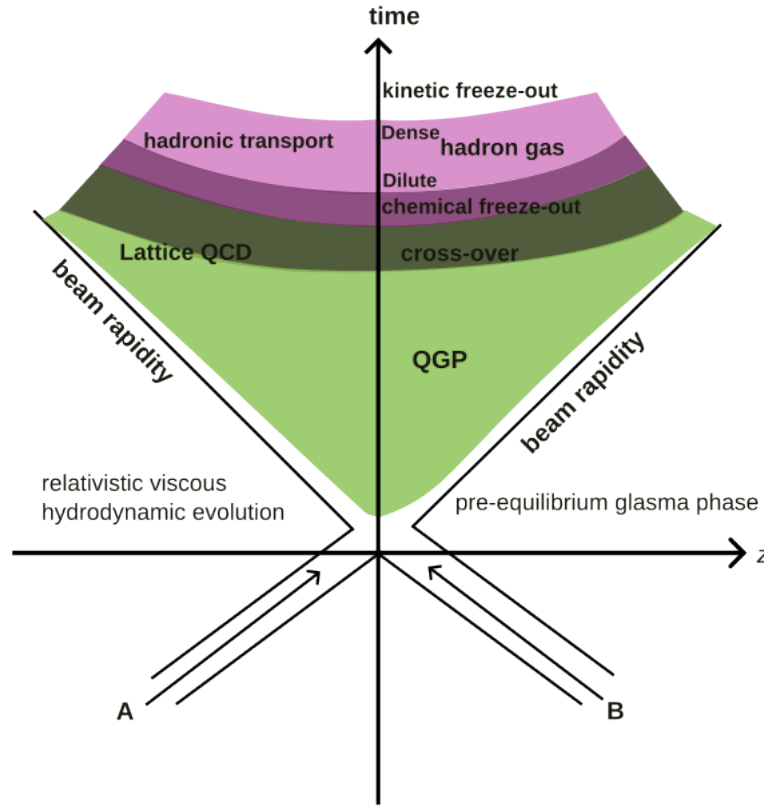
including its temperature, density, and viscosity. The QGP is characterized by a high degrees of freedom, where quarks and gluons behave as nearly free particles helps to understand the strong interactions that govern the behaviour of fundamental particles. The transition from the hadronic phase to the QGP phase involves significant changes in the entropy and energy density of the system.

3. **Freeze-out** ($\tau_{ch} < \tau < \tau_f$) : After thermalisation, the system undergoes “chemical freeze-out” at critical temperature T_{ch} and proper time τ_{ch} , where particle interactions become less frequent, fixing the relative abundances of the particles. Next, hadronisation occurs as quarks and gluons recombine into stable particles and system transition into the hadronic phase. In this phase, stable hadrons interact through the residual strong force. The system then progresses to “kinetic freeze-out” at T_f and proper time τ_f , where remaining interactions essentially cease, fixing particle momenta. This marks the conclusion of the dynamic evolution of the strongly interacting matter.

Upon achieving equilibrium after the collision, the prevailing hypothesis posits a subsequent hydrodynamic evolution within the system, akin to the smooth, cohesive flow characteristic of a liquid. The salient feature of this hydrodynamical system lies in its minimal shear viscosity, often referred to as a “perfect liquid” [45]. Shear viscosity is the resistance a fluid presents against deformation. Minimal shear viscosity indicates that gluons and quarks interact strongly, defining the state of “sQGP” (strongly interacting Quark-Gluon Plasma) [46]. Unlike the confined state of quarks within hadrons, the sQGP allows quarks and gluons to interact strongly in a deconfined state. The QGP produced at the LHC and RHIC is thus recognized as the sQGP [29], demonstrating behavior more akin to a strongly interacting fluid rather than a gas of nearly-free quarks and gluons [46].

1.4 Collision geometry and kinematic observables

It is important to understand the geometry of the collision in high energy experiments such as at the LHC. The arrangement and orientation of the detectors, as well as the angles and momentum of the particles, are crucial for interpreting collision events, that helps in reconstructing particle trajectories, determining energy distributions, and analysing collision dynamics. In the conventional coordinate system which is used in a heavy-ion collision considers: z direction aligned with the beamline, and the point where particles collide is termed as the interaction point (IP_z), measured along the z -direction. The y -axis is vertical, and the x -axis

**FIGURE 1.3:**

Schematic description of the evolution of the system created by two heavy-ion colliding beams (A and B) in time and space (beam direction, z). First, there's a pre-equilibrium phase, then it turns into strongly interacting Quark-Gluon Plasma (sQGP). Finally, the system reaches chemical freeze-out, becoming a state where particles form a hadronic gas.

is horizontal, perpendicular to the beamline. The azimuthal angle, φ is an angular coordinate that signifies the rotation of a particle around the beamline in the plane perpendicular to the beam direction. It ranges from 0 to 2π , representing a full circle around the beamline. The angle relative to the beam axis is called polar angle, denoted as θ . In relativistic heavy-ion collisions, the total energy (E) of a particle is a combination of its rest mass energy and kinetic energy. For highly relativistic particles, where the kinetic energy vastly exceeds the rest mass energy, the total energy approximates the particle's momentum. Transverse momentum (p_T) is the component of momentum perpendicular to the direction of beam axis. It is a conserved quantity in the plane perpendicular to the beam axis. High p_T particles often result from jet production, where quarks or gluons fragment into a spray of particles. Measuring p_T helps in studying the energy loss of partons in the QGP and hadronisation [47].

Rapidity, y which is an important observable in the particle physics is given mathematically:

$$y = \frac{1}{2} \ln \left(\frac{E + p_z}{E - p_z} \right), \quad 1.3$$

where E is the total energy of the particle and p_z is the component of momentum along the direction of beam axis. *Pseudorapidity*, is another alternative parameter that is used to describe the direction of a particle's momentum relative to the beamline. It is determined using the polar angle (θ) of the particle in the laboratory frame, estimating how close a particle's trajectory is to the beamline. It is defined as:

$$\eta = -\ln \left(\tan \left(\frac{\theta}{2} \right) \right). \quad 1.4$$

At relativistic speeds, it is assumed that mass of the particles, $m \ll p$, i.e, $E \rightarrow p$. Thus, $y \approx \eta$ for relativistic particles. High η values indicate particles travelling close to the beamline (**Figure 1.4**), while lower values suggest particles moving more perpendicular to it. Measurement of pseudorapidity (η) is preferred in high-energy experiments in place of rapidity, y since the mass of particles is not experimentally directly measurable. Also, differences in pseudorapidity between particles remain Lorentz-invariant under boosts along the z -axis, making pseudorapidity a preferred choice for describing particle positions [47].

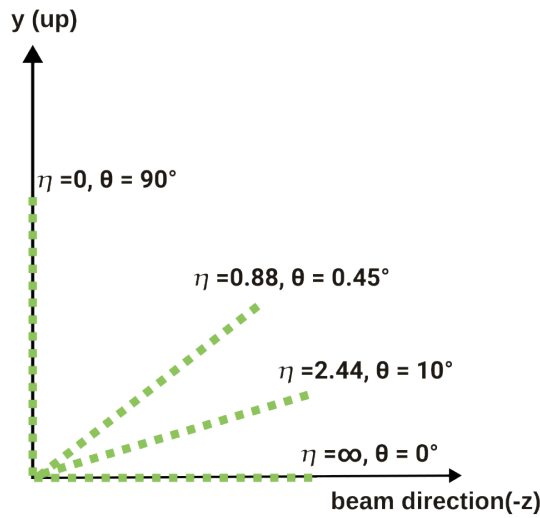


FIGURE 1.4:

Sketch of the coordinate system at ALICE, which is visualised as a cylinder, with its center aligned at the interaction point (IP_z).

1.5 Centrality of the collisions

The quantities like number of participants (N_{part}), spectators (N_{spec}), or binary collisions (N_{coll}) are some key parameters to understand the geometry of particle collisions. N_{part} represents the total count of nucleons (protons and neutrons) that actively participate in the collision, reflecting the density and volume of the interacting region. N_{spec} refers to nucleons in the colliding nuclei that do not engage directly in the collision but remain outside the interaction zone, influencing the global geometry and particle emission. N_{coll} measures the total count of individual nucleon-nucleon collisions within the nucleus-nucleus collision, directly related to the energy deposited in the collision zone. While quantities like N_{part} , N_{spec} or N_{coll} can't be directly measured in a collision, centrality, a measurable parameter, serves as a proxy for these geometric quantities. Centrality is defined as the degree of overlap between colliding nuclei. Impact parameter (b) defines the transverse distance between the centers of the colliding nuclei and determines the size of the overlapping region in a nucleus-nucleus collision.

Higher centrality corresponds to more central collision with greater overlap between the nuclei as shown in **Figure 1.5**, leading to increased particle production and a higher probability of QGP formation. In contrast, “least central” collisions occur when the nuclei barely overlap, resulting in fewer interactions and different physics outcomes. The significance of centrality lies in its ability to influence the dynamics of the collision, where different centralities yield distinct physics phenomena, such as varying particle yields, energy distributions, and the formation of different states of matter [48].

1.6 Signatures of QGP formation

The signatures of QGP are identified through the study of particles produced during the hadronisation phase of the system. However, to confirm presence of QGP, it is essential to analyse observables that remain unaffected by the hadronisation process but are sensitive to the conditions prevalent during the QGP phase [33]. A few of the important signatures are discussed below:

1.6.1 Strangeness enhancement

The manifestation of strangeness enhancement in Quark-Gluon Plasma is believed to arise from an increased strangeness content compared to normal hadronic matter [49,50]. In the initial state, strange quarks do not exist as valence quarks; however, their creation is facilitated during the collision due to their

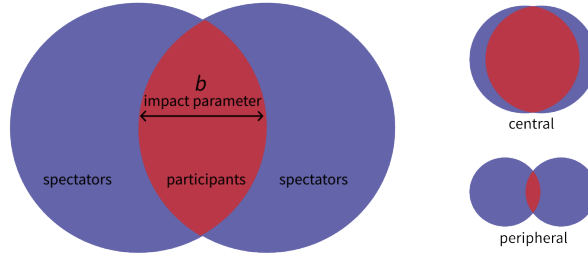
**FIGURE 1.5:**

Illustration depicting impact parameter in a heavy-ion collision. Spectators are particles that observe the collision, participants actively engage in the collision process, and binary collisions involve direct interactions between individual nucleons.

relatively lighter mass compared to other heavier quark flavors, such as charm or bottom quarks. This production occurs through processes like string fragmentation, gluon splittings ($g \rightarrow s\bar{s}$) etc. The introduction of these strange quarks by these processes contribute to an increase in the ratio of strange to non-strange particles within the system so created during the collision.

A dense concentration of up (u) and down (d) quarks is found in the QGP. As quarks are fermions, they follow the Pauli exclusion principle, which asserts that two identical fermions cannot occupy the same quantum state at the same time. It impedes the creation of $u\bar{u}$ and $d\bar{d}$ pairs because the existing up and down quarks in the QGP may already occupy the available quantum states. But the creation of $s\bar{s}$ pairs is favoured, despite their higher mass relative to up and down quarks. This preference can be attributed to the dynamics of the QGP, where the energy available during heavy-ion collisions is sufficient to produce strange quarks. This enhancement can be interpreted within a purely hadronic framework, wherein the abundance of strange quarks gradually increases through a series of rescattering processes. To understand this, an examination of particles less likely to be produced by hadronic rescattering, such as $\bar{\Lambda}$ (composed of $\bar{u}\bar{d}\bar{s}$) and multistrange baryons, becomes essential [48].

In string fragmentation models, the production dynamics of strange quarks differ from those of up and down quarks, with the former being heavier, leading to a reduction in their overall production. This discrepancy is particularly pronounced in comparison to p–p collisions. Intriguingly, heavy-ion collisions exhibit a discernible relative increase in the production of strangeness compared

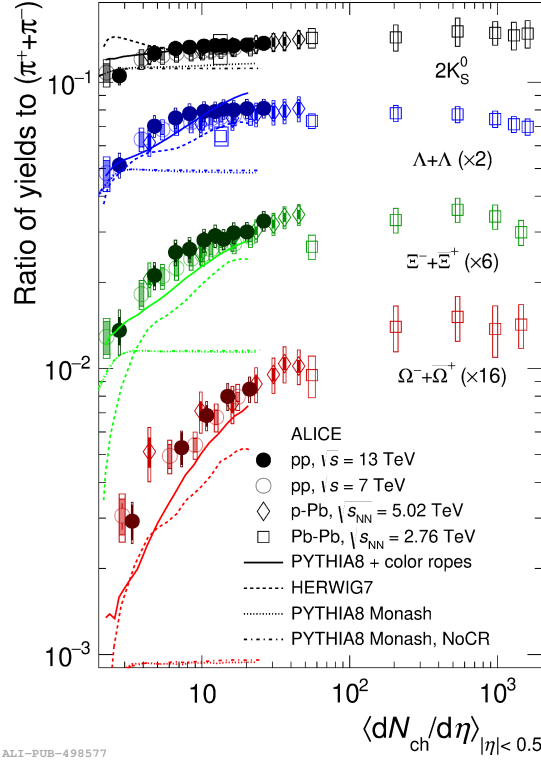


FIGURE 1.6:

Strangeness enhancement reported by ALICE in [51]. Integrated strange hadron to pion ratios as a function of $\langle dN_{\text{ch}}/d\eta \rangle$. An increase in the yield up to $\langle dN_{\text{ch}}/d\eta \rangle \approx 10^2$ can be seen and a flattening of yield after it. The model calculations are from microscopic string fragmentation models (various tunes of PYTHIA8 and HERWIG7) for p-p, $\sqrt{s_{\text{NN}}} = 13\text{TeV}$.

to p-p collisions. This divergence is illustrated in Figure 1.6, showing the yield ratios of various strange particles (K_0 , Λ , Σ , Ω) relative to the yield of pions.

1.6.2 Jet quenching and high p_T suppression

Jet quenching is a key signature of the presence of QGP and its properties [52]. When coloured quarks traverse the QGP, they interact with other coloured partons, leading to energy dissipation through a process known as *gluon-bremsstrahlung*. In this mechanism, gluons are emitted from the quarks as they engage in strong interactions with the medium, analogous to how charged particles emit photons in electromagnetic Bremsstrahlung.

As the system expands and hadronization begins, high-energy partons produce collimated sprays of particles, called *jets*. However, when these jets move through the QGP, they lose energy due to interactions with the plasma, resulting in *jet quenching*. This phenomenon manifests as a reduction in the jet's energy and an increase in its radius, observable in experimental event displays [53]. For instance, in cases where a dijet pair is created at the periphery of the plasma, one

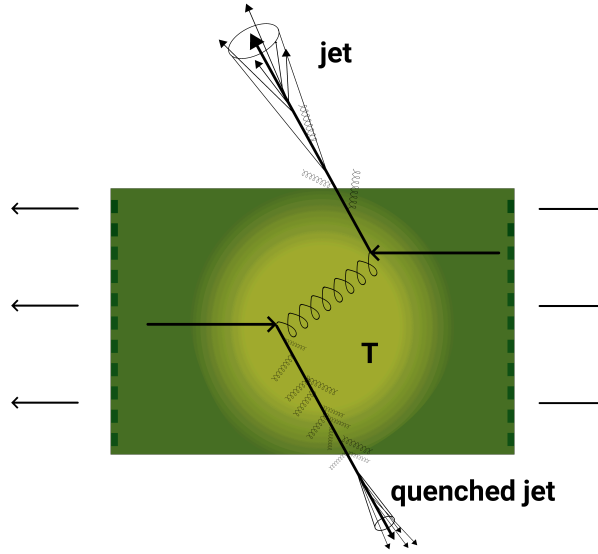


FIGURE 1.7:

Schematic representation of Jet quenching wherein the jet that goes in up direction is more or less unaffected whereas the one going in down direction is quenched in the QGP medium.

jet traverses the QGP while its partner moves away. The jet that interacts with the QGP undergoes significant energy dissipation, leading to a lower energy and wider radius compared to the other jet. This indicates that the jet has been quenched. In a heavy-ion collision, if QGP is created the result would be a strong jet and a much weaker jet production. These move in opposite direction to each other. The weaker jet will contain more particles. A schematic view of jet production in an experiment where jet-quenching has occurred is shown in **Figure 1.7**.

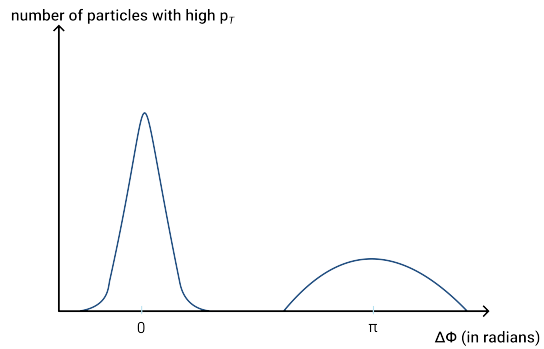


FIGURE 1.8:

Illustration of quenched and un-quenched jet. Trigger jet is the un-quenched jet is represented by the left peak. It contains more high transverse momentum, p_T particles compared to quenched jet, shown by the right peak.

The number of particles with high transverse momentum (p_T) as a function of the azimuthal angle ($\Delta\Phi$) between these particles and a reference jet is shown in **Figure 1.8**. The left peak represents the un-quenched jet, and the right peak represents the quenched jet. The un-quenched jet has a higher number of particles with high p_T due to its higher initial energy or momentum and the absence of quenching.

High hadron p_T suppression is a phenomenon closely associated with jet quenching. This effect implies that when a Quark-Gluon Plasma (QGP) is formed during a collision, there will be a reduced observation of hadrons with high transverse momentum (p_T). The underlying reason for this suppression is the energy loss that occurs as high-energy partons traverse the QGP, which results in fewer high-energy jets being detected. Jet quenching specifically requires a particular geometry, wherein jets are produced near the edge of the QGP. In contrast, high p_T suppression can be observed without such geometric constraints. The suppression effect leads to a shift in the transverse momentum spectrum of hadrons towards lower values, indicating a significant loss of energy among the high-energy partons as they pass through the plasma. This suppression can be observed regardless of the jet production location relative to the QGP, making it a more general signature of the QGP formation in heavy-ion collisions.

1.6.3 J/ψ suppression

Quarkonium is a flavourless meson, i.e., a meson which comprises of a heavy quark and the corresponding anti-quark. It was theoretically predicted that the phenomenon of deconfinement induced by the QGP can result in quarkonium suppression. This is based on the idea that an adequately hot and deconfined medium possesses the capacity to dissolve any binding of quarkonium, leading to its suppression in the heavy-ion collisions. This process of quarkonium suppression, often referred to as the “melting” of quarkonia, serves as a signal of the QGP phase transition.

Different quarkonia are anticipated to experience dissolution at distinct temperatures within the evolving medium. The J/ψ , which has constituents $c\bar{c}$, is the most intuitive quarkonium probe [54] of QGP formation. The J/ψ meson, characterised by a rest mass of 3.1 GeV, is believed to be produced through hard parton-parton interactions in the initial stages of heavy-ion collisions. This means the production yield of J/ψ mesons would align with the number of initial binary parton collisions. Also, one might anticipate detecting more of these charmonium states due to the increased production of c-quarks. It is predicted though that the production of J/ψ mesons is modified when QGP is formed during the collision [54]. This is because in the presence of a QGP, the interaction between the charm and anti-charm quark experiences a weakening effect, primarily influenced by colour-charged quarks and gluons. This phenomenon is known as “Debye screening” that is observed in electromagnetic plasmas also. In normal matter, c-quarks are more prone to combine with each other as there are limited free quarks

available for pairing. In contrast, within a QGP there is an abundance of free quarks. So when the energy density rises, a decrease in the amount of charmonia is seen due to screening. The energy required to dissociate J/ψ is estimated to be about 2.1 times the critical temperature for a QGP (denoted as T_c). For the excited state, the dissociation energy is expected to be much lower, approximately 1.1–1.2 times T_c as per Lattice QCD calculations [55].

The same suppression phenomenon is also seen for another quarkonia, the bottomonium (Υ), representing a coupled quark-anti-quark pair, $b\bar{b}$. Despite the considerably greater mass compared to other charmonium states, the principle of suppression is supposed to be similar as for J/ψ . Quarkonium suppression is analysed relative to collisions where no medium is assumed, such as in p–p collisions. Thus, the ratio of yields exhibit variations due to medium effects. This can be quantified by the nuclear modification factor [56], defined as:

$$R_{AA} = \frac{d^2 N^{AA} / dp_T d\eta}{T_{AA} \cdot d^2 \sigma_{pp} / dp_T d\eta}, \quad 1.5$$

with T_{AA} representing the nuclear overlap function in nucleus-nucleus collision, evaluated with a Glauber-Model Monte Carlo calculation [57], and is $= \frac{\langle N_{coll} \rangle}{\sigma_{inel}^{NN}}$ where $\langle N_{coll} \rangle$ is the average number of elementary p–p collisions in an A–A collision, and σ_{inel}^{NN} is the inelastic nucleon-nucleon crosssection. R_{AA} can be simplified as:

$$R_{AA} = \frac{\text{yield in A – A}}{\langle N_{coll} \rangle \cdot \text{yield in p – p}}. \quad 1.6$$

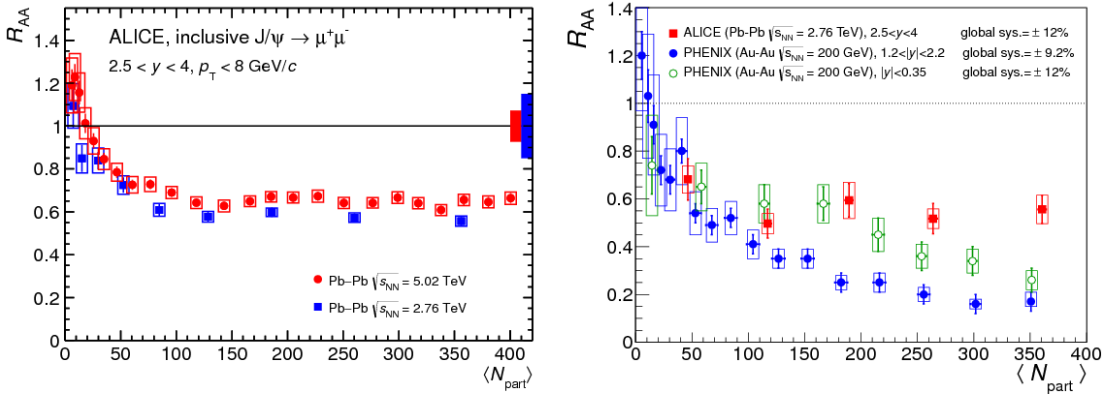


FIGURE 1.9:

A comparison of nuclear modification factor, R_{AA} for $J/\Psi \rightarrow \mu^+ \mu^-$ production between Pb–Pb collisions at $\sqrt{s_{NN}} = 5.02$ TeV and $\sqrt{s_{NN}} = 2.76$ TeV [58](on left). ALICE measurements of R_{AA} for Pb–Pb $\sqrt{s_{NN}} = 2.76$ TeV compared to PHENIX for Au–Au collisions $\sqrt{s_{NN}} = 200$ GeV [59] are also shown.

In **Figure 1.9**, the nuclear modification factor is shown for inclusive J/ψ as a function of $\langle N_{\text{part}} \rangle$, average number of participants for Pb–Pb collisions from ALICE. R_{AA} is closer to one towards least central events, close to p–p conditions. While $J/\psi \rightarrow \mu^+ \mu^-$ suppression is observed at high centralities, away from p–p collisions. A suppression of J/ψ observed is more pronounced with an increasing number of participants (N_{part}), indicating that as collisions become more central, the suppression is expected from screening effects. However, compared to experiments like those at the Relativistic Heavy Ion Collider (RHIC), the suppression at LHC is less prevalent even if this same suppression trend is observed. This observation however, is in line with the regeneration scenario, where more energetic collisions produce additional $c\bar{c}$ pairs, favouring the regeneration of charmonium and compensating for the in-medium melting [48]. Indeed, if there was no regeneration and only suppression mechanisms were involved, one would expect a lower nuclear modification factor at LHC than at RHIC due to the larger temperature of the QGP at LHC.

1.6.4 Flow

When heavy ions collide, the created QGP acts like a perfect fluid and expands together in a coordinated/collective way. This collective behaviour is in contrast to a simple superposition of p–p collisions. *Flow* refers to the collective motion of the particles produced in the aftermath of the collision. This phenomenon serves as an important signature for the presence of QGP, as it indicates that the produced medium behaves not as a disjointed collection of particles but rather as a coordinated entity. Of the various types of flow, collective flow describes this coordinated motion of particles, resembling the fluid-like behaviour of a system. It reflects the interactions and pressure gradients within the QGP [60].

Radial flow specifically pertains to the outward motion of the particles from the central region of the collision. The term “radial” is used because particles tend to move away from the geometric center of the collision zone. This outward expansion is a consequence of the pressure gradients developed in the highly compressed and hot medium formed during the collision. Radial flow explains the transverse expansion of the QGP as seen in the p_{T} spectra of π^\pm , K^\pm , and $p(\bar{p})$ as shown in **Figure 1.10** from [61]. In different collision centralities, the peaks and shapes of the spectra change, with the peak being higher in more central collisions that matches with predictions from hydrodynamics. In these central collisions, the QGP fireball expands evenly and faster than in peripheral collisions, resulting in increased radial flow. Heavier particles are influenced more by radial flow, resulting in distinct patterns in their momentum distributions.

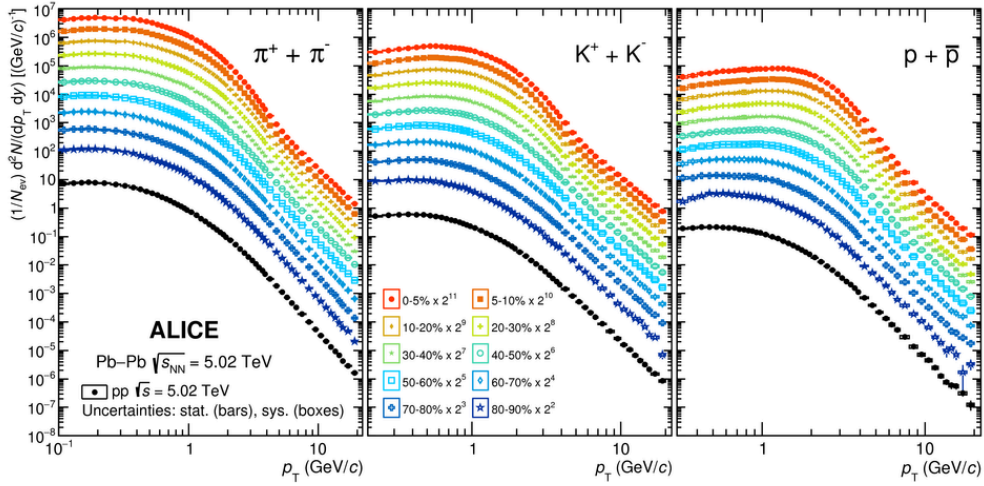


FIGURE 1.10:

Transverse momentum spectra of π^\pm (left), K^\pm (middle) and $p(\bar{p})$ (right) measured for different centrality classes in p-p and Pb-Pb collisions at $\sqrt{s_{NN}} = 5.02$ TeV (ALICE) [61].

Anisotropic flow arises when the initial geometrical shape of the collision zone is not uniform. When heavy ions collide off-center, the initial shape becomes asymmetrical, similar to an *almond*. This happens because the pressure in the medium is stronger in one direction (say, x) compared to the other direction (say, y) as shown in **Figure 1.11**. This asymmetry is called anisotropic flow. It refers to the preferential distribution or collectivity of particles in a certain direction, creating a geometrical shape that is not uniform in all directions.

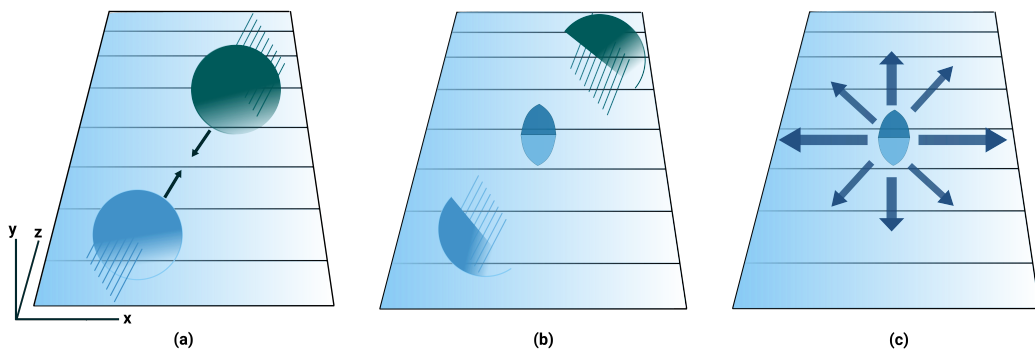


FIGURE 1.11:

Schematic depicting a heavy ion collision wherein the plane shown is the event plane. During the collision of heavy ions, their nuclei overlap and interact. The plasma then expands more significantly in the x -direction compared to the y -direction, leading to the development of an elliptic anisotropic flow. (a) The two ions approach each other. (b) Post-collision, the ions that directly collide are referred to as participants, while the remaining ions are called spectators. (c) The pressure gradients are greater in the x -direction than in the y -direction.

Hydrodynamic models that describe this flow suggest that QGP behaves as a strongly coupled, resembling a perfect fluid [62]. By “perfect fluid,” it is meant that the fluid flows smoothly without much resistance. This smooth flow suggests that the particles within the QGP medium have very short mean free paths [63]. If particles had large mean free paths or more room to move around, the particles would spread out randomly after the collision [63]. The fact that particles do not spread out means there’s something keeping them close together. Anisotropy of the distributed particles is calculated by first performing Fourier expansion of their azimuthal distribution and then measuring its Fourier coefficients/flow harmonics as [64]:

$$v_n = \langle \cos(n[\varphi - \Psi_n]) \rangle \quad 1.7$$

where, v_n is the n -th order flow harmonic, Ψ_n is the n -th order symmetry plane, φ is the azimuthal angle of produced particles. Fourier/Flow coefficients/harmonics refer to the different patterns or shapes in the spatial anisotropy. First harmonic, v_1 corresponds to directed flow, v_2 represents elliptic flow [65], v_3 represents triangular flow and v_4 is quadratic flow [64]. It is observed that the QGP exhibits fluid-like properties, expanding as a coordinated entity rather than a disjointed collection of particles. This collective expansion results in various types of flow, such as radial flow, where particles move outward from the collision center, and anisotropic flow, which arises from the initial geometric asymmetries of the colliding nuclei. Radial flow is evident in the transverse momentum spectra, with heavier particles experiencing more pronounced effects. Anisotropic flow, characterised by patterns like elliptic and triangular flow, reflects the initial collision geometry and the pressure gradients within the QGP. Hydrodynamic models that account for these flows suggest that the QGP behaves as a nearly perfect fluid, with very short mean free paths for its constituents, leading to smooth, collective expansion.

Early investigations into anisotropic flow primarily focussed on elliptic flow (second harmonic flow) represented by v_2 . It arises from the almond-shaped geometry of the matter produced in the collision. Recent studies have expanded their focus to include fluctuations in the flow coefficients. These fluctuations stem from differences in various factors at the initial stage of collision, encompassing factors like nucleon positions and colour charges within the colliding nuclei [66]. Furthermore, fluctuations lead to the presence of v_3 and v_4 at all centralities, highlighting their impact [67,68].

The ALICE collaboration's measurement of the centrality-dependent integrated flow at midrapidity is shown in **Figure 1.12**. The results compare v_n values measured in Pb–Pb collisions at $\sqrt{s_{\text{NN}}} = 2.76$ and 5.02 TeV are given and compared with hydrodynamic calculations. In part (a) of this figure, anisotropic flow is shown integrated over the transverse momentum p_T interval of $0.2 < p_T < 5.0$ GeV/ c as a function of centrality using two-particle and multi-particle cumulants (with $|\Delta\eta| > 1$). Parts (b) and (c) show the ratios between $v_n\{2, |\Delta\eta| > 1\}$, and $v_2\{4\}$ at 5.02 and 2.76 TeV. Integrated flow exhibits a rise with increasing centrality, reaching up to 40–50% centrality. Among the flow coefficients, v_2 demonstrates the most pronounced dependence on centrality compared to v_3 and v_4 . To suppress non-collective correlations, a η gap between the measured particles is considered.

1.6.5 Fluctuations

Fluctuations in various measurable quantities are expected to become significant at the onset of quark-gluon plasma formation, near the critical point, or during the phase transition as the system expands. These fluctuations, characterised by higher-order moments of distributions beyond the first moment, provide critical insights into the dynamics of the processes involved in collisions. Enhanced

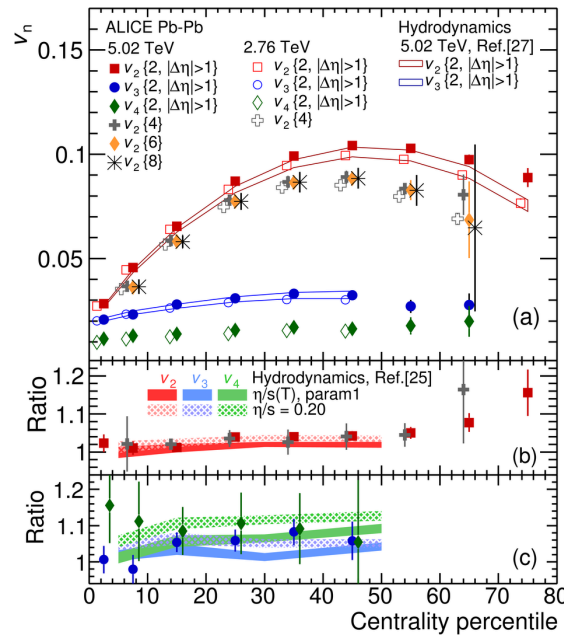


FIGURE 1.12:

ALICE integrated flow measurements for the flow coefficients $v_n\{m\}$, n different harmonics from different orders of m -particle correlations as a function of centrality in Pb–Pb collisions at $\sqrt{s_{\text{NN}}} = 2.76$ TeV (open markers) and $\sqrt{s_{\text{NN}}} = 5.02$ TeV (closed markers) [69]. Hydrodynamic calculations are taken from [70] in (a) and from [71] in (b).

fluctuations, particularly in observables such as particle multiplicity and transverse momentum, are expected during transitions between hadron gas and QGP phases [72].

During phase transition, such as the transition from hadron gas to QGP, if there is critical point, fluctuations in the observables become more pronounced. Specifically at this point, the correlation length diverges, leading to an increased fluctuation signal. To explore these fluctuations, measurement of various event characteristics, including multiplicity, net charge, and mean transverse momentum can be performed. However, these measurements are not solely reflective of physical processes but also include statistical fluctuations and limitations inherent to data collection and detector capabilities. Consequently, accurate analysis requires large datasets to minimise statistical noise and reveal the true nature of the fluctuations.

Scaled variance, often denoted as ω , is a statistical measure that quantifies the relative fluctuations in a distribution. It is defined as:

$$\omega = \frac{\sigma^2}{\mu} \quad 1.8$$

where σ^2 is the variance and μ is the mean of the distribution. In the context of heavy-ion collisions: μ becomes $\langle N_{\text{part}} \rangle$. This ratio provides a normalized measure of the dispersion of the particle multiplicity or other observables, allowing for comparisons across different collision systems or energies. A higher scaled variance indicates greater volume fluctuations in particle production, which can signal the presence of critical phenomena associated with the QGP formation. ALICE in [73] has measured the scaled variance denoted as: $\omega_{\text{ch}} = \sigma_{\text{ch}}^2 / \langle N_{\text{ch}} \rangle$, of charged-particle multiplicity distributions wherein $\langle N_{\text{ch}} \rangle$ is mean and σ_{ch}^2 is the variance of the distribution, respectively. In **Figure 1.13**, panels (a), (b) and (c) on the left shows mean, standard deviation, and scaled variance of distributions with $\langle N_{\text{part}} \rangle$. It shows that the average number of charged particles produced in a collision increases with the number of participating nucleons and the standard deviation, which represents the spread or dispersion of the multiplicity distribution, that increases with $\langle N_{\text{part}} \rangle$. In contrast, the scaled variance, ω_{ch} which quantifies the amplitude of event-by-event fluctuations [74,75] relative to the mean, decreases with increasing $\langle N_{\text{part}} \rangle$, indicating that central collisions exhibit smaller relative fluctuations in charged-particle multiplicity compared to peripheral collisions. Both HIJING and the AMPT (string melting) models successfully reproduce first two trends, but fail

to produce ω_{ch} trend. While the particle multiplicities are directly proportional to the cross sections, the distributions' widths are influenced by various sources of fluctuations and correlations. These include long-range correlations, Bose–Einstein effects, resonance decay processes, and the constraints imposed by charge conservation. Panels on the right of **Figure 1.13** show a comparison between ALICE [73] and PHENIX [76] results. The scaled variance, ω_{ch} is larger at the LHC energy compared to RHIC energies for the same acceptance. It suggests that while higher energy collisions lead to a larger number of particles produced, the relative fluctuations in multiplicity are also larger at higher energies.

Transverse momentum fluctuations are another essential fluctuations observable in the study of the QGP. These fluctuations are calculated by identifying charged particles, measuring their transverse momentum (p_{T}) and then calculating $\langle p_{\text{T}} \rangle$ event-by-event. The p_{T} distribution of the particles is expected to follow a Boltzmann-like distribution in a thermalised system, which is indicative of a well-defined temperature. A higher mean p_{T} suggests that particles are more energetic, which can be a sign of effective thermalisation. Conversely, if the mean p_{T} is low, it may indicate that the system has not yet reached thermal equilibrium.

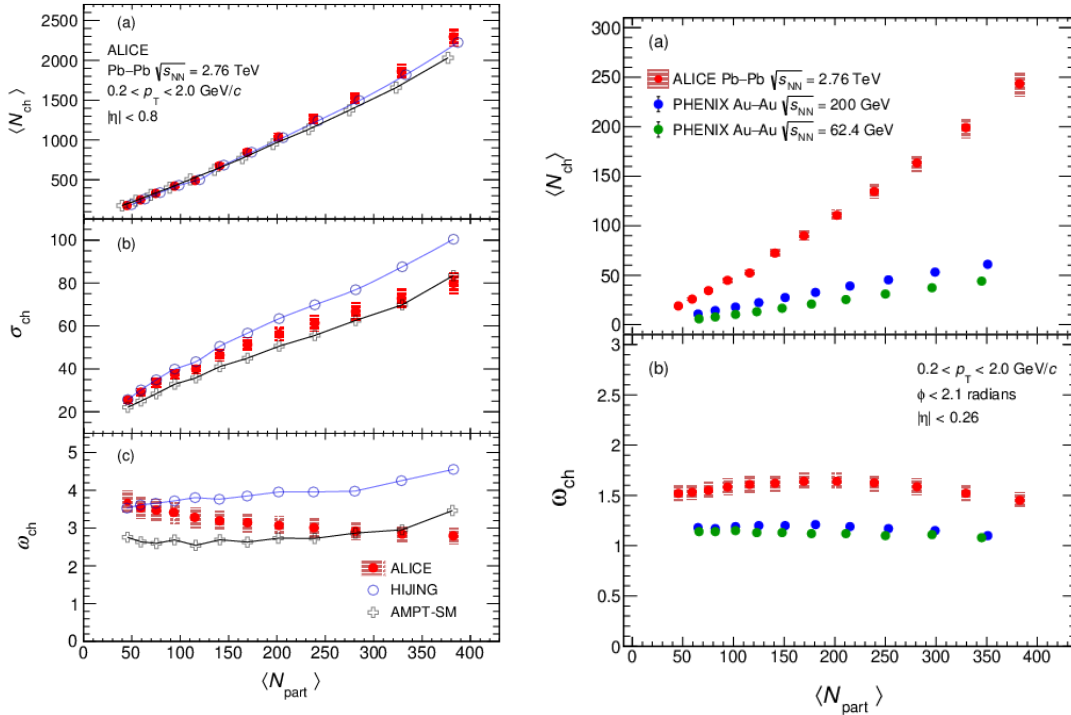


FIGURE 1.13:

Mean ($\langle N_{\text{ch}} \rangle$), standard deviation (σ_{ch}^2), and scaled variance (ω_{ch}) of charged-particle multiplicity distributions as a function of the number of $\langle N_{\text{part}} \rangle$, participating nucleons for experimental data along with HIJING and AMPT (string melting) models for Pb–Pb collisions at $\sqrt{s_{\text{NN}}} = 2.76$ TeV, shown in (a), (b), (c) respectively on the left. Comparison of these results with PHENIX are shown on the right [73].

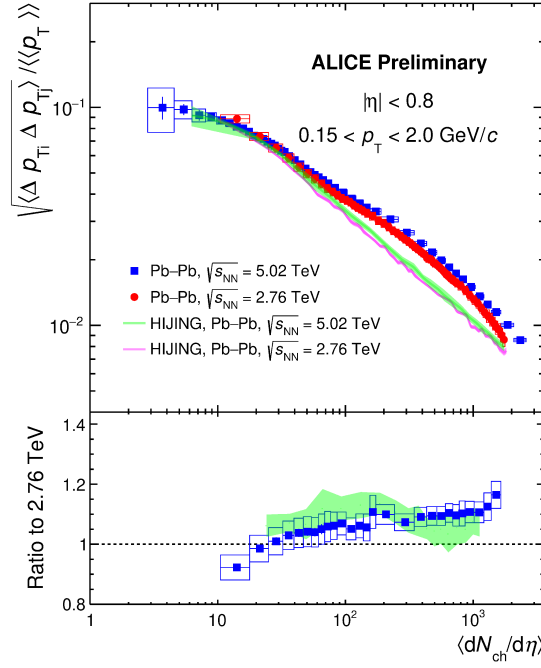


FIGURE 1.14:

ALICE mean transverse momentum, p_T event-by-event fluctuations measurements in Pb–Pb collisions at $\sqrt{s_{NN}} = 2.76$ and 5.02 TeV and their model comparisons with HIJING [77].

ALICE has observed that transverse momentum fluctuations decrease with increasing centrality in Pb–Pb collisions, suggesting that more central collisions lead to a more thermalised and collective state of the QGP (Figure 1.14). This behaviour aligns with hydrodynamic model predictions, which indicate that the collective expansion of a thermalized QGP leads to a suppression of fluctuations.

For studying non-statistical density fluctuations in the particle production, intermittency analysis methodology was suggested [78,79]. This analysis technique involves calculating normalized factorial moments (NFM), which quantify fluctuations across different size scales. Intermittency is characterised by a power-law behaviour of NFM, which indicates the presence of self-similar or scale-invariant structure within the system. Exponents obtained from the power-law behaviour can be linked to phase transitions and critical phenomena. For instance, in the field of heavy-ion collisions for the study of quark-gluon plasma, intermittency analysis has been employed to investigate the quark-hadron phase transition. Despite some challenges, such as low bin multiplicities that have historically complicated the interpretation of results, intermittency remains a crucial tool for probing the dynamics of nuclear matter under extreme conditions.

Recent advancements in high-energy collider experiments, which provide high charged particle density per bin, have rejuvenated interest in intermittency analysis. For example, the STAR experiment at RHIC has reported the first measurements of intermittency in Au-Au collisions over a broad range of collision energies from 7.7 to 200 GeV [80]. These measurements report a power-law behaviour in normalized factorial moments, and the scaling index, ν decreasing from peripheral to central collisions. Similar attempts have been made by the NA49 experiment (p+p, C+C, Si+Si, Pb+Pb) at 158A GeV/c [81] as well as by the NA61/SHINE experiment in p+p, p+Pb, Be+Be, Ar+Sc and Xe+La collisions [82]. These studies provide insights into the QCD phase transition and the underlying dynamics of heavy-ion collisions, highlighting the need for further investigations of experimental data at various energies. In this work, the charged particle multiplicity distributions in this two dimensional (η, φ) phase space recorded using ALICE detector for Pb–Pb collisions at $\sqrt{s_{\text{NN}}} = 5.02$ TeV are studied with intermittency methodology.

1.7 Outline of thesis

Event-by-event multiplicity fluctuation analysis using intermittency methodology on Pb–Pb data from ALICE experiment is the main subject of this thesis. The normalized factorial moments of charged particles produced in mid-rapidity have been measured for different centralities and transverse momentum bins. The research work presented in this thesis is spread over six chapters, and these chapters are organised as follows: **Chapter 1** introduced some of the basic concepts of high energy physics. **Chapter 2** introduces the concept of moments, intermittency, fractal parameters and experimental searches for the critical point of nuclear matter, phase diagram using these methods. **Chapter 3** gives highlights of the LHC experiment facility and the ALICE detector. Analysis details and results from the MC and experimental data analysis are given in **Chapter 4**. It also includes details on the event and track selection cuts, final results and also discusses the results of normalized factorial moments analysis of charged particles generated using PYTHIA8/Angantyr at $\sqrt{s_{\text{NN}}} = 2.76, 5.02$ TeV. A brief summary and conclusions of the research work performed are given in **Chapter 5**. Supplementary information is given in Appendices.

ANALYSIS METHODOLOGY

The quest to understand the nature of strong interactions, described by Quantum Chromodynamics (QCD), has been a driving force in heavy-ion collision research for decades. At high temperatures and densities, these collisions are predicted to transform ordinary hadronic matter, composed of protons and neutrons, into a state where quarks and gluons are deconfined and is known as the Quark-Gluon Plasma (QGP) [7]. This exotic state possesses distinct properties from traditional hadronic bound states, challenging our fundamental understanding of the matter. Exploring QGP and phase transition of hadronic matter into QGP and vice versa requires probing its unique characteristics using various analysis methodologies, tools and techniques. Among these one of the efficient and widely studied statistical analysis methodologies is the intermittency analysis proposed in 1980's for heavy-ion collisions [78,79].

This chapter gives a brief overview and related concepts of nuclear matter and QCD *phase diagram*. It also presents the intermittency analysis methodology used in this thesis to analyse experimental data and Monte Carlo events. The discussion begins with a detailed look at the intricate structure of the QCD phase diagram, focusing on the specific region of the phase diagram where the existence of QGP is predicted. Further, order parameters, essential tools for discerning the phase transition are discussed. The Polyakov loop [83] is highlighted, alongside other key parameters that signal the transformation from hadronic to QGP phases, such as the chiral condensate and strangeness saturation. Lattice QCD [84] is introduced briefly as a crucial theoretical framework used to study the QCD phase transition at extreme conditions.

Through simulations of quark-gluon interactions on a discretized space-time lattice, it becomes possible to compute the distribution of particles across the lattice points [85]. Deviations from a uniform distribution in these calculations reveal the presence of local density fluctuations [72]. These fluctuations gather valuable information regarding the underlying dynamical processes within the system and can be investigated using intermittency analysis, a tool that utilises specific observables sensitive to these fluctuations, such as scaled factorial moments [86].

In this chapter, in addition to the methodology of intermittency analysis, the results from the heavy-ion collision experiments of NA49 [81], NA61 [87], and STAR [80] are also presented. These ongoing efforts have given valuable insights into the utility of intermittency analysis in investigating the properties of the QGP.

2.1 QCD phase structure

The understanding of matter at extreme temperature (T) and baryochemical potential[†] (μ_B) is encapsulated within the QCD phase diagram, shown in **Figure 2.1** adapted from [88], a map depicting the different phases of matter predicted by Quantum Chromodynamics (QCD). Early theoretical frameworks, such as the Statistical Bootstrap Model (SBM) proposed by Hagedorn [89], hinted at the existence of a limiting temperature (T_H). At this temperature, a transition of phase to a new state of matter was predicted to take place. Furthermore, the concept of asymptotic freedom in QCD, established in [20], suggests that at sufficiently high densities (large μ_B), quarks and gluons become weakly interacting, potentially signifying another distinct phase of matter [12]. These ideas led to classifying potential QCD phase transitions [90], focusing on *deconfinement* [91], where quarks and gluons are no longer confined within hadrons, and *chiral restoration*, where the spontaneous symmetry breaking responsible for hadron masses is lifted.

2.1.1 Deconfinement

A scenario where quarks and gluons are no longer confined within hadrons is a state of deconfinement for quarks and gluons. It's a dramatic shift in the nature of strong interaction, akin to the transformation of water molecules. In its solid state (ice), water molecules are locked in a rigid, ordered structure. However, when heated beyond the freezing point, a phase transition occurs, and the molecules transit to a liquid state. This liquid state exhibits a more fluid and disordered

[†]baryon density

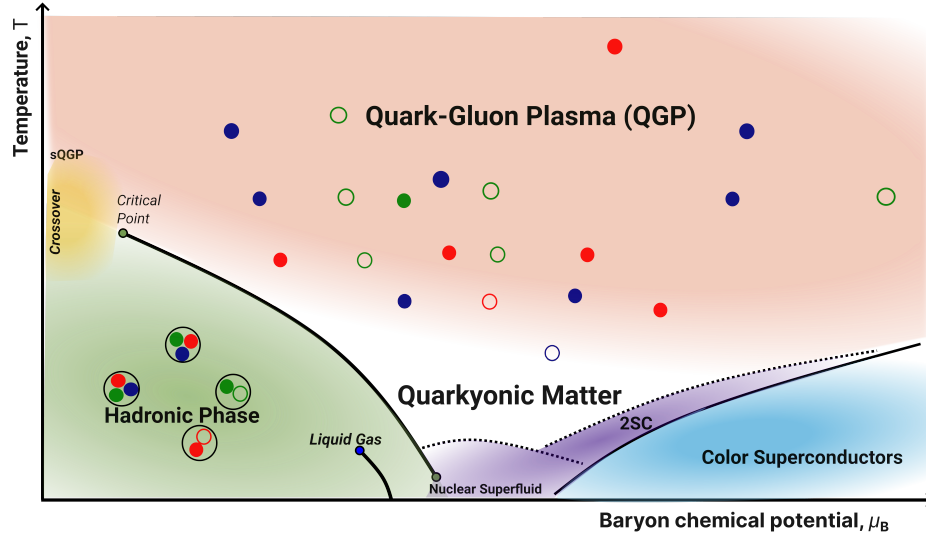


FIGURE 2.1:

Schematic phase diagram of nuclear dense matter with boundaries outlining various states of QCD matter adapted from [88].

arrangement. Various models have been proposed to understand the confinement of quarks in hadrons at high energy and temperature.

The Bag Model [92] presents a simple framework where valence quarks are considered free within a “bag,” which is maintained by a confining pressure. According to this model, deconfinement can be visualised as a gradual process where hadrons overlap, ultimately leading to the bag’s dissolution at the Hagedorn temperature [91,93]. In this model, hadrons are envisioned as regions of space (bags) where quarks are confined by a vacuum pressure. As the temperature of the system approaches the Hagedorn limit (T_H), the energy density increases, leading to a proliferation of hadronic states. At this critical point, the hadronic bags start to overlap, allowing quarks to move more freely across larger volumes, signalling the onset of deconfinement. However, this simplistic picture requires a detailed field theoretical approach in QCD to accurately describe the quark deconfinement.

An early model by Hagedorn [89] proposed to understand the behaviour of hadronic matter at finite temperature utilised the concept of a hadron resonance gas. This model suggests that at a temperature above T_H as energy is added to the system, new particles are produced rather than increasing the energy of existing states of hadronic matter. This phenomenon leads to an exponential growth in the number of hadronic resonances, which ultimately results in the emergence of a limiting temperature. At high temperatures and densities, the behaviour of hadronic and baryonic states is governed by statistical mechanics,

and their distribution is influenced by the partition function. The density of hadronic states, which primarily consists of mesons, depends on the resonance mass m and the temperature T_H , typically $\simeq 0.19$ GeV determined from the Regge slope parameter. This density must align with Boltzmann factor, $e^{-m/T}$. This factor represents the probability of a given state at a temperature T and appears in the partition function. When $T > T_H$, the integral over the mass m diverges, indicating that the hadronic description becomes inadequate. This divergence serves as an indicator that the system can no longer be described using hadronic degrees of freedom, pointing toward a phase transition to QGP. The model not only describes the limiting behaviour of hadronic matter but also allows for calculation of the critical value of the baryonic chemical potential, μ_B which influences the density of baryonic states. The baryonic Boltzmann factor given as, $\exp[-\frac{m_B - \mu_B}{T}]$ balances the contribution of baryonic states, where m_B represent mass of a baryon. As baryon chemical potential increases, the temperature at which hadronic matter can exist decreases. This relationship is described by the limiting temperature: $T = (1 - \frac{\mu_B}{m_B})T_B^H$. At zero temperature ($T = 0$), the critical value of μ_B is calculated from this formulation, $\mu_B > 1$ GeV. When μ_B is sufficiently high (approaching or exceeding m_B), hadronic matter becomes thermodynamically unstable, signaling a transition to the deconfined state, thereby connecting high baryon densities with the instability of hadronic matter and the onset of QGP formation.

2.1.2 Chiral restoration

In QCD, the vacuum is not an empty void but a dynamic medium filled with fluctuations of quark and gluon fields. In the absence of interactions, quarks are massless according to the QCD Lagrangian. However, the QCD vacuum is characterised by non-trivial condensates, such as the quark condensate $\langle \bar{q}q \rangle$, which arise due to strong interactions. These condensates indicate the spontaneous breaking of chiral symmetry [94], a fundamental symmetry of the QCD Lagrangian in the massless limit. The presence of a non-zero quark condensate $\langle \bar{q}q \rangle$, in the vacuum implies that quarks acquire an effective mass, known as the constituent quark mass. This mass is significantly larger than the bare quark mass and arises due to the interactions with the QCD vacuum fluctuations. The non-perturbative nature of these interactions makes the constituent quark mass, highlighting the complexity of the QCD vacuum. As the system's temperature increases or its density rises, the QCD vacuum undergoes a transformation. At sufficiently high temperatures or densities, the quark condensate melts, leading to the restoration of chiral symmetry [95]. This chiral symmetry restoration is

accompanied by a reduction in the constituent quark mass, signalling a transition to a phase where quarks behave more like their bare, massless counterparts. At finite values of T and μ_B , the QCD phase diagram has been studied in the context of chiral symmetry. The quark condensate, which has a vacuum value of approximately $-(0.24\text{GeV})^3$, serves as an order parameter for chiral symmetry [96]. A key concept that underpins this phenomenon is asymptotic freedom [19], which refers to the property of QCD where the coupling between quarks becomes weaker at higher energy scales (or shorter distances). This behaviour implies that at extremely high temperatures and densities, quarks behave more like free particles, reducing the strength of interactions that lead to chiral symmetry breaking. As the temperature approaches T_c , the interactions weaken, facilitating restoration of chiral symmetry and transition to the QGP phase.

2.2 Phase diagram

A contemporary and current understanding of different phases and features of the QCD phase diagram are illustrated in **Figure 2.1** [97,98]. The theoretical predictions are considered to be robust at finite temperature for both low ($\mu_B \ll T$) and extremely high baryon densities ($\mu_B \gg \Lambda_{\text{QCD}}$). Λ_{QCD} is the energy scale that marks the transition from perturbative (weak coupling) to non-perturbative (strong coupling) behaviour in QCD.

Hadronic to QGP Phase: A transition from hadronic to QGP phase is a critical part in the phase diagram. This transition occurs under extreme conditions of temperature and/or baryon chemical potential, where quarks and gluons become deconfined from within the hadrons. At zero baryon chemical potential ($\mu_B = 0$), many studies of the transition from hadronic state to QGP phase have been extensively studied through lattice QCD theory. As per this, nature of the transition is dependent on the number of quark flavours (N_f) and colours (N_c) [99,100]. For $N_c = 3$, $N_f = 0$, a first-order phase transition is observed, with a critical temperature $T_c \simeq 270$ MeV [101]. For $N_f > 0$ (light flavours), when considering realistic masses for the up, down, and strange quarks, the transition is predicted to be a crossover rather than a first-order transition [102,103]. Analysis in [104,105] suggest this crossover occurs within a temperature range of 150 MeV to 200 MeV, known as the pseudo-critical temperature (T_{pc}) [106]. Above the T_{pc} , even though the system is in the QGP phase, strong correlations and pre-formed hadrons can still exist, both at $\mu_B = 0$ [94,107] and at non-zero μ_B [108–110].

Critical point: Critical point marks the boundary where the crossover at low baryon chemical potential transforms into a first-order phase transition that separates the hadron gas and quark-gluon plasma phases of QCD. Fluctuations in the observables are predicted to rise near this point [111]. Study of fluctuations [72] is a major focus of heavy-ion experiments, since detecting these fluctuations could provide definitive evidence for QCD critical point's existence. At finite μ_B , lattice calculations become less reliable, however, QCD *critical point* is predicted by most of the chiral models ($\mu_B = \mu_E$, $T = T_E$), at E as shown in Figure 2.2. At this point, the phase transition [90] changes character: for $\mu_B > \mu_E$, the transition is first-order, while for $\mu_B < \mu_E$, it is a crossover [112–115]. Furthermore, it is hypothesised that another critical point, labelled *F*, may exist in the lower temperature and higher baryon density region of the phase diagram (μ_F , T_F). The precise position of these critical points (*E* and *F*) is strictly dependent on the mass of strange quark, temperature (*T*) and baryon chemical potential (μ_B) at the phase boundary.

Quarkyonic Matter: Quarkyonic matter as shown in Figure 2.1 is a unique phase predicted by QCD that emerges under conditions of extremely high baryon density. This phase offers deeper insights into the non-perturbative regime of QCD, particularly in extreme environments where traditional hadronic descriptions break down.

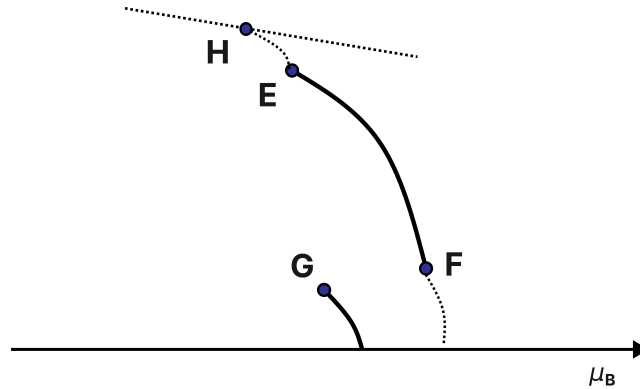


FIGURE 2.2:

Characteristic points on the QCD phase diagram. Point E represents the hypothesised QCD critical point. Point F denotes another critical point associated with quark-hadron continuity. Point G indicates the critical point related to the liquid-gas transition of nuclear matter. Point H marks a region resembling an approximate triple point. Sketch adapted from [88].

The Statistical Model [116] defines a chemical freeze-out line in the QCD phase diagram based on the assumption that there is no interaction between mesons, baryons, and resonances at thermal equilibrium. Although this line does not

represent a true phase boundary, it is expected that lies in close proximity to the actual phase transition line. At low baryon chemical potentials ($\mu_B < m_N$, where m_N is the nucleon mass), mesons dominate the thermal degrees of freedom due to their lower masses and higher abundance. This dominance is because mesons are bosons and can occupy the same quantum state, leading to a significant contribution to thermodynamic quantities.

However, as μ_B increases, baryons become increasingly significant, dominating the thermodynamic properties of the system. This shift occurs because baryons, which are fermions, have a different statistical behaviour compared to mesons. The increasing density of baryons at higher chemical potentials alters the composition and dynamics of the matter present in the system. It is likely that there exists a *critical point*, denoted as point H in **Figure 2.2**, at (T_H, μ_H) , where $\mu_H = 350 \sim 400$ MeV, at $T_H = 150 \sim 160$ MeV. At this point, the thermodynamic importance of baryons surpasses that of mesons, signaling a significant shift in the matter composition. In the limit of an infinite number of colours ($N_c = \infty$), a finite baryon density gives rise to a cold, dense phase known as quarkyonic matter [117]. In this phase, quarks remain confined within baryons, but the sheer density of baryons alters the system's properties markedly. For finite N_c , a vestige of this phase manifests as a triple point, denoted by H in the **Figure 2.2**, marking the transition region between hadronic matter, quarkyonic matter, and deconfined quark-gluon plasma.

Color superconductivity: For asymptotically large baryon chemical potentials ($\mu_B \gg \Lambda_{\text{QCD}}$), weak-coupling QCD methods become applicable. In this phase, the attractive interaction between quarks lead to the formation of Cooper pairs, analogous to electron pairing in conventional superconductors [118]. These quark pairs condense, breaking colour symmetry and resulting in a superconducting state where colour charges are expelled, similar to the Meissner effect observed in the electromagnetic superconductors. This analogy yields the formation of Cooper-like pairs of quarks at low temperatures, giving rise to colour superconductivity (CSC) [117–119]. Theoretical models, such as the Nambu–Jona-Lasinio (NJL) model [120] and the Color-Flavor Locked (CFL) phase [121], predict various colour superconducting phases depending on the density and the quark masses involved. The NJL model is a simplified effective field theory that captures some of the non-perturbative features of QCD, particularly the dynamics of quark interactions and the formation of condensates. This model helps to study the mechanisms of pairing and symmetry breaking in quark matter. In the CFL phase, which is predicted by QCD at asymptotically high densities, quarks of all

three colours (red, green, and blue) and flavours (up, down, and strange) pair up, forming a particularly symmetric and stable state. This phase is characterized by a gap in the excitation spectrum, indicating the presence of a stable ground state, and the breaking of both colour and flavour symmetries. The CFL phase represents a highly ordered state of matter, where the pairing of quarks leads to unique properties, such as the potential for superfluidity and the expulsion of colour charges, analogous to the behaviour of conventional superconductors [122–124].

Liquid-Gas phase transition The liquid-gas phase transition of nuclear matter marked in the **Figure 3.1** is relevant at low temperatures and around the baryon chemical potential, $\mu_B = \mu_{\text{NM}} \simeq 924 \text{ MeV}$ [125]. In this region, a non-vanishing nuclear matter baryon density begins to form, marking the onset of the liquid-gas phase transition. As μ_B reaches $\mu_B = \mu_{\text{NM}}$, the baryon density n_B increases from zero to $n_0 = 0.17 \text{ fm}^{-3}$, the normal nuclear density. This variation signifies the formation of droplets of nuclear matter, akin to the behaviour observed in a liquid-gas phase transition. As the system crosses this threshold, it undergoes a first-order phase transition where nuclear matter begins to condense out of the vacuum, forming a dense liquid-like phase from a dilute gas-like phase. The critical point of the second-order phase transition marks the end of first-order transition line, denoted as point G, shown at (μ_G, T_G) , in **Figure 2.2**. Low-energy heavy-ion collision experiments suggest that $\mu_B \sim \mu_{\text{NM}}$ and $T_G = 15 \sim 20 \text{ MeV}$ [126]. The liquid-gas phase transition is a fundamental aspect of nuclear matter, as it relates to the balance between attractive, which promotes clustering and condensation, and the repulsive force at short distances, which prevents collapse.

After the discussion on various points of the phase diagram shown in **Figure 3.1**, the next section will briefly introduce few other concepts related to it.

2.3 Order parameters

In the context of phase transition from a hadron gas to a quark-gluon plasma (QGP), several order parameters are utilised to identify and understand the transition. Among these, the Polyakov loop [83], the chiral condensate, and fluctuations of conserved charges play significant roles.

2.3.1 Breaking of chiral symmetry

A spontaneous chiral symmetry breaking occurs at $T = \mu_B = 0$ in the QCD vacuum, associated with the formation of a non-zero chiral condensate [127].

Chiral symmetry serves as a fundamental symmetry of QCD for massless quarks, which is broken dynamically by strong interactions [100]. The spontaneous breaking is in a way similar to the alignment of spins in a ferromagnet, in which there is formation of a non-zero magnetization in the ground state. However, as mentioned earlier also, the order parameter of the chiral symmetry breaking in hadronic matter is the quark condensate $\langle \bar{q}q \rangle$, which is the vacuum expectation value of the quark bilinear operator constructed from the quark fields, q and \bar{q} as [128]:

$$\langle \bar{q}q \rangle = \langle \bar{q}_R q_L \rangle + \bar{q}_L q_R \rangle \quad 2.1$$

where q_L and q_R denote the left-handed and right-handed quark fields, respectively. A non-zero value of this condensate indicates that the vacuum expectation values of the left-handed and right-handed quarks are not independent, leading to the mixing of these components and thus breaking the chiral symmetry [127]. This mixing is a manifestation of the vacuum structure of the QCD, where quark pairs are constantly being created and annihilated, contributing to the overall condensate.

As the temperature increases, there is restoration of the chiral symmetry which means that the quark-gluon interactions no longer favour the formation of quark-antiquark pairs, leading to a symmetric phase where the condensate vanishes. These high temperatures are achieved in heavy-ion collisions where the chiral condensate decreases and approach zero when the critical temperature (T_c) is reached as discussed earlier in Section 2.1.2. The transition can be studied by examining the temperature dependence of the chiral condensate: $\langle \bar{q}q \rangle(T) \rightarrow 0$ as $T \rightarrow T_c$ [95].

2.3.2 Polyakov loop

Polyakov loop provides a measure of the free energy associated with a static quark in the medium, making it particularly useful for understanding finite-temperature QCD [83,129]. The QCD phase transition is marked by the restoration of chiral symmetry and the deconfinement of quarks and gluons as described earlier. The chiral condensate serves as an order parameter for chiral symmetry breaking, with its expectation value decreasing as the temperature rises, signalling the restoration of chiral symmetry in the QGP phase. On the other hand, the Polyakov loop is an order parameter specifically for the confinement-deconfinement transition, providing insights into the deconfinement of quarks.

Polyakov loop, $P(\vec{x})$ is defined mathematically as trace of Wilson line $L(\vec{x})$ in Euclidean space time, given by [83,130]:

$$L(\vec{x}) = \mathcal{P} \exp \left[-ig \int_0^\beta A_4(x, x_4) dx_4 \right] \quad 2.2$$

where \mathcal{P} is used for path ordering, and g for gauge coupling, $A_4(x, x_4)$ is the temporal component of the gauge field, $\beta = \frac{1}{T}$ is the inverse temperature. The path ordering ensures that the gauge fields are ordered along the path of integration. The Polyakov loop $P(\vec{x})$ is defined as the normalised trace of this Wilson line:

$$P(\vec{x}) = \frac{1}{N_c} \text{tr} L(\vec{x}) \quad 2.3$$

where N_c refers to the number of colours (typically =3). The expectation value of Polyakov loop, $\langle P \rangle$ serves as an order parameter for the confinement-deconfinement phase transition.

$\langle P \rangle$ is zero at low temperature, i.e., in the confined phase [131,132], reflecting the infinite free energy required to insert a static quark into the medium. This corresponds to the fact that quarks are confined within hadrons, and it is energetically prohibitive to separate them. The expectation value in this phase is zero that means between a quark and an anti-quark potential grows indefinitely with distance. This is indicative of confinement. In the deconfined phase (high temperatures), the expectation value $\langle P \rangle$ becomes non-zero. This indicates a static quark has a finite free energy, and can move freely in the QGP. Here, a non-zero expectation value shows that the potential between a quark and an anti-quark saturates at a finite value for large separations, indicating deconfinement [133–135].

2.4 Phase transition and universality

Broadly classifying, phase transition [136,137] can be of two types, viz., first-order and second-order phase transition. If there are finite discontinuities in thermodynamic quantities, then it is first-order phase transition (PT). It has exception in case of free energy, which has to be described differently near phase transition. Opposite to first-order phase transition, the second-order is characterised by continuous but non-analytic behaviour of thermodynamic quantities. In this case, fluctuations of long-wavelength and low energy are present, leading to an infinite correlation length at the transition point. In particle physics, this

corresponds to massless particles that act as quanta of these long-range modes. In the nuclear matter phase diagram, as shown in **Figure 3.1** the first-order phase transition line separates the hadron gas and QGP phase. The endpoint of this line marks QCD critical point (CP). As mentioned above, one key aspect of this transition is chiral symmetry breaking and restoration.

For the system near CP or undergoing second-order phase transition, the thermodynamics of the system gets simplified due to scaling laws. There is a divergence of the correlation length (ξ) which results in scale invariance [137]. This property helps to study transitions in various systems. As a result, diverse systems can be described using a small number of universality classes. Exponents obtained from critical points of the system are called *critical exponents*, quantify these universality classes. They depend only on symmetries and spatial dimensionality of the system, not on its microscopic details. For instance, in case of fractals, the critical exponents give quantification of the universality class to which the fractal system belongs [138,139]. For universal systems with simple models, predictions about the nature and behaviour of phase transition can be made [140].

For example, simple models like the 3D-Ising model [115] for magnetization provides help to know about divergent behaviour of the various thermodynamic quantities when the system is undergoing second-order phase transition. It describes ferromagnetism in statistical mechanics using discrete spin variables, that can have two values ($s_i = \pm 1$). These spins are arranged on a three-dimensional lattice, and allowed to interact with their adjacent neighbours. The Hamiltonian, which represents the energy of a configuration, is given by:

$$H = -J \sum_{\langle i,j \rangle} s_i s_j - h \sum_i s_i \quad 2.4$$

where, J is the interaction strength between neighbouring spins, $\langle i, j \rangle$ denotes the sum over nearest-neighbour pairs, and h is the external magnetic field [141]. The partition function, \mathbb{Z} sums over all possible s_i configurations:

$$\mathbb{Z} = \sum_{\{s_i\}} e^{-\beta H} \quad 2.5$$

where, $\beta = \frac{1}{k_B T}$ is the inverse temperature (with k_B being Boltzmann's constant and T the temperature). Near the critical point, the correlation length ξ diverges, and the system exhibits critical behaviour given by power-law singularities. In 3D Ising model, thermodynamic quantities which show critical behaviour at temperature, T_c are: magnetization (M); a measure of the net alignment of spins

in response to the external field; susceptibility (χ), which describes how strongly the magnetization responds to changes in the external field; and specific heat (C), which measures the heat required to change the system's temperature. These quantities are given as power-laws at T_c :

$$\begin{aligned} \text{Magnetization : } M &\propto |T - T_c|^\beta, \\ \text{Susceptibility : } \chi &\propto |T - T_c|^\gamma, \\ \text{Specific heat : } C &\propto |T - T_c|^\alpha. \end{aligned} \tag{2.6}$$

where β , γ and α are the critical exponents [141] that describe the system's behavior near the critical point. These exponents are universal and provide insights into the nature of the phase transition.

2.5 Lattice QCD simulations

The above discussion suggests that the critical properties are expected to be universal and robust. However, the values of parameters, such as, critical temperature are dependent on the microscopic parameters of the theory. At present, simulations on a discretized lattice remain the sole reliable approach to gaining insights into the behaviour of microscopic dynamics. In other words, lattice QCD [18,84] enables the study of QCD in regimes where perturbative methods fail, such as the study of phase transitions, including the confinement-deconfinement transition and chiral symmetry restoration.

In lattice QCD, the continuous space-time is replaced by a discrete lattice with a finite number of points. The quark fields are defined on the lattice sites and QCD action in the continuum is then reformulated on this discrete lattice. A finite lattice is generated, with lattice spacing a and volume $V = L^3 \times T$, where L is the spatial extent and T is the temporal extent. The gauge field configurations are sampled using Monte Carlo methods, such as the Metropolis algorithm [142] or Hybrid Monte Carlo (HMC) [143]. Physical observables, such as the chiral condensate and Polyakov loop, are calculated on the sampled configurations. The expectation values of these observables are obtained by averaging over many configurations. Results obtained on the lattice are extrapolated to the continuum limit by taking the lattice spacing $a \rightarrow 0$ and thermodynamic limit by taking volume $V \rightarrow \infty$. It is notably established by lattice QCD as well that at zero μ_B , the transition from hadronic matter to quark-gluon plasma (QGP) is a smooth crossover occurring at $\simeq 155$ MeV [33,144]. Lattice QCD is used to investigate the existence or non-existence of QCD critical point at finite μ_B [145,146].

The QCD partition function to study phase transition at a finite T and μ_B is given by [147]:

$$\mathbb{Z}(T, \mu_B) = \int \mathcal{D}U \det M(U, \mu_B) e^{-S_G[U]} \quad 2.7$$

where, S_G is the gauge action, $\det M(U, \mu_B)$ is the determinant of the fermion matrix M , that depends on field configurations U and μ_B .

At zero μ_B , the fermion determinant ($\det M(U, \mu_B)$) in the partition function is real and positive, which allows for straightforward numerical simulations using Monte Carlo methods. However, when μ_B is non-zero, the fermion determinant becomes complex. It introduces several difficulties, but the primary issue is the oscillating nature of contributions in the simulations. In lattice QCD, physical observables are calculated by summing over many field configurations. When the fermion determinant is complex, the positive and negative phases in this sum nearly cancel each other out, making it extremely difficult to compute the integral accurately. The severity of the sign problem increases exponentially with the volume (e.g., highly dense parts of the phase diagram), which presents a fundamental barrier to reliable simulations for large systems. Identifying critical point is thus challenging due to this sign problem, but several techniques (*Taylor* expansion, *Reweighting* method) have been developed to tackle this issue [148].

In any case, the validity of these many ways to tackle the sign problem at finite μ_B is limited and the results, if any, should be taken with a pinch of salt.

2.5.1 Critical exponents

Understanding critical exponents is essential for characterising phase transitions and identifying universality classes. Phase transitions, such as those occurring in magnetic systems or liquid-gas transitions, exhibit a range of behaviours that can be classified based on the underlying symmetries and dimensionality of the system. At a phase transition, systems can be categorised into different universality classes, which share the same critical exponents despite differing microscopic interactions.

The free energy (F) [141] of a system near a phase transition is crucial in understanding the nature of the transitions. Free energy, defined as the thermodynamic potential that measures the amount of work a system can perform at constant temperature (T) and volume (V), helps to predict the stability of different phases. The system's free energy $F(T, V)$ near a first-order transition within the thermodynamic limit is given as:

$$F(T, V) = V \min(f_1(T), f_2(T)) \quad 2.8$$

where $f_1(T)$ and $f_2(T)$ are the free energy densities of the two phases. The phase with the lower free energy density, $f(T)$ dominates. This results in a discontinuous jump in the order parameter, indicating a first-order transition.

For second-order transitions, the free energy F near the critical point involves a smooth but non-analytic dependence on the order parameter ϕ . The Landau free energy expansion is:

$$F(T, \phi) = F_0(T) + a(T)\phi^2 + b(T)\phi^4 + \dots \quad 2.9$$

where $a(T) \propto (T - T_c)$ changes sign at the critical temperature T_c , leading to spontaneous symmetry breaking and the development of a non-zero order parameter ϕ , whereas $b(T)$ plays a role in stabilizing the free energy. Near T_c , the behaviour of thermodynamic quantities is governed by *critical exponents*, traditionally symbolised by the letters $\alpha, \beta, \gamma, \delta, \eta$ and ν [141,149,150], and are defined as:

$$\begin{aligned} \text{Order parameter : } \phi &\propto |T_c - T|^\beta, \\ \text{Specific heat : } C &\propto |T - T_c|^{-\alpha}, \\ \text{Susceptibility : } \chi &\propto |T - T_c|^{-\gamma}, \\ \text{Equation of state (EoS) : } \langle |\phi| \rangle &\sim H^{1/\delta}. \end{aligned} \quad 2.10$$

The equation of state (EoS) is valid in the limit, $\frac{T-T_c}{T} = 0, H \rightarrow 0$. Magnetization, M acts as an order parameter in the magnetization model, whereas this role is played by chiral condensate in the QCD. Susceptibility of the system quantifies the degree to which the order parameter is sensitive when there are variations in the magnetic field, H [141,151].

The relations in **Equation 2.10**, with the exception of EoS, are defined for the case of zero magnetic field ($H = 0$). The last two exponents η and ν are associated with the correlation function. η expresses the spatial fluctuations of the order parameter, measures the correlation between fluctuations at two distant points. ν characterises the divergence of **correlation length** ξ near the critical point, given by:

$$\xi \propto |T - T_c|^{-\nu} \quad 2.11$$

All these exponents which give information about the universality class of the transition. Near the CP, physical quantities exhibit power-law behaviour characterised by these critical exponents, which are universal. They are also not

independent; they are related to each other through the following four scaling laws [150].

2.5.2 Scale invariance

Scale invariance is a concept in the study of critical phenomena and phase transitions, signifying the property of a system that looks same at all length scales. During second-order phase transition at CP, several key features emerge. One of the most significant is the divergence of the correlation length, ξ (Equation 2.11) which measures the distance over which fluctuations are correlated. At critical temperature T_c , the correlation length $\rightarrow \infty$, implying that fluctuations occur over increasingly large scales, leading to a loss of a characteristic length scale within the system. This divergence of the correlation length is the basis of scale invariance.

The Renormalization Group (RG) theory formalises the concept of scale invariance [152]. The RG approach involves a process known as coarse-graining, where the system is iteratively averaged over short-wavelength fluctuations to focus on long-wavelength modes. This effectively changes the resolution at which one observes the system. Through this process, the RG theory identifies fixed points in parameter space where the system exhibits scale invariance. These fixed points correspond to critical points where the physical properties of the system remain invariant under RG transformations. Understanding how the parameters, or coupling constants, in the Hamiltonian change with scale near the critical point provides insights into the universal behaviour of the system, exhibiting scale invariance. Specifically, it predicts that correlation functions and other observables exhibit power-law behavior as the system approaches criticality. These power-law correlations and fluctuations serve as specific experimental signatures of phase transitions. These signatures help experimentalists in distinguishing the nature of the phase transition and the existence of a critical point. Effective field theories near the critical point leverage scale invariance to simplify the description of the system by focusing on long-wavelength modes. These theories capture the essential physics without requiring detailed knowledge of short-wavelength interactions, providing a framework for studying phase transitions [151].

2.6 Local density fluctuations

In a heavy-ion collision, particles are produced in large numbers. The density distribution of these particles in a given spatial region provides a measure of how

these are produced within the collision zone. This density distribution may not be uniform and thus may fluctuate from point to point due to the stochastic nature of particle production and/or interactions among the particles. Mathematically, these fluctuations can be calculated by the variance of the particle number density within a given volume.

Consider a spatial region V within the collision zone. The local density ρ of the particles (e.g., quarks or hadrons) in this volume can be expressed as:

$$\rho = \frac{N}{V} \quad 2.12$$

Density fluctuations arise due to the stochastic nature of particle production and interactions among the produced particles in the heavy-ion collision. As two

heavy-ions collide at ultra-relativistic energies, a hot and dense medium is created where quarks and gluons are liberated from confinement, forming a quark-gluon plasma. As the system so formed evolves and cools, it undergoes a phase transition back to the hadronic matter state. During this process, critical fluctuations [153] manifest as significant variations in local density of particles. These fluctuations are indicative of the system's proximity to the

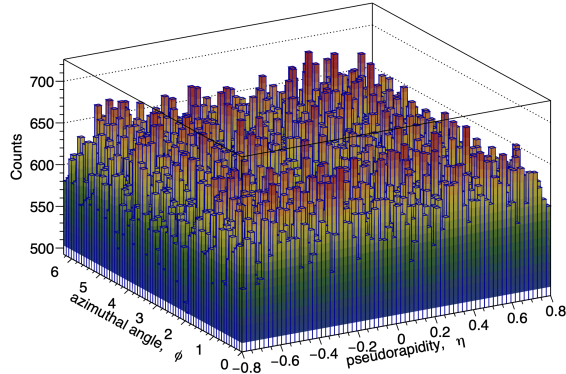


FIGURE 2.3:

Depiction of a heavy-ion collision event showing local density fluctuations in $\eta - \varphi$ phase space.

critical point. By analyzing these density variations, one can gain insights into the nature of the phase transition. These fluctuations are due to changing energy density and temperature conditions, making these a vital probe of the QCD phase diagram. Statistically, these fluctuations in the density of particles, as defined in Equation 2.12, are given by the variance:

$$\text{var}(\rho) = \langle \rho^2 \rangle - \langle \rho \rangle^2 \quad 2.13$$

Further, the *density-density correlation function* can be used to measure correlations between particle densities at different points in space. For any two points separated by a distance r in space, it is given by:

$$C(r) = \langle \rho(x)\rho(x+r) \rangle - \langle \rho(x) \rangle \langle \rho(x+r) \rangle \quad 2.14$$

where $\rho(x)$ represents the local density at point x . In, for example, pseudorapidity space, r can be interpreted as the difference in pseudorapidity between two

particles. It measures how the density at one point x is correlated with the density at another point $x + r$ accounting for the random fluctuations in the system.

Away from the phase transition, the function exhibits exponential decay in the form $C(r) \sim \exp(-r/\xi)$, where ξ is the correlation length. At the phase transition, the correlation length diverges, that is $\xi \rightarrow \infty$, leading to a power-law decay in the correlation function, given as:

$$C(r) \sim \exp(-r/\xi)/r^{d-2} \quad 2.15$$

where d is the spatial dimension. The general form of the correlation function at phase transition is: $C(r) \sim 1/r^{d-2+\nu}$, where ν is a critical exponent that characterizes the degree of fluctuation in the system. This power-law behaviour indicates that the density fluctuations are correlated over large distances. In the context of high-energy heavy-ion collisions, where pseudorapidity η and azimuthal angle φ define the phase space, the distance r can be interpreted as the difference in pseudorapidity between two particles. The power-law behaviour of the correlation function in this phase space indicates the emergence of large density fluctuations, which will be indicator of critical behaviour in the system.

2.7 Factorial moments and intermittency

Fluctuation analysis of local density fluctuations in heavy-ion collisions can reveal how clusters of particles, of all sizes, emerge and exhibit collective behaviour without a specific characteristic scale. This in turn is indicative of the critical nature of the system. Self-similar structures also manifest as pronounced local density fluctuations. Thus, by examining fluctuations in observables, one can infer underlying processes that govern phase transition and the presence of self-similarity in the system [154,155]. This connects directly to the concept of scale invariance and universality discussed in the Section 2.4.

It is well known that heavy-ion collisions produce many strongly interacting particles. The multiplicity distributions of these particles carry essential information about the state of the matter and its phase transition [156]. Near a phase transition, fluctuations in particle densities become pronounced and exhibit specific scaling properties, which can be effectively captured using statistical tools such as factorial moments [86]. These moments are effective in distinguishing dynamical fluctuations — those arising from the physical processes of the collisions and statistical fluctuations, which are random variations inherent in any measurement, within the contours of intermittency analysis. The study of intermittency in multiparticle production using the method of factorial moments

was first proposed several years ago [78,79]. Recent studies show that one can estimate the possible critical region of the QCD critical point and understand the nature of phase transition by using the intermittency analysis together with the estimated freeze-out parameters [157–159]. Intermittency has been reported in experimental data from various collision systems, including e^+e^- annihilation [160–162], muon-hadron [163,164], hadron-nucleon [165,166] and nucleus-nucleus collisions [167–169]. Recently, the idea for the study of intermittency at LHC energies [156,170] is proposed in 2012 where the event-by-event spatial configurations of charged particles are suggested to be measured using normalized factorial moments.

To study self-similarity in particle multiplicity distributions in a two-dimensional phase space, various statistical tools are used. These tools are helpful to analyse the many-particle states in heavy-ion collisions. A two dimensional analysis framework of intermittency in which pseudorapidity (η) and azimuthal angle (φ) is suggested as phase space, to look at spatial configurations is outlined here. This tool includes the *inclusive q -particle* distributions. Integral form of these distributions over regions of phase space provide the expected particle multiplicities, and the fluctuations in their number. The inclusive q -particle distribution (symmetrized), ρ_q , that is defined for momentum phase space in [86], can be defined for $\eta - \varphi$ phase space as:

$$\rho_q = \frac{1}{\sigma_{\text{tot}}} d\sigma_q(\eta_1, \varphi_1, \dots, \eta_q, \varphi_q) / \prod_{i=1}^q d\eta_i d\varphi_i \quad 2.16$$

where q particles with pseudorapidities η_1, \dots, η_q and azimuthal angles $\varphi_1, \dots, \varphi_q$ have the inclusive cross-section $\sigma_q(\eta_1, \varphi_1, \dots, \eta_q, \varphi_q)$, which is independent of any other produced particle's presence and location (i.e., it involves integrating over all the possible distributions of other particles). The variables η_i and φ_i represent the position of i -th particle in the two-dimensional phase space, and σ_{tot} denotes the total cross-section of the process being studied. For identical particles, integrating (Equation 2.16) over a domain Ω of the two-dimensional (η, φ) phase space gives:

$$\begin{aligned} \int_{\Omega} d\eta_1 d\varphi_1 \dots d\eta_q d\varphi_q \rho_q(\eta_1, \varphi_1, \dots, \eta_q, \varphi_q) \\ = \langle n(n-1)\dots(n-q+1) \rangle \end{aligned} \quad 2.17$$

In above equation, n defines the multiplicity of identical particles in Ω phase space of an event, and the angular brackets ($\langle \dots \rangle$) indicates an average over

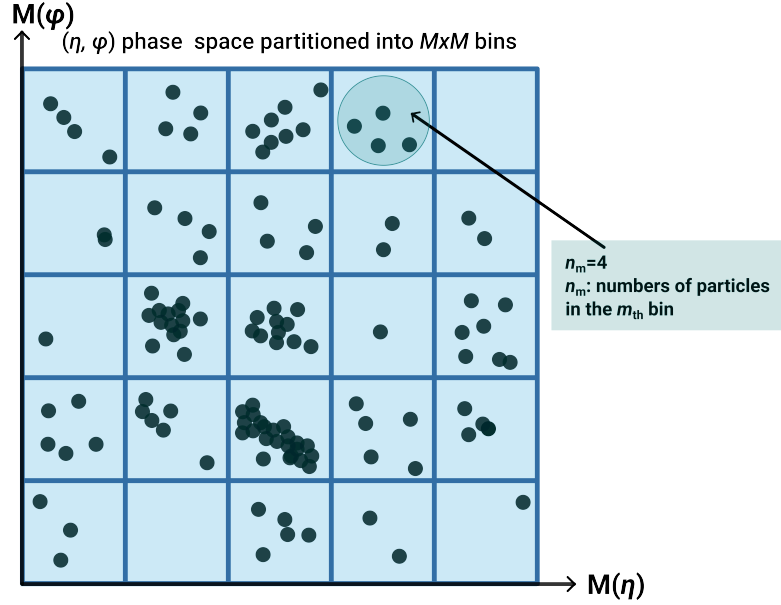


FIGURE 2.4:

Schematic representation of two dimensional (η, φ) phase space partitioned into $M \times M$ bins (where $M = 5$ in figure is shown) to calculate factorial moments.

all events. To obtain results that are statistically significant, Equation 2.17 is averaged over all events. The examination of how the multiplicities scale with the size / the number of bins in phase space is key to draw important conclusions.

Consider, a phase space (two dimensional) cell Ω_m , with a volume $\delta\Omega = \delta\eta \cdot \delta\varphi$. The total phase space, with volume Ω , is partitioned into M^2 non-overlapping bins of equal volume $\delta\Omega$. Evidently, $\Omega = M^2 \delta\Omega$, where 2 refers to the dimensionality of the phase space. Let, the multiplicity of particles in the m -th cell Ω_m be n_m . For example Figure 2.4 shows the (η, φ) phase space partitioned into 25 bins where $M = 5$, then n_m is the bin multiplicity, i.e., number of filled circles within each m -th cell. Moments can then be defined averaged over bins and are particularly useful in understanding the nature of local density fluctuations. The moments of particle multiplicities help to understand the nature of particle distributions within the Ω phase space. The q -th order factorial moment, in particular, captures the deviations from Poissonian (random) distributions and is sensitive to non-trivial correlations and clustering of particles. The q -th order *normalized factorial moments* (NFM) [78,79], are then defined as:

$$F_q^V(M) \equiv \frac{1}{M^{D=2}} \sum_{m=1}^{M^{D=2}} \frac{\langle n_m(m-1) \dots (n_m - q + 1) \rangle}{\langle n_m \rangle^q} \quad 2.18$$

where, $n_m \equiv \bar{\rho}_m \delta\Omega$. These moments are crucial in describing the system near phase transitions, where fluctuations become significant and exhibit scaling behaviour. $F_q^V(M)$ in Equation 2.18 are called vertical moments. Here, first average over the collection of events ($\langle \dots \rangle$ denote averaging over the set of events) and then over the phase space bins is taken. In a similar manner, horizontal factorial moments for 2 dimensions can also be defined as [78,79]:

$$F_q^H(M) \equiv \frac{\left\langle \frac{1}{M^2} \sum_{m=1}^{M^2} n_m (m-1) \dots (n_m - q + 1) \right\rangle}{\left\langle \frac{1}{M^2} \sum_{m=1}^{M^2} n_m \right\rangle^q} \quad 2.19$$

where an average over the set of events is taken after the average over phase space bins [171].

It can be observed that the horizontal and vertical moments are identical when there is a single phase space cell, i.e., $M = 1$. Vertical moments are locally normalised, making them sensitive only to fluctuations within each individual cell, rather than to fluctuations in the overall shape of the particle distribution. However, horizontal moments are influenced by the distribution's form across bins in the events and thus, captures bin to bin fluctuations. If $f_q^e(M)$ represents factorial moment of e^{th} event with order q , then for the multiplicity n_{me} in the m^{th} bin, it is defined as:

$$f_q^e(M) = \frac{1}{M^2} \sum_{m=1}^{M^{D=2}} n_{me} (n_{me} - 1) \dots (n_{me} - q + 1) \quad 2.20$$

and so the NFM given in Equation 2.19 can be simply written as:

Normalized Factorial Moments (NFM)

$$F_q(M) = \frac{\langle f_q^e(M) \rangle}{\langle f_1^e(M) \rangle^q} \quad 2.21$$

In this equation, $\langle \dots \rangle$ is the averaging over the events. In this work, the NFM as defined in Equation 2.21 and proposed in [156,170] are calculated for central Pb–Pb collisions. (η, φ) phase space of each event within the kinematic acceptance is partitioned in a square $(M \times M)$ matrix, where M is an integer ≥ 2 . The maximum value that M can take is limited by the detector resolution. For each M , factorial moments are determined for each bin with bin multiplicity $\geq q$, where ‘ q ’ is the order of the monent. From this, the event factorial moments as

defined in Equation 2.20 are determined. Then NFM as defined in Equation 2.21 are calculated for all events. The NFM of order q then can be studied as function of various variables.

2.7.1 M -scaling

The key measurable is the behaviour of normalized factorial moments as a function of the number of phase space bins (M), which is inversely proportional to bin size ($\delta\Omega$). This behaviour is directly linked to how the points or particles are distributed in the phase space also known as spatial configurations. If the particle distributions exhibit a characteristic length scale, the factorial moments will approach a constant value, i.e., $F_q(\delta\Omega) \rightarrow \text{constant}$ as $\delta\Omega \rightarrow 0$. However, if the system exhibits scale invariance, typical characteristic of critical systems, the normalized factorial moments (Equation 2.21) will follow a scaling law, following the relation:

$$F_q(\delta) \propto (\delta)^{-\phi_q}, \quad \delta \rightarrow 0 \quad 2.22$$

It can be rewritten in the form of number of phase space bins, M as:

$$F_q(M) \propto (M^2)^{\phi_q} \quad 2.23$$

This suggests that the normalized factorial moments, $F_q(\delta\Omega)$ follow a power law behaviour with regards to decreasing bin size [78,81,157,158,172,173] and this is termed as **intermittency**.

Intermittency is defined as the self-similarity of the many-particle states spectrum when it is examined at different scales [86].

The inclusive particle distributions ρ_q defined in Equation 2.16 and the density-density correlation functions C_q in Equation 2.14 are measures used to describe the distribution and correlations of particles in phase space. As the resolution $\delta\Omega \rightarrow 0$, the scaling behaviour captured by ϕ_q suggests that ρ_q becomes increasingly sensitive to small-scale fluctuations, leading to a divergence. It indicates that at very small scales, the fluctuations in particle density become very large. Further, the density-density correlation function in a critical system follows a power-law behaviour. This means that the correlation function remains same (up to a multiplicative factor) under the rescaling of distances that is system lacks a characteristic length scale, leading to scale invariance. The divergence of ρ_q and C_q at small bin sizes reflect the fact that at very small scales, the system

exhibits extremely large fluctuations, indicative of the self-similar behaviour of the particle distributions. It implies that similar patterns of particle clustering appear at every scale, which is a direct consequence of the *intermittency* in the system. Bialas and Peschanski [78,79] were the first to introduce the use of normalized factorial moments to study dynamical fluctuations in particle density distributions obtained in heavy-ion collisions. It is demonstrated that the scaled factorial moments of multiplicity distributions exhibit a power-law dependence on the resolution in phase space called *resolution scaling*, a concept inspired by the theory of turbulence in liquids. Specifically, it is proposed that the normalized factorial moments follow the scaling behaviour as in Equation 2.23 in case there are dynamical fluctuations. This power-law behaviour is called *M*-scaling. These moments effectively filter out statistical fluctuations, leaving only the dynamical fluctuations that indicate non-trivial interactions and correlations among particles. The exponent, ϕ_q in Equation 2.23 is referred to as the intermittency index, an indicator of the strength of the intermittency [78].

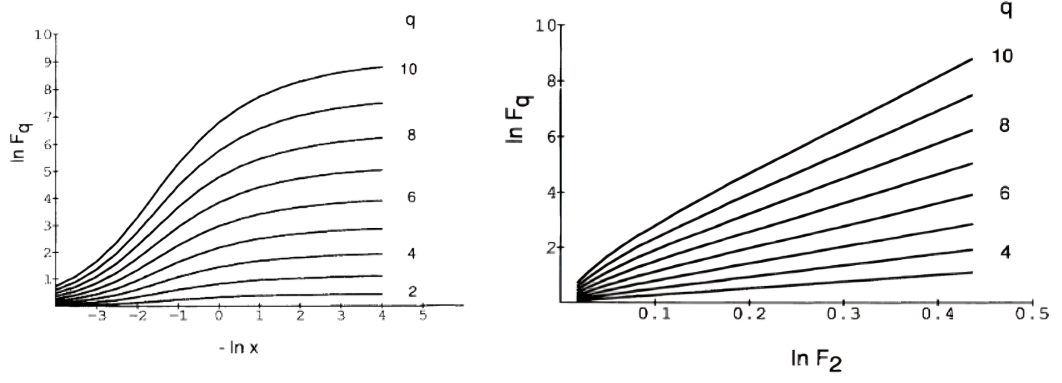
Near the QCD critical point, the value of ϕ_q is predicted to be $5 \times \frac{q-1}{6}$ for baryons and $2 \times \frac{q-1}{3}$ for pions (in the transverse momentum p_T phase space) [157,173]. It is also worthy to note that intermittency can also be observed in the first-order transition since density fluctuations in this region can be large enough and even follow a power-law geometry [174]. It is essential to acknowledge this connection, as a potential explanation requiring further investigation rather than a definitive conclusion.

2.7.2 *F*-scaling and scaling exponent (ν)

In [175], intermittency has been studied in the context of Ginzburg-Landau (GL) theory, which is a mean-field theory. It offers a macroscopic view of the phase transition, predicting the scaling behaviour of q -th order NFM, F_q as a function of second-order NFM, F_2 as [175–177]:

$$F_q(M) \propto F_2(M)^{\beta_q}, \quad 2.24$$

where, $\beta_q = \phi_q/\phi_2$. The exponent β_q depends on different critical parameters than on what ϕ_q depends. It should be noticed that the strict power law of Equation 2.24 implies that β_q is not only independent of $\delta\Omega$, the size of the bins; but also of the dimension of the bins in phase space. As if the intermittency analysis is performed for other than two dimensions (η, φ), the values of β_q would still persist.

**FIGURE 2.5:**

$\ln F_q$ vs bin size, x and $\ln F_q$ vs $\ln F_2$ as per GL description of critical systems [175].

The power-law behaviour of Equation 2.24 is termed as F -scaling [156]. Within GL description for critical system undergoing second-order phase transition, F -scaling is observed. However, in general systems where M -scaling is washed out or is absent [175,178], F -scaling may be observed. This is because of the specific critical parameters that ϕ_q depends on vary with temperature of the system and are not known in the dynamical evolution of collision system. However, F -scaling of Equation 2.24 is a visible behaviour independent of whether M -scaling (Equation 2.23) is fully realised near the QCD critical point, since β_q is independent of those critical parameters. This is evident from Figure 2.5 where the relationship between $F_q(M)$ and M (given as x in the figure) is a curve, but the relationship between $F_q(M)$ and $F_2(M)$ is still linear [179]. To describe the general impact of the phase transition, regardless of considering the details of specific critical parameters, the scaling exponent [156,178] is expressed by a power-law relationship between β_q and q as:

Scaling exponent

$$\beta_q \propto (q - 1)^\nu \quad 2.25$$

The dimensionless exponent, ν known as *scaling exponent* characterises F -scaling of all orders. This Equation 2.25 underscores the independent nature of the ν in relation to the dimensions of phase space bins. The critical value of ν is predicted to be equal to 1.304 for second-order phase transition in the entire space phase based on GL theory [175,180] as shown in Figure 2.6 where β_q as a function q based on GL theory is given by the solid line. Data points for nuclear data from KLM [165] and EMU01 [181] experiments are also shown.

In Ising model simulations performed in [84,182], magnetic dipoles (spins) in a lattice on a more microscopic level can be considered as representing hadron production. In this model, taking the regions with net spin-up as hadron presence, while net spin-down regions as their absence, the second-order phase transition at a critical temperature in which the spatial configurations of the spins would then resemble the collective behaviour of the hadrons in the heavy-ion collisions. .

NFM are calculated for those spatial configurations using intermittency methodology and scaling exponents are determined at different temperatures. The black line in Figure 2.7 represents the temperature-dependent scaling exponent $\nu(T)$ from the Ising model, ranging from 1.04 at T_c to 1.56 at lower temperatures, with an average value of 1.304. Another study predicted a value of 1.0 for the two dimensional Ising model calculations [178,183]. The authors in [170] introduce the SCR model (Successive Contraction and

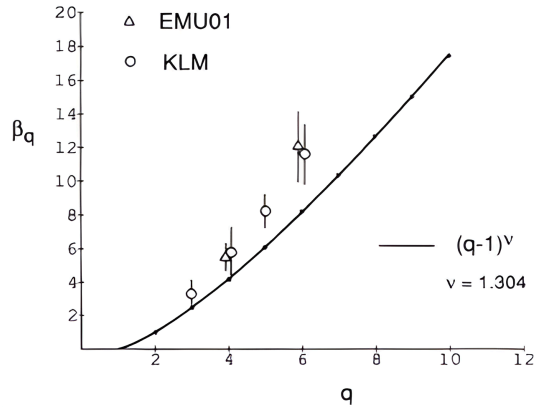


FIGURE 2.6:

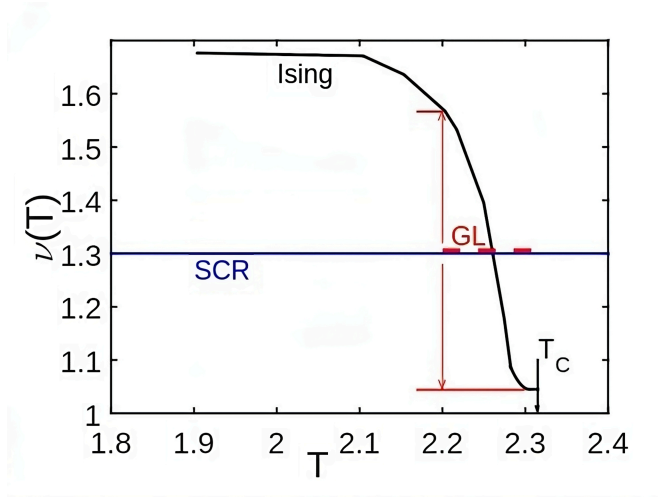
β_q as a function q determined within GL theory (solid line) is shown [175] along with nuclear data results from KLM [165] and EMU01 [181] experiments.

Randomization) to model dynamics of phase transition, where two key processes are incorporated:

- Contractions: The quarks and anti-quarks in dense regions of the plasma are redistributed together, representing the confinement force that pulls them into hadrons.
- Randomization: The quarks anti-quarks in less dense regions are randomly distributed, representing the thermal randomization that opposes the ordered confinement

By repeatedly applying these two processes, SCR simulates conditions similar to what is expected in QGP transformation into a gas of hadrons near the phase transition temperature.

Results from the analysis as described above are given by the blue line in Figure 2.7 aligning closely with the GL value. It highlights the consistency of ν value between different models. These robust observations motivate for determining ν from the LHC where the hadronic matter transforms to QGP.

**FIGURE 2.7:**

Temperature dependence of scaling exponent, $\nu(T)$ from Ising model (black line), GL theory (red dashed line) and SCR model (blue line) [170].

A range of model based studies [171,184–186], without subtracting background give scaling exponent value of > 1.7 as summarised in Table 2.1. These values of ν from the models are due to backgrounds, where ν cannot be calculated once the background is subtracted. It is important to note that a value of $\nu > 1.3$ do not imply greater fluctuations, as it may well be the consequence of a smaller ϕ_2 [178].

Model/Theory	Value of ν
GL Theory (with kinetic term) [175]	1.304
GL Theory (without kinetic term) [175]	1.316 ± 0.012
2D Ising Model [178]	1.0
SCR Model [170]	1.41
AMPT, Pb–Pb $\sqrt{s_{NN}} = 2.76$ TeV [184]	1.79 ± 0.10
AMPT, Au–Au $\sqrt{s_{NN}} = 200$ TeV [186]	1.86 ± 0.07
UrQMD, p–p $\sqrt{s_{NN}} = 13$ TeV [187]	1.743 ± 0.016
EPOS3, Pb–Pb $\sqrt{s_{NN}} = 2.76$ TeV [185]	1.80 ± 0.16
PYTHIA/Angantyr, Pb–Pb $\sqrt{s_{NN}} = 5.02$ TeV [171]	1.945 ± 0.01
NA22, p–p $\sqrt{s_{NN}} = 13$ TeV [188]	1.49
EMU01 and KLM [165,181]	1.55 ± 0.12

TABLE 2.1:

Value of scaling exponent (ν) summarised for some of the theoretical and experimental studies.

2.7.3 Fractal observables

A fractal is a complex geometric shape that exhibits self-similarity across different scales, meaning that its structure is repeated at various levels of magnification. Fractals are characterized by a fractional dimension that exceeds their topological dimension, reflecting their intricate patterns and irregularities. A homogeneous fractal distribution implies that the statistical properties of the particle distribution are invariant under scaling transformations, meaning that the probability of finding particles within a given volume $\delta\Omega$ remains constant across different regions of the phase space. The power-law behaviour associated with homogeneous fractal dimension is self-similar across different scales (i.e., scale-invariant). This scale invariance will then be reflected in the NFM as well.

From [Equation 2.23](#), it can be shown more generally that the relation between fractal dimensions and intermittency can be mathematically expressed as [\[86\]](#):

$$D \cdot \phi_q = (q - 1) \cdot d_q \quad 2.26$$

where D is the dimensionality of the phase space and d_q is the anomalous dimension of the set, obtained by subtracting the Rényi dimension[‡], D_q from D [\[189,190\]](#) as:

$$d_q = D - D_q \quad 2.27$$

D_q , Rényi dimensions extend the concept of fractal mass[§], information and correlation dimension[¶]. From [Equation 2.26](#) and [Equation 2.27](#), it can be concluded that in critical systems, NFM follow intermittent power-law, given by [\[86\]](#):

$$F_q(M) \propto (M^D)^{\phi_q}, \quad 2.28$$

$$D_q = D \left(1 - \frac{\phi_q}{q - 1} \right)$$

D_q being independent of q suggests a monofractal system. On the other hand, a change of D_q with increasing q indicates a multifractal system, where fluctuations exhibit different scaling behaviours for different scales or regions [\[179\]](#).

[‡]used for studying multifractal systems where different parts of the fractal may exhibit different scaling properties

[§]describes how the total mass (or number of points) in a fractal scales with the size of the observation window.

[¶]measures how the number of pairs of points within a certain distance scale with the distance itself.

In [191], investigations were carried to understand the fractal nature of the fluctuations using intermittency. It studies the effects of superimposing multiple fractal distributions on the strength of the intermittency signal. A theoretical p -model, a type of multiplicative cascade model that generates self-similar, fractal-like structures through a process of repeated division and redistribution of a conserved quantity, such as energy or intensity was used. In each division step, the available quantity is split between two offspring based on a probability parameter p . The parameter values ($p = 0.7$) are so chosen that the *energy* or *intensity* is assigned to one offspring in each division step, leading to an uneven distribution that manifests as strong intermittency and large local fluctuations. Effect of number of sources on fractal dimensions for order parameter defined by “ i ” were studied as shown in Figure 2.8(a). It shows the fractal dimensions D_i for a simulated p -model with $p = 0.7$. D_i is measured from 1000 simulated events, each containing nine particles. Intermittency signal is seen to diminish as two, five, and ten fractal sources are superimposed, highlighting the transition from strong to weak intermittency. The figure shows that the *intermittency signal weakens when multiple fractal sources are combined into a single event* [191].

Further extending the investigations, D_i across various types of particle collisions, e^+e^- collisions, proton-proton ($p-p$) reactions, and both central and peripheral heavy ion collisions are compared which showed that (Figure 2.8(b)) the intermittency signal is strongest in simpler systems, such as the e^+e^- two-jet data, and *progressively weakens in more complex systems with higher multiplicities, such as central heavy ion collisions*. This trend is suggestive of the behaviour of NFM establishing that complexity and multiplicity of subprocesses in particle collisions play a crucial role in the observed intermittency strength. It is seen that the strength of intermittency, which refers to the large fluctuations in

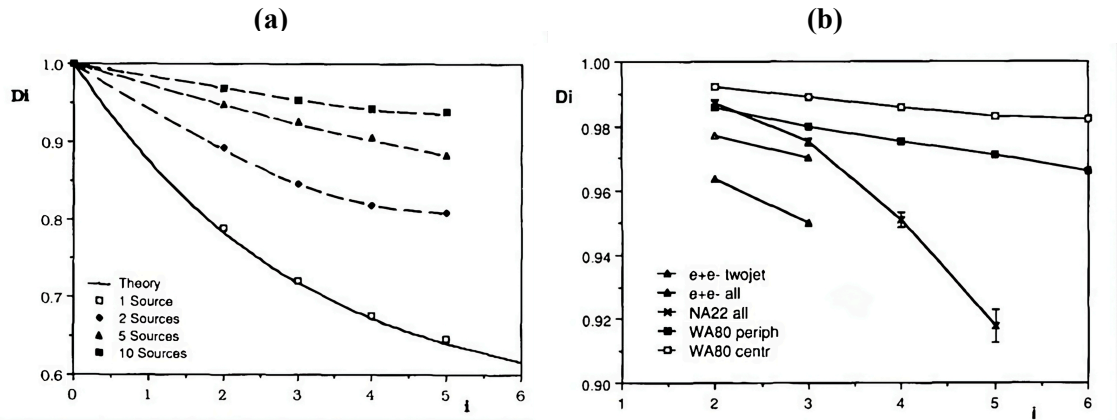
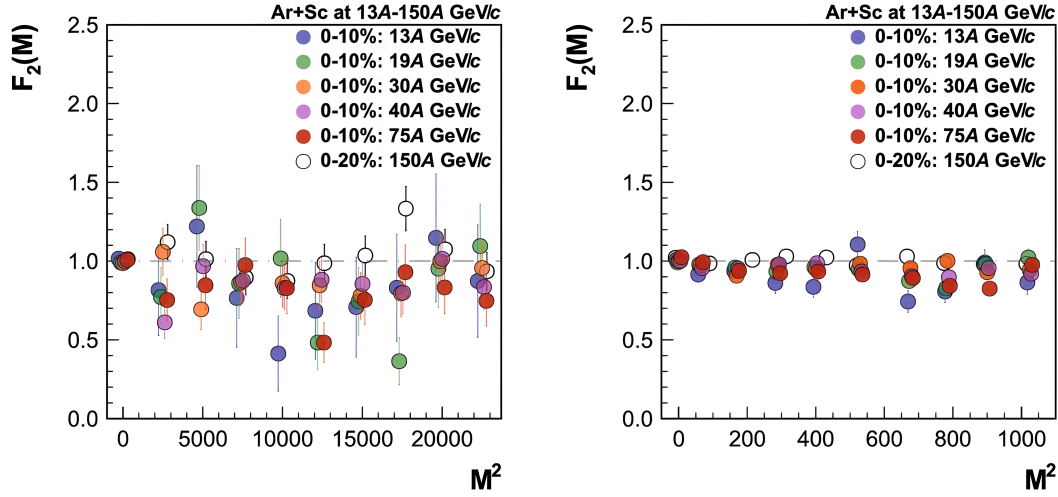


FIGURE 2.8:

D_i as a function of i for different (a) sources and (b) for different collision systems [191].

**FIGURE 2.9:**

Intermittency analysis results for proton number from the NA61/SHINE experiment for Ar+Sc collision energies summarised [87].

particle densities over small spatial intervals, tends to decrease with increasing multiplicity whereas it is also known that higher multiplicities often result from the superposition of multiple independent subprocesses within a single collision event.

2.7.4 Recent experimental review

At Super Proton Synchrotron (SPS), CERN [192] a few experimental programmes are going on to search for critical point in the nuclear matter phase diagram by measuring nuclear collisions for different systems at various energies.

For instance, the NA49 experiment has explored different system sizes of colliding nuclei (p+p, C+C, Si+Si, Pb+Pb) at 158A GeV/c [81] while the NA61/SHINE experiment has varied energies in p+p, p+Pb, Be+Be, Ar+Sc and Xe+La collisions [82] to locate the critical point but the NA61/SHINE experiment searches, focused on central $^{40}\text{Ar}+^{45}\text{Sc}$ collisions by varying beam momenta, utilising second-order scaled factorial moments of proton multiplicity distributions to analyse density fluctuations in transverse momentum space. Figure 2.9 summarises the results of proton intermittency results of NA61/SHINE [87], where the scaled factorial moments calculated from multiplicity distributions of protons are found to be nearly flat with increasing M^2 . It shows that the scaled factorial moment are independent of the number of partitions of the cumulative transverse momentum space. Also, $F_2(M)$ doesn't show power law growth with M^2 with M^2 for $1^2 \leq M^2 \leq 150^2$ (left) and $1^2 \leq M^2 \leq 32^2$ (right). The open circles show the results from $^{40}\text{Ar}+^{45}\text{Sc}$ 0–20% central collisions at 150A GeV/c while the closed circles are for 0–10% central $^{40}\text{Ar}+^{45}\text{Sc}$ collisions at 13A, 19A,

30A, 40A, and 75A GeV/c [193]. Power-law behaviour indicative of critical is not observed and thus no intermittency is observed at NA61/SHINE for Ar+Sc collisions. Similar results are obtained for Pb+Pb [82] system from this experiment. **Figure 2.10** shows the calculated chemical freeze-out points from NA61/SHINE across different collisions, showing no definitive evidence of its existence [87]. The lack of a significant signal from this experiment could be due to various factors, including statistical limitations, experimental conditions, or the actual absence of critical phenomena within the explored parameter space.

First measurements of intermittency have been performed at RHIC in Au+Au collisions at $\sqrt{s_{NN}} = 7.7\text{--}200$ GeV reported recently in [80,194]. The μ_B values corresponding to these range between 20, 40 MeV at chemical freeze-out in the phase diagram (**Figure 2.1**). The factorial moments are calculated in transverse momentum space (p_x, p_y) for charged particles (p, \bar{p}, K^\pm and π^\pm). The background subtraction is done using mixed event method, where $\Delta F_q(M) = F_q(M)^{\text{data}} - F_q(M)^{\text{mix}}$. With background subtraction, $\Delta F_q(M)$ rise with increasing M^2 as shown in **Figure 2.11**, but cannot fit a strict scaling behaviour in whole M^2 range. However, a scaling behaviour in $\Delta F_q(M)$ with $\Delta F_2(M)$ scaling, is observed at all energies as

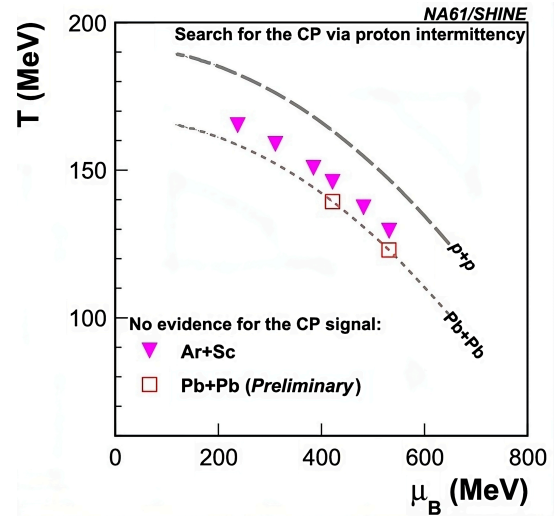


FIGURE 2.10:

NA61/SHINE diagram showing chemical freeze-out temperature as a function of baryon-chemical potential. The values calculated from p+p interactions are shown by the dashed line, while the dotted line is for central Pb+Pb collisions. Colored points highlight reactions (Ar+Sc and Pb+Pb) where the search of the critical point was done [87,195].

shown in **Figure 2.12**. It is interesting as for the similar energies, UrQMD doesn't show any power-law [196]. Based on this behaviour, the extracted scaling exponent, ν is calculated and it shows a monotonic increase from peripheral to more central Au+Au collisions (**Figure 2.13**). Moreover, ν is seen to have a non-monotonic energy dependence on collision energy. It reaches a possible minimum value at around $\sqrt{s_{NN}} = 27$ GeV for the 0–5% central collisions. In mid-central (10–40%) collisions, however, a constant energy dependence is observed, with ν showing an increasing trend with increasing centre of mass energy.

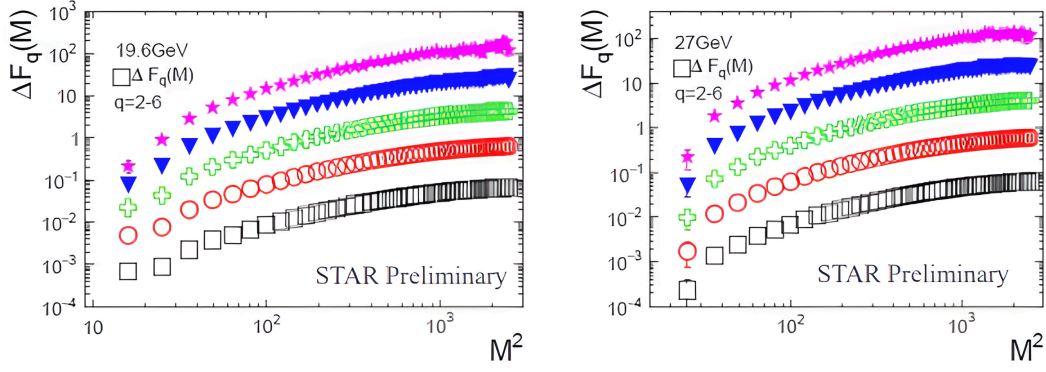


FIGURE 2.11:

$\Delta F_q(M)$ as a function of bin numbers, M^2 in 0–5% central Au+Au collisions at $\sqrt{s_{NN}} = 19.6, 27$ GeV [194].

It is difficult to conclude whether this dependence is associated with the existence of critical point. More detailed dynamical modelling of heavy-ion collisions with a realistic equation of state are required. It is also important to mention that a similar energy dependence has been found in the fourth-order net-proton cumulant ratios in the same energy region [197], which is suggested as a signature of the QCD critical point. Further, comparing to theoretical prediction of ν for GL

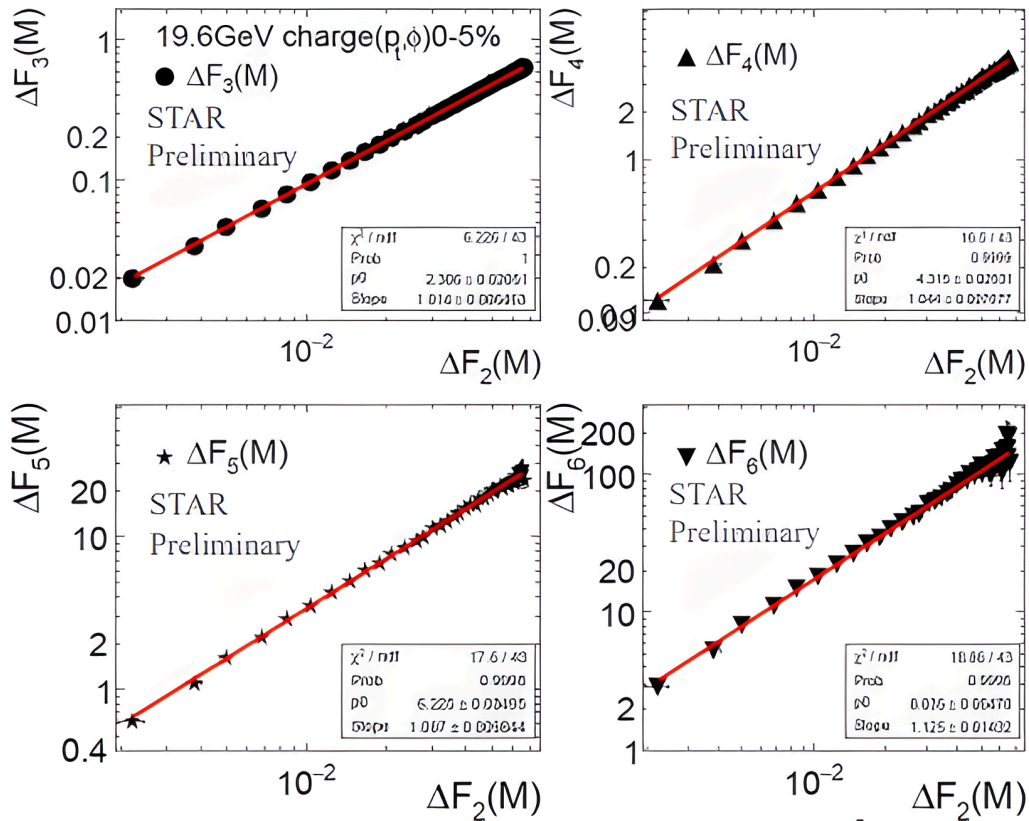


FIGURE 2.12:

The measured $\Delta F_q(M)$ ($q=3-6$) as a function of $\Delta F_2(M)$ in 0–5% Au+Au collisions at $\sqrt{s_{NN}} = 19.6$ GeV on a logarithmic scale [194].

theory and 2D-Ising model (given in **Table 2.1**) given for the entire phase space and whole acceptance level, the observed ν is much smaller, whereas it may be noted that the calculation of ν is not derived from the same parameters. These observations raise important questions about the dynamics of the phase transition that drives heavy-ion collisions. The intricate fluctuations that are observed in experimental data prompt further exploration into the mechanisms that govern the phase change between hadronic matter and QGP. This study underscores the

importance of analysing ALICE data at LHC energies, as it offers a unique opportunity to investigate critical phenomena and the understanding of phase transition in the uncharted areas of phase diagram. The sensitivity of the fractal and intermittency observables to local density fluctuations suggests that these techniques could unveil new aspects of critical behaviour in QCD matter. By systematically probing the phase space at varying collision energies, we can deepen our understanding of the fundamental properties of QGP and gain insights into the QCD phase transition's nature.

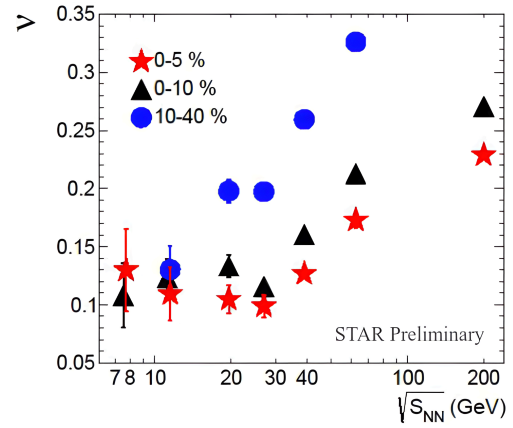


FIGURE 2.13:

Energy dependence of scaling exponent, ν , of charged hadrons in Au+Au collisions at $\sqrt{s_{NN}} = 7.7\text{--}200$ GeV. Red stars and blue circles represent ν in most central collisions (0-5%) and central collisions (10-40%), respectively [80,194].

EXPERIMENTAL SETUP

The Large Hadron Collider (LHC) [6,198,199] is the world's largest and most powerful particle accelerator at CERN (European Organization for Nuclear Research) laboratory in Geneva. It is around 27 km circular accelerator ring located underground at the border between Switzerland and France. LHC was initially designed to collide high-energy protons and heavy ions (Pb) [200], but Xenon ions were also collided in 2018 and there will be a short period of collisions between oxygen ions in 2025. One of the detectors at the LHC is the **ALICE** detector (A Large Ion Collider Experiment) [11]. ALICE is specifically designed to study heavy-ion collisions. An overview of the ALICE detector is presented in **Section 3.2**.

3.1 LHC

In 1994, the Large Hadron Collider's approval marked significant milestone by the CERN Council, intending to supersede the Large Electron-Positron collider (LEP) [6], dismantled in 2000. Spanning a circumference of 26.7 km and 100 meters beneath the earth's surface, the LHC comprises of two concentric rings of beam pipes, situated 100 m underground near the Geneva border between France and Switzerland. It stands as the world's largest and the most potent collider, capable of reaching center-of-mass energies of up to 14 TeV in p–p collisions. **Figure 3.1** shows a visualisation of CERN accelerator complex, for a complete overview see Ref. [201].

The LHC operates with two beam pipes through which highly energetic hadron beams circulate one clockwise and other anti-clockwise, utilising PS and SPS

accelerators as injectors. Around interaction points along the ring, four main experiments are strategically positioned, as briefly introduced next.

3.1.1 Main experiments

ATLAS [202] (A Toroidal LHC ApparatuS): The ATLAS experiment, a cornerstone of the LHC, is a general-purpose detector designed to explore fundamental questions in particle physics. With a toroidal magnetic system, it captures and analyses data from high-energy proton-proton collisions. ATLAS played a pivotal role in the discovery of the Higgs boson, a breakthrough that garnered the 2013 Nobel Prize in Physics. Beyond the Higgs, ATLAS investigates phenomena such as dark matter, extra dimensions, and new particles that could reshape our understanding of the universe. Its large-scale collaboration involves scientists worldwide, fostering a comprehensive approach to particle research.

CMS [203] (Compact Muon Solenoid): As the LHC's second general-purpose detector, CMS mirrors ATLAS in its quest for a deeper understanding of particle physics. Positioned at another interaction point, CMS independently verifies findings and conducts its own investigations. CMS has made significant contributions to Higgs boson studies and explores a broad spectrum of topics, including supersymmetry, dark matter, and the behaviour of quarks and gluons. With a

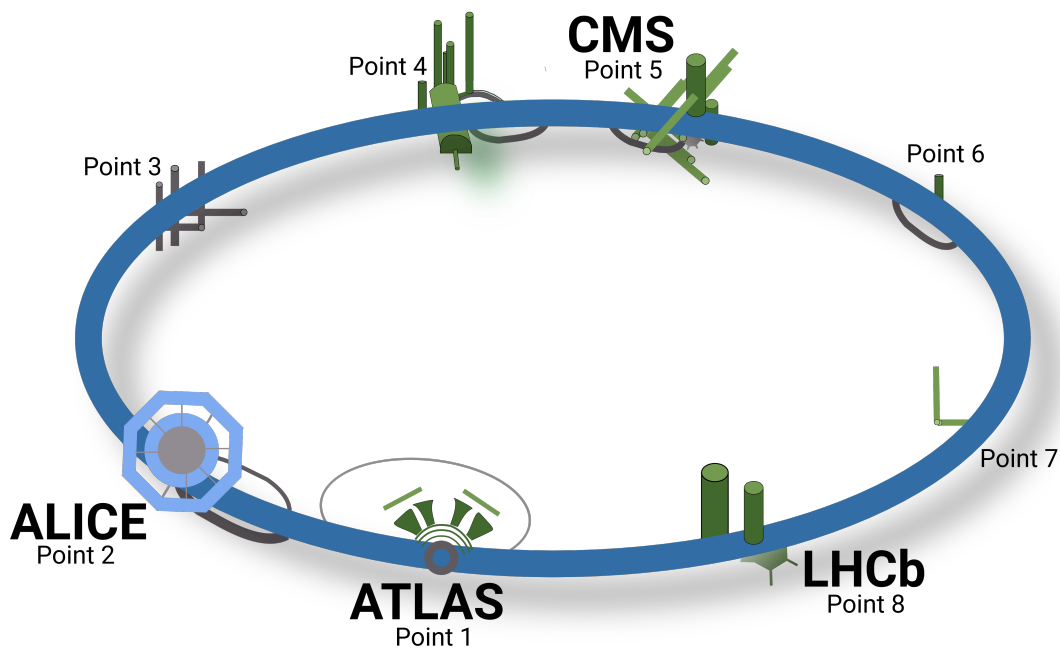


FIGURE 3.1:

Illustration visualising LHC accelerator complex with it's four main experiments and additional access points.

compact yet powerful design, CMS enables precision measurements critical to unravelling the mysteries of the subatomic world.

ALICE [11] (A Large Ion Collider Experiment): ALICE stands apart as a specialised experiment focused on heavy-ion collisions, providing insights into extreme conditions similar to the early universe. By studying Quark-Gluon Plasma, ALICE explores the transition from normal matter to the state characterized by the deconfined existence of quarks and gluons. This unique approach sheds light on the universe's formative stages and helps understand the primordial state of matter. ALICE's emphasis on heavy-ion physics contributes distinct perspectives to the broader LHC research landscape.

LHCb [204] (LHC beauty): LHCb takes a forward approach, concentrating on beauty (b) quarks and their role in the fundamental composition of matter in the universe. Investigating the differences between matter and antimatter, LHCb aims to unravel the mysteries of CP violation. By focusing on beauty quarks, the experiment delves into rare decays and explores phenomena that could explain the preference of universe for matter over antimatter. LHCb's contributions extend our understanding of fundamental symmetries and unfold the complexities of particle interactions.

In addition to these main experiments, there are several smaller and more specialized experiments at LHC, such as:

TOTEM [205] (TOTal, Elastic and diffractive cross-section Measurement): Situated around the CMS interaction point, TOTEM experiment specializes in studying the behaviour of protons post-collision in the very forward region. This experiment provides crucial information on total cross-sections, elastic scattering, and diffractive processes. TOTEM's investigations enhance our understanding of proton dynamics and contribute valuable insights into the fundamental aspects of particle interactions.

LHCf [206] (LHC forward): LHCf, positioned around the ATLAS interaction point, focuses on the particles produced in the very forward region. By studying these particles and their cascades, LHCf aims to deepen our understanding of cosmic rays and their interactions in the Earth's atmosphere. This experiment provides complementary data to high-energy cosmic ray studies, offering a unique perspective on the particles originating from outer space.

FASER [207] (ForwArd Search ExpeRiment): FASER is a novel experiment designed to explore a relatively uncharted realms of particle physics. Positioned along the LHC beamline, it focuses on detecting light and weakly interacting

particles that may escape the main detectors. This compact yet potent experiment enhances the sensitivity of LHC to hidden particles. It contributes to our knowledge for physics that goes beyond the Standard Model. FASER's strategic location allows it to probe new physics scenarios that might elude traditional detectors.

MoEDAL [208] (Monopole and Exotics Detector at the LHC): MoEDAL specialises in the search for magnetic monopoles and other exotic, highly ionising particles. Situated at a dedicated interaction point in the LHCb cavern, MoEDAL employs a range of detectors sensitive to unusual signatures associated with hypothetical monopoles. By investigating these unique particles, MoEDAL aims to broaden our understanding of particle physics and potentially uncover phenomena not predicted by the Standard Model. Its distinctive approach complements the broader research landscape at the LHC.

NA61/SHINE [209] (SHINE - SPS Heavy Ion and Neutrino Experiment): NA61/SHINE, situated at the Super Proton Synchrotron (SPS) accelerator of CERN, is a versatile experiment designed to investigate the properties of strongly interacting matter. It plays an important role in the SPS research program, focusing on studying the phase diagram of the nuclear matter under various conditions. One of its primary goals is to explore the nuclear matter phase diagram and hence to search for the critical point.

A detailed discussion of these experimental setups are available in the cited references.

3.1.2 Parameters of heavy-ion beams

Information about various parameters of particle beams is required for interpreting measurements from experiments conducted at the accelerators. This section provides a brief overview to the critical beam parameters which are essential for understanding the experimental outcomes such as at the LHC. An extensive discussion on accelerator physics colliding is available in [210].

In collider experiments, the center-of-mass energy, denoted by \sqrt{s} , is given for relativistic particles colliding with energies E_1 and E_2 as:

$$\sqrt{s} = E_1 + E_2 \quad 3.1$$

In heavy-ion collisions, the center-of-mass energy per nucleon-nucleon pair is expressed as:

$$\sqrt{s_{\text{NN}}} = \frac{Z}{A} \sqrt{s} \quad 3.2$$

where $\frac{Z}{A}$ defines charge-to-mass ratio of the ions, and \sqrt{s} represents the collision energy equivalent to that of a proton-proton collision. The equation describes how the overall energy translates into effective energy per nucleon during heavy-ion collisions. For instance, a 3.5 ZTeV beam yields a center-of-mass energy, $\sqrt{s_{\text{NN}}}$ for a collision between nuclei with $Z = 82$ and $A = 208$ is 2.76 TeV using **Equation 3.2**:

$$\sqrt{s_{\text{NN}}} = \frac{Z}{A} \sqrt{s} = \frac{82}{208} \times 3.5 \text{ TeV} \approx 2.76 \text{ TeV} \quad 3.3$$

The trajectory of a particle beam within the collider ring can be approximated by Hill's equation [210], a second-order differential equation that describes beam dynamics:

$$\frac{\partial^2 x}{\partial s^2} + \frac{1}{\beta(s)} x = 0 \quad 3.4$$

where $\beta(s)$ is a function representing the focusing strength of the beam, and x is the transverse position of the particle. The transverse beam size, $\sigma(z)$, is related to $\beta(z)$ [210] by:

$$\sigma(z) = \sqrt{\varepsilon \beta(z)} \quad 3.5$$

with z being the position along the nominal beam path and ε representing the beam emittance. The emittance ε , which quantifies spread of the beam in both position and momentum phase space, remains constant throughout the collider ring.

β -function, at the interaction point is denoted as β^* and is optimised to maximise the interaction rate between the colliding beams. β -function close to interaction point is given by:

$$\beta(s) = \beta^* \left(1 + \frac{z^2}{\beta^{*2}} \right) \quad 3.6$$

showing that a smaller β^* results in a steeper increase in $\beta(s)$ away from the interaction point. This indicates a tighter beam focus at the interaction point. This beam divergence (say, D) at the interaction point, a critical parameter for focusing, can also be expressed as:

$$D = \frac{\sqrt{\varepsilon}}{\beta^*} \quad 3.7$$

To manage the background noise and prolong the beam's operational lifetime, the beams can be angled at the interaction point, known as the crossing angle.

The interaction number occurring in a given period of time in a collider is termed as its luminosity. It measures the interaction rate and is thus defined by:

$$\mathcal{L} = \frac{dN}{dt} \frac{1}{\sigma_r} \quad 3.8$$

where $\frac{dN}{dt}$ represents the interaction rate and σ_r is the reaction cross section [211]. Luminosity is influenced by various factors. This includes properties of beams as well as the characteristics of the target and the projectile nuclei. Electromagnetic processes at the LHC typically exhibit cross sections on the order of 180 barns, significantly higher than hadronic processes (7 barns) [212]. This high cross section for electromagnetic interactions can lead to a rapid decline in peak luminosity [213]. To control luminosity, various methods are employed, such as adjusting beam separation, modifying β^* , or decreasing the number of colliding bunches. For experiments requiring lower luminosity, luminosity levelling is utilised to maintain a constant luminosity at a reduced level. This is achieved by continuously adjusting either the beam separation or β^* . Once these adjustments reach their maximum, luminosity will decay as usual. This particular approach was followed at the ALICE interaction point in 2018 when the heavy-ion operations were taking place in LHC [214].

Additionally, in the LHC [198], RF buckets are spaced 2.5 nanoseconds apart. Satellite bunches are the ions adjacent to the main bunch. Collisions involving these satellite bunches can contribute to experimental background and must be managed to avoid interference with the primary measurements. Details of the LHC heavy-ion beam parameters during data collection phases are given in Table 4.1.

3.2 ALICE experiment

Among the primary experiments at CERN, LHC is ALICE (A Large Ion Collider Experiment) [11,215,216], which is dedicated to studying heavy-ion collision. ALICE was proposed in 1993 with a Letter of Intent (LOI) outlining the experimental goals and technical requirements after the study of QGP began in 1980s at CERN's SPS and Brookhaven's AGS [216,217]. A technical proposal followed in 1996, and CERN Council approved the project in 1997 [218]. The experiment

was designed to handle the large multiplicities of charged particles expected in central Pb–Pb collisions, aiming to track up to 8000 particles per unit of rapidity and measure a wide range of particle energies. As of today, the ALICE collaboration today consists of more than 1900 members from about 170 institutions in 40 countries [11]. Primary goal of this collaboration is to study the properties of strongly interacting matter under extreme energy densities as mentioned in [218], specifically the formation and properties of the QGP by studying ultra-relativistic heavy-ion collisions. This section provides an overview of the ALICE coordinate system, its detector subsystems and data collection related information.

The ALICE experiment is positioned within the LHC ring at Point 2 [215]. Its coordinate system is defined such that the axis that points towards the tunnel going to one of the largest experiment, ATLAS is taken to be z -axis. y -axis is the upward direction, while the axis pointing towards the LHC ring is taken as x -axis. In this system, polar angle θ is the angle of the particle relative to the beam axis and by convention helps to determine pseudorapidity, $\eta = -\ln(\tan(\theta/2))$.

For high-momentum (p) particles, the pseudorapidity, η is often used as an approximation of rapidity because the particle's rest mass is negligible relative to its total energy [210]. Pseudorapidity is defined as:

$$\eta = \frac{1}{2} \ln \left(\frac{p + p_L}{p - p_L} \right) \approx \frac{1}{2} \ln \left(\frac{E + p_L}{E - p_L} \right) \quad 3.9$$

where p is the particle's total momentum, p_L is the longitudinal component of the momentum along the z -axis and E is the particle's total energy.

The coordinate system divides the detector into two sides: the A-side (positive η) towards the ATLAS tunnel, and the C-side (negative η) towards the CMS tunnel. The acceptance of ALICE's subsystems is characterised by pseudorapidity, η and azimuthal angle, φ , wherein mid-rapidity is $|\eta| < 0.9$ or an angle of $\approx \pm 45^\circ$ in the $x - y$ plane [219]. This region captures a large fraction of the produced particles, allowing various analysis to understand collision dynamics and the properties of QGP.

ALICE detector is a massive and complex apparatus, approximately 16 meters in height, 16 meters in width, and 26 meters in length, with a total weight of about 10,000 tonnes. Schematics of the complete ALICE Detector is given in **Figure 3.2**. The detector can be broadly taken to be consisting of two main parts, the central barrel and the muon arm, each serving distinct purposes [219,220].

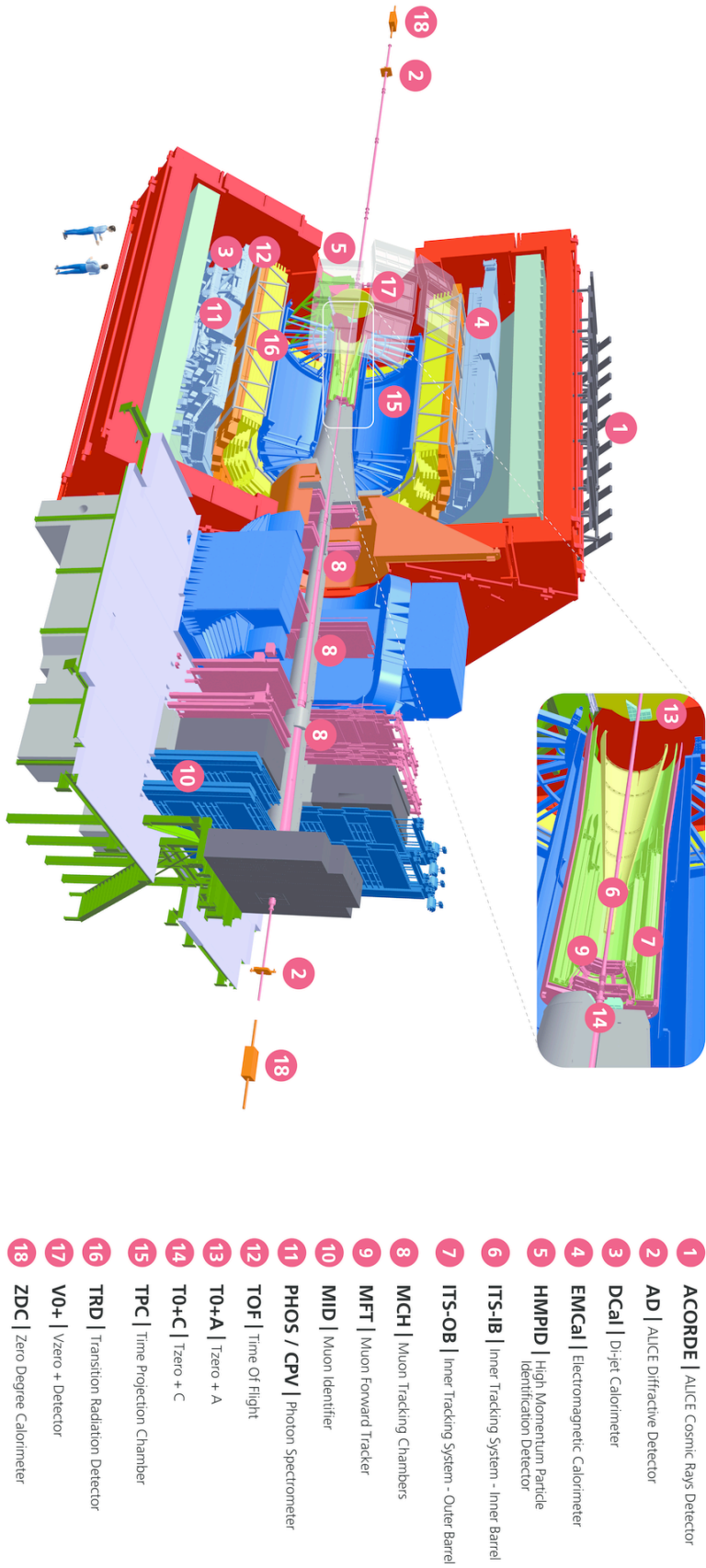


FIGURE 3.2:
Schematics of ALICE Detector showing subsystems with labels [219]. Data recorded by detectors numbered as 6,7,15 and 17 is used in this thesis.

Central Barrel: This component is located inside a large solenoid magnet generating a uniform magnetic field of 0.5 Tesla [221]. It is crucial for particle tracking and identification. Key subsystems within the central barrel include:

1. Inner Tracking System (ITS) [218]: Comprised of six-layers of silicon detector enabling high-precision particle tracking.
2. Time Projection Chamber (TPC) [218]: Enables tracking and particle identification, extending a wide momentum range from low to high momentum.
3. Time Of Flight (TOF): Measures the time particles take to traverse the detector, aiding in particle identification.
4. Transition Radiation Detector (TRD): Enhances particle tracking and momentum resolution by utilising transition radiation to distinguish between different types of charged particles, particularly at high energies.
5. High-Multiplicity Particle Identification Detector (HMPID): Used for particle identification in high-multiplicity environments.
6. PHOton Spectrometer (PHOS) and ElectroMagnetic Calorimeter (EMCAL): Calorimeters are specialized detectors designed to measure electromagnetic radiation, including high-energy photons, electrons, pions, and jets. They function alongside the Charged-Particle Veto (CPV) detector. CPV eliminates the contribution of charged particles, ensuring accurate measurement of photons originating from strong interactions or radiative decays.
7. ACORDE: A cosmic ray detector positioned atop the solenoid magnet to trigger cosmic ray events.

Muon Arm: Positioned in the forward region, this subsystem includes the forward muon spectrometer and a dipole magnet. It is essential for reconstructing heavy quarkonia states through muon pairs. The dipole magnet bends the trajectories of muons, which are then detected using an absorber and a tracking system.

In addition to the central barrel and muon arm, ALICE features several detectors in the forward region, including:

1. ZDC: The Zero Degree Calorimeter (ZDC) [222] is used to measure spectator nucleons escaping the collision. Neutron spectators, which travel in straight-line trajectories due to their lack of magnetic charge, must be correctly aligned with the ZDC to ensure accurate measurements. Instruments positioned between the interaction point and the calorimeters could intercept neutron spectators unless accounted for. Additionally, to preserve the ZDC's efficiency, the internal crossing angle introduced by the muon dipole requires compensation through an external beam crossing angle [220].
2. Photon Multiplicity Detector (PMD): Used to measure photon multiplicities.

3. Forward Multiplicity Detector (FMD): Extends multiplicity measurements to large values of $|\eta|$ so as to study the system's bulk properties.
4. V0 Detectors: Used for centrality determination and triggering discussed in following sections.

In this thesis, the V0 detector shown in **Figure 3.2** is used for centrality determination and triggering. The TPC is used for the central regions of pseudorapidity and is combined with the ITS to reconstruct tracks of charged particles. Detail of these detectors is given below.

3.2.1 Inner Tracking System (ITS)

The Inner Tracking System (ITS) [218,223] is the innermost detector of the ALICE experiment, designed with six concentric layers of silicon detectors to provide precise tracking and particle identification, particularly for low-momentum particles. The ITS plays a fundamental role in determining primary collision vertex and identifying secondary vertices, particularly those from particle decays in heavy-ion collisions. Additionally, it complements the Time Projection Chamber (TPC) in the tracking and identification of particles across a broad range of momenta.

The ITS is positioned around the beam pipe, with its six layers extending from 3.9 cm to 43 cm from the interaction point (IP), covering a pseudorapidity range of $|\eta| < 0.9$.

The ITS is composed of three sub-detectors: Silicon Pixel Detectors (SPD), Silicon Drift Detectors (SDD), and Silicon Strip Detectors (SSD) as shown in **Figure 3.3**. The SPD layers, closest to the beam, are essential for vertex deter-

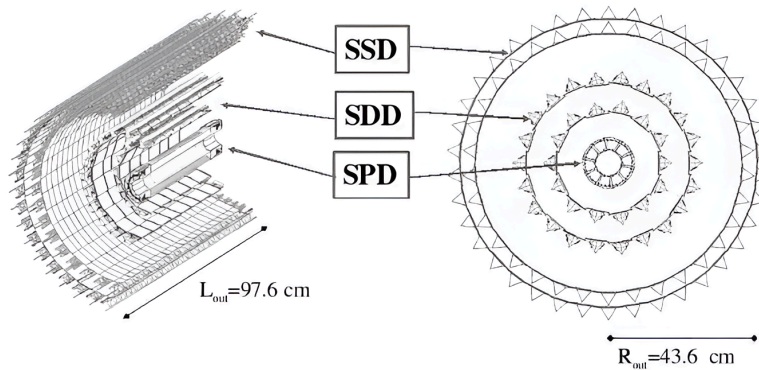


FIGURE 3.3:

Sketch of the Inner Tracking System (ITS) taken from [224], illustrating its components: Silicon Pixel Detector (SPD), Silicon Drift Detector (SDD), and Silicon Strip Detector (SSD).

mination and tracking low-momentum particles. These layers feature a large number of channels – 3,276,800 in the first layer and 6,553,600 in the second layer – allowing for precise 2D spatial resolution, which is vital as close to beam pipe, high particle density is expected. SPD layers are highly granular, crucial for managing the dense particle environment in heavy-ion collisions. These layers, located at 3.9 cm and 7.6 cm, are instrumental in determining the primary vertex with a resolution of about $100\ \mu\text{m}$. The SDD layers are located at 15 cm and at 23.9 cm, handle lower particle densities and provide energy loss measurements (dE/dx) for particle identification. The outermost SSD layers, at 38 cm and 43 cm, match reconstructed tracks with those from the TPC and provide spatial resolutions enhancing tracking precision.

3.2.2 Time Projection Chamber (TPC)

The Time Projection Chamber (TPC) [218,225] is the primary tracking and particle identification detector within the ALICE experiment, located in the central barrel with schematic diagram as shown in Figure 3.4. This has cylindrical shape and spanning a radial distance of 85 cm to 250 cm and a total length of 5 meters along the z-axis, enclosing an active volume of $90\ \text{m}^3$ filled with a gas mixture of $\text{Ne}/\text{CO}_2/\text{N}_2$ (90/10/5) [218]. This detector is crucial for reconstructing the trajectories of charged particles, measuring their momentum, and identifying them across a wide pseudorapidity range, up to $|\eta| < 0.9$ with standard resolution and extending to $|\eta| < 1.5$ with reduced momentum resolution. The measurable p_T range is from $0.1\ \text{GeV}/c$ upto $100\ \text{GeV}/c$.

As charged particles pass through the TPC, they ionise the gas, creating ion-electron pairs along their path. The TPC's uniform electrostatic field of $400\ \text{V}/\text{cm}$ causes the electrons to drift towards the end-cap readout chambers, while the ions drift towards the central cathode. The position and timing of these electrons, combined with the magnetic field's influence on their curved trajectories, allow for the reconstruction of the particles three-dimensional paths.

The TPC's tracking capabilities are enhanced by the Bethe-Bloch formula [226], which describes the energy loss of charged particles as they move through the gas. The energy loss, expressed as $\frac{dE}{dx}$, is dependent on the particle's velocity and is used in conjunction with momentum measurements to identify the particle species. At intermediate velocities ($0.1 < \beta_y < 1000$), the Bethe-Bloch relation is particularly effective in distinguishing between different particle types [226,227]. This identification is most precise in the low momentum region ($p_T < 1\ \text{GeV}/c$), where particles are well-separated, and less effective in the

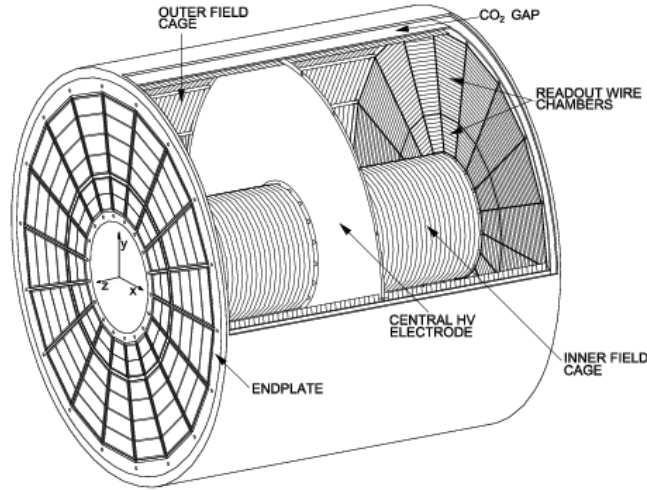


FIGURE 3.4:

Sketch of the Time Projection Chamber (TPC) taken from [225]. It shows high voltage electrode positioned at the center of the drift volume. The endplates are divided into 18 sectors, each containing 36 readout chambers.

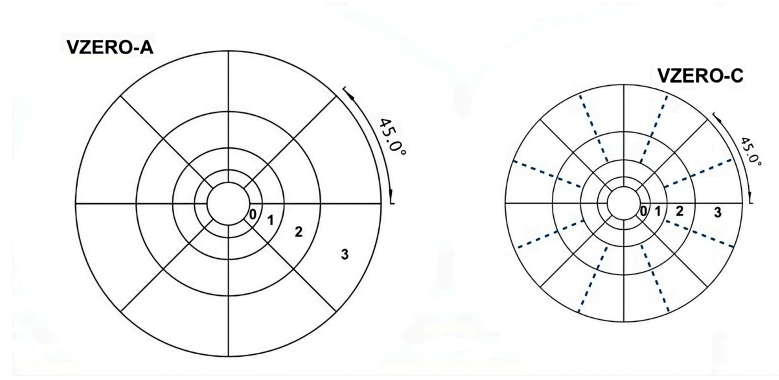
relativistic region ($p_T < 3 \text{ GeV}/c$). However, with statistical methods like unfolding, the TPC can still contribute to particle identification at higher momenta.

To maintain its high-performance tracking and identification capabilities, the TPC underwent a significant upgrade to improve ALICE's detection systems for Run3 [228,229].

3.2.3 V0 Scintillators

The V0, also many a times referred to as “VZERO” [215,219] detector system in ALICE comprises scintillator arrays (shown in Figure 3.5) positioned on both sides of the interaction point for triggering and centrality measurements. Each detector includes four scintillator rings that detect charged particles, converting their energy into photons. These photons are amplified by photomultipliers, generating a shower of electrons to enhance the signal.

The V0 detectors primarily function as triggers and measure collision centrality. V0-A and V0-C, located on the A and C sides of ALICE, respectively, measure particle multiplicities in their pseudorapidity regions: V0-A covers $2.8 < \eta < 5.1$, and V0-C covers $-1.7 < \eta < -3.7$ [215]. Although the V0 detectors have full azimuthal coverage and are segmented into eight azimuthal sectors and four radial sectors, their sparse azimuthal resolution makes them less suitable for differential flow analysis. They are used as reference regions for cumulant analysis instead.

**FIGURE 3.5:**

Sketch of V0-A and V0-C taken from [230]. Both are divided into 4 rings and 8 segments. In V0-C, the scintillator segment on both sides of dashed lines are joined to the same photomultiplier.

3.2.4 Triggering

In high-energy physics experiments like ALICE, not all collisions can be recorded due to limitations in the data readout rate. To manage the vast amount of collision data, a trigger system is implemented to select a fraction of the collisions based on certain criteria. Most physics analysis in ALICE focus on low transverse momentum phenomena, which often lack clear signals for triggering. To ensure that relevant data is captured, ALICE employs a minimum bias (MB) trigger system. This trigger activates when there is detection of minimal activity, primarily with the V0 detector [230], or sometimes with the SPD.

The V0 detector is composed of two scintillator arrays on opposite sides of the interaction point and plays a central role in minimum bias triggering. Each V0 detector segment has a threshold set to detect energy deposition equivalent to that of a minimum-ionising particle. The configuration of these triggers can vary depending on the data-taking period, for example different magnetic field settings required adjustments to the trigger criteria in case of 2010 Pb-Pb collisions and for Xe-Xe collisions. For instance, in Pb-Pb collisions, two main MB triggers were used: MBand, coincident V0-A and V0-C signals, and MBor, which required signals in either V0-A, V0-C, or SPD [219].

The Xe-Xe data-taking introduced a more stringent trigger configuration because of low magnetic field, which increased the likelihood of electromagnetic interactions [231]. To filter out background events, signals from V0-A, V0-C, ZNA, and ZNC needed to coincide. It ensured full efficiency for hadronic interactions within the 0–90% centrality, which was validated against a control trigger that relied on the signals coincidences from V0-A and V0-C.

ALICE's data-taking process relies heavily on Central Trigger Processor (CTP), which records data from various fast detectors and determines trigger decisions. It further instructs the Data AcQuisition (DAQ) system to record the event if the trigger criteria are met [219]. The CTP supports multiple trigger classes, with minimum-bias triggers being the most fundamental. These triggers are designed to capture all hadronic interaction events while minimising bias from the trigger decisions. To further refine the dataset, other trigger conditions are used, such as high-multiplicity triggers for p–p collisions, central and semi-central triggers for Pb–Pb collisions, and rare probe triggers, which require specific energy deposits or particle detections above certain thresholds [219].

3.3 ALICE: Particle reconstruction and data formats

During ALICE's data-taking, raw data is recorded and later processed through a procedure called “reconstruction.” This process transforms the raw, unstructured data into a structured format, enabling the identification of individual particles and the extraction of their kinematic properties.

At the outset of the reconstruction process is the calibration of data for each detector, which ensures that the data accurately reflects the collision events. Calibration involves aligning detectors parameters, identifying bad or noisy elements, and adjusting timing and amplitude. This data is taken from both collision data as well as dedicated calibration runs. After calibration, the primary vertex of the collision is determined using vertex finding algorithms, which analyse the spatial distribution of detected particles. Track reconstruction algorithms then trace the trajectories of these particles across multiple detectors, creating a coherent picture of each particle's path. The centrality of the collision, which indicates how head-on the collision was, is also determined using calibrated signals from detectors like the V0. This process is crucial for categorising events during analysis. Once reconstruction is complete, the data volume is significantly reduced, making it manageable for various physics analysis. The final reconstructed data is stored in a standardised format, for efficient access and analysis. A brief explanation of algorithms in vertex finding, track reconstruction, and software in ALICE is given below:

3.3.1 Vertex determination

Detailed track reconstruction in the central barrel detectors of the ALICE follows a preliminary vertex identification using the two layers of the Silicon Pixel Detector [219]. Initially in these layers, clusters create segments, and the point

of intersection for most of the tracklets is identified as preliminary vertex. This vertex is used as the starting point for track reconstruction algorithms. After the tracks are reconstructed, a more precise vertex is evaluated separately for both ITS–TPC tracks and TPC–only tracks. This process begins by approximating the vertex position through the propagation of tracks to their closest approach, nominal beam axis. This approximation is refined through a precise vertex fit after removal of outliers, further reducing the influence of outliers. The final vertex position, especially when based on ITS–TPC tracks, offers significantly higher resolution compared to the preliminary estimate [219,232,233].

3.3.2 Track reconstruction

Within the central barrel of ALICE, the charged particle tracks are reconstructed through a sophisticated algorithm that operates on clusters [219]. These are obtained by associating measurements such as position, amplitudes, times, and the corresponding errors into clusters in each detector. The track reconstruction employs a Kalman filter [234], a mathematical technique used for estimating the state of a system from noisy measurements. This technique is particularly well-suited for tracking in high-energy physics, as it iteratively updates the estimates of a particle’s trajectory by combining prior estimates with new measurements, thus refining the track parameters at each step.

Track reconstruction begins in TPC by seeding tracks with the help of clusters that are located at large radii. Alternatively, both clusters and preliminary vertex information can also be used. A tracklet is defined as a short segment of a track, typically formed by linking two or more clusters that are spatially close and consistent with a particle’s trajectory. These tracklets serve as the initial seeds for full track reconstruction. An inward propagation of tracks is performed and are then updated as they encounter TPC clusters. Algorithms that search for tracks with shared clusters help suppress multiple reconstructions of the same particle. After the tracks meet minimum quality criteria, they are propagated to the inner radius of the TPC, with its TPC–only parameters stored for further analysis.

Tracks are propagated layer by layer in the ITS after the tracking is extended outside of TPC. A penalty factor accounts for any missing hits, ensuring a robust track quality parameter. This penalty factor adjusts the track’s quality metrics to reflect the uncertainty introduced by the absence of certain measurements, thus maintaining the integrity of the reconstruction process [233]. The best track fits are selected using the Kalman filter [234], which, by accounting for multiple

scattering and energy-loss effects, allows for the reconstruction of low transverse momentum particles.

After an inward propagation and a second outward iteration, the tracks are further updated and matched to hits in outer detectors like the TOF and TRD. In a final inward iteration, the tracks are refitted, ensuring the best possible estimates for the track parameters. Ultimately, global ITS–TPC tracks, which offer the highest precision, are stored either with or without a constraint to the primary vertex. The secondary vertices that result from particle decays, photon conversions are recognized on the basis of their decay topology, allowing for the reconstruction of particles that decay after the primary interaction. The tracking parametrisations at each step of the reconstruction process has varying acceptance (the range of angles and momenta where the detector can reliably measure tracks), efficiency (the probability of detecting a track), and transverse momentum resolution (accuracy in measuring momentum perpendicular to the beam).

Global ITS–TPC tracks are generally the most accurate estimates because they combine the precise tracking of the ITS with the high momentum resolution of the TPC; but they have limited acceptance in φ . The two innermost layers of ITS upto 20%, specifically the SPD, were offline for the 2010 data-taking period. This issue was largely resolved for Run 2 by improving the cooling system of ITS. TPC–only tracks, which are reconstructed solely using the TPC, offer uniform track acceptance throughout the detector, with their only significant limitations coming from the borders of

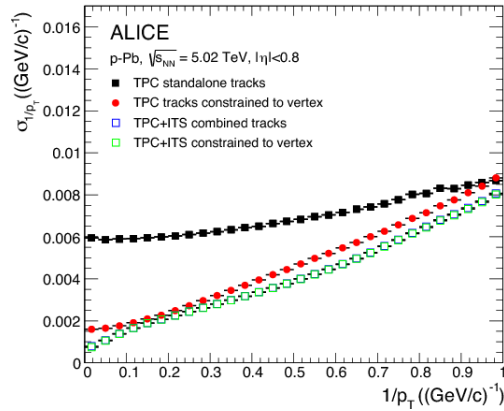


FIGURE 3.6: The transverse momentum (p_T) resolution for TPC–only and matched ITS–TPC tracks compared with and without constraining to the primary vertex for p–Pb collisions at $\sqrt{s_{NN}} = 2.76$ TeV [219].

the readout chambers, where the tracking may not be as precise. **Figure 3.6** compares transverse momentum (p_T) resolution for different track parameterisations. It shows that p_T resolution for TPC–only tracks is generally poorer compared to global tracks because of the increased distance between TPC and the interaction point, as well as additional material the tracks must pass through. This results in larger uncertainties in momentum measurements. However, this issue can be partially alleviated by applying a constraint to the TPC–only tracks during the

track fit step, where the tracks are forced to pass through the primary vertex. This improves the accuracy of the transverse momentum estimation by leveraging the known position of the primary vertex, thereby compensating for the reduced resolution. For low transverse momentum particles ($p_T < 10 \text{ GeV}/c$), the resolution of TPC-only tracks is of a similar magnitude to that of ITS-TPC global tracks. However, TPC-only tracks suffer from higher contamination from secondary particles [219]. The iterative tracking process, which involves repeated updates and refinements of track parameters, enhances both the efficiency and accuracy of the reconstruction. The use of the Kalman filter throughout these stages is crucial, as it allows for the integration of new measurements while accounting for uncertainties, such as noise and multiple scattering. This ensures that the reconstructed tracks are as accurate as possible, ultimately improving the overall quality of the data analysis.

3.3.3 Data formats and software

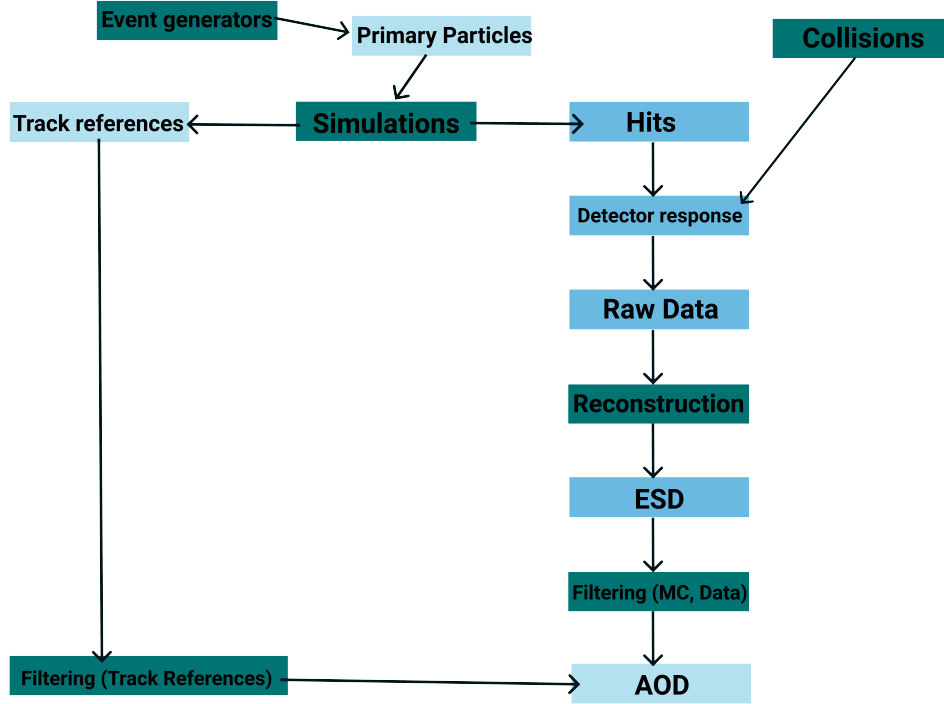
As discussed above, in the ALICE experiment a multi-stage reconstruction process transforms raw data collected during particle collisions into usable physics information. Initially, data recorded during experiments is converted into reconstruction points. This step includes calibrating detectors and using the primary vertex from the SPD (Silicon Pixel Detector) to establish track seeds. Once the reconstruction points are obtained, tracks are reconstructed using the Kalman filter algorithm. The primary vertex is then recalculated based on the reconstructed tracks, resulting in the Event Summary Data (ESD). The ESD contains detailed information about tracks and vertices. The ESD is subjected to a filtering process where signals from various detectors, are refined to produce the Analysis Object Data (AOD). The AOD is the final format used for physics analysis and is significantly smaller in size compared to the corresponding ESD objects.

Monte Carlo simulations are integral to any heavy-ion collision reconstruction process, providing a means to model detector effects and physics. Using event generators like PYTHIA [235] for proton-proton collisions and HIJING [236] for heavy-ion collisions, simulated particles are created and propagated through virtual detector geometry created using GEANT [237], toolkit to generate hits and track references. The simulated *primary particles* [238] are the particles generated by the event generator and are commonly used as the particles containing information about the collision and evolution of the plasma. This simulation gives the output which is similar to the raw data. A reconstruction process similar to the one used for experimental data reconstruction, to produce Event Summary

Data (ESD) objects is used on the raw data level information from simulation. The ESD objects are then subjected to a filtering process, leading to the creation of Analysis Object Data (AOD) objects. Track references from simulations aid in the analysis of particle interactions by providing a means to compare reconstructed tracks with their true counterparts [215]. The analysis process is typically faster when conducted on AOD files due to their streamlined internal structure compared to ESD files. AOD files contain processed data that is optimized for quicker analysis. However, certain analyses may require detailed information that is only available in the ESD objects, which store raw and reconstructed data. Therefore, while many physics analyses can be efficiently performed using AOD files, some may still necessitate the use of ESD files for more detailed or specific information. Both the formats suffice for a physics analysis in general. The whole workflow step-by-step is visualised in **Figure 3.7**.

In ALICE the data acquisition process is managed by a three-level triggering system directed by the Central Trigger Processor (CTP). The triggers – Level 0 (L0), Level 1, and Level 2 – select events based on the timing and type of detector signals, ensuring that only relevant events are stored. The collected data is processed offline using a distributed computing grid (LHC Computing Grid, LCG), with AliPhysics framework [239–241] written in object-oriented programming language C++ developed by the ALICE Collaboration. Every analysis task is written as a C++ class and handles both real and simulated data. AliPhysics in turn uses a collection of tools (mostly classes) from AliRoot framework [240,242] developed by ALICE. This software, built on the C++ based ROOT framework [243], also filters data from ESDs into AODs which enables faster physics analysis. ROOT is a collection of C++ libraries aimed for data analysis in large experiments developed basically for High Energy Physics. It is extensively employed across all the experiments at CERN, due to its suitability for tasks like linear algebra, function plotting, fitting, and histogram presentation, among other capabilities. ROOT also has a tightly integrated C/C++ Interpreter, CINT5, which can interpret, compile C/C++ scripts. This enables ROOT to evaluate C/C++ code dynamically during runtime.

In ALICE data taking is organised into periods and runs, to manage the experimental conditions and configurations. Periods represent extended intervals with consistent global conditions, while runs are shorter periods with stable operating conditions. For example, the 2015 Pb–Pb data is labelled “LHC15o”. Each dataset can be reconstructed multiple times, referred to as passes, to incorporate software improvements.

**FIGURE 3.7:**

Visualisation of the workflow from event generation to the final data format used for analysis. The **green boxes** are the processes, the **light blue boxes** are the data formats used in this thesis and the **blue boxes** are the step in between. The diagram highlights several key stages and data formats in this process.

3.3.4 Centrality determination

Centrality determination in heavy-ion collisions is a critical component for understanding the collision geometry. The impact parameter b represents the distance between the centers of two colliding nuclei. It cannot be directly measured, but inferred through the centrality of the collision. Centrality is defined as a percentile of the total hadronic interaction cross section σ_{aa} , and is related to the charged-particle multiplicity density $\frac{dN_{ch}}{d\eta}$ observed in the detectors. The most central collisions, with the smallest impact parameter $b \approx 0$, correspond to lower centrality values.

ALICE uses several methods to estimate centrality, with the primary method being the “V0 amplitude” approach [244]. This method involves summing the amplitudes from the V0A and V0C detectors, which are designed to detect charged particles in the forward direction. Distribution of the events as a function of V0 amplitude is fitted with a Glauber Monte Carlo model [57], which is a statistical approach that simulates the collision geometry. This model calculates N_{part} and N_{coll} , which are then used to estimate centrality classes. N_{part} denotes the number of participating nucleons and N_{coll} denotes the number of binary

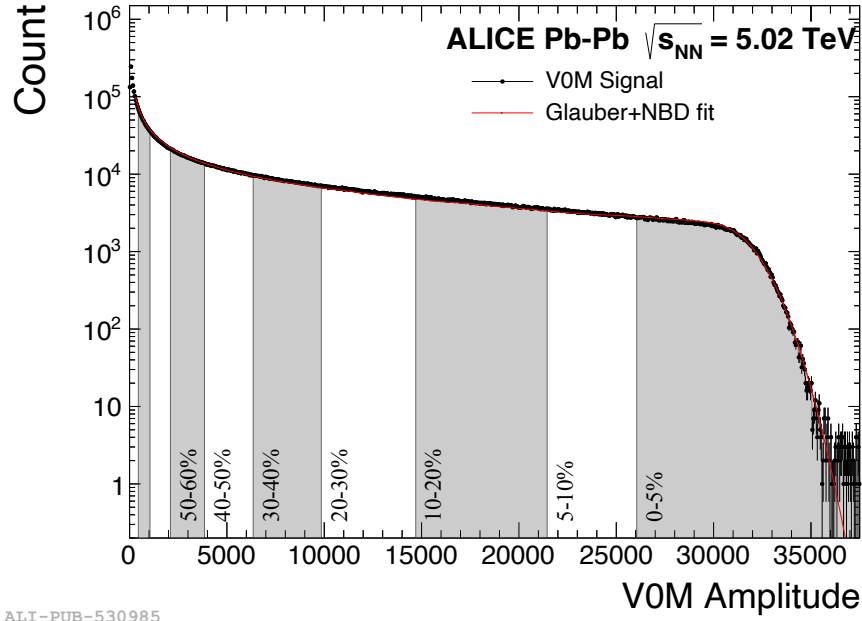
nucleon-nucleon collision. These quantities are then used to estimate centrality classes. The number of participating nucleons N_{part} is determined by calculating the overlap volume of the two nuclei. This is done by integrating the nucleon density distributions over the collision volume. The number of binary collisions N_{coll} is then computed based on the overlap area, using the inelastic nucleon-nucleon cross section [245]. Mathematically, the Glauber model involves several key components. The model starts by considering the distribution of nucleons within each nucleus, typically described using a nuclear density profile, often modelled as a Woods-Saxon distribution. This profile is used to compute the probability of a nucleon-nucleon collision based on the impact parameter b .

In ALICE, the Glauber model employs a two-component approach to describe particle production. The first component is associated with soft processes, which are assumed to scale with the number of participating nucleons N_{part} . The second component relates to hard processes, which scale with the number of binary collisions N_{coll} . The overall particle production can thus be described by a two-component model [244]:

$$N_{\text{sources}} = fN_{\text{part}} + (1 - f)N_{\text{coll}} \quad 3.10$$

describes a linear combination of N_{part} and N_{coll} , weighted by the parameter f . The parameter f controls the relative contribution of soft (low-energy) and hard (high-energy) processes to the collision dynamics. The Glauber model fit, which utilizes this equation, provides a way to estimate the total hadronic cross-section. From this, centrality classes are defined, and the impact parameter corresponding to 90% of the total hadronic cross-section is identified, helping to categorize the collision events based on their overlap and intensity.

In addition to the V0 amplitude method, centrality can also be estimated using other detector systems, such as the SPD or the TPC, and by the energy deposited in the Zero Degree Calorimeters (ZDCs). Each method provides a different resolution, with the V0 amplitude method typically offering the best centrality resolution. To ensure accurate centrality determination, the distributions of particle multiplicity are compared with model predictions, and a fit is performed to match the measured data with the expected distribution. The result is a classification of events into centrality classes, allowing for detailed studies of collision dynamics and the properties of the quark-gluon plasma. The fit is applied to collisions with sufficiently large V0 signals to ensure the maximum efficiency of event selection and collision purity. This approach excludes peripheral collisions

**FIGURE 3.8:**

Distribution of events as a function of the sum of the signal amplitudes from the V0A and V0C detectors for Pb–Pb, $\sqrt{s_{NN}} = 5.02$ TeV. The line in red color represents the fit using the Negative Binomial Distribution (NBD) coupled with the Glauber model. Numbers in percentages, that are shown correspond to centrality intervals. Figure taken from [241].

falling in the 90–100% range from the fit due to their lower signal-to-noise ratio and less reliable measurement accuracy.

Centrality definitions based on V0 signal amplitudes can introduce a bias compared to direct impact parameter measurements. This bias arises from fluctuations in the V0 multiplicity, which can affect the centrality classification. Despite these potential biases, the discrepancies between centrality definitions based on V0 signals and impact parameters are generally minimal for collisions in the centrality range of 0% to 80%. This range encompasses most of the significant collision events used for physics analysis.

Figure 3.8 shows Glauber model fit (red colour line) to the V0 signal amplitude sum (black line). Figure also marks the centrality intervals determined by this fit, which are used to categorise the collision events. This method classifies the collisions with a high degree of precision and hence helps to get resulting physics with a better understanding of the collision geometry and dynamics

INTERMITTENCY ANALYSIS

This chapter provides a comprehensive account of the analysis performed on the various datasets investigated for the study of intermittency, as defined in **Chapter 2**. The experimental data from ALICE experiment [11] at LHC [47] is mainly analysed which is subject to various cuts and conditions before the analysis. The description of these various cuts making use of the Monte Carlo (HIJING [246]) studies and their optimization etc. is given in this chapter followed by the observations and results on the observables studied. An outline of the systematic uncertainties affecting measurements, along with the various factors contributing to these uncertainties is also given. Lastly, a two dimensional intermittency analysis performed on events generated using standalone PYTHIA8/Angantyr [235] event generator is discussed.

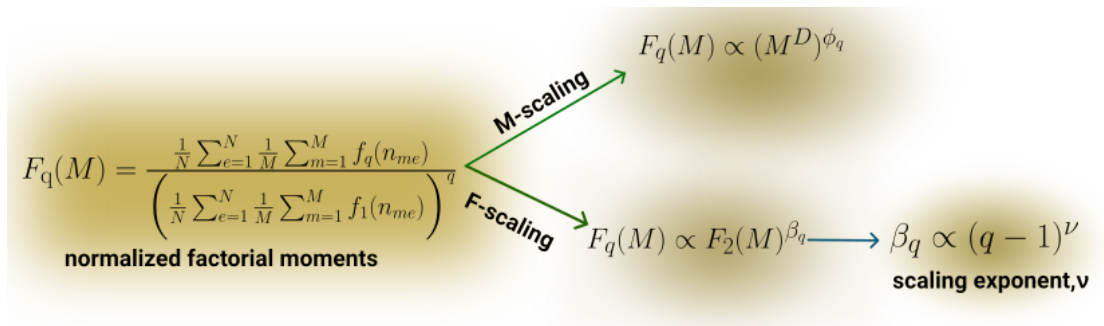


FIGURE 4.1:

Observables: Normalized factorial moments (NFM) of order q as function of number of bins, M in the D dimensional phase space and the scaling behaviours of NFM. M is the number of bins along each dimension so as to have total M^D bins in the phase space.

4.1 Data samples

Present work pertains to the experimental data analysis of the charged particles produced in the Pb–Pb collisions at $\sqrt{s_{\text{NN}}} = 5.02$ TeV. Data analyzed is recorded for symmetric collisions of ^{208}Pb ions during two different periods with one larger dataset of 260×10^6 events and the smaller dataset of 78.4×10^6 events. These datasets were taken during the second heavy-ion run (commonly termed as Run II) of the LHC in 2015 and 2018. The ALICE data and its reconstruction scheme is structured to accommodate the varied data-taking conditions across different periods, as highlighted in [Section 3.3.3](#). Each period is typically divided into numerous runs, often exceeding one hundred, necessitating careful verification of data usability for physics analyses. The datasets used in this analysis are named as LHC15o and LHC18q,r. The total statistics of this Run II data is larger as compared to data from Pb–Pb collisions at $\sqrt{s_{\text{NN}}} = 2.76$ TeV recorded during Run I in 2010, 2011 ([Table 2.1](#)). With this enhanced statistics and improved reconstruction routines, one can explore moments studies in more finer transverse momentum bins and higher centralities. Also, the advantage of larger statistics facilitates the reduction in statistical uncertainties. A list of all data-taking periods and runs considered in this study are given in [Appendix B](#).

<i>LHC Run</i>	<i>Year</i>	<i>System</i>	$\sqrt{s_{\text{NN}}}$ (TeV)	<i>Events/</i> 10^6	β^* (m)	<i>crossing angle, α</i> (μrad)
<i>I</i>	2010	Pb–Pb	2.76	14.2	3.5	0
	2011	Pb–Pb	2.76	49 ^l	1.0	60
<i>II</i>	2015	Pb–Pb	5.02	78.4	0.8	60
	2017	Xe–Xe	5.44	1.3	10.0	60
	2018	Pb–Pb	5.02	260 ^l	0.5	60

TABLE 4.1:

Data samples of heavy-ions collected over the span of different years during Run I and II of LHC operation are tabulated giving collision system, center of mass energy per nucleon pair, statistics etc. Datasets used in the present work from specific periods are in bold. “Events” column lists the count of events triggered by minimum bias trigger criteria. The total event counts from the 2011 and 2018 data samples include a combination of minimum bias, central, and semi-central triggered events.

^lNumber of events are categorised using minimum bias, central, and semi-central triggers.

4.2 Monte Carlo simulation samples

To understand and interpret experimental observations and results, Monte Carlo (MC) studies are vital. For each experimental dataset, the ALICE collaboration has simulated events with event generators, such as HIJING and PYTHIA for heavy-ion and p–p collisions respectively. The simulations encompass the entire event generation and the propagation of particles through the detector material, by modelling the detector response through detector simulation code GEANT [237,247]. This is essential for understanding how generated events will be detected and measured in the experiment. By employing a full simulation approach, generated events can be directly compared to those expected in the experiment, thereby facilitating the study of various detector effects. These effects include finite detection efficiency, which refers to the likelihood that a particle will be detected based on its energy and trajectory, as well as the resolution impacts on measured quantities like transverse momentum (p_T). The efficiency of track reconstruction, which varies with p_T , is obtained from these MC simulations. These simulations are referred to as “full simulations” (reconstructed level). “Generator-level” simulations, on the other hand, are limited to the event generation process without simulating the detector response.

The simulation studies not only help in studying detector related effects but also the effects of physical origin. It is because different methodologies are used by event generators to simulate collision’s initial state and its subsequent time evolution. HIJING effectively models the initial stages of particle production, including jet production and energy loss mechanisms, it does not account for interactions within the medium. This includes parton recombination and important collective phenomena such as elliptic flow, necessary for a comprehensive understanding of QGP [246]. HIJING is the only event generator for which events are available at the reconstructed level for the Run II Pb–Pb runs. The MC event samples from ALICE production are enlisted in Table 4.2. At the generator level, EPOS–LHC [248] events are also analysed in this work (Section 4.5.2.5).

4.3 Event selection

The sub sections below outline the event selection cuts applied in the present study for the analysis of Pb–Pb data. These selections are important for ensuring high-quality reconstruction and for isolating hadronic interaction events by filtering out background events, forming component of the standard data preparation protocol in ALICE [219].

<i>ALICE Data</i>	<i>Reconstructed level MC</i>			<i>Generator Level MC</i>		
	<i>Genera- tor</i>	<i>Events 10⁶</i>	<i>Production Name</i>	<i>Genera- tor</i>	<i>Events 10⁶</i>	<i>Production Name</i>
LHC15o	HIJING	3.55	LHC20eja	EPOS– LHC	54.94	EPOSLHC GEN LHC22d1d2
LHC18q,r	HIJING	3.23	LHC20e3a	EPOS– LHC	50	EPOSLHC GEN LHC22d1c2

TABLE 4.2:

Monte Carlo event samples simulated as per the detector settings in the ALICE Run II.

For the analysis, events must include a reconstructed primary vertex located close to the nominal interaction point at the center of the detector, ensuring compatibility with subdetector acceptance. In order to avoid contamination from pile-up events, where multiple hadronic interactions are recorded as a single event, these occurrences are identified and excluded from the analysis to maintain the accuracy of the physics results.

In addition to the primary hadronic interactions of interest, colliding ions can also engage in electromagnetic interactions. These electromagnetic events show significantly larger cross sections compared to the hadronic interactions at high energies, but they tend to produce fewer particles; for instance, electromagnetic dissociation can result in a nucleus emitting just a single neutron. Such events primarily contribute to very peripheral centrality classes. Various cuts for selection of the good events for the analysis are discussed below.

4.3.1 Physics selection

Physics selection cuts are the first event selection cuts applied to select the good events from the data for analysis. For this, events are chosen according to the specified trigger class. Further, various selection criteria are implemented for the rejection of background and minimise the impact of pile-up events. Minimum-bias (MB) trigger named as **kINT7** in AliROOT [242] framework of ALICE is used in the present work to select event samples from data and MC.

- **Trigger cut**

The ALICE trigger system is designed to handle the high data rates produced by the collisions, filtering out uninteresting events while retaining those that are likely to yield valuable physics insights [232]. The system has a set of triggers that include both hardware and software components. kINT7 is a hardware

trigger primarily focused on capturing minimum-bias events, which are events that do not require specific conditions to be met, thus allowing for a wide range of collision outcomes to be recorded. Technically, it is a V0AND trigger which requires signals from both V0A and V0C (Section 3.2.3) detectors to be present simultaneously to activate the trigger [230,249]. It is particularly important for studies involving the production of particles that may not be associated with high-energy jets or other specific signatures.

- **Primary vertex cut**

Each collision event in ALICE has characteristic primary interaction vertex. This vertex represents the point where the primary collision takes place and this serves as a crucial reference for analysing the resulting particle interactions. Alongside the primary vertex, events may also contain pile-up vertices [250], that arise from multiple collisions happening in quick succession and secondary vertices, that are formed from decay of particles or material interactions. An accurate primary vertex reconstruction is essential to have correct understanding of the event evolution and hence the spatial distribution of particles produced in the collision. The primary vertices of an event sample are typically distributed around the nominal interaction point, which serves as the designated center of experimental setup. Although this distribution is narrower in the plane than that in the transverse direction relative to the beam, it can extend several tens of centimeters along the beam direction (the z axis). This elongated distribution reflects the nature of the collisions and the geometry of the detector setup.

To reconstruct primary vertex of an event, multiple approaches are employed. Initially, a preliminary estimate is made using Silicon Pixel Detector (SPD) tracklets, which are short segments of tracks detected by the innermost layers of the Inner Tracking System (ITS). After the preliminary estimation, a more refined determination of the primary vertex is conducted at the final stage of reconstruction. This process uses global tracks that combine data from the Time Projection Chamber (TPC) and the ITS. An alternative method involves estimating the primary vertex using TPC-only tracks, which do not incorporate information from the ITS detector. The position of primary vertex obtained from these three methods agree within less than 1 cm across all three spatial dimensions for majority of events [219]. The precision of primary vertex determination is influenced by finite resolution of particle trajectories and the number of particles involved in the process of vertex reconstruction. An accurate vertex position is estimated if higher number of particles are detected whereas for events with few

particles, not all methods will successfully identify at least one interaction vertex [251,252].

In this work for event selection, events that have their primary vertex derived from the global ITS–TPC tracks, which is also the default vertex selection are considered for analysis. The analysis by default takes vertex estimated from SPD tracklets in case the vertex from global tracks is not evaluated. If neither of these options is available, the TPC–only tracks are used. Events for which primary vertex is not found at all are rejected for further analysis. This selection is performed by the `AliAODEvent` class in AliPhysics [239].

To ensure the reliability of the reconstructed primary interaction vertex, it is required that at least one track must contribute to its determination. Events having their reconstructed vertex along the beam direction (v_z) with $|v_z| \leq 10$ cm, that is at maximum 10 cm from nominal vertex are considered for the analysis. This condition for event selection is crucial because the charged particle geometrical acceptance in the subdetectors depends on v_z . The acceptance is symmetric in pseudorapidity at the nominal interaction point ($z = 0$), but as the distance from this point increases, the acceptance can increase on one side of the detector and decrease on the other. The 10 cm limit necessitates a uniform tracking acceptance in both the ITS and the TPC for the pseudorapidity range of $|\eta| \leq 0.8$. This event selection criteria has been varied to estimate systematic uncertainties. Details regarding the determination of systematic uncertainties associated with this selection criteria are in Section 4.5.3.2.

4.3.2 Centrality estimators

Heavy-ion collision centrality in ALICE is discussed in Section 3.3.4. The method discussed is applied to estimate centrality from V0 scintillators (V0A, V0C), the SPD or TPC along with the different approach of using the energy deposited in the ZDC. The resolution of centrality estimators as function of centrality obtained with these detectors in ALICE [219] is given in Figure 4.2.

Several centrality estimators are employed in ALICE, each utilising different methods to assess the centrality of the events. The **CL0** estimator measures centrality based on the number of clusters detected in the inner layer of the Silicon Pixel Detector (SPD). Similarly, the **CL1** estimator uses the number of clusters in the outer layer of the SPD to determine centrality. The **V0A** estimator relies on the amplitude recorded by the V0 detector on the A-side, while the **V0M** estimator aggregates the amplitudes measured by the V0 detector on both the A-side and C-side. The V0A estimator is typically reserved for asymmetric collision systems,

such as proton-lead (p-Pb) collisions, where the multiplicity distribution is not uniform. For Pb-Pb collisions, the **V0M** estimator is predominantly used, as it is a more reliable centrality measure in these symmetric systems as is clear from **Figure 4.2**. The CL0 and CL1 estimators are often utilised as variations to assess systematic uncertainties in the analyses. V0M is less affected by fluctuations in the event multiplicity [253]. The V0M centrality estimator has been used for the determination of event centrality in the present analysis. **Most central events with centrality 0–5% are used for the default analysis**. A centrality dependence of the observables is also studied for all events within the centrality range 0–80%.

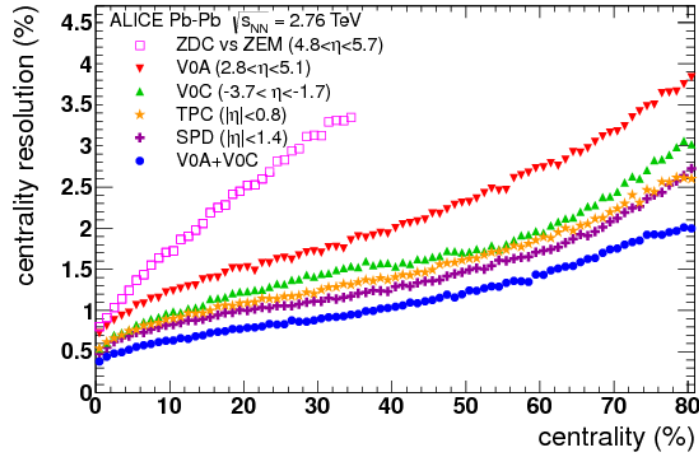


FIGURE 4.2:

Centrality resolution of various centrality estimators used in ALICE during Pb-Pb collisions at $\sqrt{s_{\text{NN}}} = 2.76 \text{ TeV}$ [219].

4.3.3 Pileup rejection

The particles in particle accelerators like the LHC are organized in “bunches”. Bunched beams enable multiple particles to collide simultaneously, enhancing the likelihood of interactions during experiments. This can create situation where collisions may take place involving particles from the same bunch or from adjacent bunches. Pile-up events occur when multiple collisions take place within a single bunch crossing, which can stem from either the same or adjacent bunches. In the ALICE experiment, the average number of collisions occurring within a single bunch crossing, denoted as μ , is less than 1, but this value can vary significantly based on the collision system and beam conditions [219]. Under high interaction rates, multiple interactions can be recorded in a single event, leading to additional vertices located near the primary interaction vertex, resulting in an inflated track count associated with the primary vertex. Such misassignments can compromise the accuracy of measurements and hence distorting the results.

Pile-up events can occur within the same bunch crossing, known as *in-bunch* pile-up events. The average number of hadronic interactions being low during Pb–Pb collisions in Run I (of the order of $10^{-5} - 10^{-4}$) and Xe–Xe data-taking, the potential for in-bunch pile-up events exists especially at higher interaction rates [219]. Pileup events equally impacts all the detectors, and distinguishing them relies on the reconstruction of multiple primary vertices. The other kind of pile-up events are known as *out-of-bunch* pile-up events which arise when collisions originating from different bunch crossings coincide with the nominal triggered event. A nominal event is a primary event that is triggered and recorded during a specific bunch crossing, representing the main collision of interest.

In ALICE, the TPC detector due to its long readout time, can integrate signals from as many as 4000 bunch crossings. This capability, while beneficial for capturing a wide range of interactions, can sometimes record additional tracks which may get shifted in the z -direction. The shift is due to the drift of ionized electrons created by charged particles towards the readout planes as they traverse the gas in the TPC, leading to high occupancy in the TPC. Such high occupancy can degrade the TPC performance in its track reconstruction and particle identification. The reconstruction of multiple primary vertices is critical for distinguishing *in-bunch* pile-up events from nominal events, allowing for the better understanding of the interactions occurring within a given event. Further, fast and slow detectors can be correlated to identify *out-of-bunch* pile-up events. For instance, the SPD aggregates information across 12 bunch crossings, whereas the V0 detector, which integrates over only one, can effectively differentiate between nominal events and those affected by pile-up. These methods aim to increase detector performance by selectively rejecting only the tracks associated with pile-up events. The datasets used in this analysis, as listed in Table 4.1, contains both types of pileup events. A large fraction of these recorded events have more than one collision (vertices) in the TPC readout time. To remove these events, a class `AliEventCuts` from `AliROOT` is used [242]. This removes in-bunch pile-up events with cuts based on multiple reconstructed vertices. For out-of-bunch pileup, it tags and removes events by using plots of correlation between different multiplicity/centrality estimators extracted from detectors with different readout times. Figure 4.3 and Figure 4.4 shows the correlation between multiplicity and V0M, CL0 and V0M respectively for rejection of these events. The correlation histograms are shown both before and after the application of these cuts. The code snippets of `AliROOT` which automates removal of pileup events are:

- `AliEventCuts *fEventCuts;`
`fEventCuts.SetRejectTPCPileupWithITSTPCnCluCorr(kTRUE);`

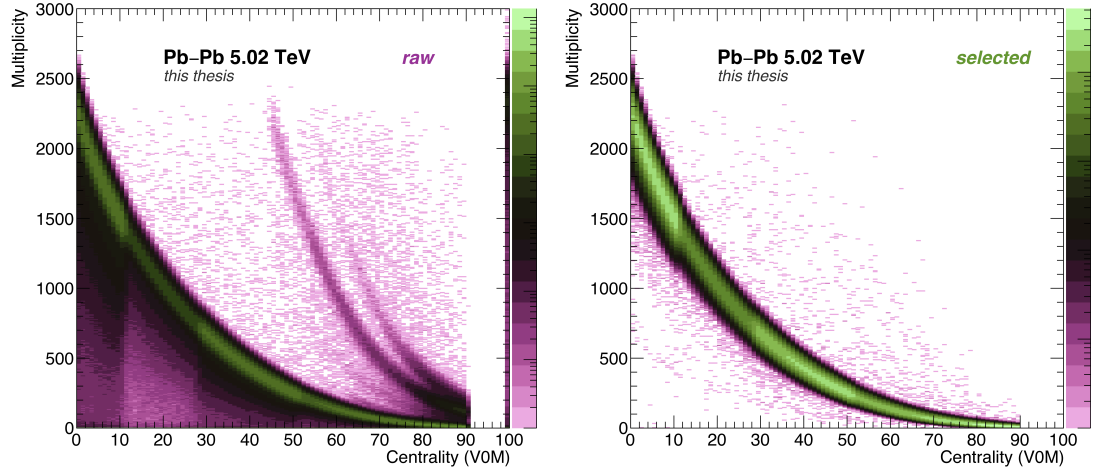


FIGURE 4.3:

ALICE: Multiplicity vs V0M percentile before (left) and after (right) the `AliEventCuts()` cuts.

This cut used in the analysis removes most of the pileup. It is observed to remove $\sim 32\%$ of the events.

In case of HIJING which has both reconstructed and generator level (Table 4.2), pileup, is simulated to better match the TPC performance observed in the data. Helper methods exist in `AliAnalysisUtils()` class of AliROOT to tag MC particles generated in and out-of-bunch pileup collisions and also the events with generated pileup. The methods used to remove pileup in HIJING are:

- `IsParticleFromOutOfBunchPileupCollision(Int t index, AliMCEvent* mcEv);`
- `IsPileupInGeneratedEvent(AliAODMCHHeader* MCHheader, TString genname="");`

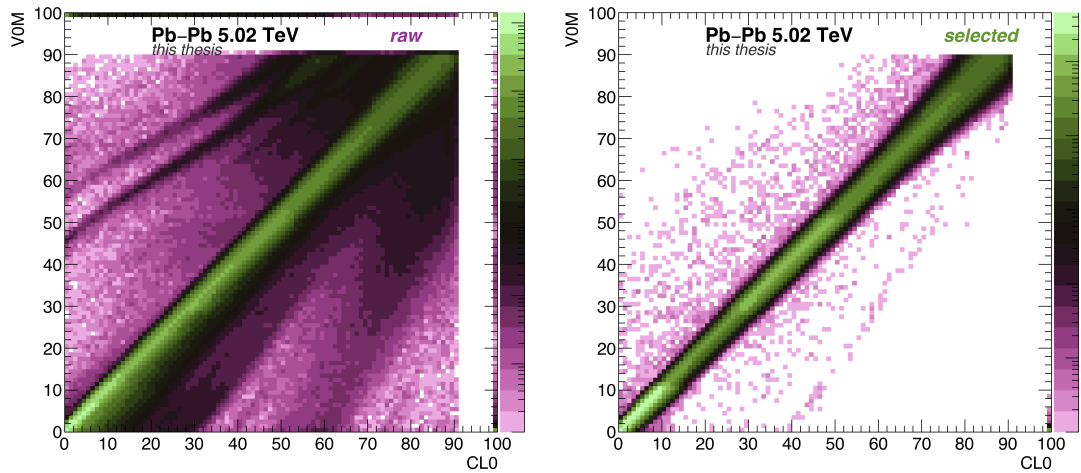


FIGURE 4.4:

ALICE: CL0 vs V0M percentile before (left) and after (right) the `AliEventCuts()` cuts.

4.4 Track selection

For the analysis of data containing events obtained after applying event selection, various cuts for track selection are applied to isolate charged particles that originate from the primary interaction vertex. This process helps to reduce contributions from false trajectories that do not correspond to physical particles, low-quality tracks and secondary particles. In ALICE, the events and charged-particle trajectory reconstruction is primarily facilitated by two main tracking detectors: the Time Projection Chamber (TPC) and the Inner Tracking System (ITS). These detectors can be utilised either in combination to get global tracks or separately for other tracking schemes. Each scheme varies in terms of efficiency and acceptance for measuring charged particles, contamination from secondary particles, and transverse momentum resolution. The ITS detector is particularly effective in providing excellent spatial resolution near the collision vertex, enabling it to distinguish tracks even in the dense environments commonly found in central Pb–Pb collisions. When a track registers a hit in at least one of the SPD layers of the ITS, it suggests that the track do not originate from a secondary vertex, such as those arising from particle decays or interactions with the material in the outer layers of the ITS or TPC. However, certain components of the ITS, particularly the SPD, have experienced periods of inactivity during data collection, leading to non-uniform acceptance across different azimuthal angles (φ). In contrast, TPC offers a more uniform acceptance across φ , with only minor modulations due to the sector boundaries of TPC. The large track lengths in TPC extending up to about 2.5 meters to its outer radius and its capacity to collect up to ~ 159 space points per track contribute to its excellent tracking performance and high transverse momentum, p_T resolution. Nonetheless, the TPC is less effective than the ITS in rejecting secondary particles, primarily due to its greater distance from the collision vertex and the presence of material than that from the ITS within its inner radius.

In the TPC, various methods are employed for track reconstruction (Section 3.3.2). Global tracks in the ALICE experiment are reconstructed from the information of both TPC and ITS, forming a standard tracking scheme of charged particles for the central barrel. This combined approach yields a high-resolution measurement of transverse momentum (p_T), which remains consistent even when tracks are constrained to the primary vertex. When comparing the TPC-only tracks to the global TPC-ITS tracks, it is noted that the p_T resolution for TPC-only tracks is similar to that of the global tracks at lower p_T values, approximately around 1 GeV/c. Nevertheless, this resolution deteriorates at higher

<i>Track selection criteria</i>	<i>Values</i>
Max. χ^2 per TPC cluster	4
Min. number of TPC clusters	70
Momentum refit in the ITS	36
Max. distance to the vertex xy, z /cm	2.4, 3.2

TABLE 4.3:

The track selection parameters used in the present analysis. These cuts are combined together in ALICE as a standard and are termed as *Filterbit 768* track cuts.

values of p_T . By imposing a constraint to the primary vertex, the p_T resolution of TPC-only tracks improves significantly, achieving values comparable to those of global TPC-ITS tracks up to approximately 10 GeV/c (**Figure 3.6**).

For reasons mentioned above, a hybrid tracking scheme has been used for the selection of tracks in this work. Initially, global TPC-ITS tracks are obtained after stringent selection criteria, which includes the requirement of at least having one hit in the SPD. In case a global track fails to meet this criteria, the corresponding TPC-only track that is constrained to the primary vertex, is then analyzed. This hybrid approach helps to maintain low secondary contamination, although it does not reach the levels observed in the global tracking scheme. Furthermore, while the acceptance in φ is nearly uniform, it does not achieve the same level of uniformity as in the TPC-only case. The intermittency analysis focusses on studying soft particles in the central collisions and refrain from any jet contamination, thus

<i>Criteria</i>	<i>Values</i>
Pseudorapidity η	≤ 0.8
Azimuthal angle, φ	2π
Wide p_T (GeV/c) intervals $\delta p_T \geq 0.6$	(0.4,1.0)
	(0.4,1.5)
	(0.4,2.0)
Narrow p_T (GeV/c) intervals $\delta p_T = 0.2$	(0.4,0.6)
	(0.6,0.8)
	(0.9,1.1)

TABLE 4.4:

Kinematic cuts and p_T intervals studied in this analysis. Different momentum ranges are used to check the dependence of analysis observables on the momentum, p_T bin width.

an upper p_T cut of 2 GeV/ c is applied. Additionally, a lower p_T cut of 0.2 GeV/ c is used to account for the decrease in TPC reconstruction efficiency at lower p_T . The transverse momentum (p_T) ranges studied in this analysis are identical to the ones studied for similar analysis of Pb–Pb collision data at $\sqrt{s_{NN}} = 2.76$ TeV from ALICE [254,255] for a direct comparison between the two energies.

A set of track selection cuts as summarized in Table 4.3 are included to significantly reduce the presence of secondary particles that do not originate from the primary vertex, as well as to eliminate false trajectories reconstructed from fake hits in the detectors or incorrect hit combinations. Each track is required to have a minimum of 70 space points out of a possible 159 in the TPC to ensure its validity and reduce the likelihood of false trajectories. Additionally, the quality of the trajectories is assessed by applying a maximum chi-squared (χ^2) value of 4.0 per cluster in the TPC, which serves to filter out tracks with poor momentum fits. For the analysis with hybrid selection of tracks, successful re-fits of both the TPC and ITS are also mandatory for these global tracks, further enhancing the accuracy of the reconstruction. Tracks that originate from secondary weak-decay topologies, commonly referred to as kinks, are systematically rejected in both tracking schemes (global and hybrid). Furthermore, the criteria for the selection of maximum DCA (distance of closest approach,) of the trajectory extrapolated to the primary vertex is consistent across both the schemes. DCA along the beam direction, z must be less than 3.2 cm, while in the transverse plane, xy it is restricted to 2.4 cm. A two-dimensional DCA selection is also implemented, which corresponds to an elliptical region defined in the DCA_z and DCA_{xy} plane. The parameters are normalized to their respective maximum values and then combined in quadrature. For the value of total relative DCA exceeding one, the track is rejected as it lies outside the defined ellipse. This additional criterion effectively reduces the number of secondary particles contaminating the track sample, thereby improving the overall quality of the data used for analysis. These are termed as *Filterbit 768*. Besides these cuts, the other track cuts are given in Table 4.4.

The impact of the event and track selection procedure on the analysis results is studied by varying the cut values given in Table 4.3 and Table 4.4. The effect is small or even negligible from most of the variations. Any differences are included as the systematic uncertainties (Section 4.5.3.2). A discussion on observations and results from the analysis follows.

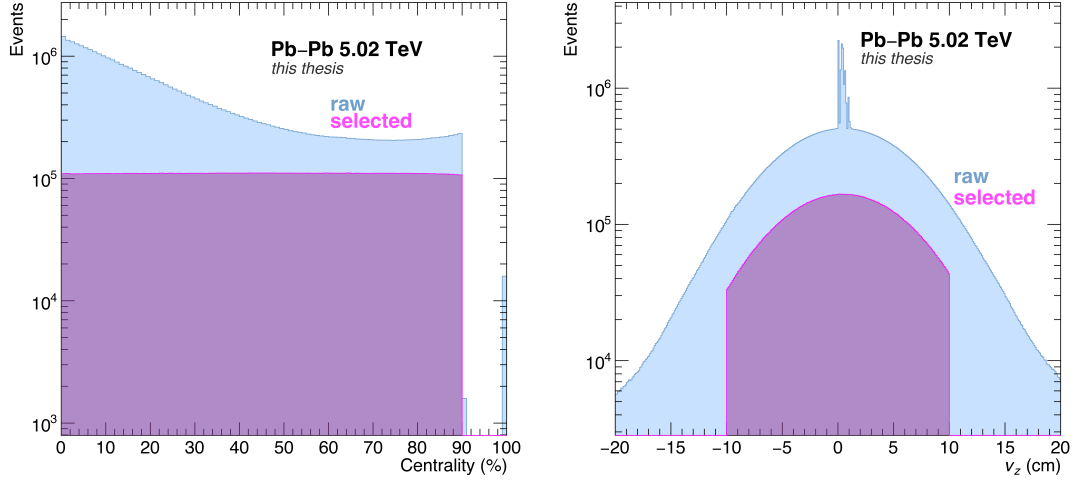
4.5 Observations and results

As discussed in **Chapter 3**, the normalized factorial moments (NFM) within the framework of intermittency analysis can furnish important information regarding the presence of remnants of critical fluctuations, or the nature of phase transition in the data. In other words, if the particle distributions within the (η, φ) phase space forms any scale-invariant patterns, the NFM are expected to exhibit intermittent behaviour, i.e., the moments will follow a power-law growth as a function of decreasing phase space bin size. The exponent of this power-law is called intermittency index and is associated with fractal dimensions of the set via **Equation 2.28**. Value of scaling index is also calculated and tested for its predictions given in **Table 2.1**. A flowchart given in **Figure 4.1** is how calculations proceed in this analysis with $D = 2$ and q being an integer ≥ 2 . First, the analysis performed for the MC HIJING is discussed followed by discussion on the experimental data analysis.

4.5.1 HIJING events analysis

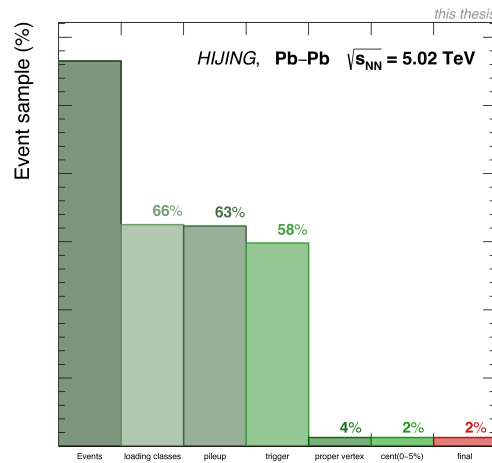
HIJING (Heavy Ion Jet Interaction Generator) [246] MC events with full simulation corresponding to the datasets from Pb–Pb collisions at $\sqrt{s_{\text{NN}}} = 5.02$ TeV (**Table 4.2**) are analysed. The HIJING [256,257] model is a Monte Carlo event generator designed for simulating high-energy heavy-ion collisions. It focuses on the early stages of these collisions, particularly the interactions between colliding nuclei and the resulting particle production. HIJING uses the Glauber model to establish the initial conditions, describing how particles are spatially and momentum-wise distributed during collisions. A key feature of HIJING is its incorporation of parton distribution functions, which detail the internal structure of nucleons and nuclei. This allows for a better understanding of particle interactions. The model effectively captures both soft processes, such as multiple parton scatterings and gluon emissions, and hard processes, including jet production and heavy quark creation. By simulating jet formation and medium interactions, HIJING events are used to test understanding of track selection and optimization for analysis code.

Figure 4.5 shows the centrality and vertex position distributions for HIJING event samples. In **Figure 4.6**, the effect of various event selection cuts (**Section 4.3**) on the total event sample is shown. It shows the percentage of left-over events at each step. After applying all the cuts, a statistics of $\sim 67 \times 10^3$ events is obtained. **Figure 4.7** shows the p_{T} , η and φ distributions of the “reconstructed” and “generator” level events of HIJING after applying event selection cuts as

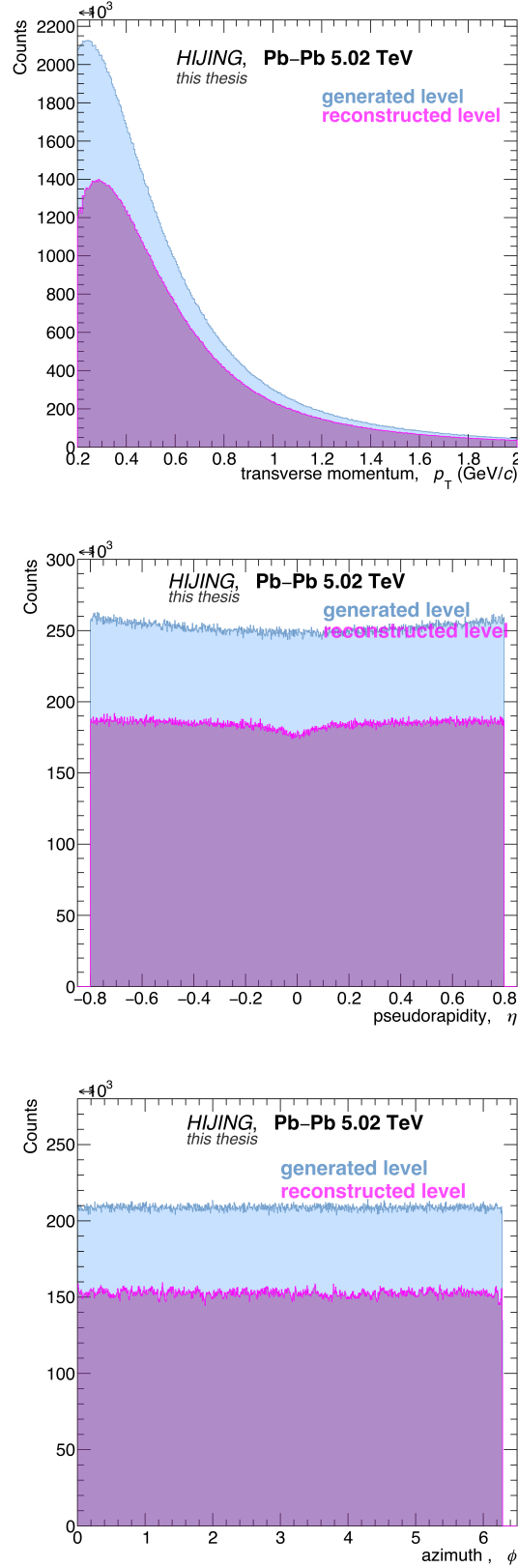
**FIGURE 4.5:**

HIJING: Centrality and vertex-z (v_z) distributions of raw and selected tracks.

discussed in [Section 4.3](#). It can be easily pointed from the figures that the multiplicity is higher at the generator level. This is due to the fact that generated multiplicity reflects the total number of particles produced based on theoretical models before any detector effects or reconstruction algorithms are applied. When track selection criteria and detector response are included to reconstruct tracks, many tracks are rejected, or not get measured and hence decreased multiplicity compared to what is generated.

**FIGURE 4.6:**

HIJING: Number of events obtained after applying various event selection cuts on the HIJING event sample. Percentage on the bars shows the approximate percentage of events obtained after applying cuts mentioned along the x -axis.

**FIGURE 4.7:**

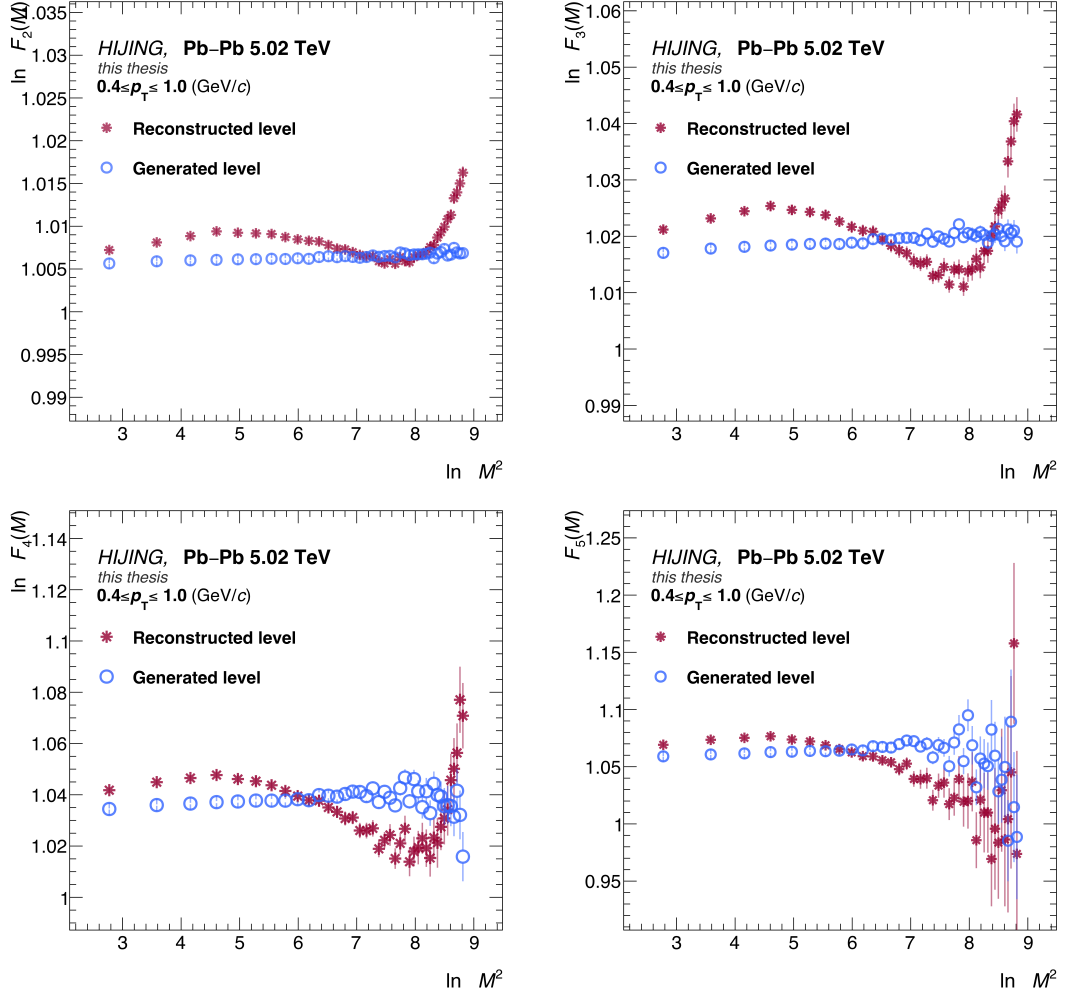
HIJING: p_T , η and ϕ distributions comparing “reconstructed level” and “generator level” tracks after the application of track cuts as given in **Table 4.3** and kinematic cuts for η , ϕ given in **Table 4.4**.

4.5.1.1 Closure study

Monte Carlo closure study is a technique used to validate the accuracy of the reconstructed events. This method involves comparing the observables calculated from global reconstructed tracks and primary tracks, which represent ideal conditions with perfect efficiency. The primary tracks, characterised by their perfect reconstruction efficiency, serve as a reference point for evaluating the performance of the reconstruction algorithms applied to the recorded experimental data.

Followed by selection of good events and track selection, analysis as described in **Chapter 2** is performed on HIJING events for Pb–Pb collisions at $\sqrt{s_{\text{NN}}} = 5.02$ TeV to obtain the observables, F_q for $q = 2, 3, 4, 5$. NFM obtained from the reconstructed tracks of HIJING are compared to those derived from the primary tracks at generator level. If the F_q ’s from the reconstructed event sample closely match with that from the generated events, it indicates that the reconstruction algorithms are performing effectively and accurately capturing the underlying physics of the model. However, it has to be noted that the detector efficiency is not always 100%. Factors such as detector inefficiencies, track losses, and misidentifications always contribute to some amount of difference between generator level and reconstructed level tracks and these factors are to be taken into consideration to derive and interpret the results. Out of these factors, tracking inefficiencies lead to the largest underestimation or overestimation of observables since these directly relate to how well charged particles are identified and measured. Thus, tracking inefficiencies are estimated and are incorporated in the observables to obtain the final correct values. For the present analysis, this exercise was done for Pb–Pb collisions study at $\sqrt{s_{\text{NN}}} = 2.76$ TeV using HIJING, and it has been shown in [258,259] that for uniform efficiencies, the F_q moments are robust against tracking efficiencies. Efficiencies for the charged particles in the acceptance of (η, φ) phase space studied in this work are found to be uniform for Pb–Pb collisions at $\sqrt{s_{\text{NN}}} = 5.02$ TeV and hence, these corrections are not implemented for calculations of $F_q(M)$. **Figure 4.8** shows the first look of $\ln F_q(M)$ vs $\ln M^2$ plots for the HIJING reconstructed and generated level tracks in the acceptance region of (η, φ) phase space.

To make an estimation of closure, without the application of efficiency corrections to $F_q(M)$, the ratios of NFM ($F_q(M)$) from reconstructed HIJING events to the corresponding $F_q(M)$ from generated level HIJING events are studied. **Figure 4.9** shows the Monte Carlo closure for $F_q(M)$, for $q = 2, 3, 4, 5$. This is for the p_T bin $0.4 \leq p_T \leq 1.0$ (GeV/c) in the two-dimensional (η, φ) phase

**FIGURE 4.8:**

HIJING: $\ln F_q(M)$ vs $\ln M^2$ (M -scaling) plots for reconstructed and generated level tracks for moment order $q = 2, 3, 4, 5$ of the charged particles.

space partitioned into $M \times M$ (82×82) bins. It may be noted that there is less than 2% difference between $F_q(M)^{\text{reco}}$ and $F_q(M)^{\text{gen}}$ within error bars, for $q = 2$ and 3 that makes a closure of $\sim 98\%$. With motivation to achieve better than 99% of closure at all values of M , a track selection on “shared TPC clusters” is tested, as discussed below.

4.5.1.2 Fraction of shared TPC clusters

To improve upon the Monte Carlo closure beyond 98% for all M values, the shared cluster fraction and findable cluster fraction cuts are studied. These cuts are vital to distinguish tracks, particularly those that are close in azimuthal angle (φ) and pseudorapidity (η). These affect TPC tracks because it serves as the primary detector in the ALICE for tracking charged particles. Signals produced by charged particles when they ionize the gas, while passing through TPC, are

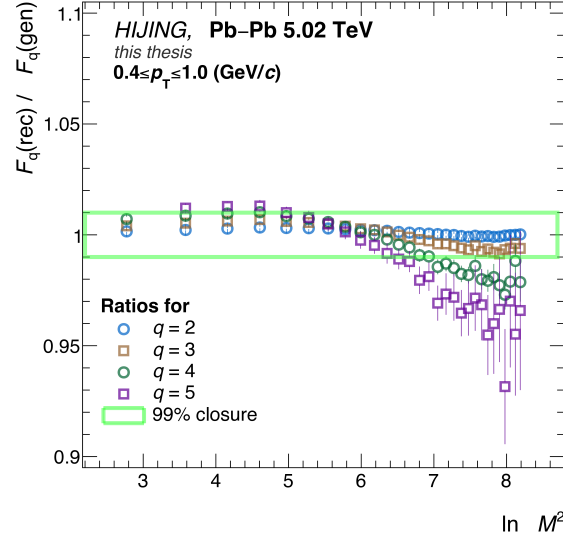


FIGURE 4.9:

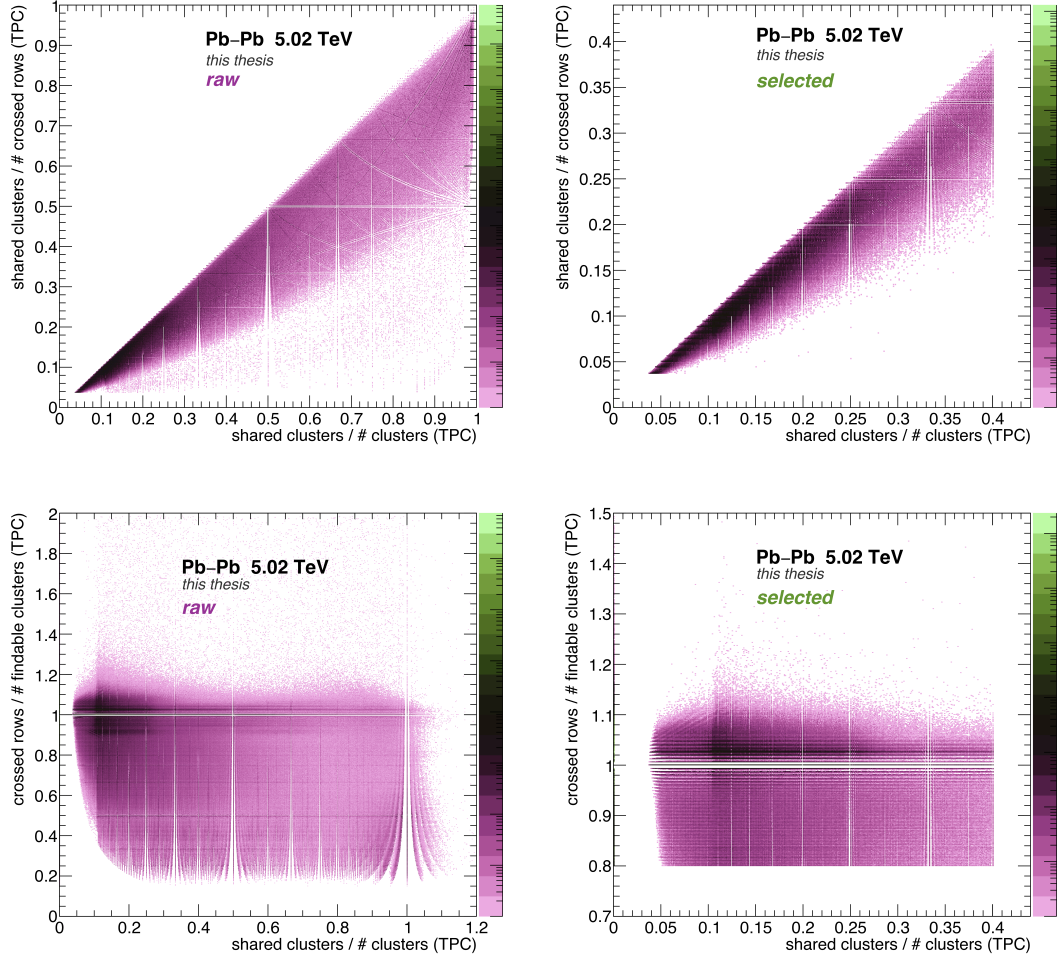
HIJING: MC closure for $F_q(M)$ ($F_q(M)^{\text{reco}}/F_q(M)^{\text{gen}}$) as function of $\ln M^2$ in $0.4 \leq p_T \leq 1.0$ (GeV/c) for $q = 2, 3, 4, 5$. The green box shows the 99% closure window.

referred as *clusters*. Each cluster corresponds to a group of ionization signals collected from the pads in the TPC's readout plane. The number of clusters associated with a track is indicative of the track's quality; more clusters generally lead to better track reconstruction. But the TPC can sometimes misidentify tracks due to space charge distortions in its drift field. This phenomenon occurs when the TPC drift field is distorted by the accumulation of positive ions, leading to inaccuracies in the reconstruction of particle trajectories. Although the shift in tracks due to these distortions are corrected upto some percentage, but these do not get corrected 100%. A significant number of tracks are relatively close to each other in heavy-ion collisions and thus have a high probability in the double identification. The track reconstruction in ALICE is briefly given in [Section 3.3.2](#) and more details, are available in [\[260,261\]](#).

<i>Criteria</i>	<i>Values</i>
Shared clusters/Crossed rows (TPC)	Mean of the histogram vs p_T
Shared clusters/Total Clusters (TPC)	0.4
Crossed rows/Findable clusters (TPC)	0.8

TABLE 4.5:

Cuts on the TPC tracks used in the analysis for selection of tracks in addition to the cuts in [Table 4.3](#) and [Table 4.4](#) for getting better closure at all M .

**FIGURE 4.10:**

HIJING: Ratio of shared clusters to crossed rows and crossed rows to findable clusters as a function of shared clusters to total clusters before (left) and after (right) applying cuts given in **Table 4.4**.

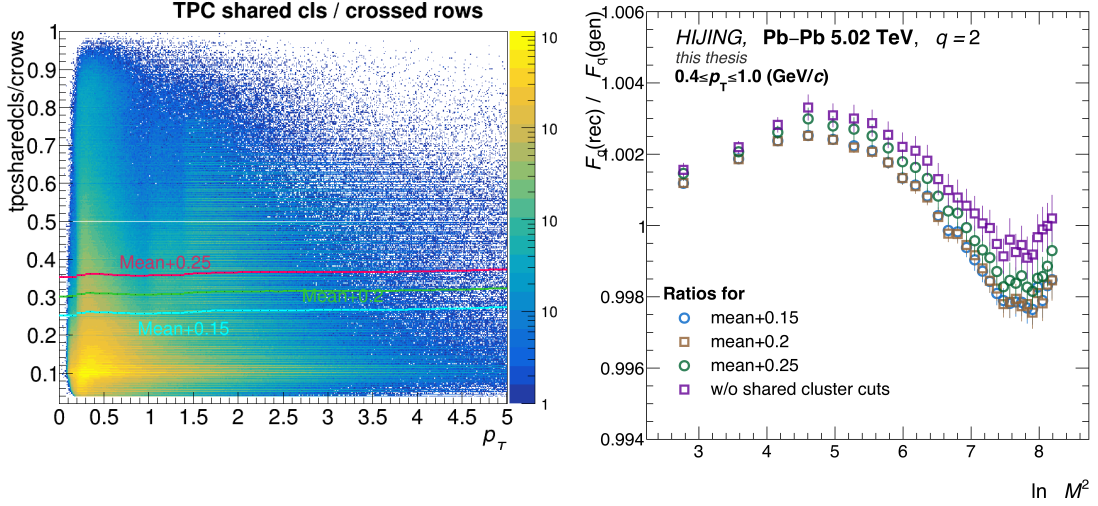
Shared cluster fraction is the ratio of TPC clusters shared between two tracks to the total number of TPC crossed rows. Crossed rows refer to the total number of pad rows that a track passes through in the TPC. Due to detector inefficiencies, not all crossed rows will produce a signal. Thus, while a track may cross many rows, only some rows will yield detectable clusters. A higher value of the shared cluster fraction indicates that multiple tracks are utilising a significant number of the same clusters for their reconstruction, i.e., a higher degree of overlap or close proximity between tracks. The *findable cluster fraction* is determined by comparing number of crossed rows to the number of findable clusters in the TPC. A findable cluster is a signal generated by a charged particle ionizing the TPC gas, which satisfies the conditions for being successfully used in track reconstruction. A higher value of this fraction suggests that a larger proportion of crossed rows are generating clusters that are suitable for use in track reconstruction, thus a

better overall tracking efficiency. The ratio of shared clusters to crossed rows and crossed rows to findable clusters as a function of shared clusters to total clusters for Pb–Pb collisions for HIJING reconstructed events at $\sqrt{s_{\text{NN}}} = 5.02$ TeV are given in **Figure 4.10**. It shows case of both before and after the application of cuts mentioned in **Table 4.5**. It is observed that tracks with significant cluster overlap with other tracks and those with smaller number of clusters from crossed rows are removed with cuts mentioned in the **Table 4.5**, that improves quality of final tracks.

With aim to possibly improve the closure, the mean of the Shared clusters to Crossed rows ratio as a function of p_{T} distribution is taken for p_{T} intervals with $\delta p_{\text{T}} = 0.1$ GeV/ c . The value of the mean is used as a maximum cut on the tracks. This value changes with p_{T} since the distribution changes with p_{T} . In addition, some trivial percentages (1%, 2%, etc.) were added to and subtracted from the obtained mean values to check the sweet spot where the closure is the best. **Figure 4.11** (left) shows the distribution with lines in different colours showing mean values plus some percentage. **Figure 4.11** (right) shows the effect of application of these cuts on the MC closure of $F_q(M)$ as function of $\ln M^2$ for $q = 2$ (also compared to the closure without these cuts as was shown in **Figure 4.9**). It is observed that mean+2.5% gives better closure than other cuts and thus has been taken as the default track cut value for further analysis. The scaling behaviour of $F_q(M)$ with $\ln M^2$ and closure so obtained with all the selection cuts is given in **Figure 4.12** for $q = 2, 3, 4, 5$. The upper panels in the figure show $F_q(M)$ vs $\ln M^2$ (**Equation 2.23**) from reconstructed and generator level analysis, and the lower panels show $F_q(M)^{\text{reco}}/F_q(M)^{\text{gen}}$, which is $\sim 1\%$ with a closure of $\sim 99\text{--}100\%$ achieved for $q = 2, 3$ and almost all M values.

4.5.1.3 Observables

For HIJING event sample from the ALICE production (**Table 4.2**) for Pb–Pb collisions at $\sqrt{s_{\text{NN}}} = 5.02$ TeV, tracks are selected after applying the selection cuts discussed above. After these cuts, the events so obtained are analysed for the intermittency study that is calculating NFM as per methodology given in **Section 2.7** to study M –scaling and F –scaling behaviour. **Figure 4.13** shows $\ln F_q$ vs $\ln M^2$ (M –scaling) plots for $q = 2, 3, 4, 5$ for generated and reconstructed 0–5% central events. A very weak dependence of the $F_q(M)$ on M^2 is observed in the reconstructed HIJING whereas the generated level events show no dependence. In $\ln F_q$ vs $\ln F_2$ (F –scaling) plot for $q = 3, 4, 5$ is given in **Figure 4.14** where it is observed that there is a very small linear dependence of F_q on F_2 . Statistical uncertainties and fluctuations in the values of F_q grow as moment

**FIGURE 4.11:**

HIJING: Shared clusters/Crossed rows vs p_T (on the left), different colours showing different mean/(mean+ different % values). On the right, $F_q(M)^{\text{reco}}/F_q(M)^{\text{gen}}$ plot with respect to $\ln M^2$ showing the effect of various cuts as discussed in Section 4.5.1.2.

order increases (like F_4 to F_5). Scaling exponent, ν is determined as per Equation 2.25 after the linear fitting to $\ln \beta_q$ vs $\ln(q-1)$ plot for the higher M values (Figure 4.15) for $q = 3, 4, 5$. Value of the scaling exponent, ν is obtained as 1.89 ± 0.19 for reconstructed and 2.10 ± 0.60 for generator level tracks. The values are greater than the predicted value of 1.304 calculated for second-order phase transition formalism in the Ginzburg-Landau theory and 1.0 predicted in 2D Ising Model. Behaviour of intermittency observables: M -scaling, F -scaling and scaling exponent (ν) in HIJING align with those already seen in other MC event generators (AMPT [184], EPOS3 [185] etc.) as also tabulated in Table 2.1.

$\ln F_q(M)$'s dependence on $\ln M^2$, in case of HIJING events analysed here, **do not show power-law**. Hence, there is no intermittency in the charged particles generated in HIJING at midrapidity for most central Pb-Pb collisions at $\sqrt{s_{\text{NN}}} = 5.02$ TeV. For such a case of particle generation, the fractal dimension, D_q is determined as defined in Equation 2.28. This is determined from intermittency index (ϕ_q) i.e., the slope obtained from the line fits performed on $\ln F_q$ vs $\ln M^2$ (M -scaling) plots for $q = 2, 3, 4, 5$. From ϕ_q values, D_q is calculated. Figure 4.16 shows D_q as a function of q . It is observed to be independent of q for reconstructed and generated level tracks. This behaviour hints towards the monofractal nature of the particle generation in HIJING.

To summarise, almost $\sim 99\%$ closure is achieved with HIJING for F_2 for $M_{\text{max}} = 62$, after using the event selection and track selection cuts discussed in

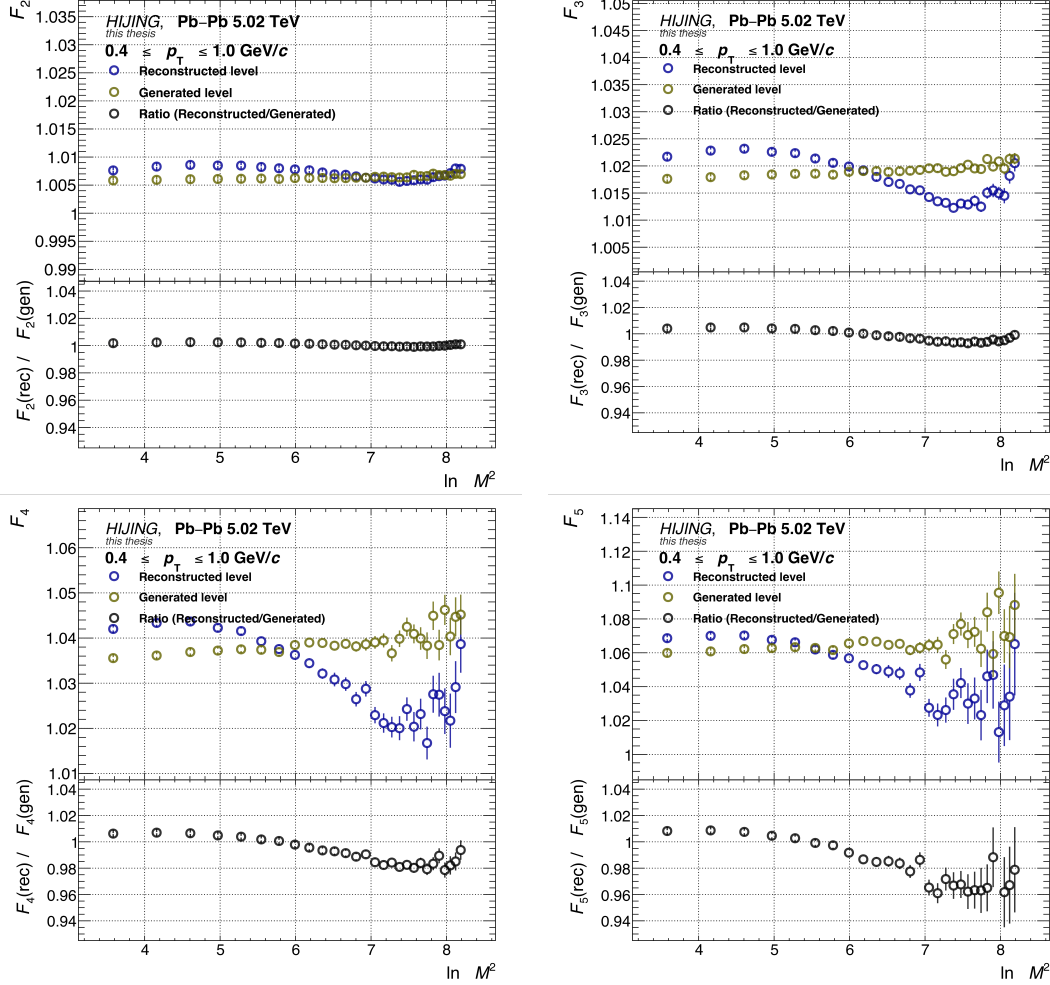
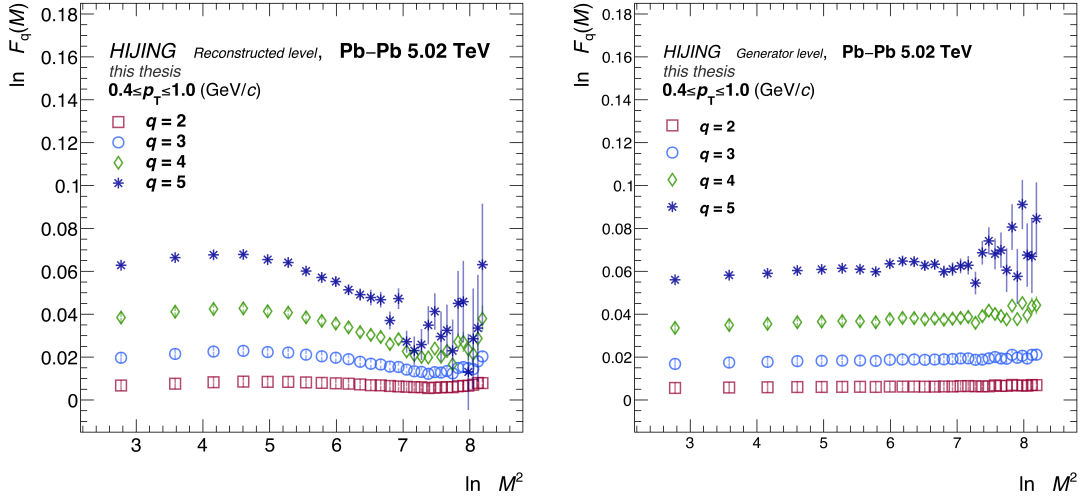


FIGURE 4.12:

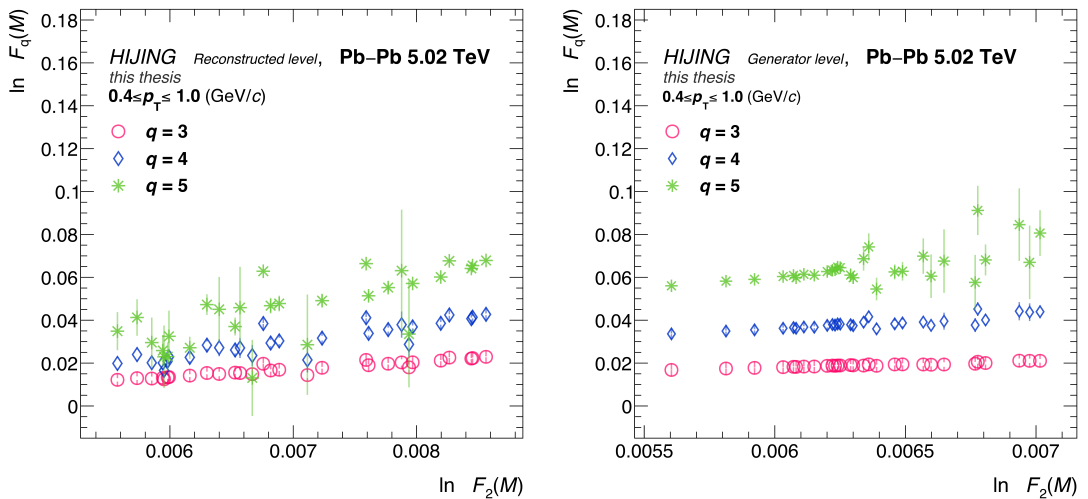
HIJING: $F_q(M)$ vs $\ln M^2$ plots for $q = 2, 3, 4, 5$ in case of reconstructed and generated level tracks (with all selection cuts discussed in [Section 4.3](#) and [Section 4.5.1.2](#)) in $0.4 \leq p_T \leq 1.0$ (GeV/c). Lower panel shows $F_q(M)^{\text{reco}}/F_q(M)^{\text{gen}}$ as function of $\ln M^2$ to check the MC closure achieved.

[Section 4.3](#) and [Section 4.5.1.2](#) respectively. TPC shared clusters were used to suppress the effect of fake track counting. NFM for $q = 2, 3, 4, 5$ are calculated for (η, φ) binning with $M = 2$ to 62, in the intervals of 2 and their scaling behaviours are studied. It is seen that neither M -scaling nor F -scaling is there in the charged particle generation with HIJING. Scaling exponent, ν is determined with value > 1.65 . Fractal parameter D_q shows no dependence on the order of the moments (q). Here, observations and results from $0.4 \leq p_T \leq 1.0$ GeV/c p_T interval are shown and discussed, however calculations are also performed for other p_T intervals, given in [Table 4.4](#). In addition, analysis is performed for other centralities (5–10%, 10–20%, 20–40%, 40–80%) and similar trends for the scaling of NFM ($F_q(M)$) have been observed with no characteristic power-law and values of ν far away from the predicted values. Results from all bins in

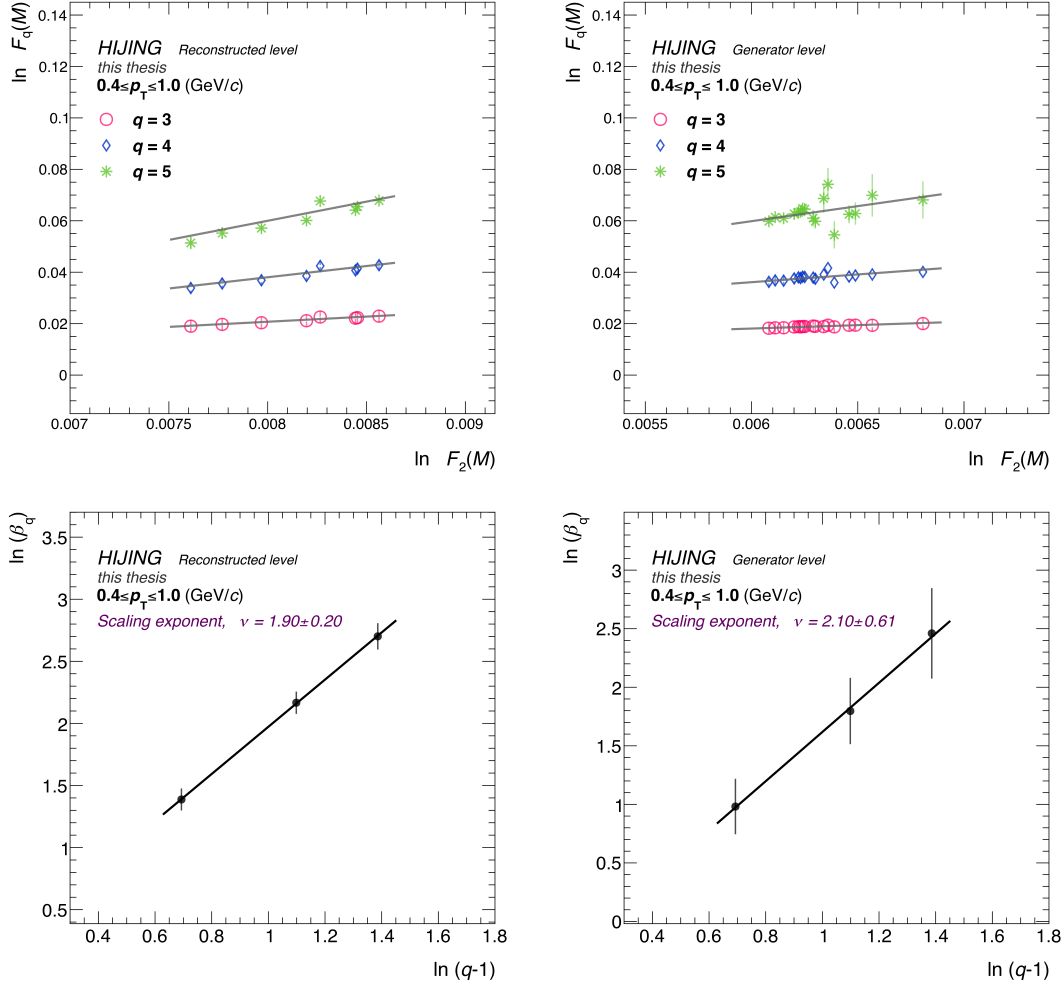
**FIGURE 4.13:**

HIJING: $\ln F_q(M)$ vs $\ln M^2$ (M -scaling) plot for charged particles in $0.4 \leq p_T \leq 1.0$ (GeV/c) for reconstructed (on the left) and generator (on the right) level tracks.

HIJING are in line with what has been observed in other independent MC studies [171,185]. HIJING does not include physics related to the medium interactions in QGP, however lack of scaling seems to be a broader phenomenon observed across different models rather than an artifact specific to HIJING. This study provides a baseline for the interpretation of the ALICE data results.

**FIGURE 4.14:**

HIJING: $\ln F_q(M)$ vs $\ln F_2(M)$ (F -scaling) plot for charged particles in $0.4 \leq p_T \leq 1.0$ (GeV/c) on which line fit is performed to get β_q for reconstructed (on the left) and generated (on the right) level tracks respectively.

**FIGURE 4.15:**

HIJING: Upper plots; $\ln F_q(M)$ vs $\ln F_2(M)$ (F -scaling) plot with line fits performed for high M values to obtain slopes, β_q ($q = 3, 4, 5$) for reconstructed and generated level tracks respectively. Lower plots; $\ln \beta_q$ vs $\ln(q-1)$ with line fit to determine the slope, ν for reconstructed and generated level tracks respectively.

4.5.2 ALICE data analysis

For the charged particles produced in various transverse momentum intervals of the Pb–Pb collisions at $\sqrt{s_{NN}} = 5.02$ TeV, as recorded by the ALICE detector at CERN during Run II of LHC operations, the intermittency analysis, as detailed in [Section 2.7](#), is performed. The various p_T bins studied are tabulated in [Table 4.4](#) where $p_T \leq 2.0$ GeV/c. The statistics of the total events available for the analysis and the events after the various event selection cuts ([Section 4.3](#)) is given in [Figure 4.17](#). After applying the vertex- z (v_z) selection cut of $|v_z| < 10$ cm, the v_z distribution is shown in [Figure 4.18](#). Distribution of v_z before applying selection cuts is given. The other quality assurance (QA) plot that is given in [Figure 4.18](#)

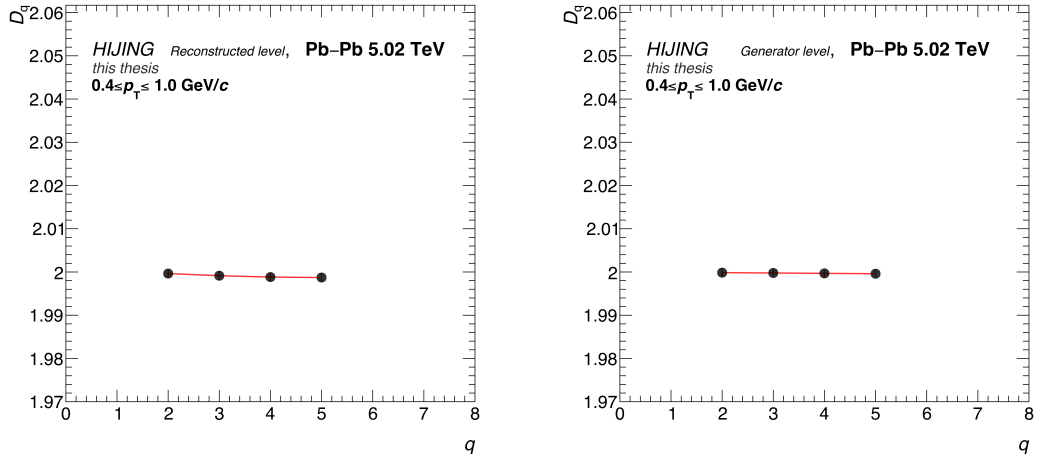


FIGURE 4.16:

HIJING: D_q vs q plot for reconstructed (left) and generated (right) simulation events. D_q is independent of q in HIJING.

is the centrality distribution of the full data and the centrality distribution of the selected events.

After the selection of good events from ALICE data, track selection cuts are applied for further analysis. The pseudorapidity distributions (η) and azimuthal angle (φ) distributions of the charged particle tracks before and after applying track selection cuts are shown in [Figure 4.19](#). Number of clusters and crossedrows in TPC are shown in [Figure 4.20](#). χ^2 distributions of particles in ITS and TPC are shown in [Figure 4.21](#). The Distance of Closest Approach (DCA) of a track to the vertex in xy, z plane is shown in [Figure 4.22](#). The observed distributions show no major fluctuations, which suggests a consistent behaviour in particle production across different events of the data. The multiplicity distributions (number of particles) of the selected charged particles recorded by these events in the various transverse momentum (p_T) bins having $|\eta| \leq 0.8$ and $0 \leq \varphi \leq 2\pi$ are given in [Figure 4.23](#). It is observed that as p_T increases, the average multiplicity decreases.

4.5.2.1 Bin content and event factorial moments

After getting the tracks selected for analysis, the charged particles recorded by ALICE and falling within the acceptance, i.e., $|\eta| \leq 0.8$ and $0 \leq \varphi \leq 2\pi$ in the selected transverse momentum bins are mapped on to the two-dimensional (η, φ) phase space, which is partitioned into M^2 bins (see [Figure 2.4](#)), with M bins along η and M bins along φ dimension of the phase space. The maximum limit of the number of bins (M) depends on the acceptable MC closure obtained with HIJING as discussed in [Section 4.5.1.1](#). In the present work, it is observed that at $M = 62$, the closure is $\sim 99.5\%$.

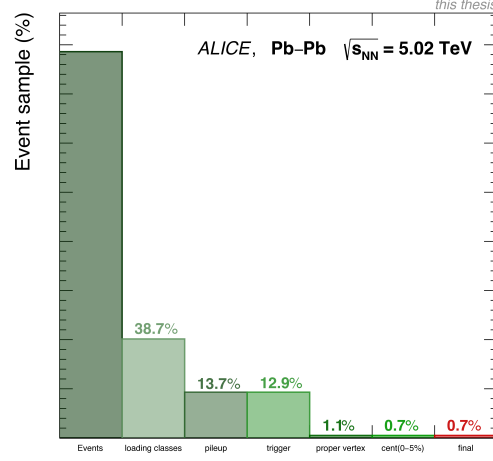


FIGURE 4.17:

ALICE: Percentage of events obtained after applying various event selection cuts on the data. Percentage on the bars show the approximate percent of events obtained after applying a particular cut.

The number of particles in each m^{th} bin of the phase space of an event (n_{me}) called *bin-content* is determined. Bin content averaged over the total bins (M^2) for an M , in an event, is given by $\langle n_{\text{me}} \rangle$. Average of $\langle n_{\text{me}} \rangle$ over all events for an M , simply called *average bin content* as function of $\ln M^2$ is shown in **Figure 4.24**. A decreasing trend of average bin content with increase in M is observed, suggesting the decrease in the number of particles per bin as we go to more and more finer bins in the phase space. This dynamics in particle number distributions in phase space is captured by the calculation of event factorial

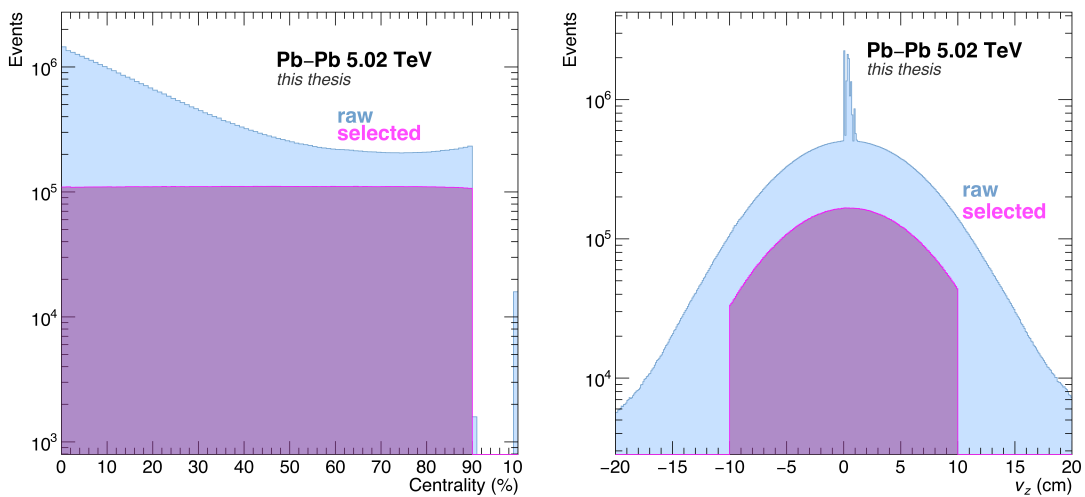


FIGURE 4.18:

ALICE: Centrality (left) and vertex- z (v_z) distributions (right) of data before and after applying event selection cuts.

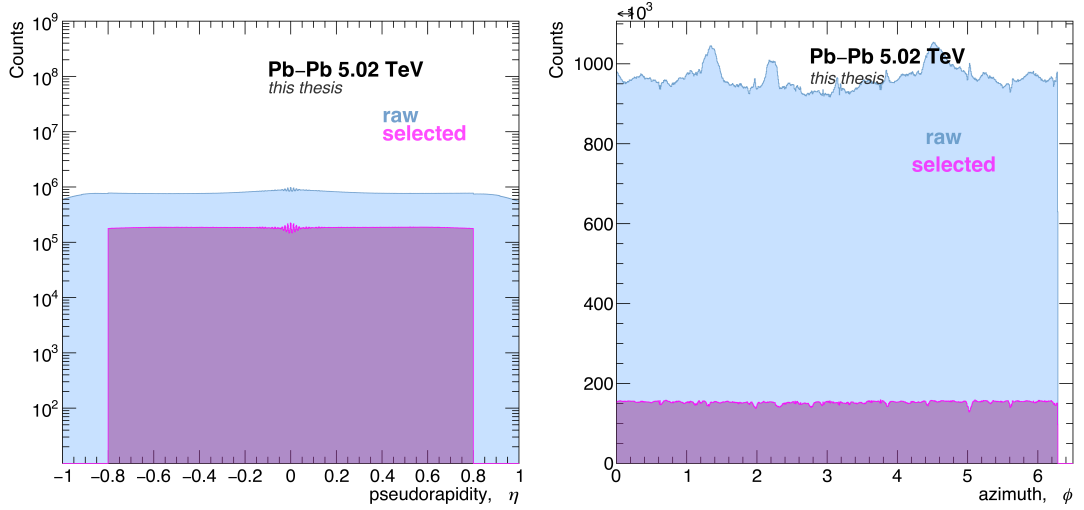


FIGURE 4.19:

ALICE: η and ϕ distributions of the charged particle tracks before and after applying track selection (Section 4.4) cuts on 0–5% centrality events.

moments ($f_q^e(M)$), Equation 2.21 calculated per M and per event for each q . A few distributions of $f_q^e(M)$ are shown in Figure 4.25 for $M = 20, 34, 50, 60$ and $q = 2, 3, 4, 5$ in case of $0.4 \leq p_T \leq 1.0$ GeV/ c bin. It is observed that as q increases, the event factorial moments become sensitive to higher order correlations. The $f_q^e(M)$ distributions tend to broaden as q increases because higher order moments capture increasingly rare fluctuations where more particles are found within a small phase space volume. On the other hand, $f_q^e(M)$ becomes more sensitive to local density fluctuations as M increases because the phase

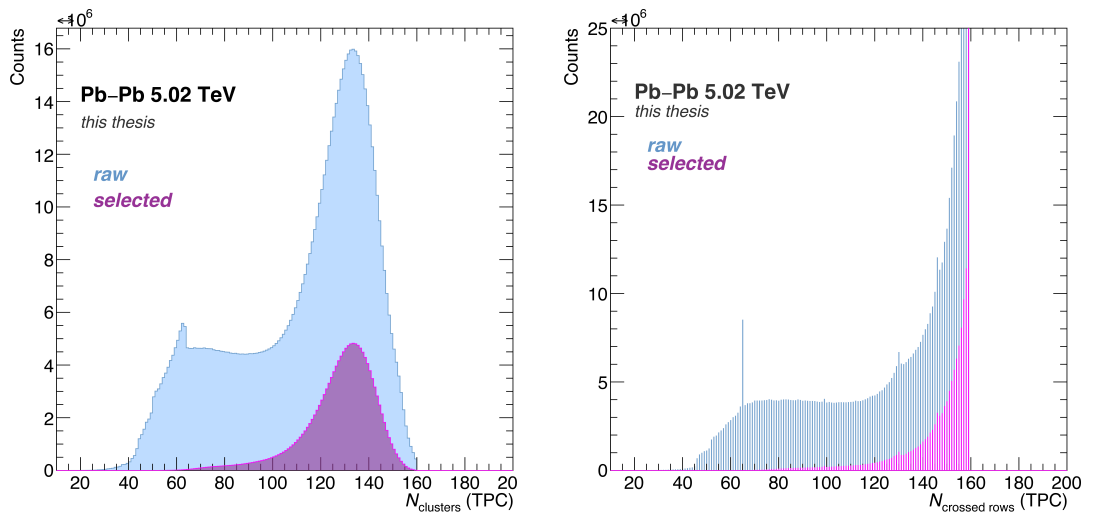


FIGURE 4.20:

ALICE: Number of clusters and number of crossed rows in TPC distributions for charged particle tracks in TPC before and after applying track selection cuts.

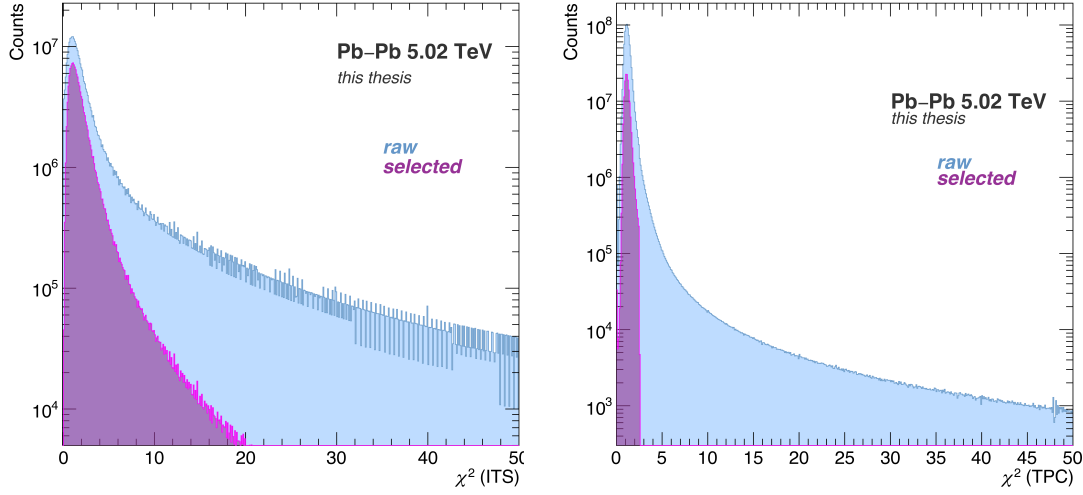


FIGURE 4.21:

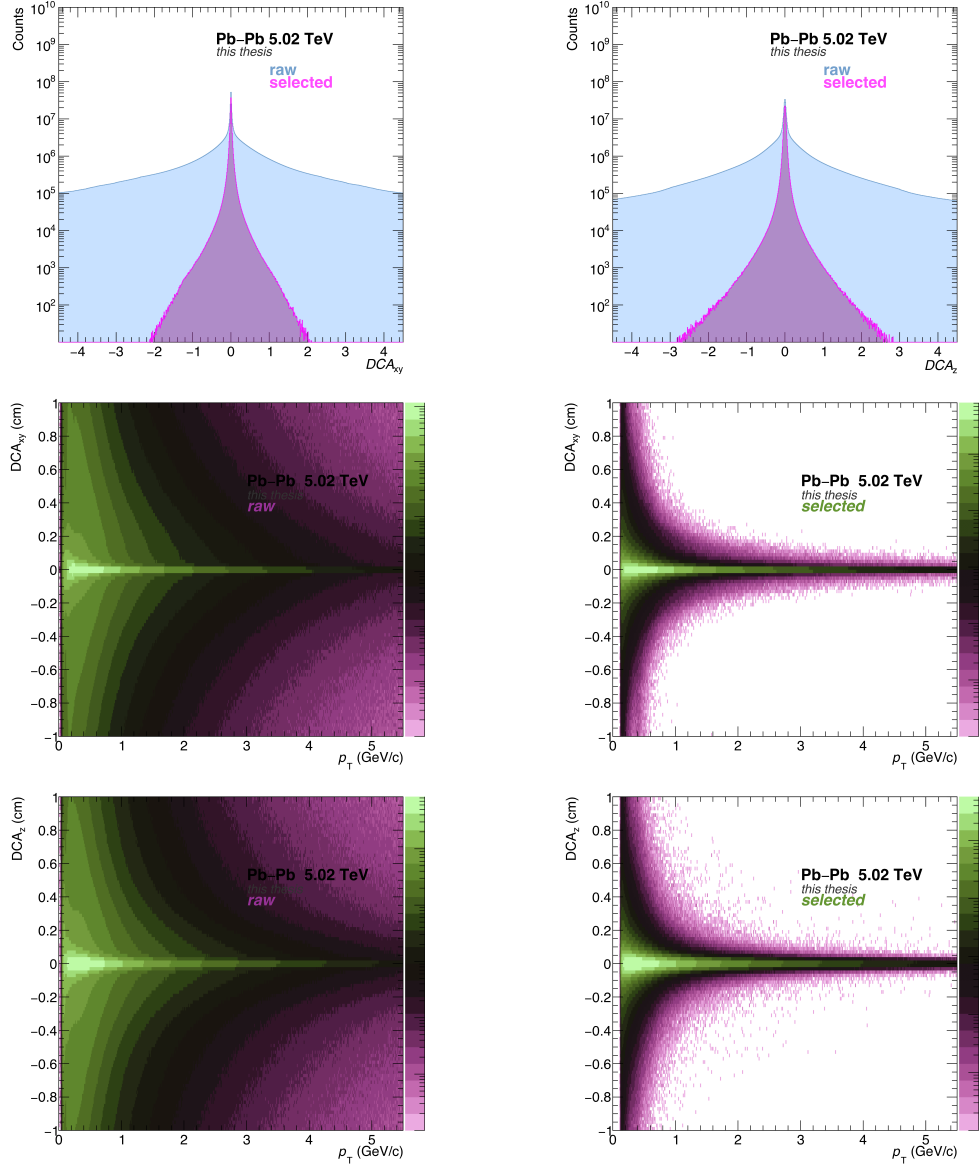
ALICE: χ^2 distributions of charged particle tracks in ITS and TPC before and after applying track selection cuts.

space is divided into a large number of smaller bins. For smaller M (i.e., fewer phase space bins), the bin sizes are large and each bin contains many particles, and fluctuations are averaged over a larger volume, resulting in smoother distributions. But as M increases, the bin size becomes small and the average number of particles per bin decreases, and local density fluctuations if present become more prominent showing an increase in the variance of $f_q^e(M)$ distributions.

4.5.2.2 Scaling behaviour of normalized factorial moments

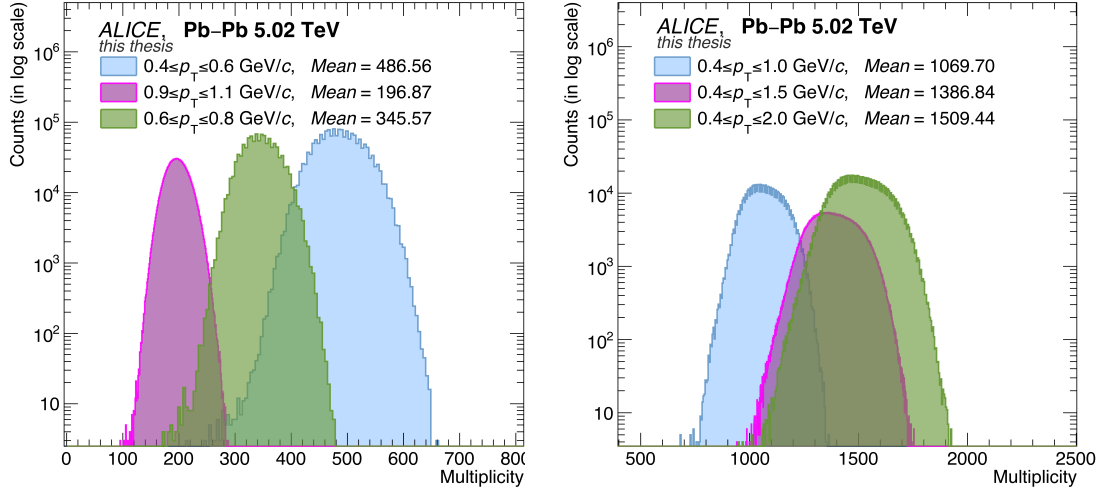
The event factorial moments of order q ($f_q^e(M)$) are normalized as defined in Equation 2.21 to obtain Normalized factorial moments, $F_q(M)$. In case of a scale invariant system, there is no characteristic bin size (or length scale) [79]. As the number of bins in phase space (M^2) increases, the factorial moments $F_q(M)$ continue to reflect the same underlying correlations. This is then reflected in M -scaling (Figure 4.1) that is power-law growth of $F_q(M)$ with M^2 . If the system is not scale invariant, there might be some growth in $F_q(M)$ at lower M^2 , but at high M^2 , the distribution should flatten out, indicating that the system has reached a characteristic scale.

M -scaling: The dependence of NFM, $F_q(M)$ on the number of bins (M) is studied through log-log plots as $\ln F_q(M)$ vs $\ln M^2$. Figure 4.26 shows these plots for charged particles recorded using ALICE for Pb-Pb collisions at $\sqrt{s_{NN}} = 5.02$ TeV in $0.4 \leq p_T \leq 1.0$ GeV/ c p_T bin with $|\eta| \leq 0.8$, $0 \leq \varphi \leq 2\pi$ and for $q = 2, 3, 4, 5$. It is observed that there is power-law growth of $\ln F_q(M)$ as function of $\ln M^2$ for all q . This demonstrates the scaling behaviour

**FIGURE 4.22:**

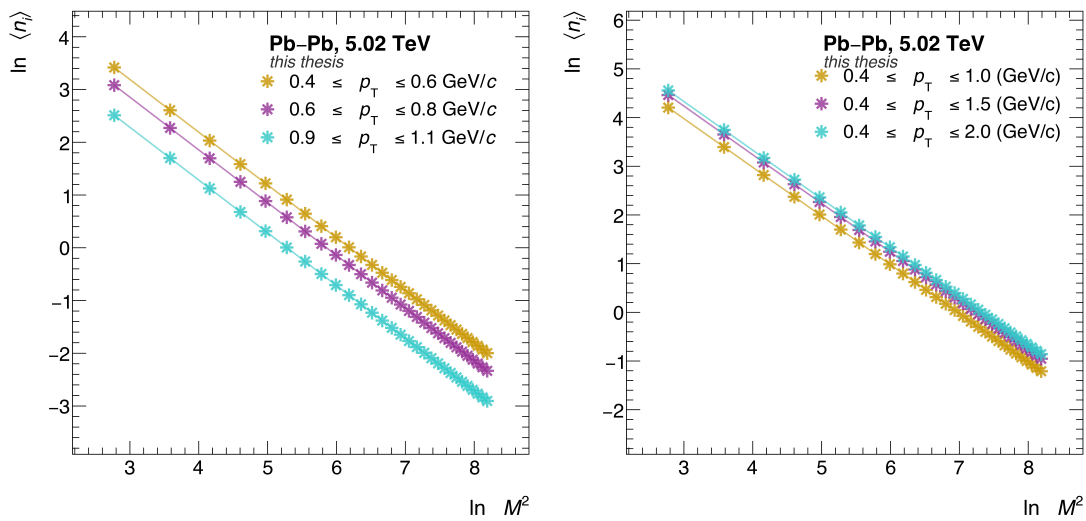
ALICE: Distance of Closest Approach (DCA) of tracks to primary vertex in xy (upper left), z plane (upper right) and as a function of p_T for raw tracks and selected tracks .

of particle density fluctuations within the phase space. This scaling behaviour as defined in [Equation 2.23](#) for relation between F_q and M is called M -scaling or *intermittency*. Multiple linear regions in the log-log plot **are observed especially the presence of linear region at high M** that characterizes the scaling of $F_q(M)$ over a range of small bin sizes. This is the region of interest where the important fluctuations are seen as power-law behaviour. It should be noted that there is an absence of any saturation or oscillatory behaviour in $F_q(M)$ as M^2 increases, unlike what is observed in HIJING ([Figure 4.9](#)) and at low energy experiments [\[262\]](#).

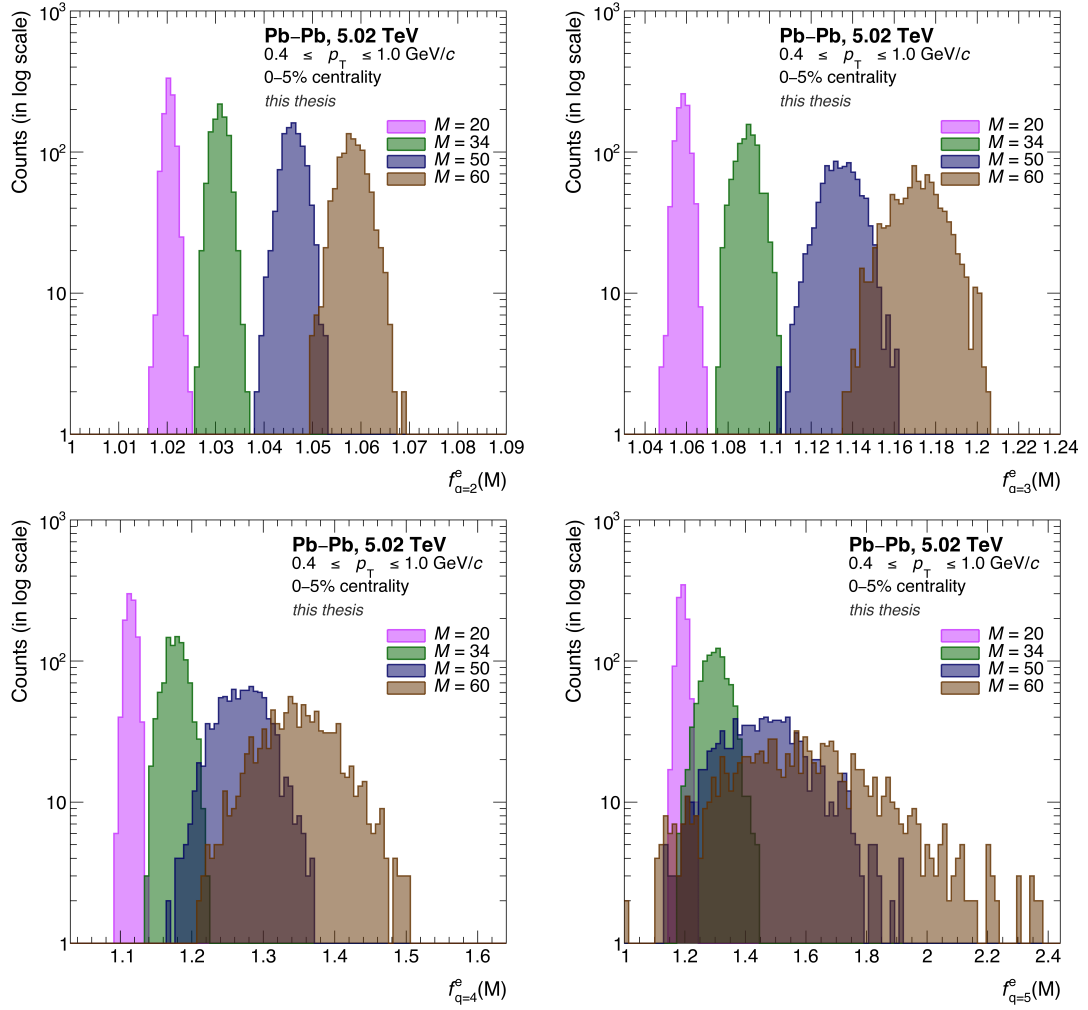
**FIGURE 4.23:**

ALICE: Charged particle multiplicity distributions in the narrow p_T bins (left) and wide (right) p_T bins within midrapidity $|\eta| \leq 0.8$ and $0 \leq \varphi \leq 2\pi$ in 0–5% central events.

From the straight line fits at higher M region of these (M -scaling) plots, intermittency index ϕ_q is obtained, as shown on right of **Figure 4.27**. Left figure shows dependence of ϕ_q on q . For reference, these values are tabulated in **Table 4.6** for all orders up to 5, in case of p_T bin $0.4 \leq p_T \leq 1.0$ GeV/ c and $0.4 \leq p_T \leq 0.6$ GeV/ c . An increasing trend of ϕ_q with q is seen whereas decreasing trend is seen as p_T bin width increases.

**FIGURE 4.24:**

ALICE: Average bin content as a function of number of phase space bins ($\ln M^2$) for the narrow (left) and wide (right) p_T bins.

**FIGURE 4.25:**

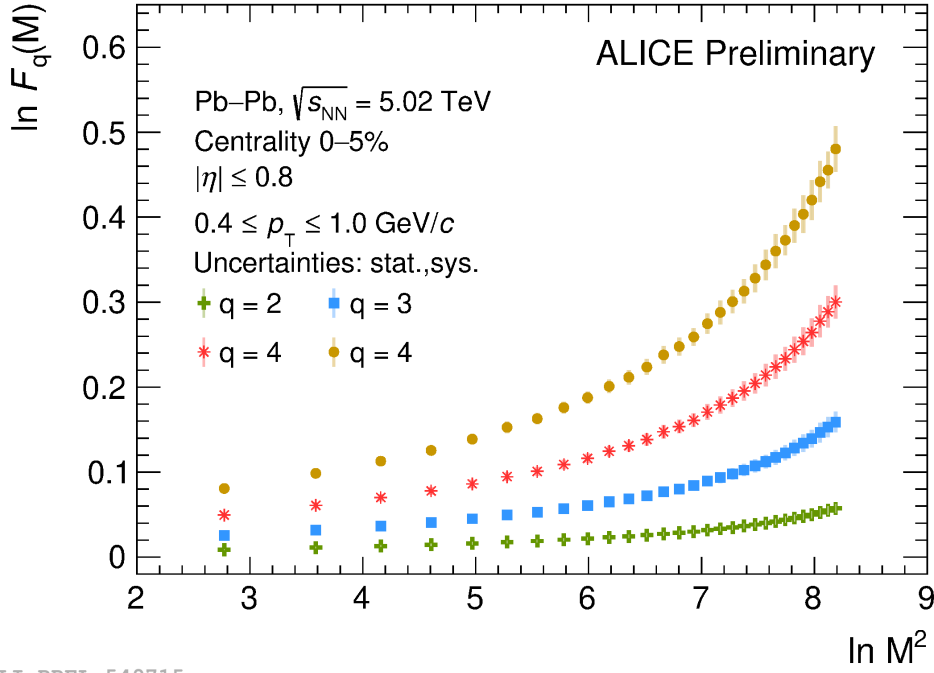
ALICE: $f_q^e(M)$ distributions for $q = 2, 3, 4, 5$ of charged particles in (η, φ) phase space partitioned into $M = 20, 34, 50, 60$ bins in $0.4 \leq p_T \leq 1.0$ GeV/c.

F-scaling: In **Figure 4.28**, $\ln F_q(M)$ for $q \geq 3$ are plotted as a function of $\ln F_2(M)$ (F -scaling) where $F_q(M)$ is observed to have linear dependence on $F_2(M)$. Thus, **F -scaling is also observed in ALICE data**. These observations for M -scaling and F -scaling behaviour are similar to what has been observed

p_T range (GeV/c)	Intermittency indices, ϕ_q			
	ϕ_2	ϕ_3	ϕ_4	ϕ_5
$0.4 \leq p_T \leq 0.6$	0.07 ± 0.00	0.17 ± 0.00	0.32 ± 0.00	0.44 ± 0.02
$0.4 \leq p_T \leq 1.0$	0.03 ± 0.00	0.08 ± 0.00	0.15 ± 0.00	0.23 ± 0.00

TABLE 4.6:

Intermittency indices (ϕ_q) summarised for $0.4 \leq p_T \leq 0.6$ GeV/c (narrow) and $0.4 \leq p_T \leq 1.0$ GeV/c (wide) p_T bins.

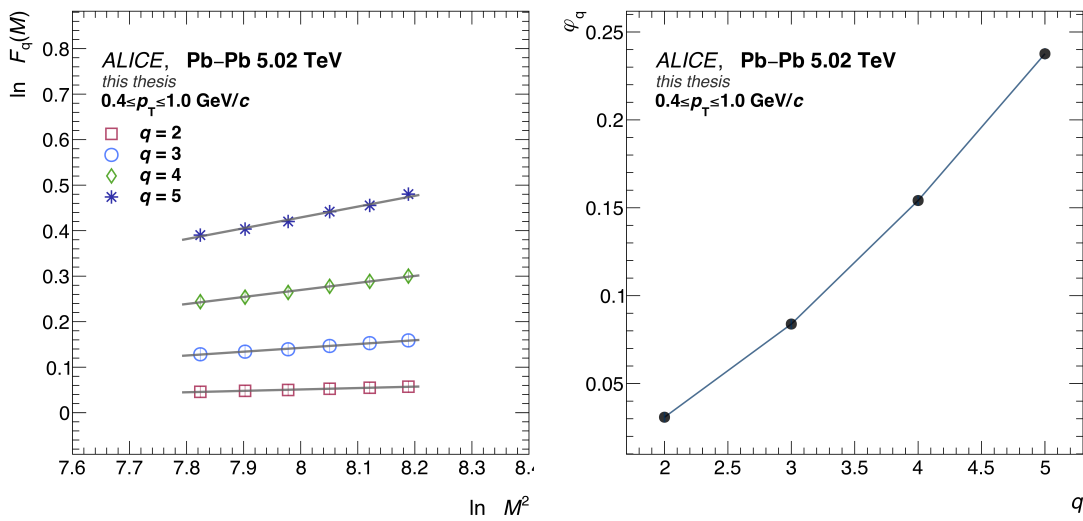


ALI-PREL-549715

FIGURE 4.26:

ALICE: $\ln F_q(M)$ vs $\ln M^2$ plot, (M -scaling) for $q = 2, 3, 4, 5$. Power-law growth of $F_q(M)$ with M^2 is observed for all orders. A linear behaviour of NFM (F_q) at high M exhibits intermittency in the data.

in the ALICE Pb-Pb Run1 data at $\sqrt{s_{NN}} = 2.76$ TeV [254,255]. The F -scaling behaviour of $F_q(M)$ with $F_2(M)$ can reveal the properties of the system under study. For the higher M values, where the $F_q(M)$ grows linearly with M , the line


FIGURE 4.27:

ALICE: M -scaling plot for higher M values with straight line fits (on the left) to calculate intermittency index ϕ_q . ϕ_q as a function of q is shown on right.

fits are performed on F -scaling plots. **Figure 4.29** shows a fit of F -scaling plot which gives slope β_q (**Equation 2.24**). As mentioned in **Section 2.7**, ϕ_q depend on critical parameters of the system while β_q is independent of them.

4.5.2.3 Scaling exponent (ν)

The scaling exponent (ν) is calculated from the line fit of $\ln \beta_q$ vs $\ln(q-1)$ plot for $q = 3, 4, 5$ (**Equation 2.25**, **Figure 4.1**). The value of scaling exponent, ν is found to be 1.44 ± 0.02 for most central 0–5% ALICE Pb–Pb data at $\sqrt{s_{NN}} = 5.02$ TeV in $0.4 \leq p_T \leq 1.0$ (GeV/c) p_T bin as shown in **Figure 4.30**. ν is predicted to be 1.304 by Ginzburg-Landau theory with formalism for second-order phase transition [175,180] and 1.0 by 2D Ising model [178,183]. A value of 1.41 is predicted for ν by the SCR (Successive Contraction and Randomization) model [170], that has been modelled with phase transition type of dynamics exhibiting critical fluctuations in spatial patterns.

The ν value obtained from the ALICE data closely aligns with the SCR model's prediction. The SCR model is a phenomenological tool developed to study the phase transitions of quark-gluon plasma (QGP) as it changes into a gas of hadrons. It involves two main processes: contraction, which brings quarks and anti-quarks together in dense areas to form hadrons, and randomization, which allows particles in less dense regions to spread out due to thermal effects. By repeatedly applying these processes, the model illustrates how confinement and thermal behaviour interacts near the phase transition temperature. Thus, results of this work suggest that the system created in the most central Pb–Pb collisions at $\sqrt{s_{NN}} = 5.02$ TeV retains remnants of critical fluctuations. This is an important outcome of this work where the experimental observation is found to be close to theoretical model-based prediction. However, to strengthen this argument before concluding about dynamics of the system formed, further investigations to extract information related to phase transition and criticality at high energy heavy-ion collisions with other methodologies may be taken up.

4.5.2.4 Fractal dimension (D_q)

Linear behaviour of $\ln F_q$ with $\ln M^2$, that is observation of intermittency, paves way for an investigation into the observables, such as fractal parameters, which shed light on the fractal nature of the system formed in the data. One of these parameters is D_q , which is intrinsically linked to the intermittency index ϕ_q . The fractal dimension (D_q) is calculated using **Equation 2.26** for values of the order of the moment, $q = 2, 3, 4, 5$. For the present analysis, in the $0.4 \leq p_T \leq 1.0$ GeV/c p_T bin, D_q is presented as a function of q is shown in

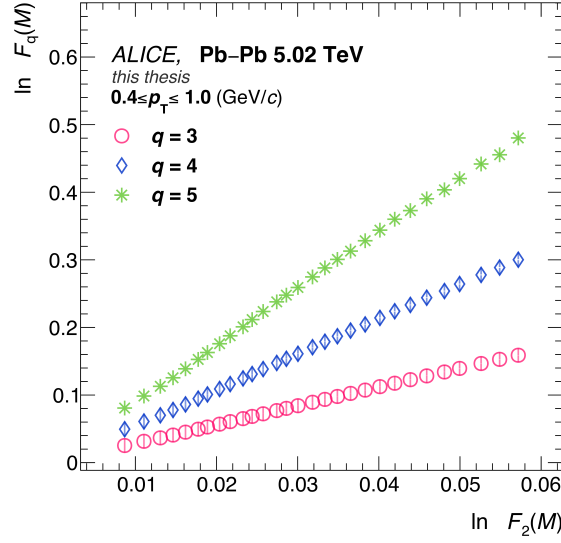


FIGURE 4.28:

ALICE: $\ln F_q(M)$ vs $\ln F_2(M)$ plot, (F -scaling) for $q = 3, 4, 5$. Power law growth of $F_q(M)$ with $F_2(M)$ is observed depicting the F -scaling in the data for all orders.

Figure 4.31. It is clearly observed that D_q decreases as q increases, indicating a multifractal nature of multiplicity fluctuations of the charged particles within the central ALICE data (Table 4.1).

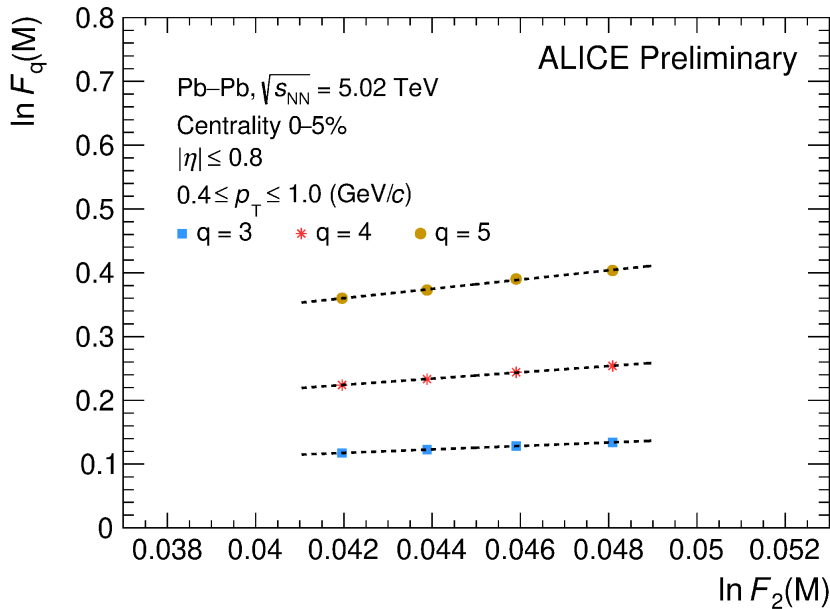


FIGURE 4.29:

ALICE: $\ln F_q(M)$ vs $\ln F_2(M)$ plot, (F -scaling) for $q = 3, 4, 5$ with the line fits in the higher M region where acceptable MC closure was obtained with HIJING. Slope values of the line fits are the β_q values ($q = 3, 4, 5$).

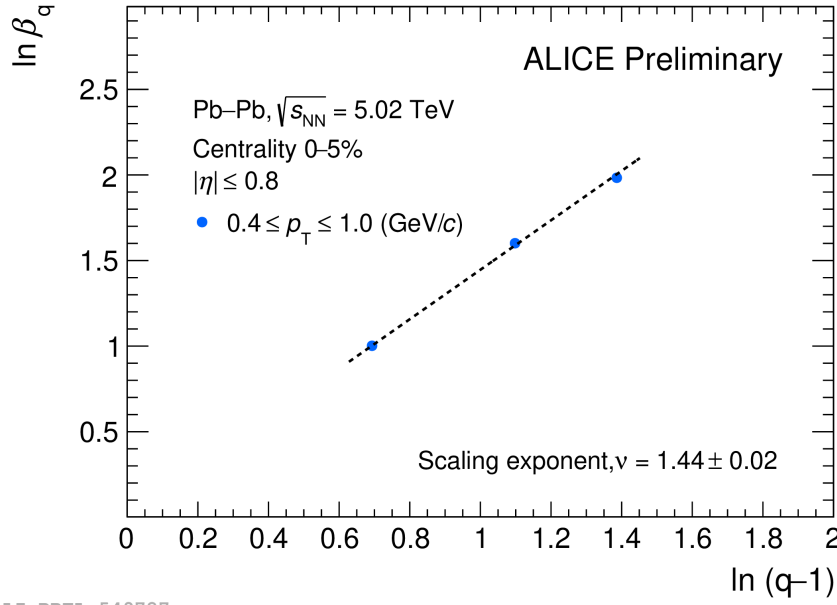
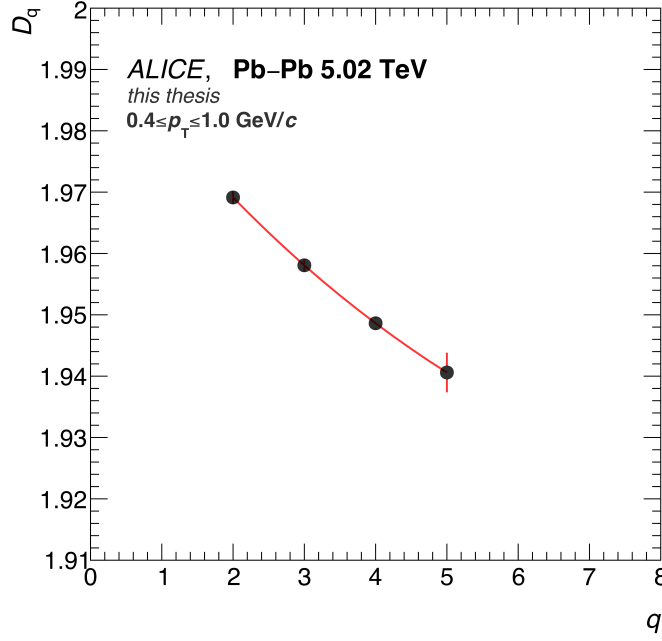


FIGURE 4.30:

ALICE: $\ln \beta_q$ as a function for $\ln(q-1)$ in the most central (0-5%) Pb-Pb collision events. The dashed line is the power-law fit to determine scaling exponent, ν .

It is pertinent to mention that for the intermittency analysis as a tool for the detection of self-similar fluctuations, there are many challenges. For heavy-ion collision events, the main being subtraction of the uncorrelated background. One possible way to take care of this intermediate background would be to perform many Monte Carlo runs and inserting fluctuations in the phase space, attempting to closely reproduce the shape of $F_q(M)$ as obtained from the data, then calculate the $F_q(M)$ from mentioned methods. For this, a good statistical test is required for the similarity of the functions. One may also calculate a complete multifractal spectrum of particles in (η, φ) phase space [86]. This means looking at both the critical tracks and the random background together as a multifractal. The main contributions to the spectrum is then the critical tracks, and the dimensionality of the phase space. NFM of different orders (q), can reproduce the spectrum of fractal dimension D_q to higher and higher orders. This is because the critical tracks may appear as a sharp peak somewhere in such a multifractal spectrum. These calculations can be taken up in the future work as this approach requires very high statistics. In addition to that, a computationally intense calculation of a dense set of (fractional) q -order NFM needs to be performed.

A comparison of the observables (M -scaling, F -scaling, ν and D_q) from data

**FIGURE 4.31:**

ALICE: D_q as a function of q for the most central (0–5%) events from Pb–Pb collisions at $\sqrt{s_{\text{NN}}} = 5.02$ TeV.

with that from MC - HIJING and EPOS–LHC [248] event samples (Table 4.2) is discussed below.

4.5.2.5 Comparison of data and Monte Carlo

Simulation events for the models (HIJING and EPOS–LHC) are taken from ALICE production. The production name of HIJING and EPOS–LHC events are given in Table 4.2. Discussion on HIJING events is already given in Section 4.5.1. A brief introduction of EPOS–LHC is given below followed by discussion on the comparative results.

EPOS is an acronym dervied from:

- **E**nergy-sharing : for cross section calculation and particle production
- **P**arton Multiple scattering
- **O**utshell remnants
- **S**creening, shadowing via unitarisation and splitting (collective effects for dense systems).

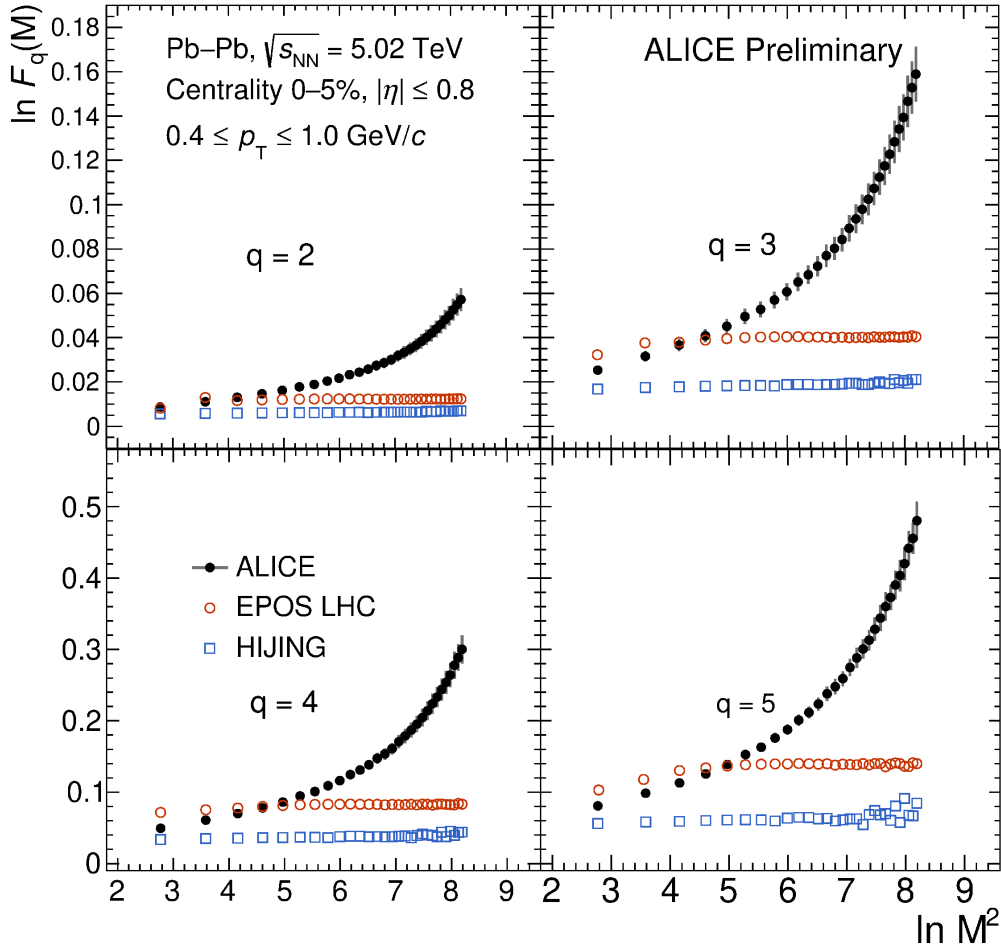
It is a semi-hydrodynamic event generator designed to simulate high-energy collisions, particularly in the context of heavy-ion physics. The model features a unique core-corona structure. The core, characterised by hydrodynamic interactions, includes regions with string density exceeding a threshold value ρ_0

at a specific proper time τ_0 . The corona is associated with non-hydrodynamic processes and encompasses areas of lower string density [263].

Interactions in EPOS are simulated using Gribov-Regge theory [264], which describes parton ladders connecting colliding nucleons and initiating parton evolution. The parton ladders account for the evolution of the partons from initial colliding nucleons. In high density core regions, EPOS facilitates multiple parton interactions (MPIs), generating a greater parton ladders number. Conversely, low density regions of corona suppresses MPIs and rely on string fragmentation for particle production. Core hadronisation follows a statistical model, whereas the corona uses a mechanism similar to PYTHIA's string fragmentation - characterised by large rapidity or low density—hadronisation. A key distinction between EPOS and other generators lies in their treatment of beam remnants: EPOS treats these remnants independently from produced partons. Unlike HIJING, EPOS is capable of generating both p–p events and heavy-ion events. The contribution of core region becomes relevant only in high-multiplicity p–p collisions where string density exceeds ρ_0 and mid-rapidity particles arise predominantly from the core; otherwise, they are generated through standard string fragmentation.

EPOS–LHC events are analysed for the intermittency study. For this, the NFM of the charged particles generated in the two-dimensional (η, φ) phase space with acceptance $|\eta| \leq 0.8$ and $0 \leq \varphi \leq 2\pi$ within $0.4 \leq p_T \leq 1.0$ GeV/c transverse momentum bin are calculated. Data results for the observables are compared with that from HIJING and EPOS–LHC.

***M*–scaling**, which examines the dependence of $F_q(M)$ on number of bins (M^2) in the phase space, has been compared for ALICE data and MC event generators. This comparison is essential for understanding the underlying physics. For the transverse momentum interval of $0.4 \leq p_T \leq 1.0$ GeV/c, results from ALICE, HIJING and the EPOS–LHC model are shown in **Figure 4.32**. The power-law behaviour of $F_q(M)$ with decreasing bin sizes, in the two-dimensional (η, φ) phase space for $|\eta| \leq 0.8$ and $0 \leq \varphi \leq 2\pi$, observed in ALICE is not explained by any of these models especially at high M . The figure clearly shows that **HIJING and EPOS–LHC underestimate the experimental data**, revealing both qualitative and quantitative differences between the data and the models at high M values. As M increases, the F_q values for the data for all q 's deviate from that of the models, indicating significant bin-to-bin scale-invariant fluctuations in charged particle production in the experiment compared to the models. In other



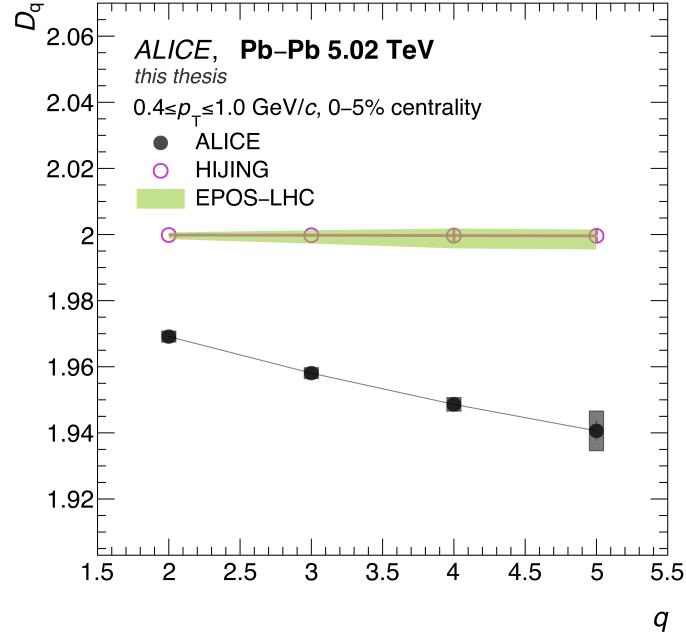
ALI-PREL-559667

FIGURE 4.32:

ALICE: Dependence of $\ln F_q(M)$ on $\ln M^2$ (M -scaling) for $q = 2, 3, 4, 5$ in the central Pb-Pb collisions at $\sqrt{s_{NN}} = 5.02$ TeV for ALICE data, HIJING and EPOS-LHC. Quantitative and qualitative difference is observed between data and models at high values of number of bins (M).

words, the physics of self-similar particle production, as indicated by power law growth of F_q with increasing M , is absent in these models.

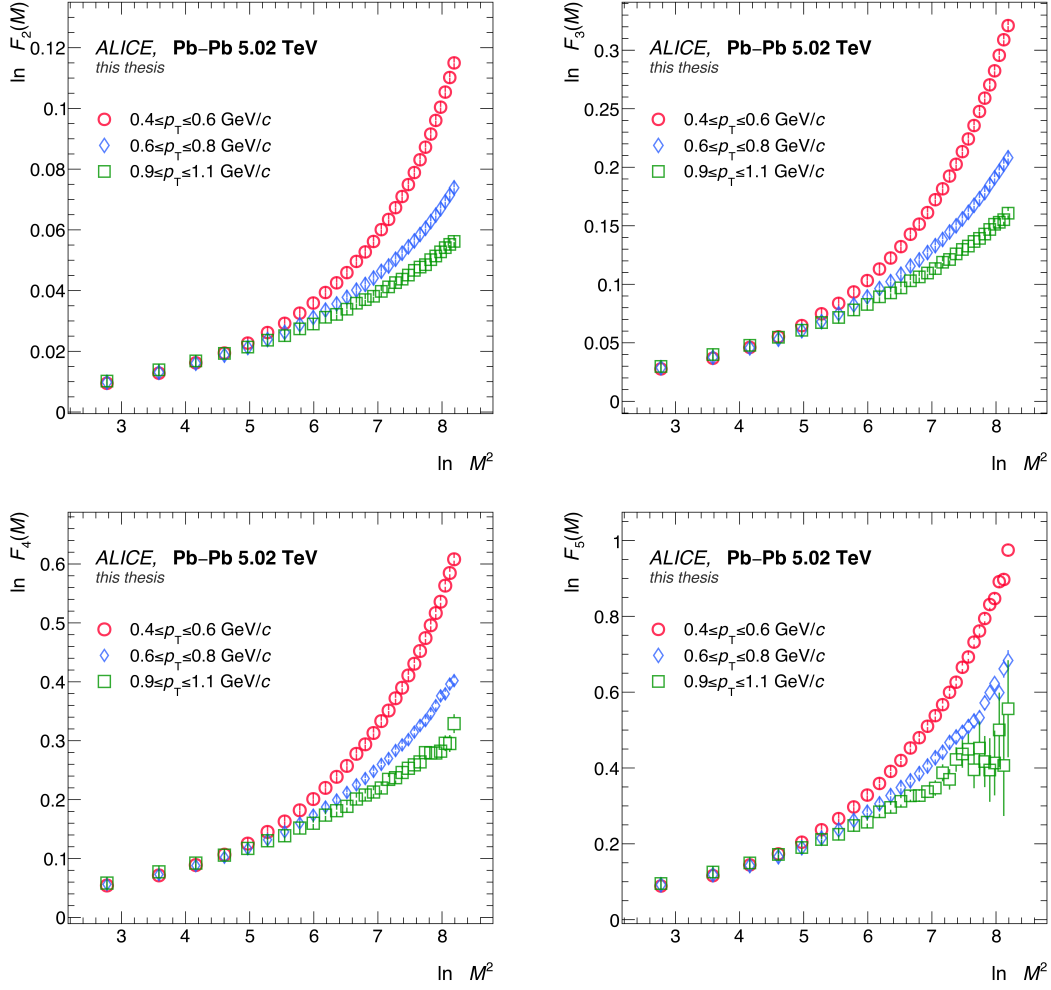
F -scaling plots, i.e., $\ln F_q(M)$ vs $\ln F_2(M)$ for $q \geq 3$, for both the MC productions from HIJING and EPOS-LHC are obtained which show a weak linear behaviour. For the region corresponding to high M , line fits are performed on these plots to obtain β_q . For all p_T bins under study, comparison of scaling exponent (ν) from experimental data and those from model show differences. Observations show that EPOS-LHC values of ν are greater than 1.6, notably higher than the scaling exponent values from ALICE data which lie between 1.33 to 1.42.

**FIGURE 4.33:**

ALICE: D_q as a function of moment order q for $0.4 \leq p_T \leq 1.0$ GeV/c range compared with HIJING and EPOS-LHC.

D_q : Whereas in data, it is observed that D_q has dependence on q . Both models do not show any dependence of D_q on q . The difference between data and MC are shown in **Figure 4.33**. This observation shows that the multifractal nature of the particle production observed in data is absent in the models which depict monofractal structures of particle generation, implying that the particle production mechanism involves a range of scales and fluctuations, rather than a single dominant scale.

One significant aspect of HIJING and EPOS-LHC is that they utilize a framework based on multiple scattering and parton interactions. These are not able to capture the complex dynamics of particle production observed in high-energy collisions. While EPOS employs a core-corona separation to distinguish between high-density and low-density regions, it may still oversimplify the interactions occurring at the interface of these regions. It uses a statistical model for hadronization in the core region and a string fragmentation approach in the corona, which may not adequately reflect the actual processes occurring in heavy-ion collisions. HIJING's treatment of hadronization also faces challenges, particularly in how it handles beam remnants and the resulting particle production [246]. Nonetheless, both the models are unable to fully account for the self-similar nature of particle production in data.

**FIGURE 4.34:**

ALICE: $\ln F_q(M)$ vs $\ln M^2$ plot (M -scaling) ($q = 2, 3, 4, 5$) for charged particles produced in narrow p_T bins with $|\eta| \leq 0.8$, $0 \leq \varphi \leq 2\pi$ in case of 0–5% most central events.

4.5.2.6 Transverse momentum (p_T) dependence

To further investigate the scaling behaviour of F_q , dependence of $F_q(M)$ moments on transverse momentum (p_T) bins is studied. All transverse momentum bins as detailed in [Table 4.4](#) are considered for this study.

The M -scaling graphs for the narrow p_T bins with a width of $\delta p_T = 0.2$ GeV/ c ($0.4 \leq p_T \leq 0.6$, $0.6 \leq p_T \leq 0.8$, $0.9 \leq p_T \leq 1.1$ GeV/ c) are shown in [Figure 4.34](#), while those for wider p_T bins with $\delta p_T > 0.2$ GeV/ c ($0.4 \leq p_T \leq 1.0$, $0.4 \leq p_T \leq 1.5$, $0.4 \leq p_T \leq 2.0$ GeV/ c) are shown in [Figure 4.35](#). A power-law growth of the normalized factorial moments $F_q(M)$ with respect to M^2 is observed across all orders and for all p_T bins. In all p_T intervals, the scaling behaviour in terms of qualitative rise is similar. However,

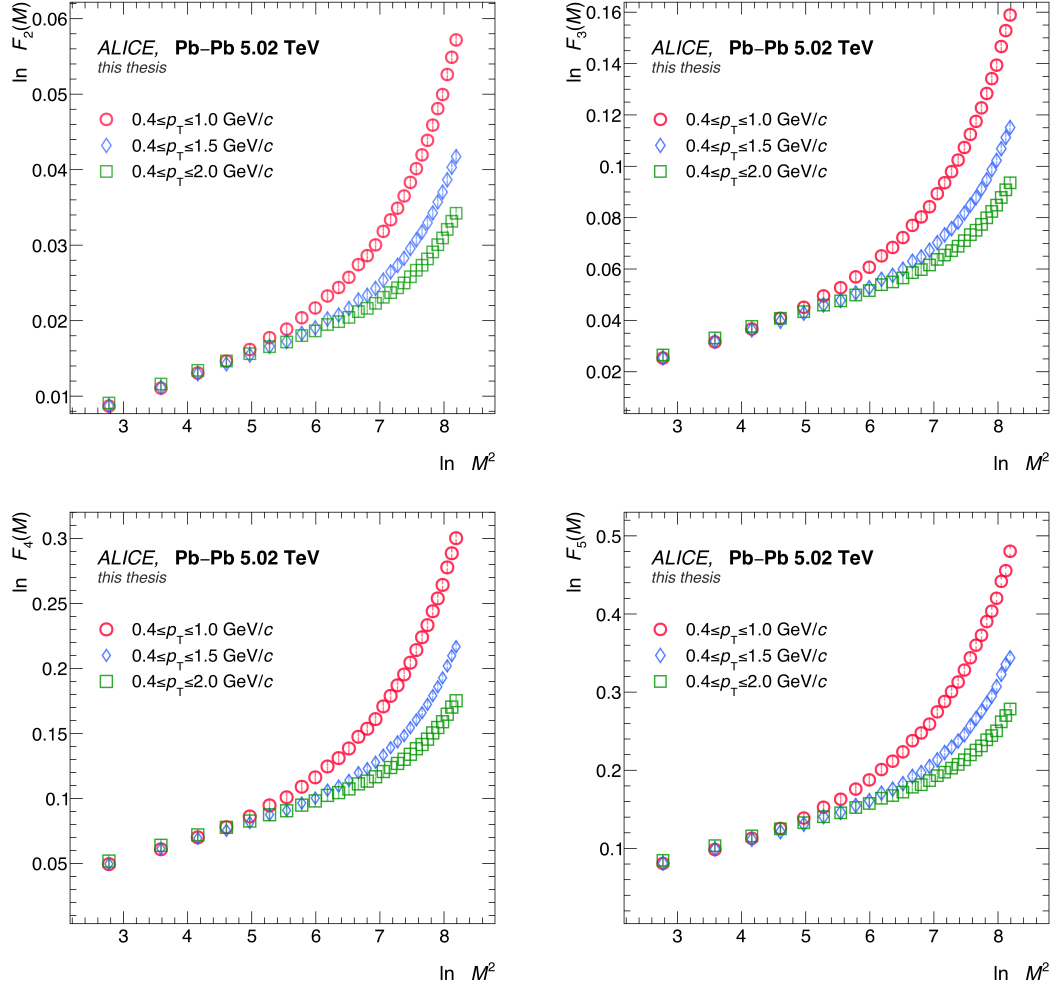


FIGURE 4.35:

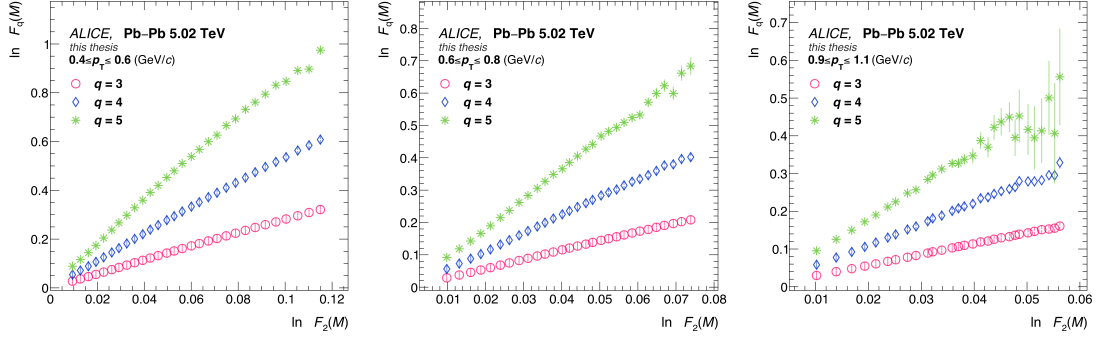
***ALICE:* $\ln F_q(M)$ vs $\ln M^2$ plot (M -scaling) ($q = 2, 3, 4, 5$) for charged particle produced in wide p_T bins with $|\eta| \leq 0.8, 0 \leq \varphi \leq 2\pi$ in case of 0–5% most central events.**

quantitatively the values of $F_q(M)$ show two features. For small values of M (< 12) where the bin sizes are large, $F_q(M)$ values are same and beyond that, the quantitative difference emerges and keeps on increasing smoothly as M increases. This is observed for all q values. At higher values of M , the bin sizes are small and at such high resolutions, only the difference in the spatial patterns of the particles due to different p_T values or due to mean multiplicity is reflected. Though, it should be noted that the differences if any, emerge only at higher bin resolutions. In other words, the fluctuations in the charged particle number density within the (η, φ) phase space increases as the phase space binning increases. In addition, the p_T intervals with high average bin multiplicity have higher values of NFM in comparison to those with lower mean multiplicity. At high p_T , specifically in the range of $0.9 \leq p_T \leq 1.1$ GeV/c, a smooth growth of

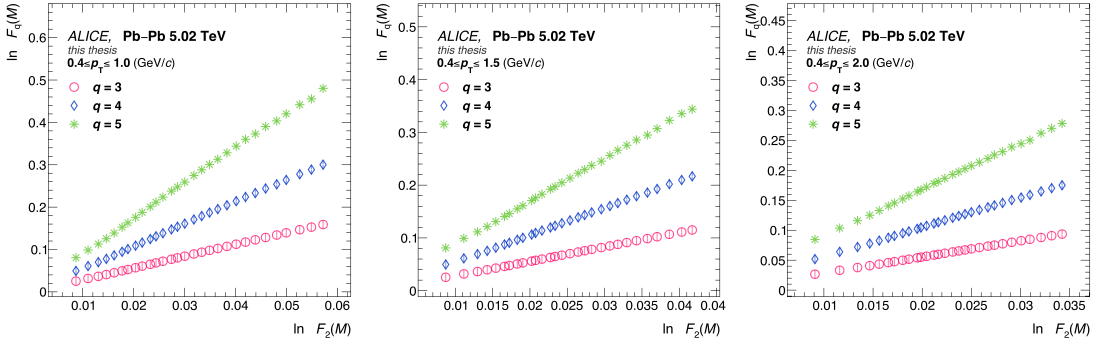
$F_q(M)$ with M is not observed for $q > 3$. This lack of smooth growth can be attributed to the reduced average bin content at higher transverse momenta in the narrow bins with $\delta p_T = 0.2$ GeV/c. As the resolution of phase space increases with increasing M , if there are insufficient bins with multiplicities exceeding the order of the moments (q), these fluctuations in $F_q(M)$ are expected to manifest.

Increasing the width of the p_T bin yields similar qualitative behaviour in M-scaling, as shown in **Figure 4.35**. As the width increases from the range of $0.4 \leq p_T \leq 1.0$ GeV/c to wider ranges like $0.4 \leq p_T \leq 1.5$ GeV/c and then to $0.4 \leq p_T \leq 2.0$ GeV/c within the acceptance of (η, φ) phase space (with $|\eta| \leq 0.8$ and $0 \leq \varphi \leq 2\pi$), there is an increase in the number of particles present in that phase space. It is observed that with the increase in the width of the p_T bin, the values of $F_q(M)$ decrease. However, there is no change in the scaling behaviour and a power-law growth of $F_q(M)$ with respect to M^2 persists, exhibiting multiple linear regions. For a wider p_T bin, for the interval of $0.4 \leq p_T \leq 2.0$ GeV/c, similar scaling behaviour is noted but with lower quantitative values for $F_q(M)$ in comparison to $0.4 \leq p_T \leq 1.0$ GeV/c bin. The same (η, φ) phase space populated with more particles for M results in decrease in the $F_q(M)$ values. Again, it is to be noted that it is only at the higher resolution of the bins, this difference is appreciably reflected in the values of the NFM for any q value.

The $\ln F_q(M)$ vs $\ln F_2(M)$ plots for the narrow p_T bins are given in **Figure 4.36**. While the same plots for wide p_T bins are shown in **Figure 4.37** for $q = 3, 4, 5$ respectively. The scaling exponent, ν is determined for each p_T interval, for the higher M region where closure is $\sim 99\%$. Notably, different p_T bins yield a similar value of ν . The scaling exponent values derived from these p_T bins are shown in **Figure 4.38** and **Figure 4.39**. Specifically, **Figure 4.38** shows the ν dependence on the wide p_T bins and **Figure 4.39** shows the ν dependence on the narrow p_T bins. The ν values for the corresponding transverse momentum bins for Pb–Pb collisions at $\sqrt{s_{NN}} = 2.76$ TeV [254,255] are also shown in the figures. For both the energies, a similar dependence of ν on p_T is seen implying ν has very little (if any) dependence on p_T . Within the bounds of uncertainties, the values are ~ 1.4 for both the energies, and very close to the predictions by SCR Model [170] that incorporate critical fluctuations. The value of ν from both the energies of ALICE closely align with these phenomenological predictions. The close correspondence between experimental results and model based predictions help to understand the dynamics of the system created in the collisions in light of SCR model. It also adds to the confidence on ν as an important parameter of the system under study.

**FIGURE 4.36:**

ALICE: $\ln F_q(M)$ vs $\ln F_2(M)$ plot (F -scaling) for $q = 3, 4, 5$ for the charged particle produced in narrow p_T bins in the mid-rapidity region of the most central events.

**FIGURE 4.37:**

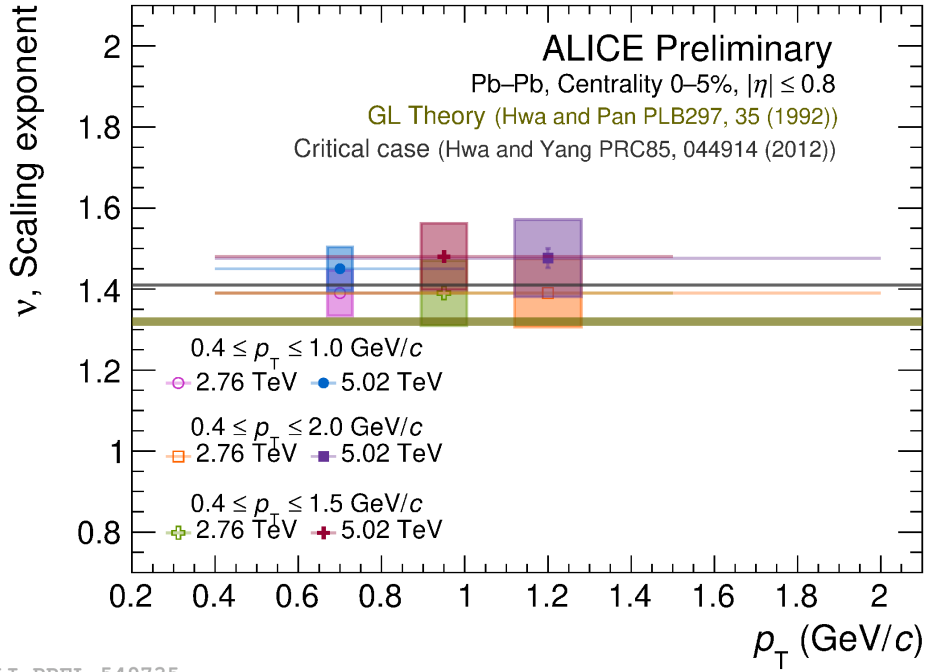
ALICE: $\ln F_q(M)$ vs $\ln F_2(M)$ plot (F -scaling) for $q = 3, 4, 5$ for the charged particle produced in wide p_T bins in the mid-rapidity region of the most central events.

The fractal dimension, D_q and its dependence on p_T bin width is shown in **Figure 4.40**. The data points reveal a consistent decreasing trend of D_q with increasing values of q across all p_T bins. This trend indicates a multifractal nature of soft charged particle production in Pb–Pb collisions at $\sqrt{s_{NN}} = 5.02$ TeV. The observed behaviour of D_q as functions of q in various p_T bins suggests that the mechanism governing soft charged particle production remains consistent across these bins, while exhibiting a multifractal nature at LHC energies.

The results discussed in this section highlight the complex dynamics involved in the particle production during high-energy heavy-ion collisions at LHC energies, providing valuable insights into the underlying processes at play.

4.5.2.7 Centrality dependence

In general, $F_q(M)$ are sensitive to the underlying multiplicity distributions of particles produced in collisions as discussed in previous **Section 4.5.2.6**. Moving



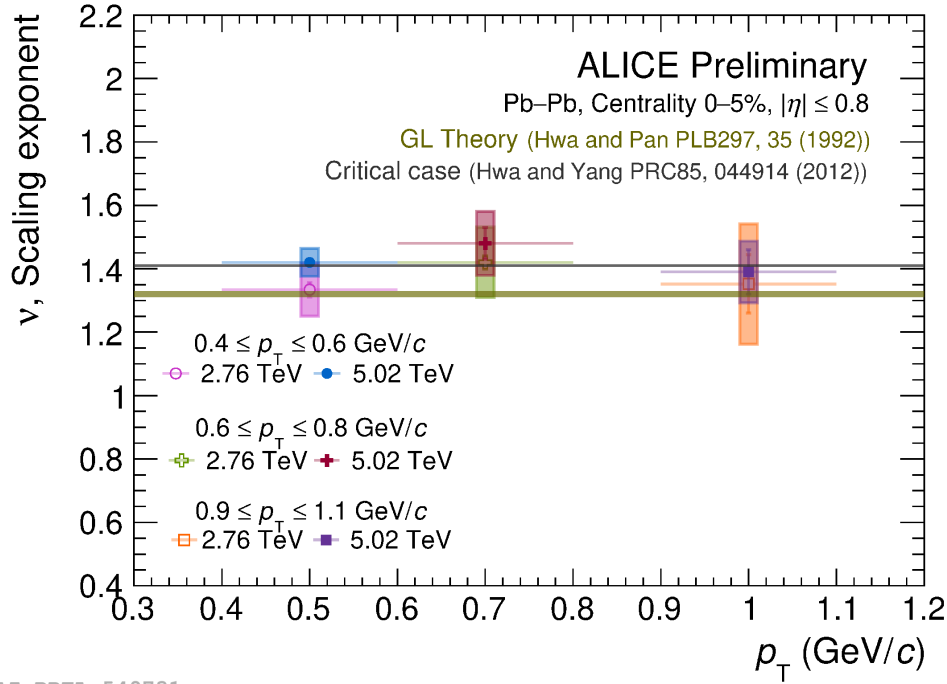
ALI-PREL-549735

FIGURE 4.38:

ALICE: Scaling exponent (ν) as a function of p_T in the wide/overlapping p_T bins. Horizontal bars show the width of the p_T bin with marker at the centre of the bin. Vertical error bars show the fitting error whereas box shows the systematic uncertainties. The values are compared with results from Pb-Pb collisions at $\sqrt{s_{NN}} = 2.76$ TeV [254] and predictions from theory and model.

from central to peripheral collisions, multiplicity decreases and thus one would generally expect fewer particles being produced and decrease in the content of phase space bins.

To investigate the dependence of M -scaling on centrality, charged particles within the kinematic acceptance of $|\eta| \leq 0.8$ and full azimuth from two p_T bins, $0.4 \leq p_T \leq 0.6$ GeV/ c and $0.4 \leq p_T \leq 1.0$ GeV/ c , are analyzed across centrality bins: 0–5%, 5–10%, 10–20%, 20–40%, and 40–80%. M -scaling (for $q = 2, 3, 4, 5$) behaviour of the charged particle data from these different centrality events is shown in **Figure 4.41** for $0.4 \leq p_T \leq 1.0$ GeV/ c bin. F -scaling is shown in **Figure 4.42**. Power-law behaviour of $F_q(M)$ is observed for all the centrality bins as was observed for default case of 0–5% central events. However, as centrality decreases, the quantitative differences among NFM for various orders of moments (q) increase. Despite these differences, M -scaling with multiple linear regions remain evident across all centralities, accompanied by a similar F -scaling as shown in **Figure 4.42**. For semi-central and peripheral collisions, fluctuations in data points are noted at high values of M^2 for $q = 4, 5$ due to



ALI-PREL-549731

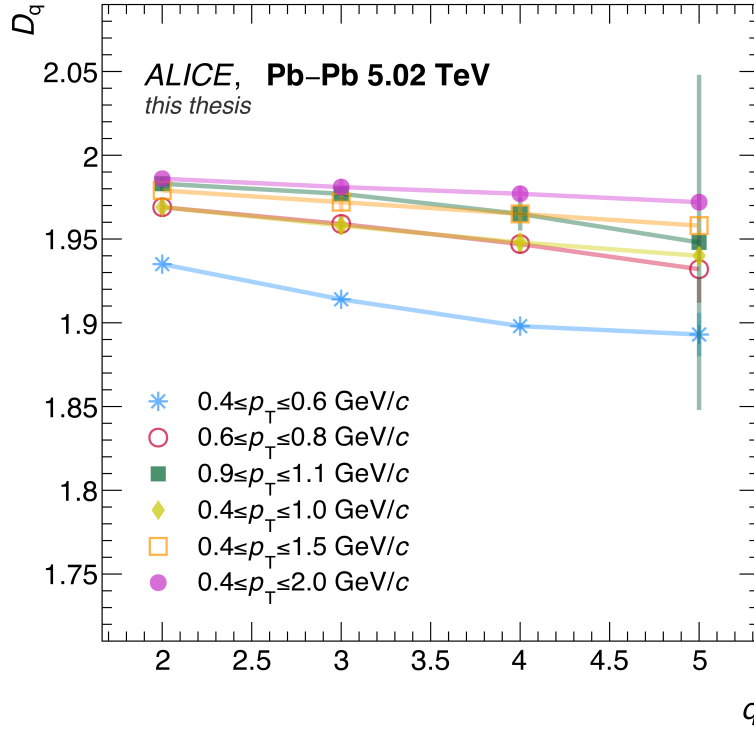
FIGURE 4.39:

ALICE: Scaling exponent (ν) as a function of p_T in the narrow/non-overlapping p_T bins. Horizontal bars show the width of the p_T bin with marker at the centre of the bin. Vertical error bars show the fitting error whereas box shows the systematic uncertainties. The values are compared with Pb-Pb $\sqrt{s_{NN}} = 2.76$ TeV [254] and predictions from theory, model.

lower statistics and reduced event multiplicity. In the higher M^2 regions of the F -scaling plots, line fits are performed to get the slope values β_q ($q = 3, 4, 5$). The scaling exponent, ν different centrality ALICE data were obtained by performing line fits on the plots of $\ln \beta_q$ vs $\ln(q - 1)$. Systematic uncertainties were determined based on variations in the analysis cuts discussed in the Section 4.5.3.2 for $0.4 \leq p_T \leq 0.6$ GeV/c and $0.4 \leq p_T \leq 1.0$ GeV/c p_T bins. The dependence of scaling exponent (ν) on the centrality is shown in Figure 4.43. This figure also includes predicted values from various models and theoretical calculations, facilitating a comprehensive comparison. Notably, it is observed that within the bounds of uncertainties, the scaling exponent (ν) is independent of the centrality in Pb-Pb collisions at $\sqrt{s_{NN}} = 5.02$ TeV.

4.5.3 Estimation of uncertainties

In this section, the methods for estimation of the statistical uncertainties on $F_q(M)$ as used in this work is given. Systematic uncertainty estimation is also given.

**FIGURE 4.40:**

ALICE: D_q as a function of moment order q for various p_T bins. Vertical error bars are the fitting errors.

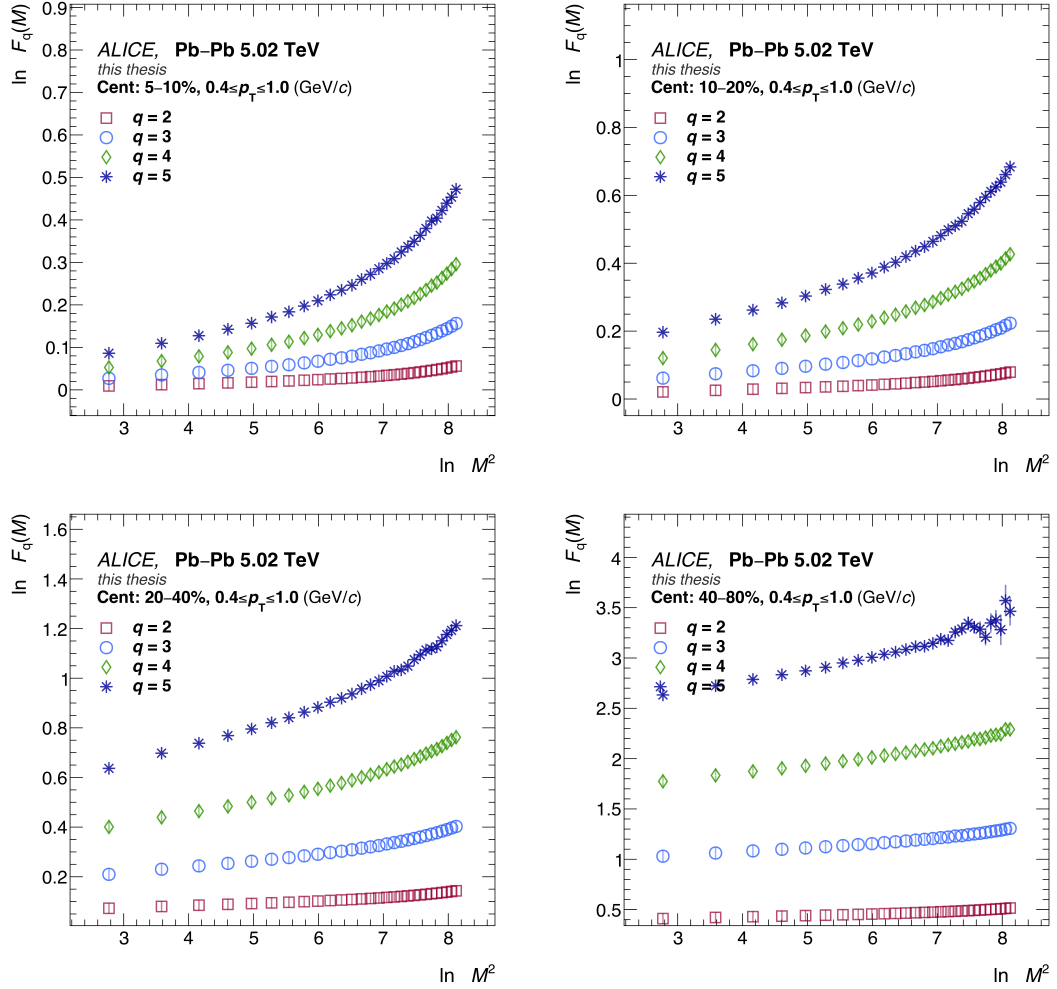
4.5.3.1 Statistical uncertainties

Statistical uncertainties in experimental measurements arise from the inherent randomness of high-energy collisions and fluctuations within the measurement processes. These uncertainties can be quantified using methods such as error propagation and sub-sampling method. In this work, to determine statistical uncertainties on F_q , the sub-sampling method is followed. In the sub-sampling method, the total number of events is divided into equal-sized independent subsamples. The calculations for each subsample yield a standard deviation that defines the statistical uncertainty, represented mathematically as:

$$\sigma_{\langle F_q \rangle} = \sqrt{\frac{1}{N-1} \sum_{i=1}^N (F_q^i - \langle F_q \rangle)^2} \quad 4.1$$

where F_q^i is NFM of the i^{th} subsample. The steps involved in this method are as follows:

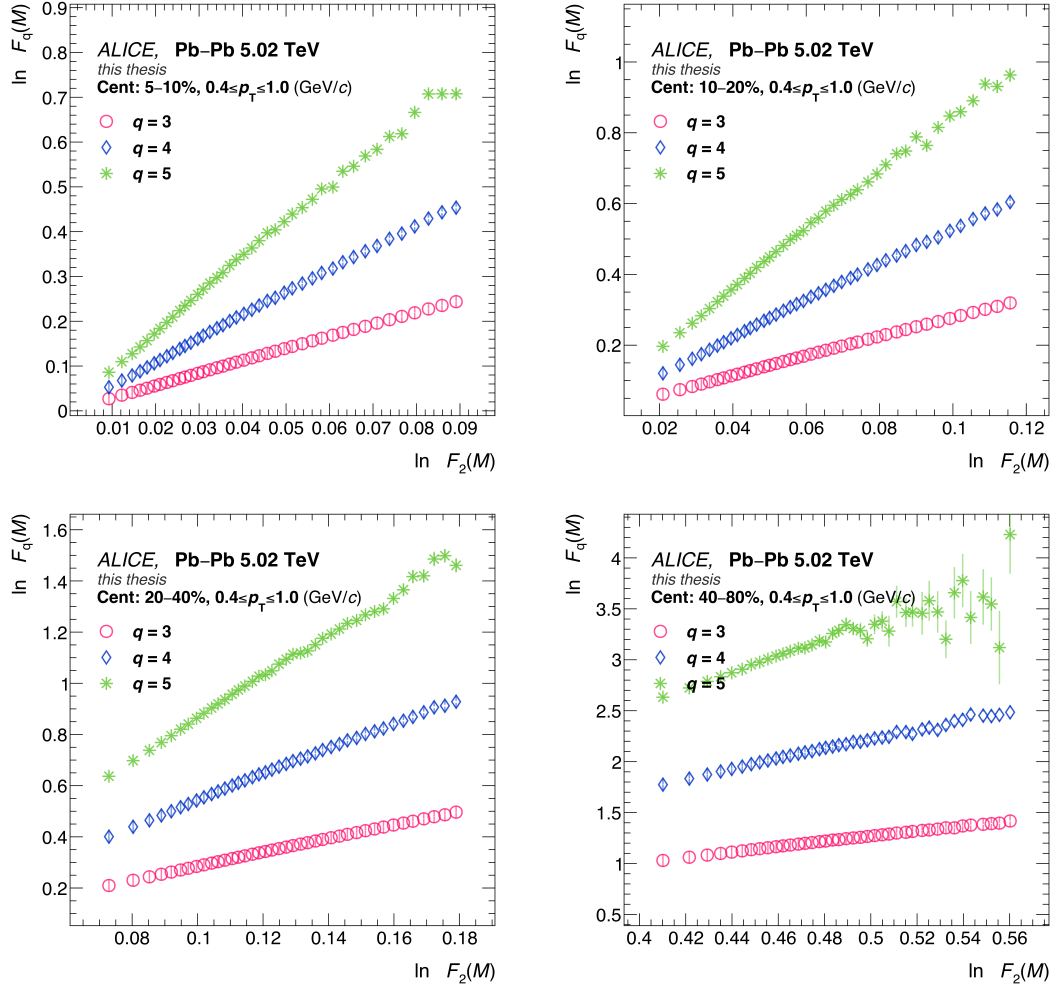
1. Divide the original dataset into N equal-sized, independent subsamples.
2. Compute the observable F_q for each subsample (F_q^i).

**FIGURE 4.41:**

ALICE: $\ln F_q(M)$ vs $\ln M^2$ (M -scaling) for $q = 2, 3, 4, 5$ for the charged particles produced in the mid-rapidity region in $0.4 \leq p_T \leq 1.0$ GeV/ c p_T bin for different centralities.

3. Calculate the mean value $\langle F_q \rangle$ across all subsamples, such as $F_q^1, F_q^2, \dots, F_q^N$.
4. Compute how much each subsample's value deviates from this mean, then square those deviations, and sum them up as defined in [Equation 4.1](#).
5. Finally, divide by $(N - 1)$ and take the square root to obtain the standard deviation, which provides an estimate of the statistical uncertainty on NFM, $F_q(M)$. It is done to remove the bias that arises when estimating a parameter from a sample.

Sub-sampling is very similar to bootstrapping [\[265,266\]](#), except that in bootstrapping, an observation can be selected multiple times within a single bootstrap sample. Unlike error propagation [\[267\]](#), sub-sampling has the advantage of being applicable even at low statistics without introducing bias in results. For the

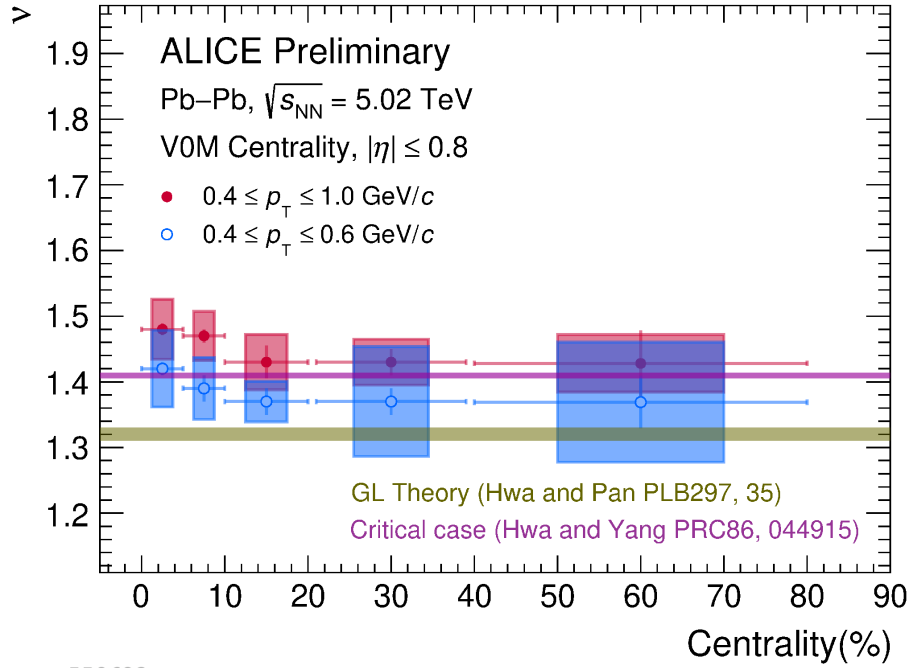
**FIGURE 4.42:**

ALICE: $\ln F_q(M)$ vs $\ln F_2(M)$ (F -scaling) ($q = 3, 4, 5$) for the charged particles produced in the mid-rapidity region in $0.4 \leq p_T \leq 1.0$ GeV/ c p_T bin for different centralities.

observables under study, sub-sampling is found to give same values of statistical uncertainties as that obtained from error propagation methodology.

4.5.3.2 Systematic uncertainties

Systematic uncertainties arise from consistent biases inherent in the experimental setup, analysis methods, or procedures, rather than from random fluctuations that can be mitigated through larger sample sizes. Specifically in high-energy physics, various factors can contribute to systematic uncertainties. For instance, discrepancies in results may stem from variations in track reconstruction, event selection cut such as vertex cut - which focus on the position of the primary interaction point etc. Understanding these variations is vital because they can significantly influence the reliability of the experimental findings.



ALI-PREL-559623

FIGURE 4.43:

ALICE: Dependence of scaling exponent, ν on centrality. Values are compared with theoretical predictions from second-order phase transition formalism in Ginzburg-Landau theory [175] and SCR model [170] with critical fluctuations. Horizontal lines on markers show the width of centrality bin.

To quantify systematic uncertainties, observables are determined by making variations in the default values of various event or track selection. This allows to observe how changes in specific parameters affect the results. Key sources of systematic uncertainties in this analysis include the absolute position of the primary vertex ($|v_z|$), the total number of clusters recorded by the Time Projection Chamber (TPC), the number of crossed rows in the TPC, and variations in the magnetic polarity of the Pb-Pb collisions in Run II operations of LHC. For default analysis, hybrid tracks from ITS and TPC (Table 4.3) are used in this work. The bias may be introduced in the analysis due to tracking scheme, TPC-only tracks are included as a variation. The cuts that have been varied for the estimation of systematic uncertainties over $F_q(M)$ are summarised in Table 4.7. For each systematics source, deviations from default values are calculated. The largest deviation observed due to each parameter is taken as its systematic uncertainty. To calculate an overall systematic uncertainty for an analysis, contributions from different sources are combined using as quadrature formula, expressed mathematically as:

<i>Systematic source</i>	<i>Default value</i>	<i>Variation</i>
<i>vertex position, v_z</i>	< 10 cm	< 7 cm
<i>Min. number per TPC crossed rows</i>	80	100
<i>Min. number per TPC clusters</i>	70	80
<i>Magnetic field polarity</i>	both	positive, negative
<i>Tracks</i>	ITS–TPC tracks <i>Filterbit 768 (Table 4.3)</i>	TPC–only tracks <i>Filterbit 128 (Table 4.8)</i>

TABLE 4.7:

Summary of parameters studied for systematic uncertainty estimations.

$$\sigma_{\text{total}} = \sqrt{\sigma_1^2 + \sigma_2^2 + \dots + \sigma_n^2}. \quad 4.2$$

σ_{total} represents the total systematic uncertainty, while σ_1^2 , σ_2^2 and σ_n^2 are the individual uncertainties from different sources. The approach ultimately contributes to a more accurate understanding of the final results.

The total systematic uncertainty associated with M -scaling ($\ln F_q(M)$ vs $\ln M^2$) and scaling exponent (ν) are obtained from these sources. Relative uncertainties are shown in [Figure 4.44](#) and [Figure 4.45](#) for these observables.

4.6 PYTHIA8/Angantyr event analysis

Collisions of protons and heavy nuclei at experiments, such as at RHIC and LHC enable the study of fundamental interactions under extreme conditions. To model these processes, event generators are used, employing Monte Carlo methods that integrate theoretical models with insights drawn from particle physics experiments [268]. These tools are essential for analysing experimental

<i>Track selection criteria</i>	<i>Values</i>
Min. number of TPC clusters	50
Max. χ^2 per TPC cluster	4
Max. distance to vertex xy, z /cm	2.4, 3.2

TABLE 4.8:

Selection cuts as a standard used for the track selection. These are termed as *Filterbit 128***.

**can be used directly by `AliESDtrackCuts::GetStandardTPCOnlyTrackCuts()` in Ali-ROOT)

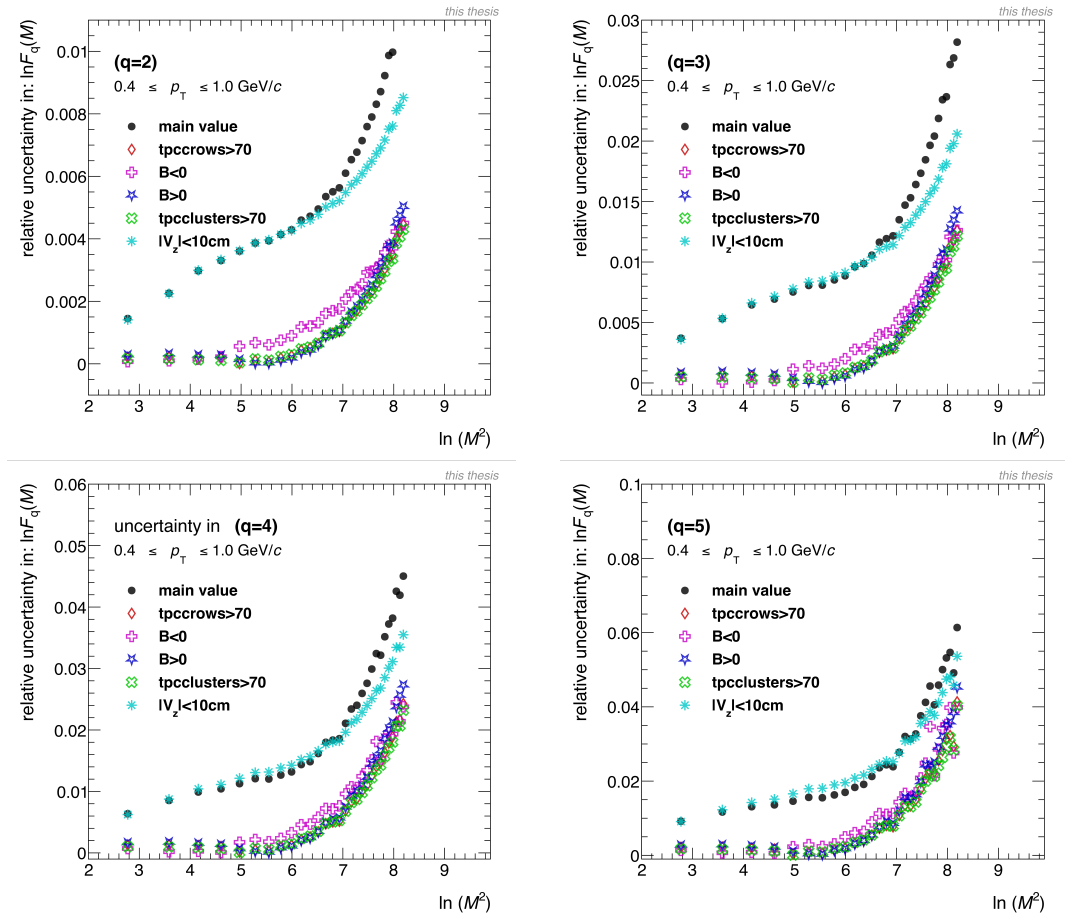


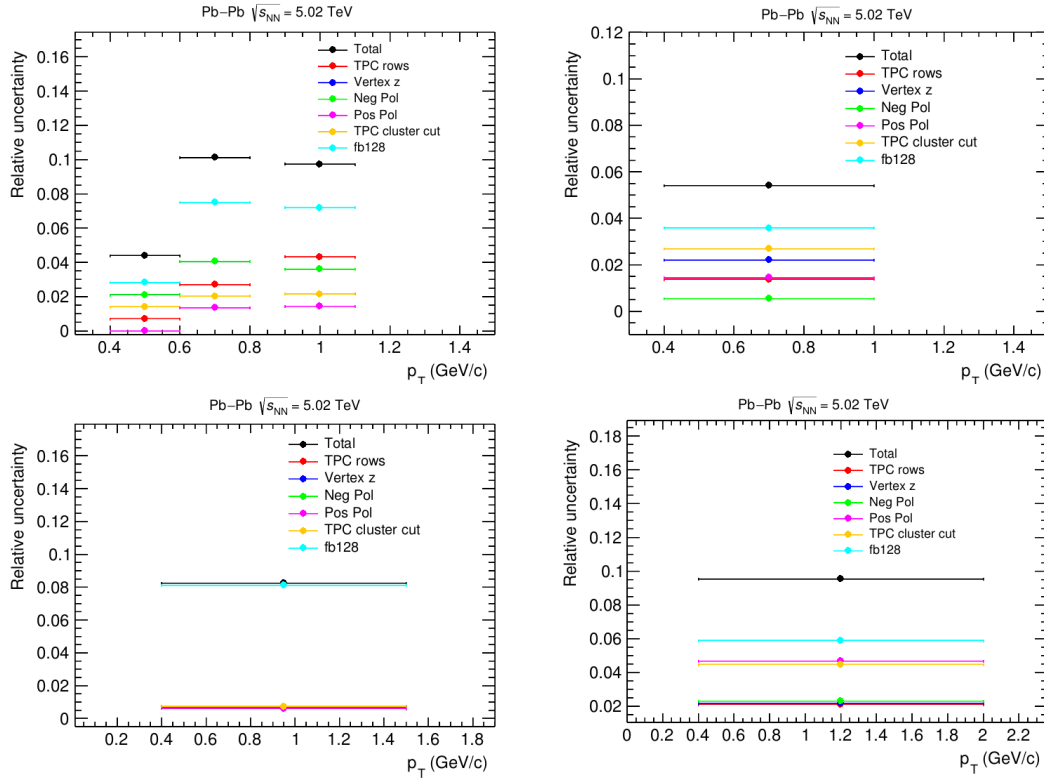
FIGURE 4.44:

ALICE: Relative uncertainties (default value/variation value) from sources mentioned in Table 4.7 in case of M -scaling ($\ln F_q(M)$ vs $\ln M^2$) for $q = 2, 3, 4, 5$.

data, understanding detector efficiencies, distinguishing signal from background events during data analysis, and verifying theoretical predictions. In addition to ALICE data analysis, intermittency analysis was also performed for the Pb–Pb collision PYTHIA8/Angantyr events at $\sqrt{s_{\text{NN}}} = 2.76$ and 5.02 TeV energies as an independent study. [171]. After a brief discussion on the PYTHIA8/Angantyr model, observations and results from this study are presented below.

In the context of proton–proton (p–p) collisions, event generators such as SHERPA [269], Herwig 7 [270], and PYTHIA8 [235] have established themselves as essential tools. Their ability to model a wide array of observables enables detailed investigations into the dynamics and mechanisms of particle collisions. Each model consists of various modules designed to mimic specific physics mechanisms involved in p–p events, including:

- Parton Distribution Functions (PDFs) to describe momentum of the colliding beams,

**FIGURE 4.45:**

ALICE: Relative uncertainties (default value/variation value) from sources mentioned in Table 4.7 for scaling exponent (ν).

- Multi-parton interactions (MPIs) for simultaneous parton collisions,
- Initial and final state radiations,
- Beam remnants,
- Hadronization and unstable hadron decays.

Details on the specific workings of these event generator modules are available in [235,271]. PYTHIA event generator is a phenomenological model for explaining p-p physics. It employs a phenomenological approach, rooted in the concept of colour string evolution and string fragmentation. In a p-p collision, multiple partons are produced which are connected by strings leading to the formation of colour strings. These strings are a consequence of the strong force, which confines quarks and gluons into hadrons. The energy stored in these strings is subsequently released through a process known as string fragmentation. It involves the breaking of the string into smaller segments, each of which eventually materializes into a hadron. The type of hadron produced depends on the energy and momentum carried by the string segment. This process continues until all the energy of the original string is exhausted, resulting in the production of a final state consisting of hadrons. PYTHIA's colour reconnection model modifies

the colour flow and the number of strings to conserve total colour charge while reducing total string length. This adjustment significantly impacts the final-state particle multiplicity and momentum distributions. While colour reconnection has been successful in reproducing certain experimental observations, such as charged particle multiplicity distributions and average transverse momentum distributions, it faces challenges in accurately describing high-multiplicity p–p collisions at the LHC. Enhanced strangeness production, near-side ridge effects, and flow-like behaviour are phenomena observed in high-multiplicity p–p collisions that are not well-described by standard PYTHIA simulations. These effects suggest the presence of collective behaviour, which is traditionally associated with heavy-ion collisions. To address these shortcomings, a modified string tension model has been introduced in PYTHIA. This model alters the strength of the colour force between quarks and gluons in high-multiplicity p–p events, thereby improving description of these emerging results.

The *Angantyr* model, an extension of PYTHIA on proton-nucleus (pA) interactions, aims to explore high-energy heavy-ion (HI) collision dynamics without assuming the formation of a thermalized QGP. This model enhances the framework for sub-collisions specifically, collisions between nucleons within pA and AA collisions. In p–Pb collisions, the proton interacts multiple times with nucleons from the lead nucleus, leading to a distinctly asymmetric pseudorapidity multiplicity distribution. This asymmetry suggests that simply superimposing independent proton-proton (p–p) collisions cannot adequately describe the resulting heavy-ion event. Instead, generating a HI event from multiple *pp* events necessitates a sophisticated superposition of several *pp*-like collisions. Glauber model, traditionally used to calculate “participants” or “wounded nucleons,” forms the basis of these simulations, with modern Monte Carlo methods accounting for position and scattering fluctuations that earlier models overlooked. Monte Carlo simulations now incorporate these fluctuations in nucleon positions within a nucleus. Additionally, Gribov [264] emphasized the importance of considering diffractively excited nucleons as significant contributors to sub-collisions. The *Angantyr* model builds upon this by applying the Good-Walker formalism [272], effectively modeling diffraction effects that emerge from fluctuations in the wave functions of the projectile and target nucleons. A critical aspect of accurately simulating HI events is distinguishing between different collision types when calculating binary collisions. This differentiation is necessary because various collision types yield distinct multiplicity distributions across different pseudorapidity ranges. To enhance this classification, the *Angantyr* model modifies the old FRITIOF model [273] to distinguish between wounded nucleons that are dif-

fractive and non-diffractive [274]. This refinement improves the categorization of wounded nucleons in various collision types, including inelastic and diffractive collisions.

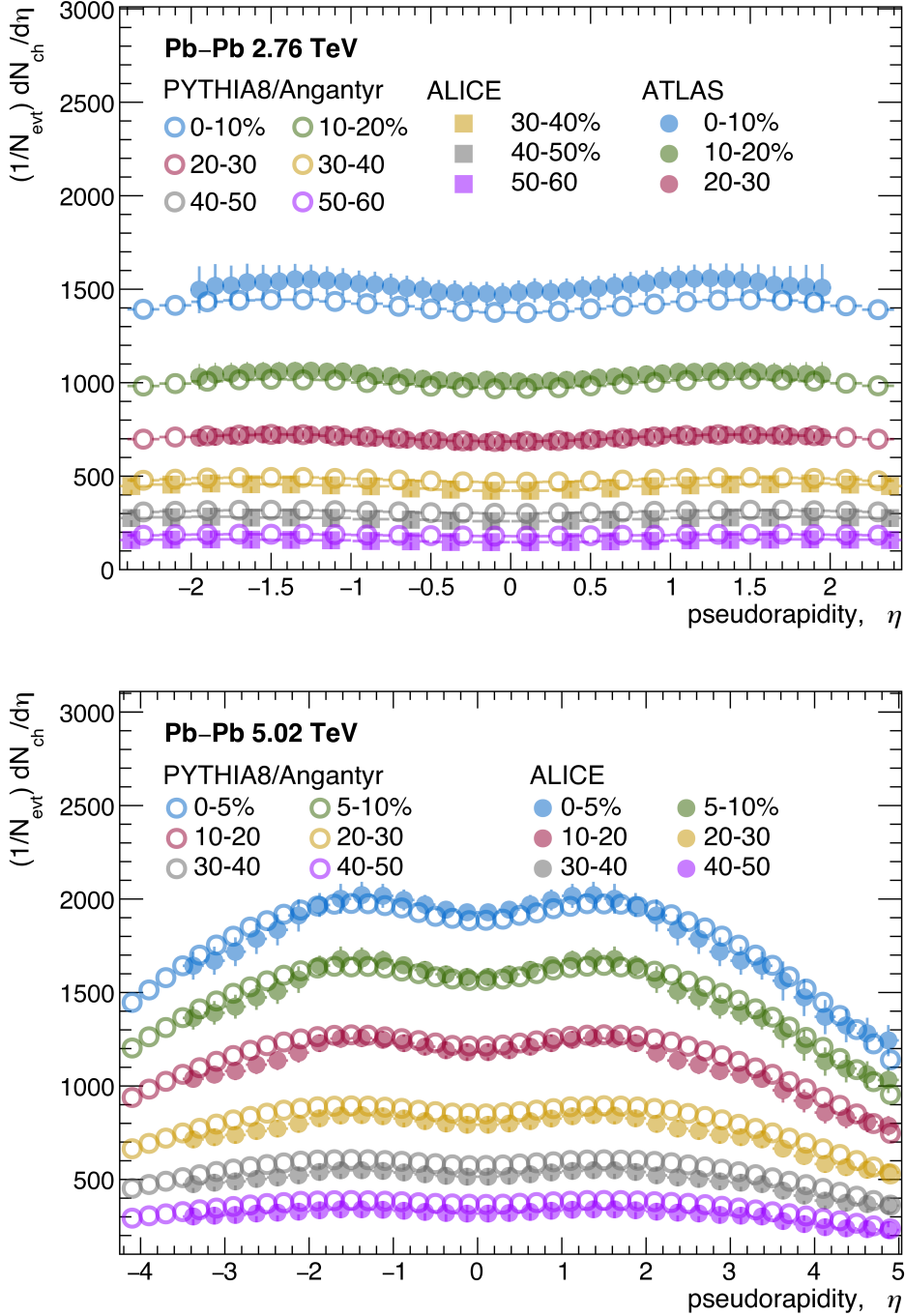


FIGURE 4.46:

PYTHIA8/Angantyr: Distributions showing comparison of the charged particle pseudorapidity for different centralities from Pb-Pb collisions using PYTHIA8/Angantyr that is shown along with same distribution from ATLAS [275], ALICE [276] at $\sqrt{s_{\text{NN}}} = 2.76$ TeV (top) and ALICE [277] at $\sqrt{s_{\text{NN}}} = 5.02$ TeV (bottom).

A comparison between Angantyr and other mostly used heavy-ion models can help better understand Angantyr model. The models HIJING [246], AMPT [278], and EPOS [248] play an important role to understand heavy-ion (HI) collisions, but they differ significantly in their approaches and underlying physics.

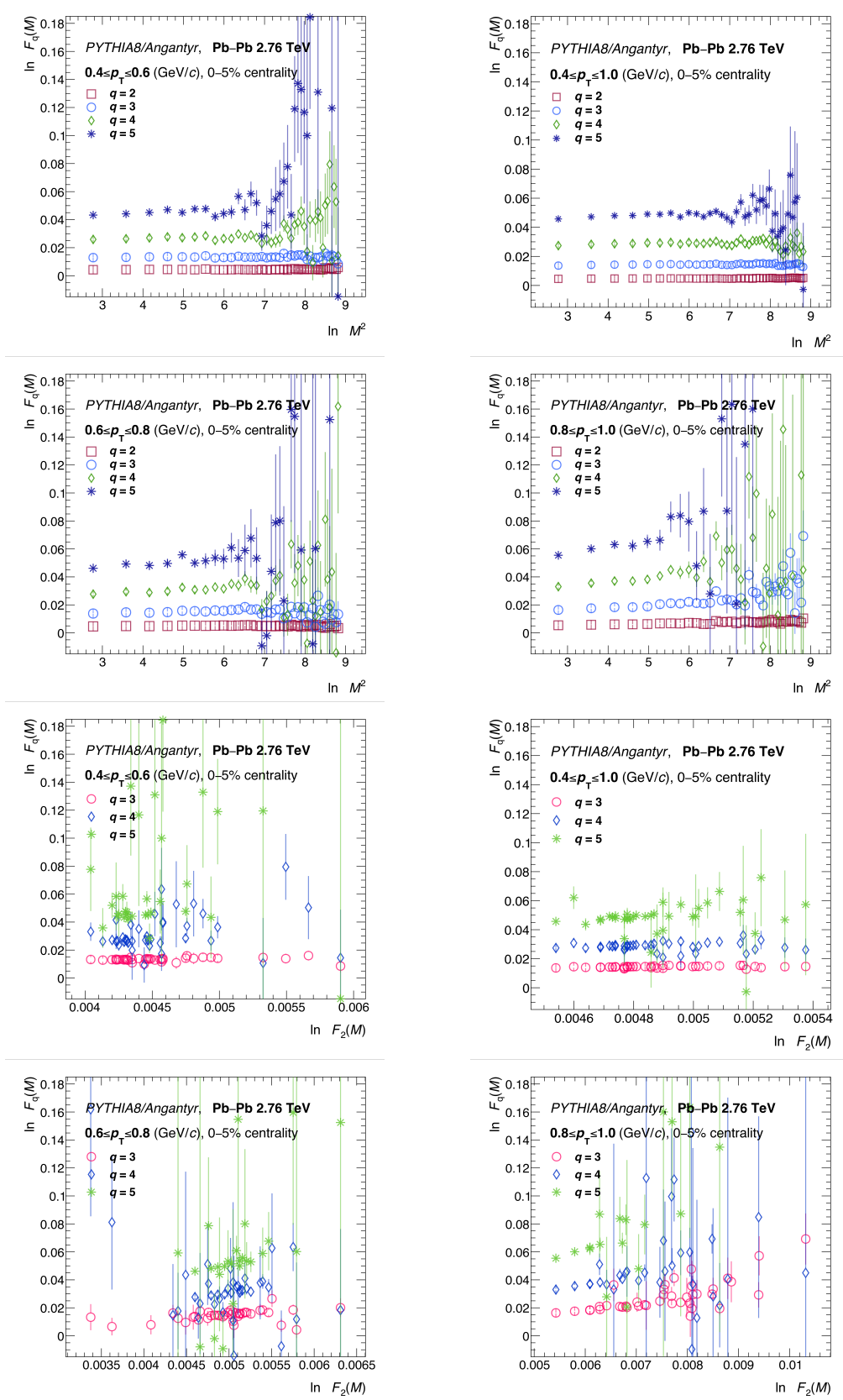
- HIJING [246], consists of two primary components: mini-jets and soft interactions. The model classifies parton interactions as either semi-hard, involving jet pairs with transverse momentum above a predefined threshold, or soft, where non-perturbative methods are applied with a defined soft parton cross-section. PYTHIA is employed to manage the kinematics of jet pairs, including radiation effects and the Lund string model for parton hadronization. Additionally, HIJING incorporates an impact parameter-dependent parton distribution to study nuclear shadowing. However, it does not distinguish between shadowing effects due to gluons and quarks. The model also addresses jet quenching for moderate and high transverse momentum observables, based on a fixed energy loss mechanism per unit length as particles traverse the medium.
- The AMPT model [278], which stands for *A Multi-Phase Transport* model, plays a significant role in exploring the flow dynamics of heavy-ion collisions at RHIC and LHC energies. The model comprises four core modules: (i) initial states, detailing the system's configuration post-collision; (ii) parton cascade, simulating the scattering and dynamics of partons; (iii) hadronisation, describing the conversion of partons to hadrons; and (iv) hadron cascade, which examines the interactions among hadrons before the system freezes out. AMPT operates in the default mode and the string melting mode. The latter assumes the formation of a quark-gluon plasma (QGP), providing the input for subsequent stages of the simulation. Parton scatterings are executed according to the Zhang Parton Cascade (ZPC) model [279], which models the dynamics of partonic collisions. Hadronisation is achieved through either the Lund string fragmentation model in the default mode, or the quark coalescence model in the string melting mode, which allows consistent recombination of quarks and anti-quarks into hadrons [280].
- EPOS [248] is another significant event generator already detailed in Section 4.5.2.5 that operates on a semi-hydrodynamic basis. It separates hydrodynamic interactions into core and corona regions based on string density [263]. The core represents areas with high string density where multiple parton interactions occur, while the corona has lower density where such interactions are suppressed. EPOS treats scatterings according to Gribov-Regge theory [264] and generates multiple parton ladders representing the initial development of partons from colliding nucleons. The model employs a

statistical hadronisation approach in the core, whereas in the corona, hadronisation resembles PYTHIA's string fragmentation method. Unlike HIJING and AMPT, which are limited to heavy-ion collision scenarios, EPOS supports the simulation of both proton–proton and heavy-ion events.

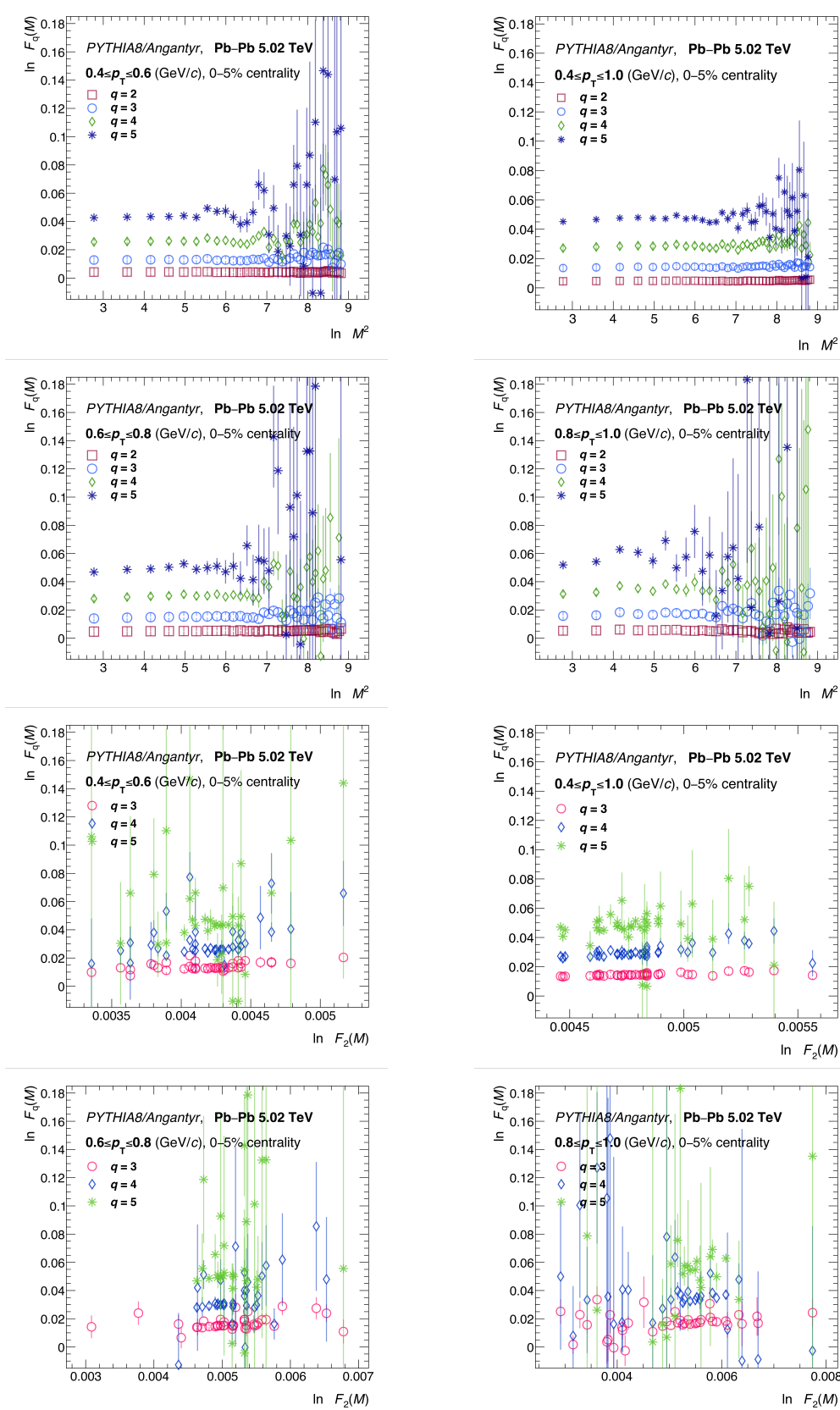
Using the PYTHIA8/Angantyr event generator, 2 million events were produced for Pb–Pb collisions at $\sqrt{s_{\text{NN}}} = 2.76$ TeV and $\sim 1\text{M}$ events at $\sqrt{s_{\text{NN}}} = 5.02$ TeV. NFM, $F_q(M)$ are calculated for the charged particles produced within the midrapidity ($|\eta| \leq 0.8$) and full azimuth for centrality ranges of 0–5%, 5–10%, 10–20%, 20–30%. Angantyr can calculate impact parameter, but in this version, it has a fudge factor associated with it. The calculation of centrality percentiles was done using sum of transverse energy, $\sum E_t$ of events, as mentioned in [235]. The pseudorapidity distributions of charged particles from the Angantyr generated events used in the analysis are studied against ALICE experimental data as shown in **Figure 4.46**. A good agreement between Angantyr and ALICE data is seen at both the energies except at the midrapidity for $\sqrt{s_{\text{NN}}} = 2.76$ TeV data. But this is similar to what has been reported and explained in [235].

Normalized factorial moments, $F_q(M)$ are calculated for $q = 2, 3, 4, 5$. Behaviour of $F_q(M)$ with increasing number of bins or decreasing size of (η, φ) phase space bins for 0–5% central events is shown in **Figure 4.47** and **Figure 4.48** for Pb–Pb at $\sqrt{s_{\text{NN}}} = 2.76$ TeV and 5.02 TeV respectively. **Figure 4.47** and **Figure 4.48** show dependence of $F_q(M)$'s ($q = 3, 4, 5$) on second-order NFM, $F_2(M)$ (F -scaling). It is observed that $F_q(M)$'s are independent of M^2 , showing the absence of M -scaling. Nonetheless, a weak dependence of $F_q(M)$ on $F_2(M)$ is observed, allowing for the calculation of scaling exponent (ν). ν is thus calculated by the linear fits to $\ln \beta_q$ vs $\ln(q - 1)$ plots, where β_q is in turn calculated from fits on F -scaling plots. The scaling exponent values obtained for various p_T bins range from 1.65 – 1.9, and are way greater than the value of 1.304 predicted for second order phase transition formalism using Ginzburg-Landau theory [175]. ν is also greater than the value predicted by SCR model [170]. The ν values as a function of p_T are shown in **Figure 4.49** and are also compared with ALICE data for Pb–Pb collisions at $\sqrt{s_{\text{NN}}} = 2.76$ TeV [254], 5.02 TeV (this work).

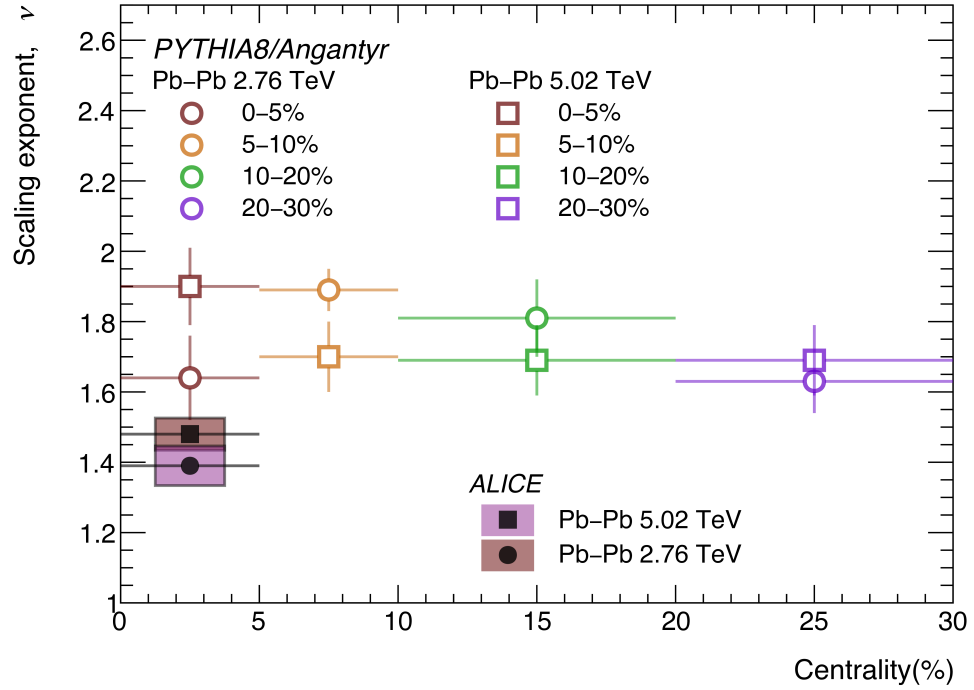
Event generator models, including HIJING, EPOS, and the Angantyr model, fail in describing the observed data from the heavy-ion collisions. Despite their sophisticated frameworks and attempts to simulate complex dynamics, these models are unable to explain when it comes to explaining the power-law behaviour exhibited by normalized factorial moments in ALICE data. The power-law


FIGURE 4.47:

PYTHIA8/Angantyr: $\ln F_q(M)$ vs $\ln M^2$ (M -scaling) and $\ln F_q(M)$ vs $\ln F_2(M)$ (F -scaling) for charged particles generated in the mid-rapidity region in $0.4 \leq p_T \leq 1.0$, $0.4 \leq p_T \leq 0.6$, $0.6 \leq p_T \leq 0.8$, $0.8 \leq p_T \leq 1.0$ GeV/c bins for 0–5% centrality of Pb–Pb collisions at 2.76 TeV.

**FIGURE 4.48:**

PYTHIA8/Angantyr: $\ln F_q(M)$ vs $\ln M^2$ (M -scaling) and $\ln F_q(M)$ vs $\ln F_2(M)$ (F -scaling) for charged particles generated in the mid-rapidity region in $0.4 \leq p_T \leq 1.0$, $0.4 \leq p_T \leq 0.6$, $0.6 \leq p_T \leq 0.8$, $0.8 \leq p_T \leq 1.0$ GeV/c bins for 0–5% centrality of Pb–Pb collisions at 5.02 TeV.

**FIGURE 4.49:**

PYTHIA8/Angantyr: Centrality dependence of scaling exponent, ν for different centralities in Pb-Pb collisions at $\sqrt{s_{\text{NN}}} = 2.76, 5.02$ TeV. ν value for ALICE experimental data at 2.76 TeV [255] and 5.02 TeV [281] (this work) is also shown for comparison.

scaling observed for normalized factorial moments suggests a level of complexity and correlation in particle production that these models struggle to capture. This discrepancy indicates that the underlying physics governing particle interactions in high-energy collisions may involve additional factors or mechanisms not fully accounted for by these models. The inability to reproduce these scaling behaviours of high resolution phase space and hence spatial configurations of the charged particle production points to potential gaps in our understanding of the dynamics at play during heavy-ion collisions, particularly regarding initial state fluctuations and non-flow contributions. By addressing these questions theoretically, one can enhance the understanding of the fundamental processes driving particle production mechanisms and ultimately to improve our ability to interpret experimental results.

SUMMARY AND CONCLUSIONS

During ultra-relativistic heavy-ion collisions at extreme energy densities, a primordial state of matter known as quark-gluon plasma (QGP) is created. These collisions provide unique opportunity to explore properties and dynamics of QGP, including study of transition of the system from deconfined QGP phase to hadronic phase and vice versa. When quarks and gluons are confined within hadrons, they exhibit a phenomenon known as chiral symmetry breaking, leading to a non-zero expectation value in vacuum for the chiral condensate. This condensate is indicative of the mass generation for quarks and is essential in characterizing the state of the matter at different energy densities. Near Quantum Chromodynamic (QCD) critical point, fluctuations in this condensate can become significant, resulting in the formation of clusters of all sizes to emerge and thus, exhibit universal characteristic of scale invariance. This in a way reflects the underlying dynamics of the phase transition from QGP to hadronic matter.

The work presented in this thesis investigates the characteristics of the system in strongly interacting hadronic matter created during heavy-ion collisions at the Large Hadron Collider (LHC) at Geneva. The primary focus is to study multiplicity fluctuations, which refer to the variations in the number of particles produced during these collisions, using intermittency methodology. Studying simulated Monte Carlo events generated for Pb–Pb collisions at LHC energies using HIJING and EPOS–LHC, insights into the baseline behaviour of the two-dimensional (η, φ) intermittency are obtained. Investigations are then carried for the charged particle experimental data from Pb–Pb collisions at $\sqrt{s_{\text{NN}}} = 5.02$ TeV. Charged particle tracks are mostly pions (π^\pm), protons (p), antiprotons (\bar{p}) and

kaons (K^\pm), detected by the ITS (Inner Tracking System) and the TPC (Time Projection Chamber) detectors of the ALICE experiment at CERN, LHC. Normalized factorial moments ($F_q(M)$) of the multiplicity distributions of these charged particles in (η, φ) phase space, which is partitioned in M bins along each dimension, are calculated where $|n| \leq 0.8$ and $0 \leq \varphi \leq 2\pi$. Most-central (0–5%) events which have high particle number density per bin are analysed. Scaling behaviour of the $F_q(M)$ for $q = 2, 3, 4, 5$ is studied for its dependence on the number of bins (M^2), known as M -scaling ($\ln F_q(M)$ vs $\ln M^2$) and as a function of second order normalized factorial moments ($F_2(M)$), known as F -scaling ($\ln F_q(M)$ vs $\ln F_2(M)$) across various transverse momentum ranges with $p_T \leq 2.0$ GeV/ c . For data, a power-law growth of $\ln F_q(M)$ with $\ln M^2$ (M -scaling) for all q 's reveals the presence of non-Poissonian dynamic fluctuations in the Pb–Pb collisions at $\sqrt{s_{NN}} = 5.02$ TeV, albeit lower in magnitude to what is observed at $\sqrt{s_{NN}} = 2.76$ TeV. Observation of this behaviour indicates the presence of intermittency and scale invariant fluctuations in the charged particle number density distributions of the data. Thus, data shows presence of self-similar fluctuations. However, this behaviour is inconsistent with the M -scaling behaviour seen in the event generators, viz. HIJING and EPOS–LHC, both of which have different physics. While EPOS–LHC emphasises collective effects and hadronization processes, HIJING focuses more on the hard scattering processes and the subsequent fragmentation of partons into hadrons. These models struggle to reproduce the scaling behaviours at high resolution which is observed in the experimental data and thus are inadequate to capture the underlying physics governing these fluctuations or their correlations. This calls for further refinement or alternative approaches to model the complex interactions in the system produced in heavy-ion collisions.

Normalized factorial moments (NFM) for $q \geq 3$, as a function of $F_2(M)$ are studied for data in various p_T intervals ($p_T \leq 2$ GeV/ c). This behaviour called F -scaling for the charged particles is observed in data. A scaling exponent (ν), which is dimensionless quantity, and independent of considering details of critical parameters of the system, is determined. The value of ν for the 0–5% central events in $0.4 \leq p_T \leq 1.0$ GeV/ c bin is obtained as 1.44 ± 0.02 . The scaling exponent for all p_T intervals studied here have value close to the prediction ($\nu = 1.41$) from Successive Contraction and Randomization (SCR) model but larger than that obtained for $\sqrt{s_{NN}} = 2.76$ TeV Pb–Pb data. These results show that in the soft p_T region, the charged particle density fluctuations are of similar quantitative nature and the SCR model seems to mimic dynamics of the data. A

study of dependence of ν on p_T , p_T bin width and centrality shows that ν is independent of p_T bin width with a weak dependence on the centrality of the collisions.

In addition to above, the M -scaling behaviour observed for $F_q(M)$ has been interpreted using fractal dimensions. Investigations into fractal parameters provide valuable insights into the structure of self-similar multiparticle system in the heavy-ion collisions. Analysis of ALICE data reveals that the generalized fractal dimension D_q has weak dependence on the order of the moments (q). D_q decreases as q increases, indicating multifractal nature and complex mechanism within the particle production processes. Again, failure of models to reproduce experimental results suggests additional investigations to explore how these patterns evolve with energy and collision conditions. In light of this, updates in the models can also be taken up.

An independent study of event samples from PYTHIA8/Angantyr model for Pb–Pb collisions at $\sqrt{s_{NN}} = 2.76$ and 5.02 TeV has been performed. The Angantyr model is an extension of PYTHIA on proton-nucleus (pA) interactions, aimed to explore high-energy heavy-ion collision dynamics without assuming the formation of a thermalized QGP. The intermittency observables are calculated for event samples generated within $|\eta| \leq 0.8$ for 0–5%, 5–10%, 10–20%, 20–30% centralities and many different p_T bins. No indication of the scaling behaviour of NFM with phase space bin resolution is observed for any of these centralities. The results from Angantyr are in line with the HIJING and the EPOS–LHC results.

In crux, intermittency analysis of heavy-ion collision data from CERN based ALICE experiment is performed with aim to learn about properties of matter created and the order of its transition to the hadronic phase. Charged particle data from ALICE at $\sqrt{s_{NN}} = 5.02$ TeV, for the selected tracks shows *intermittency* and hence the presence of *scale invariant dynamical fluctuations*. Multiple linear regions in M -scaling ($\ln F_q(M)$ vs $\ln M^2$) are obtained with a smooth power-law rise of $F_q(M)$ with increasing number of bins. Results show that the system formed at LHC has self-similar multiplicity fluctuations and a weak multifractal nature. A robust F -scaling is seen in all p_T bins in the soft p_T region with scaling exponent (ν) obtained as 1.44 ± 0.02 , close to the value predicted by SCR model. Scaling exponent has weak dependence on centrality. Findings of this work challenge current models like HIJING and EPOS-LHC, as neither fully captures the experimentally observed scaling behaviours and scaling exponent value. However, systematic and statistical uncertainties on ν demand further investigations with more statistics and improved track selection procedures.

Further studies at higher energies would be particularly intriguing, with possibility of calculations at higher orders of the moment and with better precision which will give more clear picture on the dynamics of the matter at extreme energies and temperature. Intermittency analysis, though complex and demands high resolution, emphasises the need for refined models in heavy-ion physics to comprehend the real and exact nature of the system formed in the heavy-ion collision at ultra-relativistic energies. This work is a step towards adding to that knowledge.

BIBLIOGRAPHY

- [1] N. Bohr, *On the Constitution of Atoms and Molecules*, Phil. Mag. Ser. 6 **26**, 1 (1913). [10.1080/14786441308634955](https://doi.org/10.1080/14786441308634955)
- [2] S. Kakani and S. Kakani, editors, *Nuclear and Particle Physics* (Viva Books Originals, 2013).
- [3] M. Gell-Mann, *The Eightfold Way: A Theory of strong interaction symmetry*, (1961). [10.2172/4008239](https://doi.org/10.2172/4008239)
- [4] J. I. Friedman and H. W. Kendall, *Deep inelastic electron scattering*, Ann. Rev. Nucl. Part. Sci. **22**, 203 (1972). [10.1146/annurev.ns.22.120172.001223](https://doi.org/10.1146/annurev.ns.22.120172.001223)
- [5] D. P. Barber and others, *Discovery of Three Jet Events and a Test of Quantum Chromodynamics at PETRA Energies*, Phys. Rev. Lett. **43**, 830 (1979). [10.1103/PhysRevLett.43.830](https://doi.org/10.1103/PhysRevLett.43.830)
- [6] L. Evans and P. Bryant, editors, *LHC Machine*, JINST **3**, S8001 (2008). [10.1088/1748-0221/3/08/S08001](https://doi.org/10.1088/1748-0221/3/08/S08001)
- [7] E. V. Shuryak, *Quark-Gluon Plasma and Hadronic Production of Leptons, Photons and Psions*, Phys. Lett. B **78**, 150 (1978). [10.1016/0370-2693\(78\)90370-2](https://doi.org/10.1016/0370-2693(78)90370-2)
- [8] T. Niida and Y. Miake, *Signatures of QGP at RHIC and the LHC*, AAPPS Bull. **31**, 12 (2021). [10.1007/s43673-021-00014-3](https://doi.org/10.1007/s43673-021-00014-3)
- [9] S. S. Adler and others, *J/ψ production in Au Au collisions at $s(NN)^{1/2} = 200\text{-GeV}$ at the Relativistic Heavy Ion Collider*, Phys. Rev. C **69**, 14901 (2004). [10.1103/PhysRevC.69.014901](https://doi.org/10.1103/PhysRevC.69.014901)
- [10] I. C. Arsene, *J/ψ Production in Pb–Pb collisions at $\sqrt{s_{NN}} = 2.76\text{ TeV}$* , J. Phys. Conf. Ser. **426**, 12023 (2013). [10.1088/1742-6596/426/1/012023](https://doi.org/10.1088/1742-6596/426/1/012023)
- [11] The ALICE Collaboration, *ALICE Website*, (2024). Available at: <https://alice.cern/experiment> [Accessed December 24, 2024.]

BIBLIOGRAPHY

- [12] J. C. Collins and M. J. Perry, *Superdense Matter: Neutrons Or Asymptotically Free Quarks?*, Phys. Rev. Lett. **34**, 1353 (1975). [10.1103/PhysRevLett.34.1353](#)
- [13] S. Navas and others, *Review of particle physics*, Phys. Rev. D **110**, 30001 (2024). [10.1103/PhysRevD.110.030001](#)
- [14] J. Bartke, *Introduction to relativistic heavy ion physics* (World Scientific, 2009).
- [15] S. K. Choi and others, *Observation of a narrow charmonium-like state in exclusive $B^\pm \rightarrow K^\pm \pi^+ \pi^- J/\psi$ decays*, Phys. Rev. Lett. **91**, 262001 (2003). [10.1103/PhysRevLett.91.262001](#)
- [16] R. Aaij and others, *Observation of $J/\psi p$ Resonances Consistent with Pentaquark States in Λ_b^0 to $J/\psi K^- p$ Decays*, Phys. Rev. Lett. **115**, 72001 (2015). [10.1103/PhysRevLett.115.072001](#)
- [17] E. Stefanovich, editor, *Quantum Electrodynamics* (De Gruyter, 2018).
- [18] K. G. Wilson, *Confinement of Quarks*, Phys. Rev. D **10**, 2445 (1974). [10.1103/PhysRevD.10.2445](#)
- [19] D. J. Gross, *Asymptotic freedom and the emergence of QCD*, in *3rd International Symposium on the History of Particle Physics: The Rise of the Standard Model* (1992)., pp. 199–232.
- [20] D. J. Gross and F. Wilczek, *Ultraviolet Behavior of Nonabelian Gauge Theories*, Phys. Rev. Lett. **30**, 1343 (1973). [10.1103/PhysRevLett.30.1343](#)
- [21] S. Weinberg, *The First Three Minutes. A Modern View of the Origin of the Universe* (1977).
- [22] H. Meyer-Ortmanns and T. Reisz, *Principles of phase structures in particle physics* (World Scientific (Singapore), 2007).
- [23] B. Sinha, *The Mini Bang and the Big Bang: From Collider to Cosmology*, in *Exciting Interdisciplinary Physics: Quarks and Gluons / Atomic Nuclei / Relativity and Cosmology / Biological Systems*, edited by W. Greiner (Springer International Publishing, 2013)., pp. 261–273.
- [24] R. Pasechnik and M. Šumbera, *Phenomenological Review on Quark–Gluon Plasma: Concepts vs Observations*, Universe **3**, 7 (2017). [10.3390/universe3010007](#)
- [25] V. A. Rubakov and D. S. Gorbunov, *Introduction to the Theory of the Early Universe: Hot big bang theory* (World Scientific, Singapore, 2017).

- [26] K.-J. Sun, R. Wang, C. M. Ko, Y.-G. Ma, and C. Shen, *Unveiling the dynamics of little-bang nucleosynthesis*, Nature Commun. **15**, 1074 (2024). [10.1038/s41467-024-45474-x](https://doi.org/10.1038/s41467-024-45474-x)
- [27] J. Rafelski, J. Birrell, C. Grayson, A. Steinmetz, and C. T. Yang, *Quarks to Cosmos: Particles and Plasma in Cosmological evolution*, (2024).
- [28] CERN, *New State of Matter Created at CERN*
- [29] I. Arsene and others, *Quark gluon plasma and color glass condensate at RHIC? The Perspective from the BRAHMS experiment*, Nucl. Phys. A **757**, 1 (2005). [10.1016/j.nuclphysa.2005.02.130](https://doi.org/10.1016/j.nuclphysa.2005.02.130)
- [30] K. Adcox and others, *Formation of dense partonic matter in relativistic nucleus-nucleus collisions at RHIC: Experimental evaluation by the PHENIX collaboration*, Nucl. Phys. A **757**, 184 (2005). [10.1016/j.nuclphysa.2005.03.086](https://doi.org/10.1016/j.nuclphysa.2005.03.086)
- [31] B. B. Back and others, *The PHOBOS perspective on discoveries at RHIC*, Nucl. Phys. A **757**, 28 (2005). [10.1016/j.nuclphysa.2005.03.084](https://doi.org/10.1016/j.nuclphysa.2005.03.084)
- [32] J. Adams and others, *Experimental and theoretical challenges in the search for the quark gluon plasma: The STAR Collaboration's critical assessment of the evidence from RHIC collisions*, Nucl. Phys. A **757**, 102 (2005). [10.1016/j.nuclphysa.2005.03.085](https://doi.org/10.1016/j.nuclphysa.2005.03.085)
- [33] J. W. Harris and B. Müller, *QGP Signatures Revisited*, (2023).
- [34] H. Satz, *The Quark-Gluon Plasma: A Short Introduction*, Nucl. Phys. A **4** (2011). [10.1016/j.nuclphysa.2011.05.014](https://doi.org/10.1016/j.nuclphysa.2011.05.014)
- [35] S. Sarkar, H. Satz, and B. Sinha, *The Physics of the Quark-Gluon Plasma* (2009).
- [36] W. Busza, K. Rajagopal, and W. van der Schee, *Heavy Ion Collisions: The Big Picture, and the Big Questions*, Ann. Rev. Nucl. Part. Sci. **68**, 339 (2018). [10.1146/annurev-nucl-101917-020852](https://doi.org/10.1146/annurev-nucl-101917-020852)
- [37] M. Kliemant, R. Sahoo, T. Schuster, and R. Stock, *Global Properties of Nucleus–Nucleus Collisions*, in *The Physics of the Quark-Gluon Plasma: Introductory Lectures*, edited by S. Sarkar, H. Satz, and B. Sinha (Springer Berlin Heidelberg, 2010)., pp. 23–103.
- [38] W. Florkowski, *Phenomenology of Ultra-Relativistic Heavy-Ion Collisions* (2010).
- [39] H. Satz, *The Thermodynamics of Quarks and Gluons*, Lect. Notes Phys. **785**, 1 (2010). [10.1007/978-3-642-02286-9_1](https://doi.org/10.1007/978-3-642-02286-9_1)

BIBLIOGRAPHY

- [40] S. Borsanyi and others, *Calculation of the axion mass based on high-temperature lattice quantum chromodynamics*, Nature **539**, 69 (2016). [10.1038/nature20115](https://doi.org/10.1038/nature20115)
- [41] F. Gelis, E. Iancu, J. Jalilian-Marian, and R. Venugopalan, *The Color Glass Condensate*, Ann. Rev. Nucl. Part. Sci. **60**, 463 (2010). [10.1146/annurev.nucl.010909.083629](https://doi.org/10.1146/annurev.nucl.010909.083629)
- [42] F. Gelis, *Some Aspects of the Theory of Heavy Ion Collisions*, Rept. Prog. Phys. **84**, 56301 (2021). [10.1088/1361-6633/abec2e](https://doi.org/10.1088/1361-6633/abec2e)
- [43] U. Heinz and R. Snellings, *Collective flow and viscosity in relativistic heavy-ion collisions*, Ann. Rev. Nucl. Part. Sci. **63**, 123 (2013). [10.1146/annurev-nucl-102212-170540](https://doi.org/10.1146/annurev-nucl-102212-170540)
- [44] Y. Akiba and others, *The Hot QCD White Paper: Exploring the Phases of QCD at RHIC and the LHC*, (2015).
- [45] B. Muller, *From Quark-Gluon Plasma to the Perfect Liquid*, Acta Phys. Polon. B **38**, 3705 (2007).
- [46] M. Gyulassy and L. McLerran, *New forms of QCD matter discovered at RHIC*, Nucl. Phys. A **750**, 30 (2005). [10.1016/j.nuclphysa.2004.10.034](https://doi.org/10.1016/j.nuclphysa.2004.10.034)
- [47] X. C. Vidal and R. C. Manzano, *Physics at LHC*, (2024). Available at: https://www.lhc-closer.es/taking_a_closer_look_at_lhc/1.physics_at_lhc [Accessed December 24, 2024.]
- [48] D. H. Perkins, *Introduction to High Energy Physics*, 4th ed. (Cambridge University Press, 2000).
- [49] J. Rafelski and B. Muller, *Strangeness Production in the Quark - Gluon Plasma*, Phys. Rev. Lett. **48**, 1066 (1982). [10.1103/PhysRevLett.48.1066](https://doi.org/10.1103/PhysRevLett.48.1066)
- [50] R. Stock, J. Baechler, J. Bartke, H. Bialkowska, R. Bock, R. Brockmann, P. Buncic, S. Chase, I. Derado, and V. Eckardt, *Strangeness Enhancement in Central S+S Collisions at 200 GeV/nucleon*, Nuclear Physics a **525**, 221 (1991). [https://doi.org/10.1016/0375-9474\(91\)90328-4](https://doi.org/10.1016/0375-9474(91)90328-4)
- [51] S. Acharya and others, *Multiplicity dependence of π , K, and p production in pp collisions at $\sqrt{s} = 13$ TeV*, Eur. Phys. J. C **80**, 693 (2020). [10.1140/epjc/s10052-020-8125-1](https://doi.org/10.1140/epjc/s10052-020-8125-1)
- [52] M. Gyulassy and M. Plumer, *Jet Quenching in Dense Matter*, Phys. Lett. B **243**, 432 (1990). [10.1016/0370-2693\(90\)91409-5](https://doi.org/10.1016/0370-2693(90)91409-5)
- [53] G. Aad and others, *Observation of a Centrality-Dependent Dijet Asymmetry in Lead-Lead Collisions at $\sqrt{s_{NN}} = 2.76$ TeV with the ATLAS*

- Detector at the LHC*, Phys. Rev. Lett. **105**, 252303 (2010). [10.1103/PhysRevLett.105.252303](#)
- [54] T. Matsui and H. Satz, *J/ψ Suppression by Quark-Gluon Plasma Formation*, Phys. Lett. B **178**, 416 (1986). [10.1016/0370-2693\(86\)91404-8](#)
- [55] K. Yokokawa, S. Sasaki, T. Hatsuda, and A. Hayashigaki, *First lattice study of low-energy charmonium-hadron interaction*, Phys. Rev. D **74**, 34504 (2006). [10.1103/PhysRevD.74.034504](#)
- [56] A. M. Sirunyan and others, *Nuclear modification factor of D^0 mesons in Pb–Pb collisions at $\sqrt{s_{\text{NN}}} = 5.02$ TeV*, Phys. Lett. B **782**, 474 (2018). [10.1016/j.physletb.2018.05.074](#)
- [57] M. L. Miller, K. Reygers, S. J. Sanders, and P. Steinberg, *Glauber modeling in high energy nuclear collisions*, Ann. Rev. Nucl. Part. Sci. **57**, 205 (2007). [10.1146/annurev.nucl.57.090506.123020](#)
- [58] J. Adam and others, *J/ψ suppression at forward rapidity in Pb–Pb collisions at $\sqrt{s_{\text{NN}}} = 5.02$ TeV*, Phys. Lett. B **766**, 212 (2017). [10.1016/j.physletb.2016.12.064](#)
- [59] B. Abelev and others, *J/ψ suppression at forward rapidity in Pb–Pb collisions at $\sqrt{s_{\text{NN}}} = 2.76$ TeV*, Phys. Rev. Lett. **109**, 72301 (2012). [10.1103/PhysRevLett.109.072301](#)
- [60] N. Herrmann, J. P. Wessels, and T. Wienold, *Collective flow in heavy ion collisions*, Ann. Rev. Nucl. Part. Sci. **49**, 581 (1999). [10.1146/annurev.nucl.49.1.581](#)
- [61] S. Acharya and others, *Production of charged pions, kaons, and (anti-)protons in Pb–Pb and inelastic pp collisions at $\sqrt{s_{\text{NN}}} = 5.02$ TeV*, Phys. Rev. C **101**, 44907 (2020). [10.1103/PhysRevC.101.044907](#)
- [62] S. A. Voloshin, A. M. Poskanzer, and R. Snellings, *Collective phenomena in non-central nuclear collisions*, Landolt-Bornstein **23**, 293 (2010). [10.1007/978-3-642-01539-7_10](#)
- [63] T. Hirano, N. van der Kolk, and A. Bilandzic, *Hydrodynamics and Flow*, Lect. Notes Phys. **785**, 139 (2010). [10.1007/978-3-642-02286-9_4](#)
- [64] S. Voloshin and Y. Zhang, *Flow study in relativistic nuclear collisions by Fourier expansion of Azimuthal particle distributions*, Z. Phys. C **70**, 665 (1996). [10.1007/s002880050141](#)
- [65] R. Snellings, *Elliptic Flow: A Brief Review*, New J. Phys. **13**, 55008 (2011). [10.1088/1367-2630/13/5/055008](#)

BIBLIOGRAPHY

- [66] U. Heinz, Z. Qiu, and C. Shen, *Fluctuating flow angles and anisotropic flow measurements*, Phys. Rev. C **87**, 34913 (2013). [10.1103/PhysRevC.87.034913](#)
- [67] B. Alver and G. Roland, *Collision geometry fluctuations and triangular flow in heavy-ion collisions*, Phys. Rev. C **81**, 54905 (2010). [10.1103/PhysRevC.82.039903](#)
- [68] K. Aamodt and others, *Higher harmonic anisotropic flow measurements of charged particles in Pb–Pb collisions at $\sqrt{s_{NN}}=2.76$ TeV*, Phys. Rev. Lett. **107**, 32301 (2011). [10.1103/PhysRevLett.107.032301](#)
- [69] J. Adam and others, *Anisotropic flow of charged particles in Pb–Pb collisions at $\sqrt{s_{NN}} = 5.02$ TeV*, Phys. Rev. Lett. **116**, 132302 (2016). [10.1103/PhysRevLett.116.132302](#)
- [70] H. Niemi, K. J. Eskola, R. Paatelainen, and K. Tuominen, *Predictions for 5.023 TeV Pb+Pb collisions at the CERN Large Hadron Collider*, Phys. Rev. C **93**, 14912 (2016). [10.1103/PhysRevC.93.014912](#)
- [71] J. Noronha-Hostler, M. Luzum, and J.-Y. Ollitrault, *Hydrodynamic predictions for 5.02 TeV Pb–Pb collisions*, Phys. Rev. C **93**, 34912 (2016). [10.1103/PhysRevC.93.034912](#)
- [72] M. A. Stephanov, K. Rajagopal, and E. V. Shuryak, *Event-by-event fluctuations in heavy ion collisions and the QCD critical point*, Phys. Rev. D **60**, 114028 (1999). [10.1103/PhysRevD.60.114028](#)
- [73] S. Acharya and others, *Charged-particle multiplicity fluctuations in Pb–Pb collisions at $\sqrt{s_{NN}} = 2.76$ TeV*, Eur. Phys. J. C **81**, 1012 (2021). [10.1140/epjc/s10052-021-09784-4](#)
- [74] G. Baym and H. Heiselberg, *Event-by-event fluctuations in ultrarelativistic heavy ion collisions*, Phys. Lett. B **469**, 7 (1999). [10.1016/S0370-2693\(99\)01263-0](#)
- [75] V. Koch, M. Bleicher, and S. Jeon, *Event-by-event fluctuations and the QGP*, Nucl. Phys. A **698**, 261 (2002). [10.1016/S0375-9474\(02\)00716-9](#)
- [76] A. Adare and others, *Charged hadron multiplicity fluctuations in Au+Au and Cu+Cu collisions from $\sqrt{s_{NN}} = 22.5$ to 200 GeV*, Phys. Rev. C **78**, 44902 (2008). [10.1103/PhysRevC.78.044902](#)
- [77] T. Tripathy, *Event-by-event fluctuations of mean transverse momentum in Pb–Pb and Xe–Xe collisions with ALICE*, J. Phys. Conf. Ser. **2586**, 12017 (2023). [10.1088/1742-6596/2586/1/012017](#)

- [78] A. Bialas and R. B. Peschanski, *Moments of Rapidity Distributions as a Measure of Short Range Fluctuations in High-Energy Collisions*, Nucl. Phys. B **273**, 703 (1986). [10.1016/0550-3213\(86\)90386-X](https://doi.org/10.1016/0550-3213(86)90386-X)
- [79] A. Bialas and R. B. Peschanski, *Intermittency in Multiparticle Production at High-Energy*, Nucl. Phys. B **308**, 857 (1988). [10.1016/0550-3213\(88\)90131-9](https://doi.org/10.1016/0550-3213(88)90131-9)
- [80] M. Abdulhamid and others, *Energy dependence of intermittency for charged hadrons in Au+Au collisions at RHIC*, Phys. Lett. B **845**, 138165 (2023). [10.1016/j.physletb.2023.138165](https://doi.org/10.1016/j.physletb.2023.138165)
- [81] T. Anticic and others, *Critical fluctuations of the proton density in A+A collisions at 158 A GeV*, Eur. Phys. J. C **75**, 587 (2015). [10.1140/epjc/s10052-015-3738-5](https://doi.org/10.1140/epjc/s10052-015-3738-5)
- [82] M. Kuich, *Highlights from the NA61/SHINE strong-interactions programme*, EPJ Web Conf. **259**, 1001 (2022). [10.1051/epjconf/202225901001](https://doi.org/10.1051/epjconf/202225901001)
- [83] A. M. Polyakov, *Thermal Properties of Gauge Fields and Quark Liberation*, Phys. Lett. B **72**, 477 (1978). [10.1016/0370-2693\(78\)90737-2](https://doi.org/10.1016/0370-2693(78)90737-2)
- [84] S. Muroya, A. Nakamura, C. Nonaka, and T. Takaishi, *Lattice QCD at finite density: An Introductory review*, Prog. Theor. Phys. **110**, 615 (2003). [10.1143/PTP.110.615](https://doi.org/10.1143/PTP.110.615)
- [85] H.-W. Lin and H. B. Meyer, editors, *Lattice QCD for Nuclear Physics* (Springer, 2015).
- [86] E. A. De Wolf, I. M. Dremin, and W. Kittel, *Scaling laws for density correlations and fluctuations in multiparticle dynamics*, Phys. Rept. **270**, 1 (1996). [10.1016/0370-1573\(95\)00069-0](https://doi.org/10.1016/0370-1573(95)00069-0)
- [87] H. Adhikary and others, *Search for a critical point of strongly-interacting matter in central 40Ar+45Sc collisions at 13A–75A GeV/c beam momentum*, Eur. Phys. J. C **84**, 741 (2024). [10.1140/epjc/s10052-024-13012-0](https://doi.org/10.1140/epjc/s10052-024-13012-0)
- [88] K. Fukushima and T. Hatsuda, *The phase diagram of dense QCD*, Rept. Prog. Phys. **74**, 14001 (2011). [10.1088/0034-4885/74/1/014001](https://doi.org/10.1088/0034-4885/74/1/014001)
- [89] R. Hagedorn, *Statistical thermodynamics of strong interactions at high-energies*, Nuovo Cim. Suppl. **3**, 147 (1965).
- [90] H. Meyer-Ortmanns, *Phase transitions in quantum chromodynamics*, Rev. Mod. Phys. **68**, 473 (1996). [10.1103/RevModPhys.68.473](https://doi.org/10.1103/RevModPhys.68.473)

BIBLIOGRAPHY

- [91] H. Satz, *Deconfinement and percolation*, Nucl. Phys. A **642**, 130 (1998). [10.1016/S0375-9474\(98\)00508-9](https://doi.org/10.1016/S0375-9474(98)00508-9)
- [92] K. Johnson, *The M.I.T. Bag Model*, Acta Phys. Polon. B **6**, 865 (1975).
- [93] G. Baym, *Confinement of quarks in nuclear matter*, Physica a **96**, 131 (1979). [10.1016/0378-4371\(79\)90200-0](https://doi.org/10.1016/0378-4371(79)90200-0)
- [94] T. Hatsuda and T. Kunihiro, *Fluctuation Effects in Hot Quark Matter: Precursors of Chiral Transition at Finite Temperature*, Phys. Rev. Lett. **55**, 158 (1985). [10.1103/PhysRevLett.55.158](https://doi.org/10.1103/PhysRevLett.55.158)
- [95] P. Gerber and H. Leutwyler, *Hadrons Below the Chiral Phase Transition*, Nucl. Phys. B **321**, 387 (1989). [10.1016/0550-3213\(89\)90349-0](https://doi.org/10.1016/0550-3213(89)90349-0)
- [96] S. Leupold and U. Mosel, *QCD Sum Rules for Vector Mesons in Nuclear Medium*, Phys. Rev. C **58**, 2939 (1998). [10.1103/PhysRevC.58.2939](https://doi.org/10.1103/PhysRevC.58.2939)
- [97] J. N. Guenther, *Overview of the QCD phase diagram: Recent progress from the lattice*, Eur. Phys. J. A **57**, 136 (2021). [10.1140/epja/s10050-021-00354-6](https://doi.org/10.1140/epja/s10050-021-00354-6)
- [98] J. N. Guenther, *An overview of the QCD phase diagram at finite T and μ_B* , Pos 13 (2022). [10.22323/1.396.0013](https://doi.org/10.22323/1.396.0013)
- [99] B. Svetitsky and L. G. Yaffe, *Critical Behavior at Finite Temperature Confinement Transitions*, Nucl. Phys. B **210**, 423 (1982). [10.1016/0550-3213\(82\)90172-9](https://doi.org/10.1016/0550-3213(82)90172-9)
- [100] R. D. Pisarski and F. Wilczek, *Remarks on the Chiral Phase Transition in Chromodynamics*, Phys. Rev. D **29**, 338 (1984). [10.1103/PhysRevD.29.338](https://doi.org/10.1103/PhysRevD.29.338)
- [101] M. Fukugita, M. Okawa, and A. Ukawa, *Finite Size Scaling Study of the Deconfining Phase Transition in Pure SU(3) Lattice Gauge Theory*, Nucl. Phys. B **337**, 181 (1990). [10.1016/0550-3213\(90\)90256-D](https://doi.org/10.1016/0550-3213(90)90256-D)
- [102] Y. Aoki, G. Endrodi, Z. Fodor, S. D. Katz, and K. K. Szabo, *The Order of the quantum chromodynamics transition predicted by the standard model of particle physics*, Nature **443**, 675 (2006). [10.1038/nature05120](https://doi.org/10.1038/nature05120)
- [103] C. DeTar and U. M. Heller, *QCD Thermodynamics from the Lattice*, Eur. Phys. J. A **41**, 405 (2009). [10.1140/epja/i2009-10825-3](https://doi.org/10.1140/epja/i2009-10825-3)
- [104] S. Borsanyi, Z. Fodor, J. N. Guenther, S. K. Katz, K. K. Szabo, A. Pasztor, I. Portillo, and C. Ratti, *Higher order fluctuations and correlations of conserved charges from lattice QCD*, JHEP **10**, 205 (2018). [10.1007/JHEP10\(2018\)205](https://doi.org/10.1007/JHEP10(2018)205)

- [105] R. Bellwied, S. Borsanyi, Z. Fodor, S. D. Katz, and C. Ratti, *Is there a flavor hierarchy in the deconfinement transition of QCD?*, Phys. Rev. Lett. **111**, 202302 (2013). [10.1103/PhysRevLett.111.202302](https://doi.org/10.1103/PhysRevLett.111.202302)
- [106] A. Bazavov and others, *Chiral crossover in QCD at zero and non-zero chemical potentials*, Phys. Lett. B **795**, 15 (2019). [10.1016/j.physletb.2019.05.013](https://doi.org/10.1016/j.physletb.2019.05.013)
- [107] C. E. Detar, *A Conjecture Concerning the Modes of Excitation of the Quark-Gluon Plasma*, Phys. Rev. D **32**, 276 (1985). [10.1103/PhysRevD.32.276](https://doi.org/10.1103/PhysRevD.32.276)
- [108] M. Kitazawa, T. Koide, T. Kunihiro, and Y. Nemoto, *Precursor of color superconductivity in hot quark matter*, Phys. Rev. D **65**, 91504 (2002). [10.1103/PhysRevD.65.091504](https://doi.org/10.1103/PhysRevD.65.091504)
- [109] H. Abuki, T. Hatsuda, and K. Itakura, *Structural change of Cooper pairs and momentum dependent gap in color superconductivity*, Phys. Rev. D **65**, 74014 (2002). [10.1103/PhysRevD.65.074014](https://doi.org/10.1103/PhysRevD.65.074014)
- [110] Y. Nishida and H. Abuki, *BCS-BEC crossover in a relativistic superfluid and its significance to quark matter*, Phys. Rev. D **72**, 96004 (2005). [10.1103/PhysRevD.72.096004](https://doi.org/10.1103/PhysRevD.72.096004)
- [111] M. A. Stephanov, K. Rajagopal, and E. V. Shuryak, *Signatures of the tricritical point in QCD*, Phys. Rev. Lett. **81**, 4816 (1998). [10.1103/PhysRevLett.81.4816](https://doi.org/10.1103/PhysRevLett.81.4816)
- [112] M. Asakawa and K. Yazaki, *Chiral Restoration at Finite Density and Temperature*, Nucl. Phys. A **504**, 668 (1989). [10.1016/0375-9474\(89\)90002-X](https://doi.org/10.1016/0375-9474(89)90002-X)
- [113] A. Barducci, R. Casalbuoni, S. De Curtis, R. Gatto, and G. Pettini, *Chiral Symmetry Breaking in QCD at Finite Temperature and Density*, Phys. Lett. B **231**, 463 (1989). [10.1016/0370-2693\(89\)90695-3](https://doi.org/10.1016/0370-2693(89)90695-3)
- [114] F. Wilczek, *Application of the renormalization group to a second order QCD phase transition*, Int. J. Mod. Phys. A **7**, 3911 (1992). [10.1142/S0217751X92001757](https://doi.org/10.1142/S0217751X92001757)
- [115] J. Berges and K. Rajagopal, *Color superconductivity and chiral symmetry restoration at nonzero baryon density and temperature*, Nucl. Phys. B **538**, 215 (1999). [10.1016/S0550-3213\(98\)00620-8](https://doi.org/10.1016/S0550-3213(98)00620-8)
- [116] R. Stock, F. Becattini, M. Bleicher, and J. Steinheimer, *The QCD Phase Diagram from Statistical Model Analysis*, Nucl. Phys. A **982**, 827 (2019). [10.1016/j.nuclphysa.2018.11.019](https://doi.org/10.1016/j.nuclphysa.2018.11.019)

BIBLIOGRAPHY

- [117] M. Huang, *QCD Phase Diagram at High Temperature and Density*, (2010).
- [118] K. Rajagopal and F. Wilczek, *The Condensed matter physics of QCD*, in *At the frontier of particle physics. Handbook of QCD. Vol. 1-3*, edited by M. Shifman and B. Ioffe (2000)., pp. 2061–2151.
- [119] M. G. Alford, A. Schmitt, K. Rajagopal, and T. Schäfer, *Color superconductivity in dense quark matter*, Rev. Mod. Phys. **80**, 1455 (2008). [10.1103/RevModPhys.80.1455](https://doi.org/10.1103/RevModPhys.80.1455)
- [120] S. P. Klevansky, *The Nambu-Jona-Lasinio model of quantum chromodynamics*, Rev. Mod. Phys. **64**, 649 (1992). [10.1103/RevModPhys.64.649](https://doi.org/10.1103/RevModPhys.64.649)
- [121] R. Anglani, M. Mannarelli, and M. Ruggieri, *Collective modes in the color flavor locked phase*, New J. Phys. **13**, 55002 (2011). [10.1088/1367-2630/13/5/055002](https://doi.org/10.1088/1367-2630/13/5/055002)
- [122] A. Schmitt, *Dense matter in compact stars: A pedagogical introduction*, Vol. 811 (2010).
- [123] B. C. Barrois, *Superconducting Quark Matter*, Nucl. Phys. B **129**, 390 (1977). [10.1016/0550-3213\(77\)90123-7](https://doi.org/10.1016/0550-3213(77)90123-7)
- [124] D. Bailin and A. Love, *Superfluidity and Superconductivity in Relativistic Fermion Systems*, Phys. Rept. **107**, 325 (1984). [10.1016/0370-1573\(84\)90145-5](https://doi.org/10.1016/0370-1573(84)90145-5)
- [125] A. Sorensen and others, *Dense nuclear matter equation of state from heavy-ion collisions*, Prog. Part. Nucl. Phys. **134**, 104080 (2024). [10.1016/j.ppnp.2023.104080](https://doi.org/10.1016/j.ppnp.2023.104080)
- [126] P. Chomaz, *The nuclear liquid gas phase transition and phase coexistence*, AIP Conf. Proc. **610**, 167 (2002). [10.1063/1.1469927](https://doi.org/10.1063/1.1469927)
- [127] D. Biswas, P. Petreczky, and S. Sharma, *Chiral condensate and the equation of state at nonzero baryon density from the hadron resonance gas model with a repulsive mean field*, Phys. Rev. C **109**, 55206 (2024). [10.1103/PhysRevC.109.055206](https://doi.org/10.1103/PhysRevC.109.055206)
- [128] D. Tong, *Chiral Symmetry Breaking*, (2024). Available at: <https://www.damtp.cam.ac.uk/user/tong/gaugetheory/5chisb.pdf> [Accessed December 24, 2024.]
- [129] K. Fukushima and V. Skokov, *Polyakov loop modeling for hot QCD*, Prog. Part. Nucl. Phys. **96**, 154 (2017). [10.1016/j.ppnp.2017.05.002](https://doi.org/10.1016/j.ppnp.2017.05.002)

- [130] L. Susskind, *Lattice Models of Quark Confinement at High Temperature*, Phys. Rev. D **20**, 2610 (1979). [10.1103/PhysRevD.20.2610](https://doi.org/10.1103/PhysRevD.20.2610)
- [131] L. D. McLerran and B. Svetitsky, *Quark Liberation at High Temperature: A Monte Carlo Study of SU(2) Gauge Theory*, Phys. Rev. D **24**, 450 (1981). [10.1103/PhysRevD.24.450](https://doi.org/10.1103/PhysRevD.24.450)
- [132] S. Nadkarni, *Nonabelian Debye Screening. 1. The Color Averaged Potential*, Phys. Rev. D **33**, 3738 (1986). [10.1103/PhysRevD.33.3738](https://doi.org/10.1103/PhysRevD.33.3738)
- [133] P. B. Arnold and L. G. Yaffe, *The NonAbelian Debye screening length beyond leading order*, Phys. Rev. D **52**, 7208 (1995). [10.1103/PhysRevD.52.7208](https://doi.org/10.1103/PhysRevD.52.7208)
- [134] A. Hart, M. Laine, and O. Philipsen, *Static correlation lengths in QCD at high temperatures and finite densities*, Nucl. Phys. B **586**, 443 (2000). [10.1016/S0550-3213\(00\)00418-1](https://doi.org/10.1016/S0550-3213(00)00418-1)
- [135] Y. Maezawa, S. Aoki, S. Ejiri, T. Hatsuda, N. Ishii, K. Kanaya, N. Ukita, and T. Umeda, *Electric and Magnetic Screening Masses at Finite Temperature from Generalized Polyakov-Line Correlations in Two-flavor Lattice QCD*, Phys. Rev. D **81**, 91501 (2010). [10.1103/PhysRevD.81.091501](https://doi.org/10.1103/PhysRevD.81.091501)
- [136] M. Schwartz, *Chiral Symmetry Breaking*, (2019). Available at: <https://scholar.harvard.edu/files/schwartz/files/9-phases.pdf> [Accessed December 24, 2024.]
- [137] A. Cheung, *Phase Transitions and Collective Phenomena* (University of Cambridge, 2023).
- [138] R. B. Stinchcombe, *Phase Transitions*, in *Order and Chaos in Nonlinear Physical Systems*, edited by S. Lundqvist, N. H. March, and M. P. Tosi (Springer US, 1988), pp. 295–340.
- [139] B. B. Mandelbrot, *The Fractal Geometry of Nature*, 3rd ed. (W. H. Freeman, Comp., 1983).
- [140] M. Hanada and N. Yamamoto, *Universality of Phases in QCD and QCD-like Theories*, JHEP **2**, 138 (2012). [10.1007/JHEP02\(2012\)138](https://doi.org/10.1007/JHEP02(2012)138)
- [141] H. Nishimori and G. Ortiz, *Elements of Phase Transitions and Critical Phenomena* (OUP Oxford, 2011).
- [142] K. Orginos, *Innovations in lattice QCD algorithms*, J. Phys. Conf. Ser. **46**, 132 (2006). [10.1088/1742-6596/46/1/018](https://doi.org/10.1088/1742-6596/46/1/018)
- [143] S. Duane, A. D. Kennedy, B. J. Pendleton, and D. Roweth, *Hybrid Monte Carlo*, Phys. Lett. B **195**, 216 (1987). [10.1016/0370-2693\(87\)91197-X](https://doi.org/10.1016/0370-2693(87)91197-X)

BIBLIOGRAPHY

- [144] J. Lee and J. M. Kosterlitz, *Finite-size scaling and Monte Carlo simulations of first-order phase transitions*, Phys. Rev. B **43**, 3265 (1991). [10.1103/PhysRevB.43.3265](https://doi.org/10.1103/PhysRevB.43.3265)
- [145] S. Ejiri, *Recent progress in lattice QCD at finite density*, Pos 2 (2008). [10.22323/1.066.0002](https://doi.org/10.22323/1.066.0002)
- [146] M. P. Lombardo, K. Splittorff, and J. J. M. Verbaarschot, *Lattice QCD and dense quark matter*, in *Compact Stars in the QCD Phase Diagram II* (2009).
- [147] S. Borsanyi, *A guide to lattice QCD thermodynamics*, (2018). Available at: <https://indi.to/tDwhG> [Accessed December 24, 2024.]
- [148] K. Nagata, *Finite-density lattice QCD and sign problem: Current status and open problems*, Prog. Part. Nucl. Phys. **127**, 103991 (2022). [10.1016/j.ppnp.2022.103991](https://doi.org/10.1016/j.ppnp.2022.103991)
- [149] A. Pelissetto and E. Vicari, *Critical phenomena and renormalization group theory*, Phys. Rept. **368**, 549 (2002). [10.1016/S0370-1573\(02\)00219-3](https://doi.org/10.1016/S0370-1573(02)00219-3)
- [150] K. Huang, *Statistical Mechanics* (John Wiley, Sons, 2000).
- [151] J. Chakravarty and D. Jain, *Critical exponents for higher order phase transitions: Landau theory and RG flow*, J. Stat. Mech. **2109**, 93204 (2021). [10.1088/1742-5468/ac1f11](https://doi.org/10.1088/1742-5468/ac1f11)
- [152] J. J. Binney, N. J. Dowrick, A. J. Fisher, and M. E. J. Newman, *The Theory of critical phenomena: An Introduction to the renormalization group* (1992).
- [153] K.-J. Sun, L.-W. Chen, C. M. Ko, and Z. Xu, *Probing QCD critical fluctuations from light nuclei production in relativistic heavy-ion collisions*, Phys. Lett. B **774**, 103 (2017). [10.1016/j.physletb.2017.09.056](https://doi.org/10.1016/j.physletb.2017.09.056)
- [154] A. Bialas and R. C. Hwa, *Intermittency parameters as a possible signal for quark-gluon plasma formation*, Phys. Lett. B **253**, 436 (1991). [10.1016/0370-2693\(91\)91747-J](https://doi.org/10.1016/0370-2693(91)91747-J)
- [155] H. Satz, *Intermittency and Critical Behavior*, Nucl. Phys. B **326**, 613 (1989). [10.1016/0550-3213\(89\)90546-4](https://doi.org/10.1016/0550-3213(89)90546-4)
- [156] R. C. Hwa and C. B. Yang, *Local Multiplicity Fluctuations as a Signature of Critical Hadronization at LHC*, Phys. Rev. C **85**, 44914 (2012). [10.1103/PhysRevC.85.044914](https://doi.org/10.1103/PhysRevC.85.044914)

- [157] N. G. Antoniou, F. K. Diakonou, A. S. Kapoyannis, and K. S. Kousouris, *Critical opalescence in baryonic QCD matter*, Phys. Rev. Lett. **97**, 32002 (2006). [10.1103/PhysRevLett.97.032002](https://doi.org/10.1103/PhysRevLett.97.032002)
- [158] N. G. Antoniou, F. K. Diakonou, X. N. Maintas, and C. E. Tsagkarakis, *Locating the QCD critical endpoint through finite-size scaling*, Phys. Rev. D **97**, 34015 (2018). [10.1103/PhysRevD.97.034015](https://doi.org/10.1103/PhysRevD.97.034015)
- [159] N. G. Antoniou, Y. F. Contoyiannis, F. K. Diakonou, A. I. Karanikas, and C. N. Ktorides, *Pion production from a critical QCD phase*, Nucl. Phys. A **693**, 799 (2001). [10.1016/S0375-9474\(01\)00921-6](https://doi.org/10.1016/S0375-9474(01)00921-6)
- [160] P. Abreu and others, *A Study of intermittency in hadronic Z0 decays*, Phys. Lett. B **247**, 137 (1990). [10.1016/0370-2693\(90\)91062-G](https://doi.org/10.1016/0370-2693(90)91062-G)
- [161] B. Buschbeck, P. Lipa, and R. B. Peschanski, *Signal for Intermittency in e^+e^- Reactions Obtained From Negative Binomial Fits*, Phys. Lett. B **215**, 788 (1988). [10.1016/0370-2693\(88\)90062-7](https://doi.org/10.1016/0370-2693(88)90062-7)
- [162] W. Braunschweig and others, *Study of Intermittency in Electron-Positron Annihilation Into Hadrons*, Phys. Lett. B **231**, 548 (1989). [10.1016/0370-2693\(89\)90707-7](https://doi.org/10.1016/0370-2693(89)90707-7)
- [163] I. Derado, G. Jancso, N. Schmitz, and P. Stopa, *Investigation of Intermittency in Muon-Proton Scattering at 280-GeV*, Z. Phys. C **47**, 23 (1990). [10.1007/BF01551907](https://doi.org/10.1007/BF01551907)
- [164] S.-S. Wang, J. Zhang, Y.-X. Ye, C.-G. Xiao, and Y. Zhong, *Intermittency exponents in p-p collisions at 400 GeV/c*, Phys. Rev. D **49**, 5785 (1994). [10.1103/PhysRevD.49.5785](https://doi.org/10.1103/PhysRevD.49.5785)
- [165] R. Holynski and others, *Evidence for Intermittent Patterns of Fluctuations in Particle Production in High-Energy Interactions in Nuclear Emulsion*, Phys. Rev. Lett. **62**, 733 (1989). [10.1103/PhysRevLett.62.733](https://doi.org/10.1103/PhysRevLett.62.733)
- [166] R. Holynski and others, *One-dimensional and Two-dimensional Analysis of the Factorial Moments in 200-GeV/nucleon P 16O and 32 S Interactions With Ag/Br Nuclei*, Phys. Rev. C **40**, (1989). [10.1103/PhysRevC.40.R2449](https://doi.org/10.1103/PhysRevC.40.R2449)
- [167] T. Akesson and others, *A Search for multiplicity fluctuations in high-energy nucleus-nucleus collisions*, Phys. Lett. B **252**, 303 (1990). [10.1016/0370-2693\(90\)90877-9](https://doi.org/10.1016/0370-2693(90)90877-9)
- [168] D. Ghosh, P. Ghosh, and A. Ghosh, *Intermittency and correlations in O-16+Ag/Br interactions at 2.1-GeV/nucleon*, Phys. Rev. C **49**, 3219 (1994). [10.1103/PhysRevC.49.3219](https://doi.org/10.1103/PhysRevC.49.3219)

BIBLIOGRAPHY

- [169] D. Ghosh, M. Lahiri, S. Das, K. Purkait, B. Biswas, J. Roychoudhury, R. Chatterjee, A. K. Jafry, and A. Deb, *Fluctuation study of pionisation in ultrarelativistic nucleus nucleus interaction*, Z. Phys. C **71**, 243 (1996). [10.1007/s002880050168](https://doi.org/10.1007/s002880050168)
- [170] R. C. Hwa and C. B. Yang, *Observable Properties of Quark-Hadron Phase Transition at the Large Hadron Collider*, Acta Phys. Polon. B **48**, 23 (2017). [10.5506/APhysPolB.48.23](https://doi.org/10.5506/APhysPolB.48.23)
- [171] S. K. Malik and R. Gupta, *Intermittency analysis of charged hadrons generated in Pb–Pb collisions at $\sqrt{s_{NN}} = 2.76$ TeV and 5.02 TeV*, Scipost Phys. Proc. **15**, 12 (2024). [10.21468/SciPostPhysProc.15.012](https://doi.org/10.21468/SciPostPhysProc.15.012)
- [172] T. Anticic and others, *Search for the QCD critical point in nuclear collisions at the CERN SPS*, Phys. Rev. C **81**, 64907 (2010). [10.1103/PhysRevC.81.064907](https://doi.org/10.1103/PhysRevC.81.064907)
- [173] N. G. Antoniou, Y. F. Contoyiannis, F. K. Diakonov, and G. Mavromanolakis, *Critical QCD in nuclear collisions*, Nucl. Phys. A **761**, 149 (2005). [10.1016/j.nuclphysa.2005.07.003](https://doi.org/10.1016/j.nuclphysa.2005.07.003)
- [174] N. G. Antoniou and F. K. Diakonov, *Ising-QCD phenomenology close to the critical point*, J. Phys. G **46**, 35101 (2019). [10.1088/1361-6471/aafead](https://doi.org/10.1088/1361-6471/aafead)
- [175] R. C. Hwa and M. T. Nazirov, *Intermittency in second order phase transition*, Phys. Rev. Lett. **69**, 741 (1992). [10.1103/PhysRevLett.69.741](https://doi.org/10.1103/PhysRevLett.69.741)
- [176] W. Ochs and J. Wosiek, *Intermittency and Jets*, Phys. Lett. B **214**, 617 (1988). [10.1016/0370-2693\(88\)90131-1](https://doi.org/10.1016/0370-2693(88)90131-1)
- [177] W. Ochs, *Multidimensional intermittency analysis*, Z. Phys. C **50**, 339 (1991). [10.1007/BF01474088](https://doi.org/10.1007/BF01474088)
- [178] R. C. Hwa, *Scaling exponent of multiplicity fluctuation in phase transition*, Phys. Rev. D **47**, 2773 (1993). [10.1103/PhysRevD.47.2773](https://doi.org/10.1103/PhysRevD.47.2773)
- [179] A. Kamal, N. Ahmad, and M. M. Khan, *Study of Anomalous Fractal Dimensions and Scaling Exponent in Ginzburg-Landau Phase Transition in 14.5 A GeV/c²⁸ Si-AgBr Interactions*, Acta Phys. Polon. B **46**, 1549 (2015). [10.5506/APhysPolB.46.1549](https://doi.org/10.5506/APhysPolB.46.1549)
- [180] R. C. Hwa and J.-c. Pan, *Intermittency in the Ginzburg-Landau theory*, Phys. Lett. B **297**, 35 (1992). [10.1016/0370-2693\(92\)91065-H](https://doi.org/10.1016/0370-2693(92)91065-H)
- [181] M. I. Adamovich and others, *Scaled factorial moment analysis of 200-A/GeV sulfur + gold interactions*, Phys. Rev. Lett. **65**, 412 (1990). [10.1103/PhysRevLett.65.412](https://doi.org/10.1103/PhysRevLett.65.412)

- [182] J. Wosiek, *Intermittency and Correlation Functions in the Ising Model in Two Dimensions*, Nuclear Physics B - Proceedings Supplements **9**, 640 (1989). [https://doi.org/10.1016/0920-5632\(89\)90177-1](https://doi.org/10.1016/0920-5632(89)90177-1)
- [183] Z. Cao, Y. Gao, and R. C. Hwa, *Scaling properties of hadron production in the Ising model for quark-hadron phase transition*, Z. Phys. C **72**, 661 (1996). [10.1007/s002880050290](https://doi.org/10.1007/s002880050290)
- [184] R. Sharma and R. Gupta, *Scaling Properties of Multiplicity Fluctuations in the AMPT Model*, Adv. High Energy Phys. **2018**, 6283801 (2018). [10.1155/2018/6283801](https://doi.org/10.1155/2018/6283801)
- [185] R. Gupta and S. K. Malik, *Intermittency study of charged particles generated in Pb–Pb collisions at $\sqrt{s_{NN}} = 2.76$ TeV using EPOS3*, Adv. High Energy Phys. **2020**, 5073042 (2020). [10.1155/2020/5073042](https://doi.org/10.1155/2020/5073042)
- [186] Y.-L. Xie, G. Chen, J.-L. Wang, Z.-H. Liu, and M.-J. Wang, *Scaling properties of multiplicity fluctuations in heavy ion collisions simulated by AMPT model*, Nucl. Phys. A **920**, 33 (2013). [10.1016/j.nuclphysa.2013.10.008](https://doi.org/10.1016/j.nuclphysa.2013.10.008)
- [187] S. Bhattacharyya, *A search for the quark-hadron phase transition in simulated pp collisions at $\sqrt{s} = 13$ TeV using UrQMD model by the scaled factorial moment method*, Eur. Phys. J. Plus **136**, 471 (2021). [10.1140/epjp/s13360-021-01325-y](https://doi.org/10.1140/epjp/s13360-021-01325-y)
- [188] R. C. Hwa, W. Ochs, and N. Schmitz, *Fluctuations and Fractal Structure*, 0th ed. (WORLD SCIENTIFIC, 1992).
- [189] E. K. Sarkisian, L. K. Gelovani, and G. G. Taran, *Fractality in central collisions of C-12 nuclei with Ne and Cu nuclei at 4.5-A/GeV/c*, Phys. Atom. Nucl. **56**, 832 (1993).
- [190] E. K. Sarkisian, L. K. Gelovani, and G. G. Taran, *Fractality and fluctuations in charged particle pseudorapidity distributions in central C (Ne, Cu) collisions at 4.5-A/GeV/c*, Phys. Lett. B **302**, 331 (1993). [10.1016/0370-2693\(93\)90404-6](https://doi.org/10.1016/0370-2693(93)90404-6)
- [191] P. Lipa and B. Buschbeck, *From strong to weak intermittency*, Phys. Lett. B **223**, 465 (1989). [10.1016/0370-2693\(89\)91634-1](https://doi.org/10.1016/0370-2693(89)91634-1)
- [192] M. Maćkowiak-Pawłowska, *NA61/SHINE results on fluctuations and correlations at CERN SPS energies*, Nucl. Phys. A **1005**, 121753 (2021). [10.1016/j.nuclphysa.2020.121753](https://doi.org/10.1016/j.nuclphysa.2020.121753)

BIBLIOGRAPHY

- [193] A. Bialas and M. Gazdzicki, *A New Variable to Study Intermittency*, Physics Letters B **252**, 483 (1990). [https://doi.org/10.1016/0370-2693\(90\)90575-Q](https://doi.org/10.1016/0370-2693(90)90575-Q)
- [194] J. Wu, *Measurement of Intermittency for Charged Particles in Au+Au Collisions at 7.7–200 GeV from STAR (Poster)*, Quark Matter 2019 - the Xxviiiith International Conference on Ultra-Relativistic Nucleus-Nucleus Collisions 1 (2019).
- [195] F. Becattini, J. Manninen, and M. Gazdzicki, *Energy and system size dependence of chemical freeze-out in relativistic nuclear collisions*, Phys. Rev. C **73**, 44905 (2006). [10.1103/PhysRevC.73.044905](https://arxiv.org/abs/10.1103/PhysRevC.73.044905)
- [196] J. Wu, Z. Li, X. Luo, M. Xu, and Y. Wu, *Intermittency of Charged Particles in the Hybrid UrQMD + CMC Model at Energies Available at the BNL Relativistic Heavy Ion Collider*, Phys. Rev. C **106**, 54905 (2022). [10.1103/PhysRevC.106.054905](https://arxiv.org/abs/10.1103/PhysRevC.106.054905)
- [197] M. Abdallah and others, *Cumulants and correlation functions of net-proton, proton, and antiproton multiplicity distributions in Au+Au collisions at energies available at the BNL Relativistic Heavy Ion Collider*, Phys. Rev. C **104**, 24902 (2021). [10.1103/PhysRevC.104.024902](https://arxiv.org/abs/10.1103/PhysRevC.104.024902)
- [198] O. S. Bruning, P. Collier, P. Lebrun, S. Myers, R. Ostojic, J. Poole, and P. Proudlock, editors, *LHC Design Report Vol.1: The LHC Main Ring*, (2004). [10.5170/CERN-2004-003-V-1](https://arxiv.org/abs/10.5170/CERN-2004-003-V-1)
- [199] M. Benedikt, P. Collier, V. Mertens, J. Poole, and K. Schindl, editors, *LHC Design Report. 3. The LHC injector chain*, (2004). [10.5170/CERN-2004-003-V-3](https://arxiv.org/abs/10.5170/CERN-2004-003-V-3)
- [200] *LHC Guide*, (2017). Available at: <http://cds.cern.ch/record/2255762>
- [201] E. Mobs, *The CERN accelerator complex in 2019. Complexe des accélérateurs du CERN en 2019*, (2019). Available at: <https://cds.cern.ch/record/2684277>
- [202] The ATLAS Collaboration, *ATLAS Website*, (2024). Available at: <https://atlas.cern/about> [Accessed December 24, 2024.]
- [203] The CMS Collaboration, *CMS Website*, (2024). Available at: <https://cms.cern/experiment> [Accessed December 24, 2024.]
- [204] The LHCb Collaboration, *Lhcb Website*, (2024). Available at: <https://lhcb-public.web.cern.ch/> [Accessed December 24, 2024.]

- [205] V. Berardi et al., *Total cross-section, elastic scattering and diffraction dissociation at the Large Hadron Collider at CERN: TOTEM Technical Design Report* (CERN, **2004**).
- [206] K. Noda, *The LHCf experiment*, AIP Conf. Proc. **1492**, 182 (2012). [10.1063/1.4763514](https://doi.org/10.1063/1.4763514)
- [207] A. Ariga et al., Technical Proposal for FASER: ForwArd Search Experiment at the LHC, **2018**
- [208] J. Pinfold et al., Technical Design Report of the MoEDAL Experiment, **2009**
- [209] N. Abgrall and others, *Report from the NA61/SHINE experiment at the CERN SPS*, (2008).
- [210] H. Wiedemann, *Particle Accelerator Physics* (Springer, **2015**).
- [211] O. S. Brüning and L. Rossi, *The High-Luminosity Large Hadron Collider*, Nature Reviews Physics **1**, 241 (2019). Available at: <https://api.semanticscholar.org/CorpusID:126892524>
- [212] B. Abelev and others, *Measurement of the Cross Section for Electromagnetic Dissociation with Neutron Emission in Pb–Pb Collisions at $\sqrt{s_{NN}} = 2.76$ TeV*, Phys. Rev. Lett. **109**, 252302 (2012). [10.1103/PhysRevLett.109.252302](https://doi.org/10.1103/PhysRevLett.109.252302)
- [213] A. J. Baltz, M. J. Rhoades-Brown, and J. Weneser, *Heavy ion partial beam lifetimes due to Coulomb induced processes*, Phys. Rev. E **54**, 4233 (1996). [10.1103/PhysRevE.54.4233](https://doi.org/10.1103/PhysRevE.54.4233)
- [214] J. Jowett and others, *The 2018 heavy-ion run of the LHC*, in *10th International Particle Accelerator Conference* (2019)., p. WEYYPLM2.
- [215] K. Aamodt and others, *The ALICE experiment at the CERN LHC*, JINST **3**, S8002 (2008). [10.1088/1748-0221/3/08/S08002](https://doi.org/10.1088/1748-0221/3/08/S08002)
- [216] C. Fabjan and J. Schukraft, *The experiments: ALICE. The story of ALICE: Building the dedicated heavy ion detector at LHC*, (2009). Available at: <https://cds.cern.ch/record/1193086>
- [217] Letter of Intent for A Large Ion Collider Experiment [ALICE], **1993**
- [218] *ALICE: Technical proposal for a large ion collider experiment at the CERN LHC*, (1995).
- [219] B. B. Abelev and others, *Performance of the ALICE Experiment at the CERN LHC*, Int. J. Mod. Phys. A **29**, 1430044 (2014). [10.1142/S0217751X14300440](https://doi.org/10.1142/S0217751X14300440)

BIBLIOGRAPHY

- [220] J. M. Jowett, M. Schaumann, and R. Versteegen, *Heavy-ion operation of HL-LHC*, Adv. Ser. Direct. High Energy Phys. **24**, 359 (2015). [10.1142/9789814675475_0021](https://doi.org/10.1142/9789814675475_0021)
- [221] R. Schicker, *Diffraction at ALICE*, (2010).
- [222] M. Gallio, W. Klempt, L. Leistam, J. De Groot, and J. Schükraft, *ALICE Zero-Degree Calorimeter (ZDC): Technical Design Report* (CERN, 1999).
- [223] *ALICE Inner Tracking System (ITS): Technical Design Report* (CERN, 1999).
- [224] P. Kuijter, *The inner tracking system of the ALICE experiment*, Nucl. Instrum. Methods Phys. Res., A **530**, 28 (2004). [10.1016/j.nima.2004.05.042](https://doi.org/10.1016/j.nima.2004.05.042)
- [225] D. Miśkowiec, *(W)hole new field: the new GEM Time Projection Chamber of ALICE*, J. Phys. Conf. Ser. **1561**, 12017 (2020). [10.1088/1742-6596/1561/1/012017](https://doi.org/10.1088/1742-6596/1561/1/012017)
- [226] H. Bethe, *Theory of the Passage of Fast Corpuscular Rays Through Matter*, Annalen Phys. **5**, 325 (1930). [10.1002/andp.19303970303](https://doi.org/10.1002/andp.19303970303)
- [227] S. Weinberg, *A Model of Leptons*, Phys. Rev. Lett. **19**, 1264 (1967). [10.1103/PhysRevLett.19.1264](https://doi.org/10.1103/PhysRevLett.19.1264)
- [228] J. Adolfsson and others, *The upgrade of the ALICE TPC with GEMs and continuous readout*, JINST **16**, P3022 (2021). [10.1088/1748-0221/16/03/P03022](https://doi.org/10.1088/1748-0221/16/03/P03022)
- [229] Upgrade of the ALICE Time Projection Chamber, **2013**
- [230] E. Abbas and others, *Performance of the ALICE VZERO system*, JINST **8**, P10016 (2013). [10.1088/1748-0221/8/10/P10016](https://doi.org/10.1088/1748-0221/8/10/P10016)
- [231] S. Acharya and others, *Centrality and pseudorapidity dependence of the charged-particle multiplicity density in Xe–Xe collisions at $\sqrt{s_{\rm NN}} = 5.44\text{ TeV}$* , Phys. Lett. B **790**, 35 (2019). [10.1016/j.physletb.2018.12.048](https://doi.org/10.1016/j.physletb.2018.12.048)
- [232] C. W. Fabjan, L. Jirdén, V. Lindestruth, L. Riccati, D. Rorich, P. Van de Vyvre, O. Villalobos Baillie, and H. de Groot, *ALICE trigger data-acquisition high-level trigger and control system: Technical Design Report* (CERN, 2004).

- [233] I. Belikov, *Event reconstruction and particle identification in the ALICE experiment at the LHC*, EPJ Web Conf. **70**, 29 (2014). [10.1051/epjconf/20147000029](https://doi.org/10.1051/epjconf/20147000029)
- [234] R. Fruhwirth, *Application of Kalman filtering to track and vertex fitting*, Nucl. Instrum. Meth. A **262**, 444 (1987). [10.1016/0168-9002\(87\)90887-4](https://doi.org/10.1016/0168-9002(87)90887-4)
- [235] C. Bierlich and others, *A comprehensive guide to the physics and usage of PYTHIA 8.3*, SciPost Phys. Codeb. **2022**, 8 (2022). [10.21468/SciPostPhysCodeb.8](https://doi.org/10.21468/SciPostPhysCodeb.8)
- [236] M. Gyulassy and X.-N. Wang, *HIJING 1.0: A Monte Carlo program for parton and particle production in high-energy hadronic and nuclear collisions*, Comput. Phys. Commun. **83**, 307 (1994). [10.1016/0010-4655\(94\)90057-4](https://doi.org/10.1016/0010-4655(94)90057-4)
- [237] S. Agostinelli and others, *GEANT4—a simulation toolkit*, Nucl. Instrum. Meth. A **506**, 250 (2003). [10.1016/S0168-9002\(03\)01368-8](https://doi.org/10.1016/S0168-9002(03)01368-8)
- [238] *The ALICE definition of primary particles*, (2017).
- [239] ALICE Analysis Repository, *Aliphysics*, (2024). Available at: <https://github.com/alisw/Aliphysics> [Accessed December 24, 2024.]
- [240] R. Brun, P. Buncic, F. Carminati, A. Morsch, F. Rademakers, and K. Safarik, *Computing in ALICE*, Nucl. Instrum. Meth. A **502**, 339 (2003). [10.1016/S0168-9002\(03\)00440-6](https://doi.org/10.1016/S0168-9002(03)00440-6)
- [241] *The ALICE experiment -- A journey through QCD*, (2022).
- [242] ALICE Software Framework, *Aliroot*, (2024). Available at: <https://github.com/alisw/AlRoot> [Accessed December 24, 2024.]
- [243] R. Brun et al., *Root-Project/root: V6.18/02*, (2020). [10.5281/zenodo.3895860](https://doi.org/10.5281/zenodo.3895860)
- [244] *Centrality determination in heavy ion collisions*, (2018). Available at: <https://cds.cern.ch/record/2636623>
- [245] A. K. Chaudhuri, *The Glauber Model, A Short Course on Relativistic Heavy Ion Collisions 3* (2014). [10.1088/bk978-0-750-31060-4ch3](https://doi.org/10.1088/bk978-0-750-31060-4ch3)
- [246] X.-N. Wang and M. Gyulassy, *HIJING: A Monte Carlo model for multiple jet production in p-p, p-A and A-A collisions*, Phys. Rev. D **44**, 3501 (1991). [10.1103/PhysRevD.44.3501](https://doi.org/10.1103/PhysRevD.44.3501)
- [247] R. Brun, F. Bruyant, F. Carminati, S. Giani, M. Maire, A. McPherson, G. Patrick, and L. Urban, *GEANT Detector Description and Simulation Tool*, (1994). [10.17181/CERN.MUHF.DMJ1](https://doi.org/10.17181/CERN.MUHF.DMJ1)

BIBLIOGRAPHY

- [248] T. Pierog, I. Karpenko, J. M. Katzy, E. Yatsenko, and K. Werner, *EPOS LHC: Test of collective hadronization with data measured at the CERN Large Hadron Collider*, Phys. Rev. C **92**, 34906 (2015). [10.1103/PhysRevC.92.034906](https://arxiv.org/abs/10.1103/PhysRevC.92.034906)
- [249] A. Data Preparation Group, *ALICE data flow*, (2017). Available at: <https://indi.to/KRtHC> [Accessed December 24, 2024.]
- [250] C. Lippmann, *Upgrade of the ALICE Time Projection Chamber*, (2014).
- [251] L. Vannucci, N. Bustreo, A. Badala, R. Barbera, G. Lo Re, A. Palmeri, A. Pulvirenti, G. S. Pappalardo, F. Riggi, and B. S. Nilsen, *Primary vertex in the ALICE experiment in absence of the event reconstruction*, Acta Phys. Hung. A **16**, 315 (2002). [10.1556/APH.16.2002.1-4.34](https://arxiv.org/abs/10.1556/APH.16.2002.1-4.34)
- [252] E. Bruna, A. Dainese, M. Masera, and F. Prino, *Vertex reconstruction for proton-proton collisions in ALICE*, (2009). Available at: <https://cds.cern.ch/record/1225497>
- [253] B. Abelev and others, *Centrality determination of Pb–Pb collisions at $\sqrt{s_{NN}} = 2.76$ TeV with ALICE*, Phys. Rev. C **88**, 44909 (2013). [10.1103/PhysRevC.88.044909](https://arxiv.org/abs/10.1103/PhysRevC.88.044909)
- [254] R. Gupta and S. Sharma, *Local multiplicity fluctuations in Pb–Pb collisions at $\sqrt{s_{NN}} = 2.76$ TeV with ALICE at LHC*, (2022). Available at: <https://indi.to/g8BZF> [Accessed December 24, 2024.]
- [255] S. Sharma and R. Gupta, *Local Multiplicity Fluctuations in Pb–Pb Collisions at $\sqrt{s_{NN}} = 2.76$ TeV with ALICE at the LHC*, Springer Proc. Phys. **304**, 860 (2024). [10.1007/978-981-97-0289-3_221](https://arxiv.org/abs/10.1007/978-981-97-0289-3_221)
- [256] X.-N. Wang, *pQCD based approach to parton production and equilibration in high-energy nuclear collisions*, Phys. Rept. **280**, 287 (1997). [10.1016/S0370-1573\(96\)00022-1](https://arxiv.org/abs/10.1016/S0370-1573(96)00022-1)
- [257] W.-T. Deng, X.-N. Wang, and R. Xu, *Hadron production in p+p, p+Pb, and Pb+Pb collisions with the HIJING 2.0 model at energies available at the CERN Large Hadron Collider*, Phys. Rev. C **83**, 14915 (2011). [10.1103/PhysRevC.83.014915](https://arxiv.org/abs/10.1103/PhysRevC.83.014915)
- [258] S. Sharma, S. K. Malik, Z. Banoo, and R. Gupta, *Normalized factorial moments of spatial distributions of particles in high multiplicity events: A Toy model study*, (2023).
- [259] C. Pruneau, S. Gavin, and S. Voloshin, *Methods for the study of particle production fluctuations*, Phys. Rev. C **66**, 44904 (2002). [10.1103/PhysRevC.66.044904](https://arxiv.org/abs/10.1103/PhysRevC.66.044904)

- [260] D. Rohr, S. Gorbunov, M. O. Schmidt, and R. Shahoyan, *Track Reconstruction in the ALICE TPC using GPUs for LHC Run 3*, in *4th International Workshop Connecting The Dots 2018* (2018).
- [261] M. O. Schmidt, *Space-point calibration of the ALICE TPC with track residuals*, EPJ Web Conf. **245**, 1003 (2020). [10.1051/epjconf/202024501003](https://doi.org/10.1051/epjconf/202024501003)
- [262] W. Kittel and E. A. De Wolf, *Soft Multihadron Dynamics*, 0th ed. (WORLD SCIENTIFIC, 2005).
- [263] K. Werner, *Core-corona separation in ultra-relativistic heavy ion collisions*, Phys. Rev. Lett. **98**, 152301 (2007). [10.1103/PhysRevLett.98.152301](https://doi.org/10.1103/PhysRevLett.98.152301)
- [264] H. J. Drescher, M. Hladik, S. Ostapchenko, T. Pierog, and K. Werner, *Parton based Gribov-Regge theory*, Phys. Rept. **350**, 93 (2001). [10.1016/S0370-1573\(00\)00122-8](https://doi.org/10.1016/S0370-1573(00)00122-8)
- [265] L. Wasserman, *All of Statistics: A Concise Course in Statistical Inference* (Springer, New York, 2004).
- [266] W. J. Metzger, *Estimating the Uncertainties of Factorial Moments*, in (2004).
- [267] C. Bohm, *Statistics and error propagation*, (2019). Available at: <https://indi.to/tYZ4g> [Accessed December 24, 2024.]
- [268] A. Buckley and others, *General-purpose event generators for LHC physics*, Phys. Rept. **504**, 145 (2011). [10.1016/j.physrep.2011.03.005](https://doi.org/10.1016/j.physrep.2011.03.005)
- [269] E. Bothmann and others, *Event Generation with Sherpa 2.2*, Scipost Phys. **7**, 34 (2019). [10.21468/SciPostPhys.7.3.034](https://doi.org/10.21468/SciPostPhys.7.3.034)
- [270] J. Bellm and others, *Herwig 7.0/Herwig++ 3.0 release note*, Eur. Phys. J. C **76**, 196 (2016). [10.1140/epjc/s10052-016-4018-8](https://doi.org/10.1140/epjc/s10052-016-4018-8)
- [271] H. Shah, *The Angantyr Model For Simulating Heavy-Ion Collisions*, 2021
- [272] M. L. Good and W. D. Walker, *Diffraction dissociation of beam particles*, Phys. Rev. **120**, 1857 (1960). [10.1103/PhysRev.120.1857](https://doi.org/10.1103/PhysRev.120.1857)
- [273] H. Pi, *An Event generator for interactions between hadrons and nuclei: FRITIOF version 7.0*, Comput. Phys. Commun. **71**, 173 (1992). [10.1016/0010-4655\(92\)90082-A](https://doi.org/10.1016/0010-4655(92)90082-A)
- [274] B. Andersson, G. Gustafson, and B. Nilsson-Almqvist, *A Model for Low p_T Hadronic Reactions, with Generalizations to Hadron - Nucleus*

- and Nucleus-Nucleus Collisions*, Nucl. Phys. B **281**, 289 (1987). [10.1016/0550-3213\(87\)90257-4](https://doi.org/10.1016/0550-3213(87)90257-4)
- [275] G. Aad and others, *Measurement of the centrality dependence of the charged particle pseudorapidity distribution in lead-lead collisions at $\sqrt{s_{\text{NN}}} = 2.76$ TeV with the ATLAS detector*, Phys. Lett. B **710**, 363 (2012). [10.1016/j.physletb.2012.02.045](https://doi.org/10.1016/j.physletb.2012.02.045)
- [276] J. Adam and others, *Centrality evolution of the charged-particle pseudorapidity density over a broad pseudorapidity range in Pb–Pb collisions at $\sqrt{s_{\text{NN}}} = 2.76$ TeV*, Phys. Lett. B **754**, 373 (2016). [10.1016/j.physletb.2015.12.082](https://doi.org/10.1016/j.physletb.2015.12.082)
- [277] J. Adam and others, *Centrality dependence of the pseudorapidity density distribution for charged particles in Pb–Pb collisions at $\sqrt{s_{\text{NN}}} = 5.02$ TeV*, Phys. Lett. B **772**, 567 (2017). [10.1016/j.physletb.2017.07.017](https://doi.org/10.1016/j.physletb.2017.07.017)
- [278] Z.-W. Lin, C. M. Ko, B.-A. Li, B. Zhang, and S. Pal, *A Multi-phase transport model for relativistic heavy ion collisions*, Phys. Rev. C **72**, 64901 (2005). [10.1103/PhysRevC.72.064901](https://doi.org/10.1103/PhysRevC.72.064901)
- [279] B. Zhang, *ZPC 1.0.1: A Parton cascade for ultrarelativistic heavy ion collisions*, Comput. Phys. Commun. **109**, 193 (1998). [10.1016/S0010-4655\(98\)00010-1](https://doi.org/10.1016/S0010-4655(98)00010-1)
- [280] B.-A. Li and C. M. Ko, *Formation of superdense hadronic matter in high-energy heavy ion collisions*, Phys. Rev. C **52**, 2037 (1995). [10.1103/PhysRevC.52.2037](https://doi.org/10.1103/PhysRevC.52.2037)
- [281] S. K. Malik, S. Sharma, and R. Gupta, *Event-by-event local multiplicity fluctuations in charged particle production at the LHC energies with ALICE*, DAE Symp. Nucl. Phys. **67**, 1003 (2024).

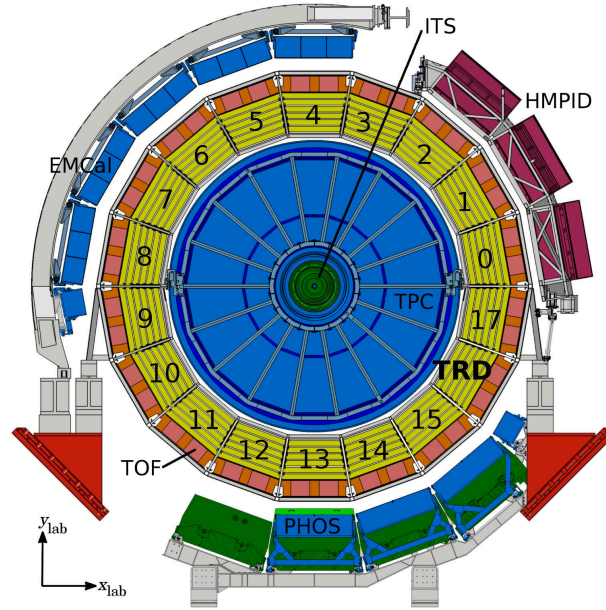
Appendix A : SERVICE WORK IN TRD

To ensure the successful operation and data collection of the ALICE experiment during LHC Runs, a comprehensive set of tasks categorized as service work has been established. This encompasses various essential activities, including detector maintenance, operational management, calibration, quality control, data processing, outreach initiatives, and coordination of managerial responsibilities within the ALICE collaboration. Doctoral candidates are required to complete a minimum of six months of service work. My service work was related to “TRD (Transition Radiation Detector) Tracking Quality Control (QC)”. The primary objective was to create important histograms in the TRD tracking QC framework, which are essential for monitoring the performance of the TRD tracking during data taking. The following sections introduce TRD, QC framework, and the specific tasks performed during my service work.

A.1 Transition Radiation Detector

The Transition Radiation Detector (TRD) [1] is an essential component designed to enhance electron identification at high transverse momentum ($p_T > 1 \text{ GeV}/c$). Its primary purpose is to facilitate measurements of light and heavy vector mesons, the dilepton continuum, and electrons resulting from open heavy flavor decays. Additionally, the TRD’s triggering capabilities are crucial for increasing the sample sizes of specific particles, such as Y mesons, high p_T J/ψ , high-mass dilepton pairs, and jets at elevated transverse momentum. Beyond its identification and triggering functions, the TRD also plays a significant role in calibration and track reconstruction at mid-rapidity.

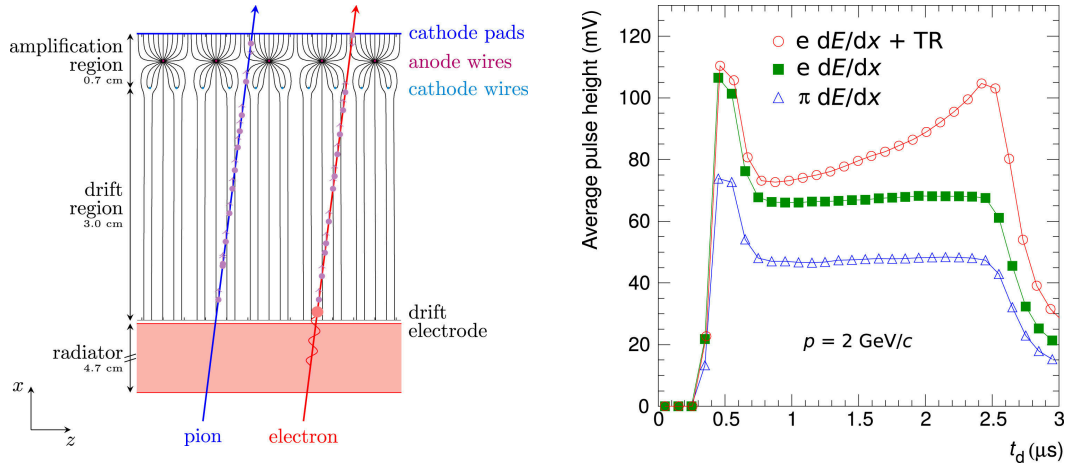
Positioned just outside the Time Projection Chamber (TPC), the TRD covers a pseudorapidity range of $-0.84 < \eta < 0.84$ and spans the full azimuthal angle. It consists of 18 supermodules as shown in fig:figa.1, each typically containing five stacks of six layers of readout chambers. Notably, three stacks located in front of the PHOS detector are omitted, resulting in a total of 522 readout chambers within the TRD. The TRD is filled with a gas mixture of xenon (Xe) and carbon dioxide (CO_2), with a nominal composition of 85% Xe and 15% CO_2 . The particle identification capability of the TRD is based on two mechanisms:

**FIGURE A.1:**

Schematic cross-section of the ALICE detector in the LHC beam direction [1].

the ionization of the gas and the emission of transition radiation (TR) by highly relativistic electrons. Transition radiation occurs when a highly relativistic particle (with Lorentz factor $\gamma > 1000$) crosses the boundary between two materials with different dielectric constants. To enhance radiation yield, multiple layers are necessary; this is achieved in the TRD using a radiator made from a fiber/foam sandwich. The emitted radiation is primarily in the X-ray domain and is very forward-peaked. For typical TR photon energies, the absorption length in xenon is less than a centimeter. This characteristic leads to a unique ionization signature at the beginning of the gas layer when TR emission occurs. In contrast, pions in the relevant momentum range do not reach high enough relativistic speeds ($\gamma < 1000$) to emit transition radiation as they pass through the radiator; however, they still ionize the gas according to the Bethe-Bloch equation.

Left panel of **Figure A.2** shows the working principle of TRD. When an electron traverses the radiator, it emits transition radiation that is absorbed at the beginning of the drift region. Additionally, as it passes through, it ionizes the gas volume. The generated charges drift toward an amplification region where avalanches occur, inducing signals on cathode pads. The average signal as a function of arrival time for pions and electrons (with and without TR) is depicted in fig:figa.2. At early times, avalanches are generated from both sides of the anode wires in the amplification region, resulting in a pronounced peak in signal detection. Subsequently, ionization from the drift region is detected, with TR-induced ionization yielding a peak at later times. The time structure of these signals is exploited through various particle identification (PID) methods to effectively separate electrons from pions. This capability is vital for enhancing

**FIGURE A.2:**

Left: Illustration of generated ionization along the path of electrons and pions through a TRD chamber. **Right:** Measured average puls height distribution as a function of the signal arrival time.

measurement precision in high-energy physics experiments, particularly those involving heavy-ion collisions where distinguishing between different particle types can significantly impact data analysis and interpretation.

A.2 Quality Control

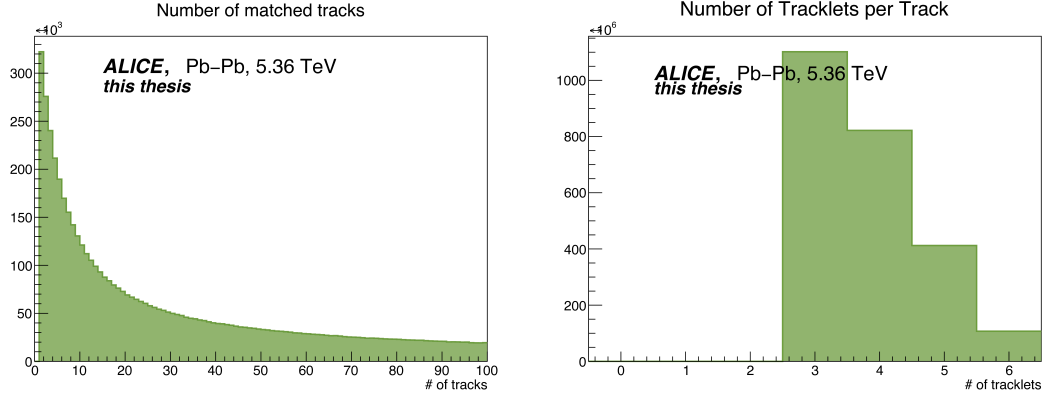
Modern physics experiments generate vast quantities of data that necessitate meticulous quality monitoring and assessment. Data Quality Monitoring (DQM) systems play a crucial role in identifying issues related to particle detectors, data transfer, and initial processing, where prompt and precise feedback is essential. These systems are complemented by Quality Assurance (QA) systems, which facilitate comprehensive evaluations of data quality before the data is prepared for physical analyses. Beginning in 2022, the QC (Quality Control) system started operating in ALICE [2,4,5] alongside the main computing software to manage the acquisition of a raw data stream at an impressive rate of 3.5 TB/s, while also performing on-the-fly compression and final quality assessments [2,4]. This integration allows the QC framework to merge the functionalities of both DQM and QA into a cohesive system. The QC framework [2] is engineered as a highly parallel system, capable of distributing computations across thousands of nodes, ensuring efficiency and scalability in processing large datasets. It comprises several key components given as:

- **Data Sampling:** It is responsible for selecting and distributing data samples based on configurable policies. These policies include methods such as pseudo-random sampling of parallel data, filtering messages by size, and applying custom filters. The core element of this process is the Dispatcher, which operates on each node where data sampling occurs and can be reconfigured during data collection.

- **QC Tasks:** consist of detector-specific algorithms executed either within the main data processing chain (on the FLPs or EPNs) or remotely on dedicated Quality Control Servers. The outputs generated from these tasks are referred to as QC Objects (or Monitor Objects), typically represented as ROOT histograms. When tasks are executed on multiple servers simultaneously, their partial results must be consolidated into complete datasets, a function managed by the Mergers[5].
- **Checkers:** perform automated evaluations of data quality by executing predefined algorithms on QC Objects. They adhere to a standard interface that supports a generic set of reusable checks alongside user-defined algorithms.
- **Aggregators:** enable users to merge detailed quality metrics into broader results that reflect the overall performance of a sub-detector.
- **Storage and Interaction:** The QC Objects and Quality Objects are stored within the QC repository. Ongoing research within the upgrade project explores machine learning techniques for conducting more advanced checks across multidimensional parameter spaces, potentially interacting directly with the repository or utilizing Checkers.
- **Post-processing Module:** executes tasks asynchronously relative to the main data flow, using data derived from QC and Quality Objects. This module can be activated manually, at regular intervals, or triggered by specific events (e.g., the start of an LHC fill or the conclusion of a data acquisition run). The outcomes are either stored directly in a database or reintegrated into the QC processing workflow.
- **User Interface:** The experiment shift crew and experts can utilize the QC GUI (QCG) to visualize stored QC Objects and Quality Objects. A user-friendly interface facilitates navigation through these objects and their display using JSROOT.

A.3 TRD Tracking QC

In ALICE data taking period of Run III, the TRD is not operating in continuous mode as it did in Runs I and II; instead, it will function exclusively in triggered mode. This shift is primarily due to bandwidth limitations, necessitating a more efficient use of available data channels. The current offline reconstruction uses clusters to form offline tracklets. These reconstructed offline tracklets contain more information than online tracklets but are not available in Run III. The readout process will now focus on tracklets, which are preliminary track segments calculated within the detector's Front-End Electronics (FEE). This change aims to optimize the data flow and ensure that only relevant information is processed for triggering events of high transverse momentum. The development

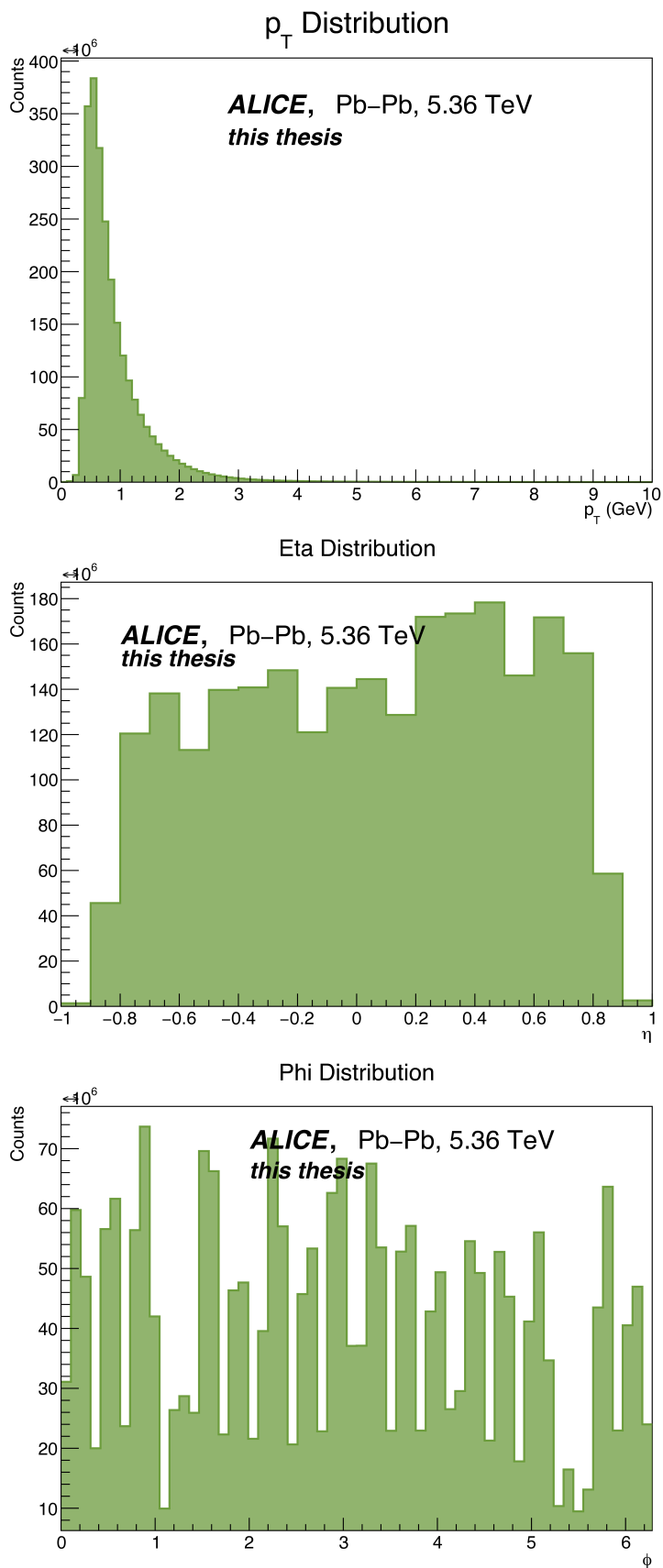
**FIGURE A.3:**

TRD QC: Number of matched TRD tracks and number of tracklets per matched TRD track.

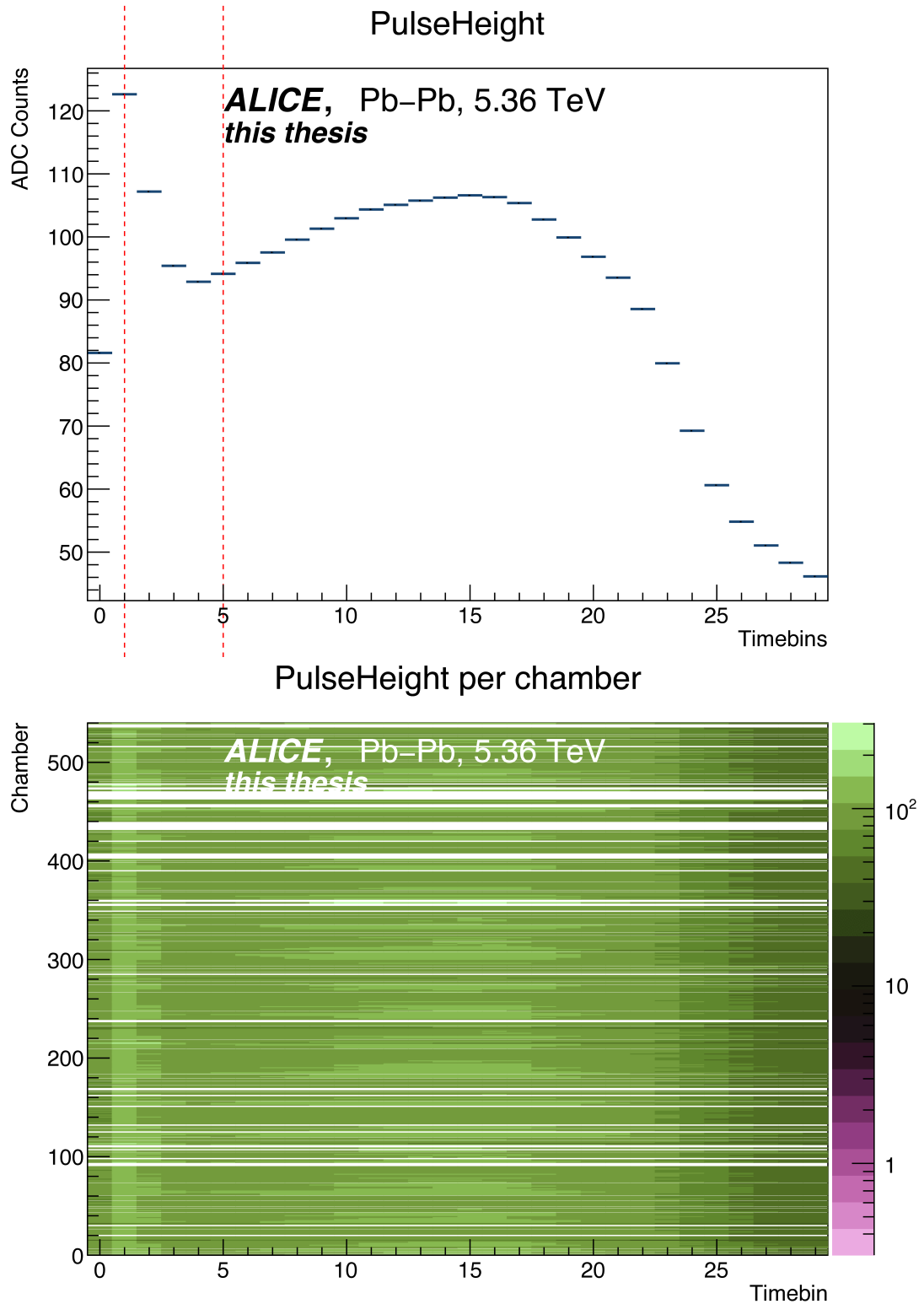
of tracking algorithms for TRD are discussed in [3]. The algorithms are plugged in O2, and then used by QC task to give output in ALICE QCG website [6].

During the service work, QC task was created to monitor the performance of the TRD tracking. The task generates histograms that are stored in the QC repository [5]. The histograms are then evaluated by the checkers to ensure that the TRD tracking is functioning correctly. The number of TRD tracks after matching with ITS, TPC and number tracklets per matched TRD track is shown in **Figure A.3**. **Figure A.4** shows the p_T , η and φ distributions of TRD tracks after matching with ITS and TPC. PulseHeight spectrum for these matched tracks as a function of drift time is shown in **Figure A.5**. The number of matched tracks in a chamber wise of TRD are given in **Figure A.6**. The η vs φ distributions showing the chamber wise view, six layers of TRD for matched TRD positive (**Figure A.7**), negative (**Figure A.8**) charged matched tracks. Average number of tracklets is shown in the same chamber wise view is shown in **Figure A.9** for all TRD matched tracks, **Figure A.10** for positive and negative charged matched tracks. All the distributions are from Pb–Pb collisions at $\sqrt{s_{NN}} = 5.36$ TeV. The run number is 559903 from LHC24ar. All the histograms are taken from AliQCG website [6] and created from the two main QC tasks worked on during the service work.

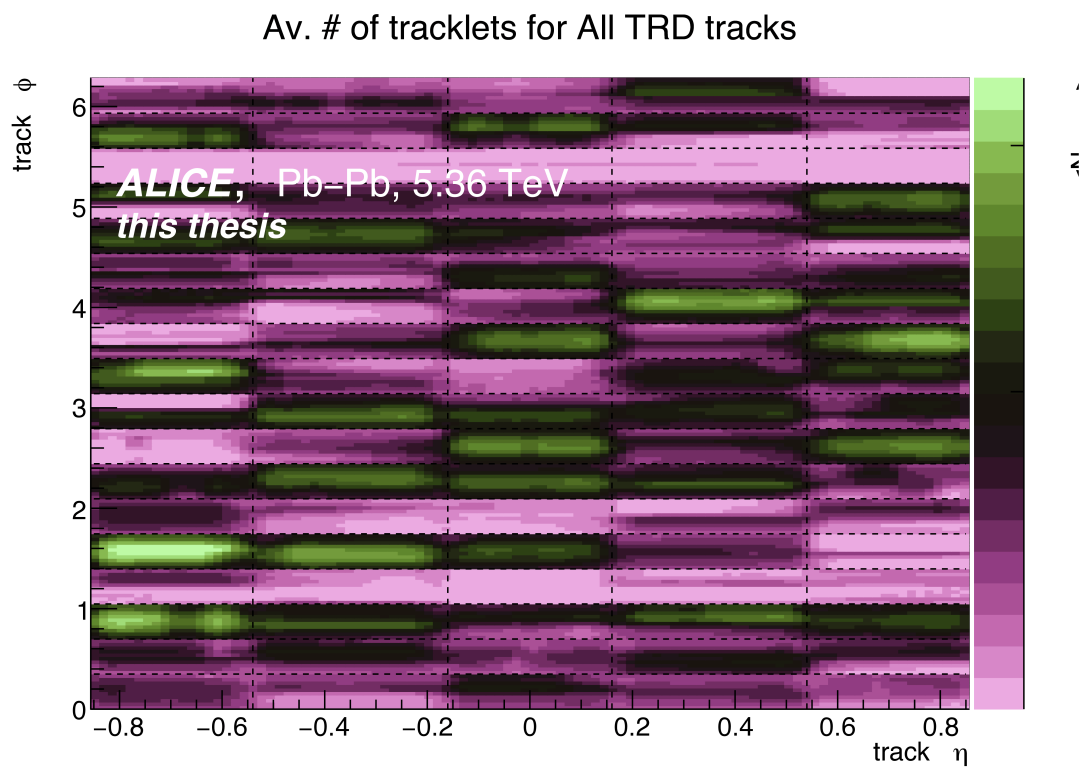
- **Tracking_QC Task**: creates histograms related to tracking performance of TRD.
- **TRD PulseHeight_QC Task**: creates PulseHeight histogram from TRD track matched to ITS–TPC.

**FIGURE A.4:**

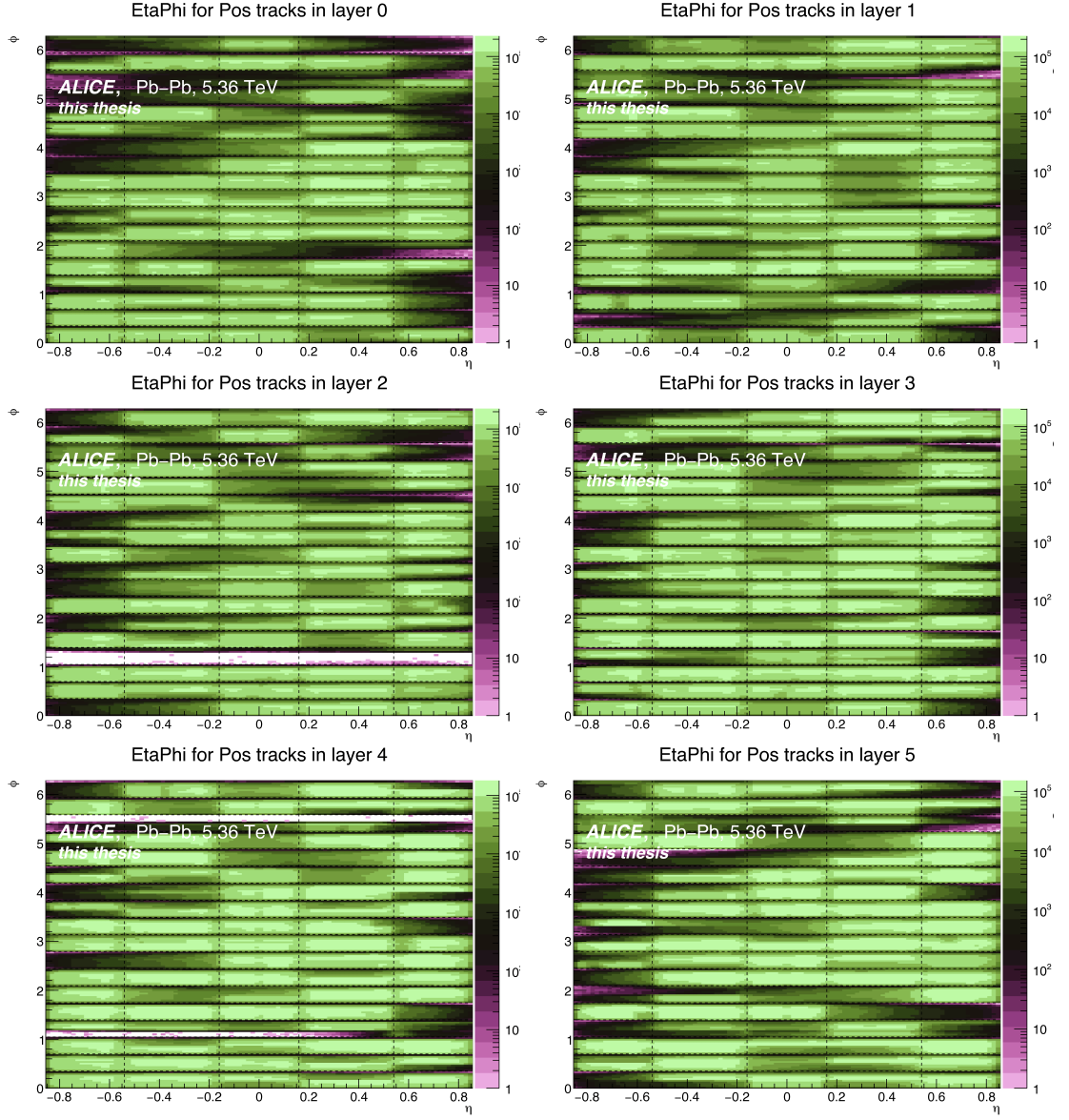
TRD QC: p_T , η , ϕ distributions for TRD matched ITS-TPC tracks.

**FIGURE A.5:**

TRD QC: Average pulse height vs. drift time plot (top), pulse height for each chamber vs. drift time plot (bottom) for matched TRD tracks.

**FIGURE A.6:**

TRD QC: η, φ distribution for all matched TRD tracks giving chamber wise view of TRD.

**FIGURE A.7:**

TRD QC: η, ϕ distribution for positive charged matched TRD tracks giving chamber wise view for the six layers of TRD.

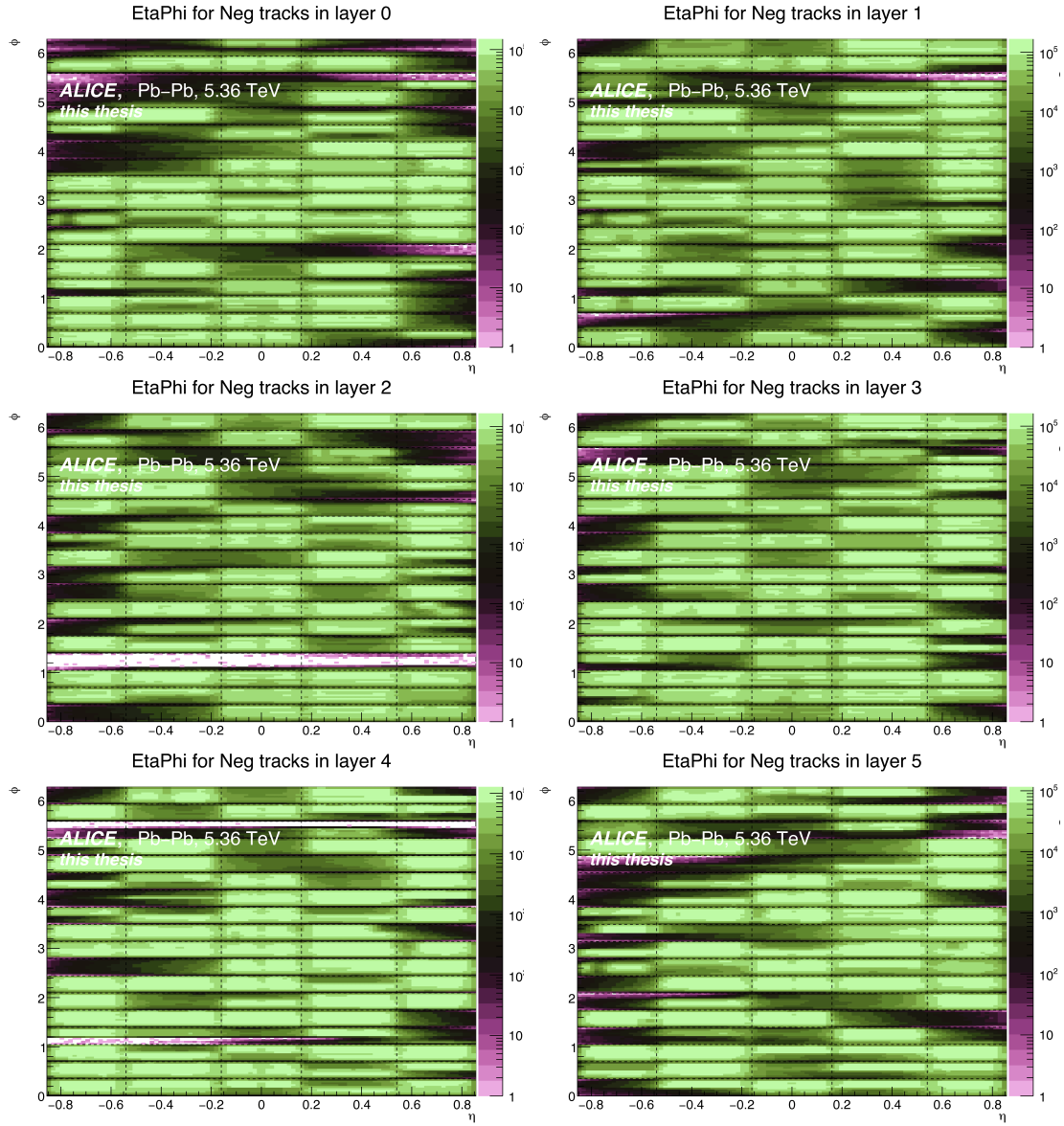
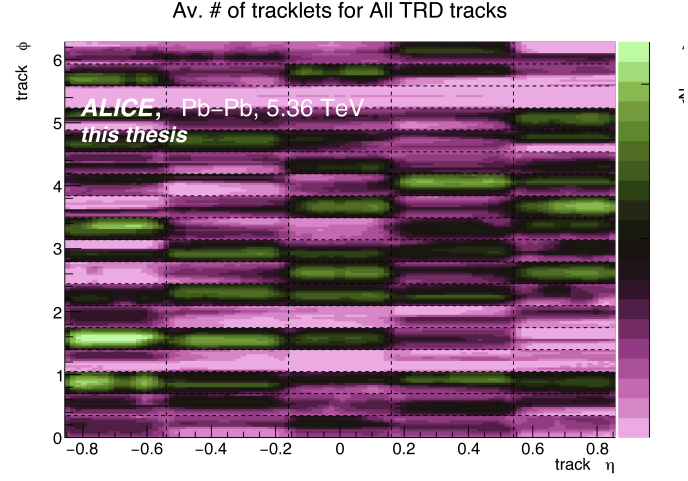
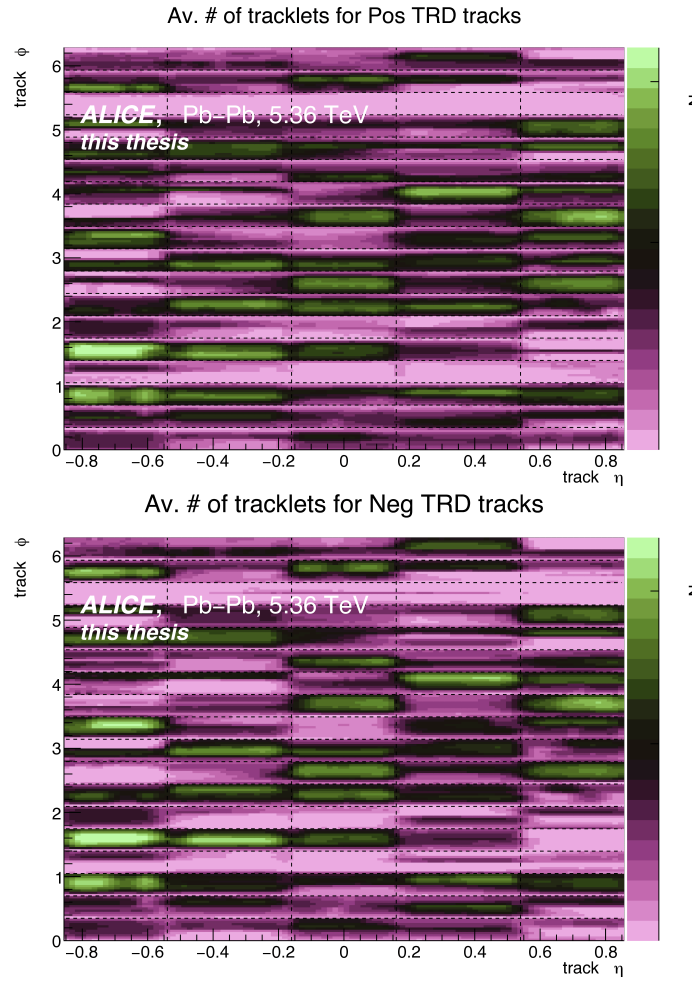


FIGURE A.8:

TRD QC: η, ϕ distribution for negative charged matched TRD tracks giving chamber wise view for the six layers of TRD.

**FIGURE A.9:**

TRD QC: η, φ distribution giving chamber wise view of the average number of tracklets for matched TRD tracks.

**FIGURE A.10:**

TRD QC: η, φ distribution giving chamber wise view of the average number of tracklets for matched positive and negative charged TRD tracks.

References

- [1] ALICE Collaboration, *The ALICE Transition Radiation Detector: construction, operation, and performance*, Nucl. Instrum. Meth. A 881 88-127 (2018).
- [2] ALICE Collaboration, *The ALICE O2 data quality control system*, EPJ Web Conf 245 01027 (2020).
- [3] M. O. Schmidt, *Space-point calibration of the ALICE TPC with track residuals*, EPJ Web Conf 245 01003 (2020).
- [4] P. Konopka, *Design and evaluation of data quality control methods for a very high bandwidth data acquisition and processing system in the future CERN/ALICE O2 framework*, AGH UST Cracow, Poland (2021).
- [5] ALICE Quality Control Repository, “<https://github.com/AliceO2Group/QualityControl>”, Accessed: 2024.
- [6] ALICE Quality Control GUI, “<https://ali-qcg.cern.ch/>”, Accessed: 2024. "

Appendix B : ANALYSIS CODES AND DATA LISTS

All analysis codes are available in AliPhysics git repository at [AliPhysics/PWGCF/EBYE/IntermittencyAnalysis/](https://github.com/AliPhysics/PWGCF/EBYE/IntermittencyAnalysis/).

In this appendix, the data taking periods and reconstruction passes used in the present work are specified. For each combination of period and pass, numbers of the runs which are selected for the analysis are listed.

B.1 ALICE Data

1. **Name:** LHC15o_pass2_AOD252,
data pattern: /pass2/AOD252/*AliAOD.root,
data directory: /alice/data/2015/LHC15o,
data type: AOD,
run list: 246994, 246991, 246989, 246984, 246982, 246948, 246945, 246928, 246871, 246870, 246867, 246865, 246864, 246859, 246858, 246851, 246847, 246846, 246845, 246844, 246810, 246809, 246808, 246807, 246805, 246804, 246766, 246765, 246763, 246760, 246759, 246758, 246757, 246751, 246750, 246434, 246431, 246424, 246392, 246391, 246276, 246275, 246272, 246271, 246225, 246222, 246217, 246185, 246182, 246181, 246180, 246178, 246153, 246152, 246151, 246148, 246115, 246113, 246089, 246087, 246053, 246052, 246049, 246048, 246042, 246037, 246036, 246012, 246003, 246001, 245963, 245954, 245952, 245949, 245923, 245833, 245831, 245829, 245793, 245785, 245775, 245766, 245759, 245752, 245731, 245729, 245705, 245702, 245692, 245683, 245554, 245545, 245544, 245543, 245542, 245540, 245535, 245507, 245505, 245504, 245501, 245497, 245496, 245454, 245453, 245450, 245446, 245441, 245411, 245410, 245409, 245407, 245401, 245397, 245396, 245353, 245349, 245347, 245346, 245345, 245343, 245259, 245233, 245232, 245231, 245152, 245151, 245146, 245145, 245068, 245066, 245064, 244983, 244982, 244980, 244975, 244918, 244917.
2. **Name:** LHC18q_pass3_AOD252,
data pattern: /pass3/AOD252/*AliAOD.root,
data directory: /alice/data/2018/LHC18q,
data type: AOD,

run list: 295581, 295584, 295585, 295586, 295587, 295588, 295589, 295610, 295611, 295612, 295615, 295665, 295666, 295667, 295668, 295671, 295673, 295675, 295676, 295677, 295712, 295714, 295717, 295718, 295719, 295720, 295721, 295723, 295725, 295753, 295754, 295755, 295756, 295758, 295759, 295762, 295763, 295786, 295788, 295791, 295816, 295818, 295819, 295822, 295825, 295826, 295829, 295831, 295853, 295854, 295855, 295856, 295859, 295860, 295861, 295881, 295908, 295909, 295910, 295913, 295936, 295937, 295941, 295942, 295943, 295945, 295947, 296016, 296060, 296061, 296062, 296063, 296065, 296066, 296068, 296074, 296123, 296132, 296133, 296134, 296135, 296142, 296143, 296191, 296192, 296194, 296195, 296196, 296197, 296198, 296240, 296241, 296242, 296243, 296244, 296246, 296247, 296269, 296270, 296273, 296279, 296280, 296303, 296304, 296307, 296309, 296312, 296375, 296376, 296377, 296378, 296379, 296380, 296381, 296383, 296414, 296415, 296419, 296420, 296423, 296424, 296433, 296472, 296509, 296510, 296511, 296512, 296514, 296516, 296547, 296548, 296549, 296550, 296551, 296552, 296553, 296594, 296615, 296616, 296618, 296619, 296621, 296622, 296623.

3. **Name:** LHC18r_pass3_AOD252,

data pattern: /pass2/AOD252/*AliAOD.root,

data directory: /alice/data/2018/LHC18r,

data type: AOD,

run list: 297117, 297118, 297119, 297123, 297124, 297312, 297315, 297317, 297332, 297333, 297335, 297336, 297363, 297366, 297367, 297372, 297379, 297380, 297405, 297406, 297413, 297414, 297415, 297441, 297442, 297446, 297450, 297451, 297452, 297479, 297481, 297483, 297512, 297537, 297540, 297541, 297542, 297544, 297558, 297588, 297590, 297595, 297624.

B.2 Monte Carlo Productions:

1. **Name:** LHC20j6a_AOD243,

data pattern: /AOD243/*AliAOD.root,

data directory: /alice/sim/2020/LHC20j6a/,

data type: AOD,

run list: 244917, 244918, 244975, 244980, 244982, 244983, 245061, 245064, 245066, 245068, 245145, 245146, 245148, 245151, 245152, 245231, 245232, 245233, 245259, 245343, 245345, 245346, 245347, 245349, 245353, 245396, 245397, 245401, 245407, 245409, 245410, 245411, 245439, 245441, 245446, 245450, 245452, 245453, 245454, 245496, 245497, 245501, 245504, 245505, 245507, 245535, 245540, 245542, 245543, 245544, 245545, 245554, 245683, 245692, 245700, 245702, 245705, 245729, 245731, 245738, 245752, 245759, 245766, 245775, 245785, 245793, 245829, 245831, 245833, 245923, 245949, 245952, 245954, 245963, 246001, 246003, 246012, 246036, 246037, 246042,

246048, 246049, 246052, 246053, 246087, 246089, 246113, 246115, 246148, 246151, 246152, 246153, 246178, 246180, 246181, 246182, 246185, 246217, 246222, 246225, 246271, 246272, 246275, 246276, 246390, 246391, 246392, 246424, 246428, 246431, 246434, 246487, 246488, 246493, 246495, 246540, 246543, 246553, 246567, 246568, 246575, 246583, 246648, 246671, 246675, 246676, 246750, 246751, 246757, 246758, 246759, 246760, 246763, 246765, 246766, 246804, 246805, 246807, 246808, 246809, 246810, 246844, 246845, 246846, 246847, 246851, 246858, 246859, 246864, 246865, 246867, 246870, 246871, 246928, 246945, 246948, 246980, 246982, 246984, 246989, 246991, 246994.

2. **Name:** LHC20e3a_AOD243,

data pattern: /AOD243/*AliAOD.root,

data directory: alice/sim/2020/LHC20e3a,

data type: AOD,

run list: 295585, 295586, 295587, 295588, 295589, 295610, 295611, 295612, 295615, 295665, 295666, 295667, 295668, 295671, 295673, 295675, 295676, 295677, 295712, 295714, 295717, 295718, 295719, 295721, 295723, 295725, 295753, 295754, 295755, 295756, 295758, 295759, 295762, 295763, 295786, 295788, 295791, 295816, 295818, 295819, 295822, 295825, 295826, 295829, 295831, 295853, 295854, 295855, 295856, 295859, 295860, 295861, 295881, 295908, 295909, 295910, 295913, 295936, 295937, 295941, 295942, 295943, 295945, 295947, 296016, 296060, 296061, 296062, 296063, 296065, 296066, 296068, 296074, 296123, 296132, 296133, 296134, 296135, 296142, 296143, 296191, 296192, 296194, 296195, 296196, 296197, 296198, 296240, 296241, 296242, 296243, 296244, 296246, 296247, 296269, 296270, 296273, 296279, 296280, 296303, 296304, 296307, 296309, 296312, 296375, 296376, 296377, 296378, 296379, 296380, 296381, 296383, 296414, 296415, 296419, 296420, 296423, 296424, 296433, 296472, 296509, 296510, 296511, 296512, 296514, 296516, 296547, 296548, 296549, 296550, 296551, 296552, 296553, 296594, 296615, 296616, 296618, 296619, 296621, 296622, 296623, 296690, 296691, 296693, 296694, 296749, 296750, 296752, 296781, 296784, 296785, 296786, 296787, 296790, 296793, 296794, 296799, 296835, 296836, 296838, 296839, 296848, 296849, 296850, 296851, 296852, 296890, 296894, 296899, 296900, 296903, 296930, 296931, 296932, 296934, 296935, 296938, 296941, 296966, 297029, 297031, 297035, 297085, 297117, 297118, 297119, 297123, 297124, 297128, 297129, 297132, 297133, 297193, 297194, 297195, 297196, 297218, 297219, 297221, 297222, 297278, 297310, 297311, 297312, 297315, 297317, 297332, 297333, 297335, 297336, 297363, 297366, 297367, 297372, 297379, 297380, 297405, 297406, 297413, 297414, 297415, 297441, 297442, 297446, 297450, 297451, 297452, 297479, 297481, 297483, 297512, 297537, 297540, 297541, 297542, 297544, 297558, 297588, 297590, 297595.

3. **Name:** EPOSLHC GEN LHC22d1d2,
data pattern: /alice/sim/2022/LHC22d1d2,
data directory: /*/*galice.root ,
data type: galice.root,
run list: 244917, 244918, 244975, 244980, 244982, 244983, 245064, 245066, 245068, 245145, 245146, 245151, 245152, 245231, 245232, 245233, 245259, 245343, 245345, 245346, 245347, 245349, 245353, 245396, 245397, 245401, 245407, 245409, 245410, 245411, 245439, 245441, 245446, 245450, 245452, 245453, 245454, 245496, 245497, 245501, 245504, 245505, 245507, 245535, 245540, 245542, 245543, 245544, 245545, 245554, 245683, 245692, 245700, 245702, 245705, 245729, 245731, 245738, 245752, 245759, 245766, 245775, 245785, 245793, 245829, 245831, 245833, 245923, 245949, 245952, 245954, 245963, 246001, 246003, 246012, 246036, 246037, 246042, 246048, 246049, 246052, 246053, 246087, 246089, 246113, 246115, 246148, 246151, 246152, 246153, 246178, 246180, 246181, 246182, 246185, 246217, 246222, 246225, 246271, 246272, 246275, 246276, 246390, 246391, 246392, 246424, 246428, 246431, 246434, 246675, 246676, 246750, 246751, 246757, 246758, 246759, 246760, 246763, 246765, 246766, 246804, 246805, 246807, 246808, 246809, 246810, 246844, 246845, 246846, 246847, 246851, 246858, 246859, 246864, 246865, 246867, 246870, 246871, 246928, 246945, 246948, 246980, 246982, 246984, 246989, 246991, 246994.
4. **Name:** EPOSLHC GEN LHC22d1c2,
data pattern: /alice/sim/2022/LHC22d1c2,
data directory: /*/*galice.root ,
data type: galice.root,
run list: 295585, 295586, 295587, 295588, 295589, 295610, 295611, 295612, 295615, 295665, 295666, 295667, 295668, 295671, 295673, 295675, 295676, 295677, 295712, 295714, 295717, 295718, 295719, 295721, 295723, 295725, 295753, 295754, 295755, 295758, 295759, 295762, 295763, 295786, 295788, 295791, 295816, 295818, 295819, 295822, 295825, 295826, 295829, 295831, 295853, 295854, 295855, 295856, 295859, 295860, 295861, 295881, 295908, 295909, 295910, 295913, 295936, 295937, 295941, 295942, 295943, 295945, 295947, 296016, 296060, 296062, 296063, 296065, 296066, 296068, 296074, 296123, 296132, 296133, 296134, 296135, 296142, 296143, 296191, 296192, 296194, 296195, 296196, 296197, 296198, 296240, 296241, 296242, 296243, 296244, 296246, 296247, 296269, 296270, 296273, 296279, 296280, 296303, 296304, 296307, 296309, 296312, 296375, 296376, 296377, 296378, 296379, 296380, 296381, 296383, 296414, 296415, 296419, 296420, 296423, 296424, 296433, 296472, 296509, 296510, 296511, 296512, 296516, 296547, 296548, 296550, 296551, 296552, 296553, 296594, 296615, 296616, 296618, 296619, 296621, 296622, 296623, 296690, 296691, 296693, 296694, 296749, 296750,

296752, 296781, 296784, 296785, 296786, 296787, 296790, 296793, 296794, 296799, 296835, 296836, 296838, 296839, 296848, 296849, 296850, 296851, 296852, 296890, 296894, 296899, 296900, 296903, 296930, 296931, 296932, 296934, 296935, 296938, 296941, 296966, 297029, 297031, 297035, 297085, 297117, 297118, 297119, 297123, 297124, 297128, 297129, 297132, 297133, 297193, 297194, 297195, 297196, 297218, 297219, 297221, 297222, 297278, 297310, 297311, 297312, 297315, 297317, 297332, 297333, 297335, 297336, 297363, 297366, 297367, 297372, 297379, 297380, 297405, 297406, 297413, 297414, 297415, 297441, 297442, 297446, 297450, 297451, 297452, 297479, 297481, 297483, 297512, 297537, 297540, 297541, 297542, 297544, 297558, 297588, 297590, 297595.

Appendix C : SUPPLEMENTARY FIGURES

C.1 Analysis of $0.4 \leq p_T \leq 0.6$ GeV/c bin

Monte Carlo closure of default p_T range $0.4 \leq p_T \leq 1.0$ GeV/c is shown in chap4. Here, small p_T bin $0.4 \leq p_T \leq 0.6$ GeV/c is discussed. It is also studied for centrality dependence. $F_q(M)$ vs $\ln M^2$ (in the upper panel) and MC closure; $F_q(M)^{\text{reco}}/F_q(M)^{\text{gen}}$ (in the lower panel) for this bin is shown in [Figure C.1](#). Closure in $q = 2, 3, 4, 5$ is compared in [Figure C.2](#).

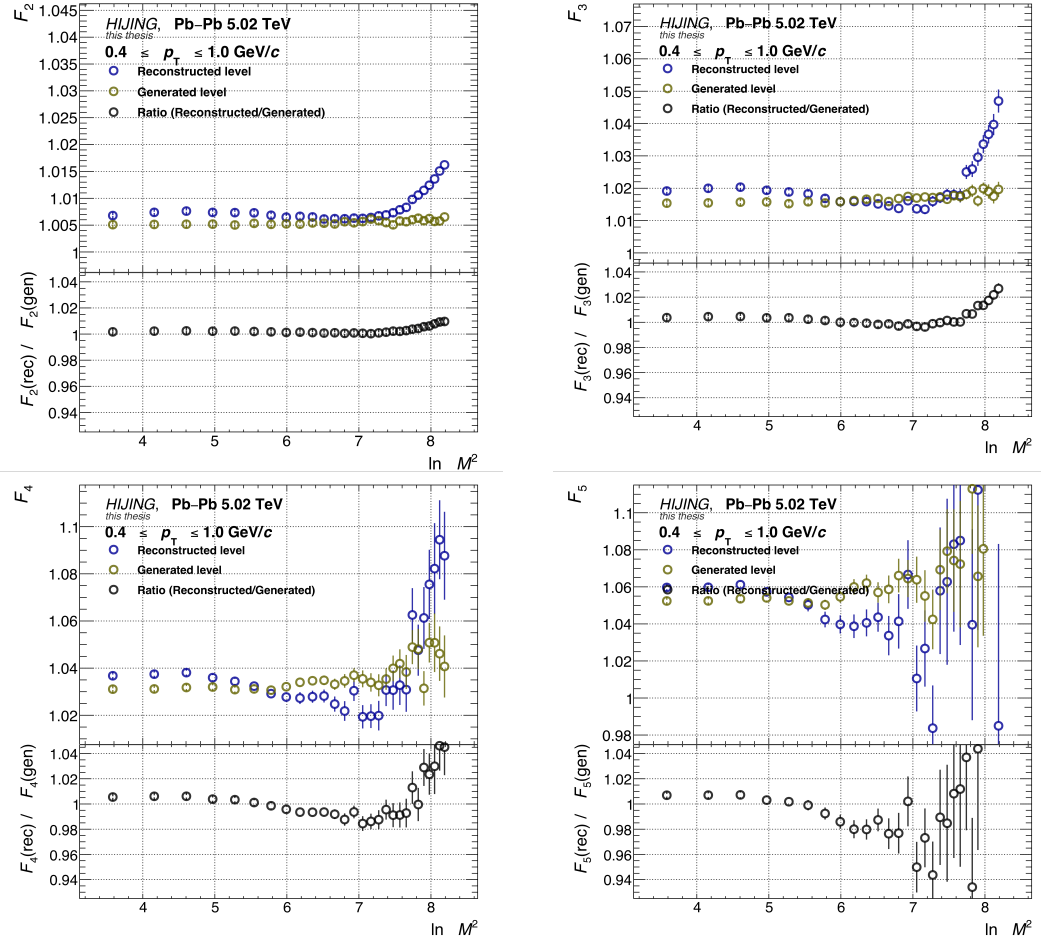
M -scaling ($\ln F_q(M)$ vs $\ln M^2$) plots are given in [Figure C.3](#) and F -scaling ($\ln F_q(M)$ vs $\ln F_2(M)$) are given in [Figure C.4](#). Both plots are shown for reconstructed and generated level tracks respectively. F -scaling line-fit are performed in higher M region for $0.4 \leq p_T \leq 0.6$ (GeV/c) to calculate β_q , $\ln \beta_q$ vs $\ln(q-1)$ is then fitted to calculate ν for reconstructed level and generated level tracks shown in $\ln F_2(M)$ vs $\ln F_q(M)$ shown in [Figure C.5](#).

C.2 Closure figures of $0.4 \leq p_T \leq 1.0$ GeV/c bin

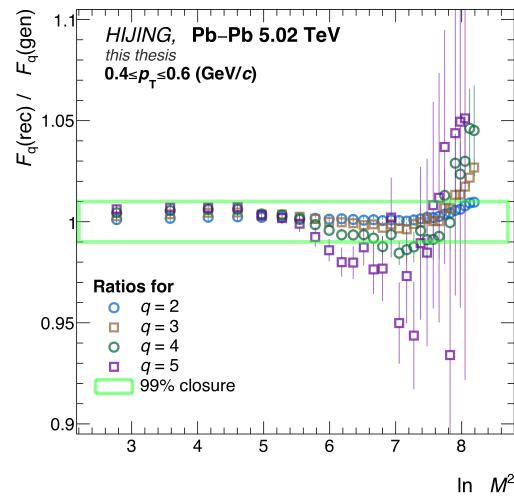
Figures showing difference in closure after using TPC shared clusters cuts are shown in [Figure C.5](#). The cuts are discussed in [Section 4.5.1.2](#) and the effect of these cuts on $q = 2$ is shown in [Figure 4.11](#). The effect on other orders ($q = 3, 4, 5$) is shown here in [Figure C.5](#).

C.3 PYTHIA8/Angantyr

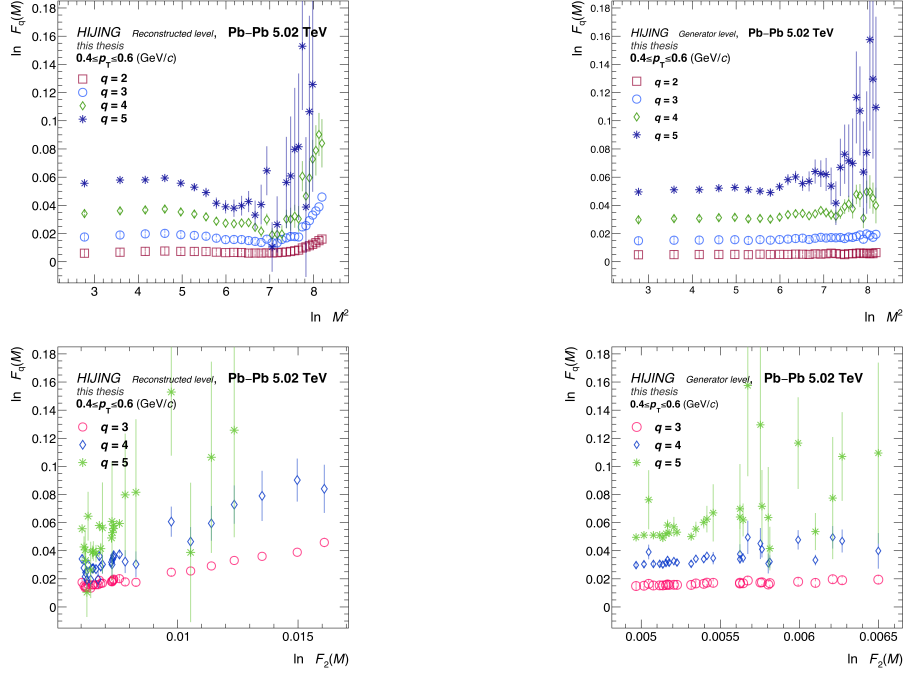
In this section, the results; $\ln F_q(M)$ vs $\ln M^2$ (M -scaling) and $\ln F_q(M)$ vs $\ln F_2(M)$ (F -scaling) plots are given for events generated for Pb-Pb collisions at $\sqrt{s_{\text{NN}}} = 2.76, 5.02$ TeV using PYTHIA8/Angantyr model. The results for most central 0–5% events are already shown in [Section 4.6](#). The figures for $\sqrt{s_{\text{NN}}} = 2.76, 5.02$ TeV in 5–10% centrality are given in [Figure C.6](#) and [Figure C.7](#).

**FIGURE C.1:**

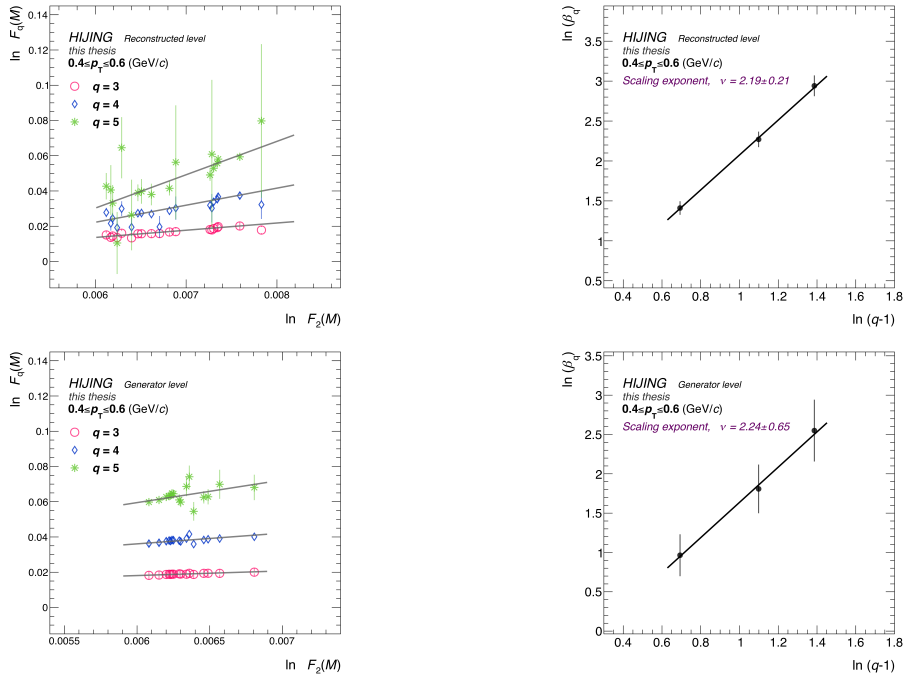
HIJING: MC closure for $0.4 \leq p_T \leq 0.6$ (GeV/c).

**FIGURE C.2:**

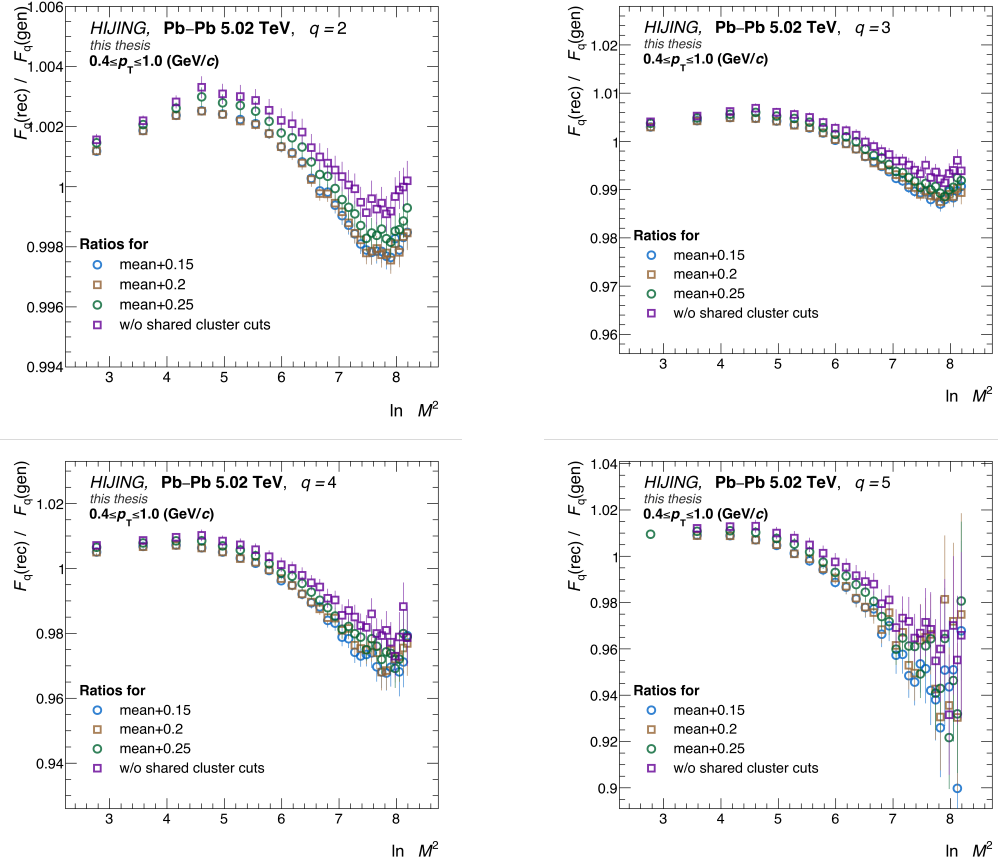
HIJING: MC closure for $F_q(M)$ ($F_q(M)^{\text{reco}}/F_q(M)^{\text{gen}}$) of charged particles in $0.4 \leq p_T \leq 0.6$ (GeV/c) for $q = 2, 3, 4, 5$. The green box shows the 99% closure window.


FIGURE C.3:

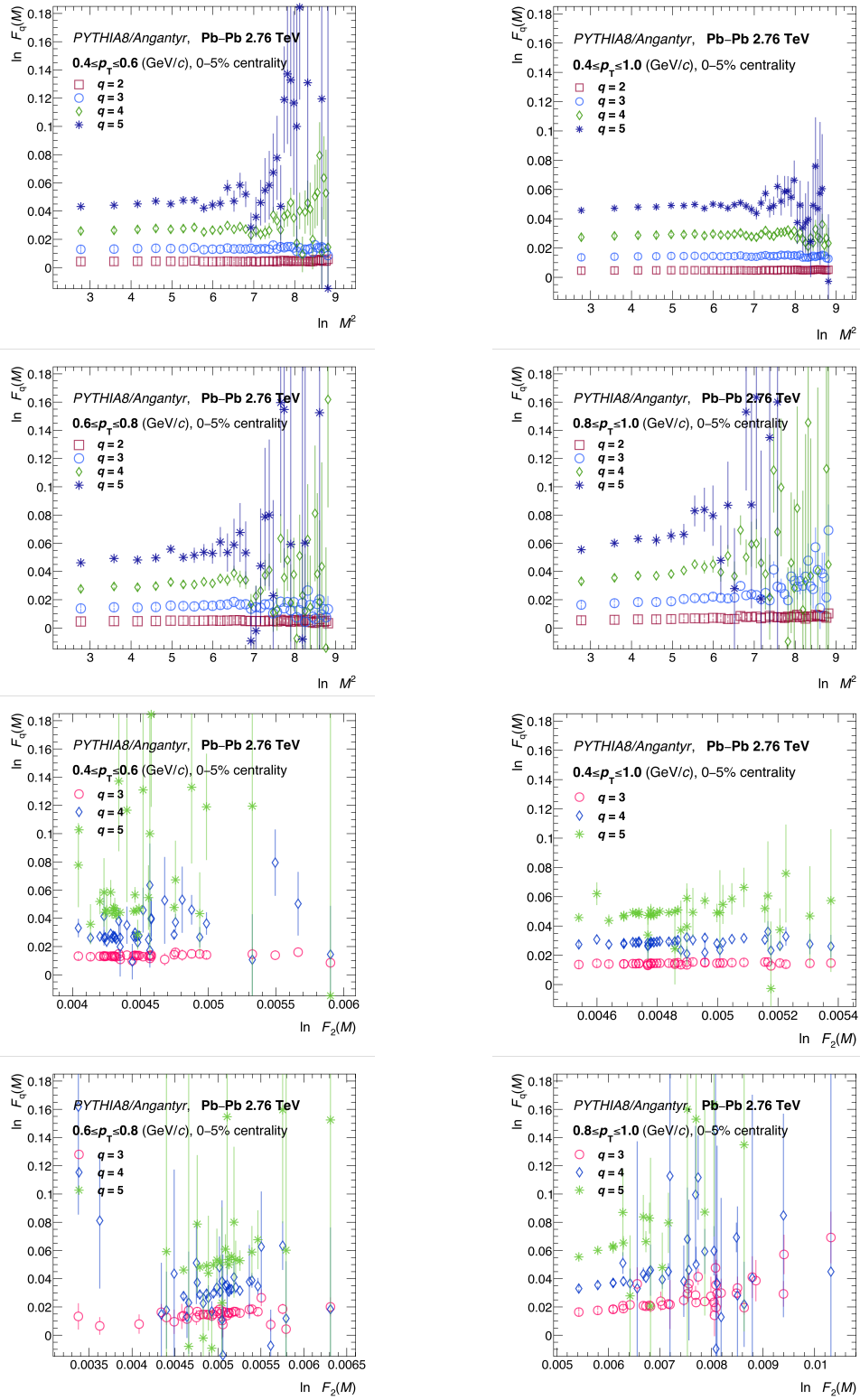
HIJING: $\ln F_q(M)$ vs $\ln M^2$ (M -scaling) plot and $\ln F_q(M)$ vs $\ln F_2(M)$ (F -scaling) plots for $0.4 \leq p_T \leq 0.6$ (GeV/c) for reconstructed level (left) and generated level (right) tracks.


FIGURE C.4:

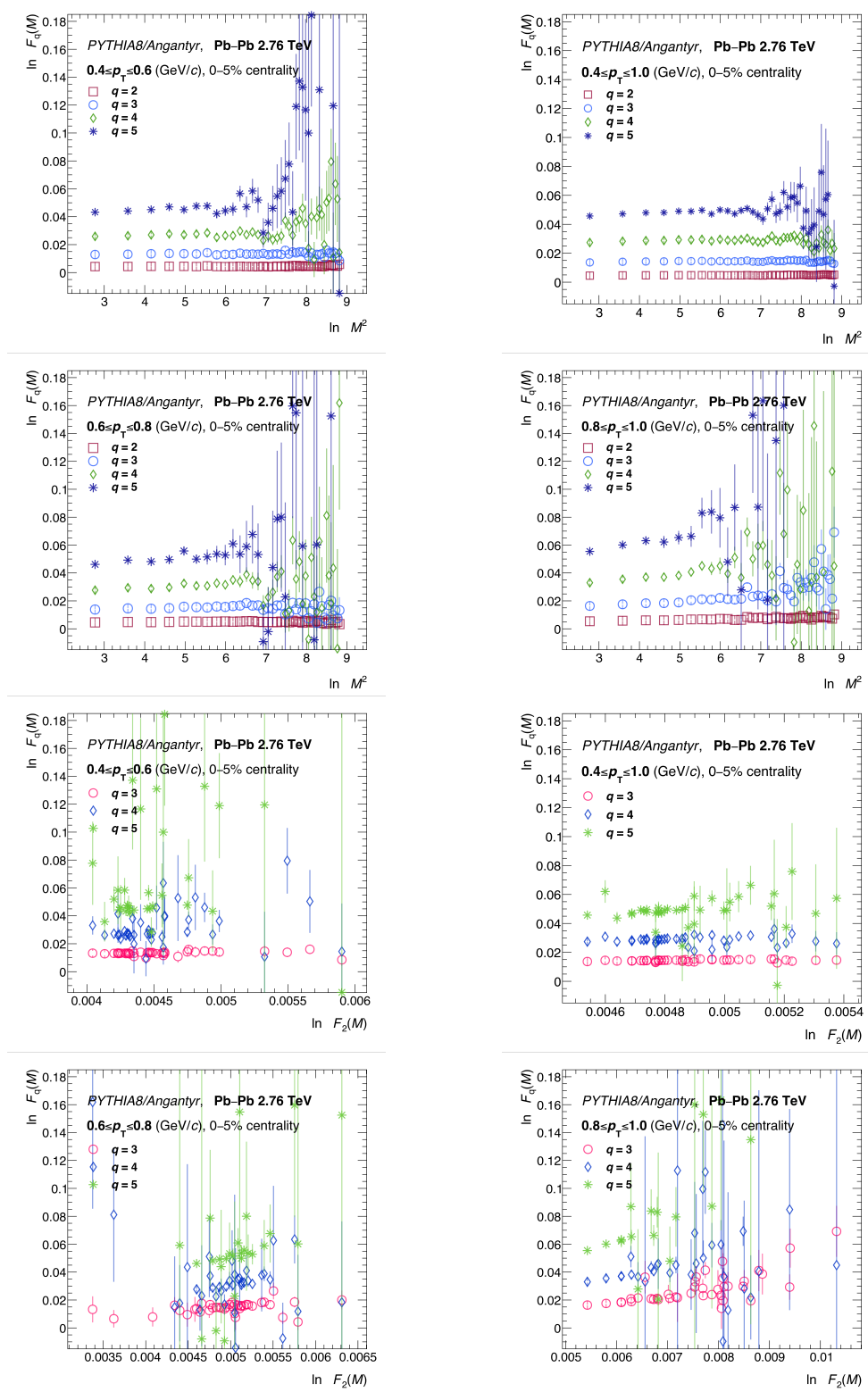
HIJING: F -scaling line-fit in higher M region for $0.4 \leq p_T \leq 0.6$ (GeV/c) to calculate β_q and ν for reconstructed level (top) and generated level (bottom) tracks.

**FIGURE C.5:**

HIJING: MC closure ratios ($F_q(M)^{\text{reco}}/F_q(M)^{\text{gen}}$) comparison for different track selection cuts for $0.4 \leq p_T \leq 1.0$ (GeV/c).


FIGURE C.6:

PYTHIA8/Angantyr $\ln F_q(M)$ vs $\ln M^2$, M -scaling and $\ln F_q(M)$ vs $\ln F_2(M)$ plot, F -scaling for $q = 2, 3, 4, 5$ (shown separately) for charged particle produced in the mid-rapidity region in $0.4 \leq p_T \leq 1.0$, $0.4 \leq p_T \leq 0.6$, $0.6 \leq p_T \leq 0.8$, $0.8 \leq p_T \leq 1.0$ GeV/c at 5–10% centrality of Pb–Pb 2.76 TeV.


FIGURE C.7:

PYTHIA8/Angantyr $\ln F_q(M)$ vs $\ln M^2$, M -scaling and $\ln F_q(M)$ vs $\ln F_2(M)$ plot, F -scaling for $q = 2, 3, 4, 5$ (shown separately) for charged particle produced in the mid-rapidity region in $0.4 \leq p_T \leq 1.0$, $0.4 \leq p_T \leq 0.6$, $0.6 \leq p_T \leq 0.8$, $0.8 \leq p_T \leq 1.0$ GeV/c at 5–10% centrality of Pb–Pb 5.02 TeV.

LIST OF PRESENTATIONS

- “Intermittency analysis of charged hadrons generated in Pb–Pb collisions at $\sqrt{s_{\text{NN}}} = 2.76$ TeV and 5.02 TeV using PYTHIA8/ Angantyr”, **LHCp** (Large Hadron Collider Physics Conference), [Virtual poster presentation](#), (Taiwan, May 2022).
- “Intermittency analysis of charged hadrons generated in Pb–Pb collision at $\sqrt{s_{\text{NN}}} = 2.76$ TeV and 5.02 TeV using PYTHIA8/Angantyr”, **ISMD 2022**, [Poster presentation](#) and [Virtual flash talk](#), (Pitlochry, Scotland 2022).
- “Intermittency analysis of charged hadrons generated in Pb-Pb collisions at 2.76 TeV and 5.02 TeV”, **HUGS 2022**, [Virtual poster presentation](#), (USA 2022).
- “Event-by-event local multiplicity fluctuations in charged particle production at the LHC energies with ALICE”, **Quark Matter 2023**, [Poster presentation](#), (Texas, USA 2023).
- “Event-by-event local multiplicity fluctuations in charged particle production at the LHC energies with ALICE”, **DAE NPSYMP 2023**, [Talk](#), (IIT, Indore 2023).
- **ALICE INDIA** Collaboration Meetings: Jammu (2022), Jammu ([2023](#)).
- ALICE-India Masterclasses, [University of Jammu](#), (February 2021, February 2022 and March 2022).

Schools and Workshops

- HEP Graduate Workshop, 2021.
- LISHEP 2021.
- MITP School 2021.
- RAPID 2021.
- HUGS 2022.
- Software Basics Workshop.

LIST OF PUBLICATIONS

Publication and conferences proceedings:

- Ramni Gupta, Salman Khurshid Malik, “Intermittency study of charged particles generated in Pb–Pb collisions at $\sqrt{s_{\text{NN}}} = 2.76$ TeV using EPOS3”, *Adv. High Energy Phys.* 2020, 5073042 ([2020](#)).
- Salman Khurshid Malik, Ramni Gupta, “Intermittency analysis of charged hadrons generated in Pb-Pb collisions at $\sqrt{s_{\text{NN}}} = 2.76$ TeV and 5.02 TeV”, *SciPost Phys.Proc.* 15 ([2024](#)).
- ALICE Collaboration, “Event-by-event local multiplicity fluctuations in charged particle production at the LHC energies with ALICE”, *DAE Symp.Nucl.Phys.* 67 1003-1004 ([2024](#)).
- Balwan Singh, Salman Khurshid Malik, Fakhar Ul Haider, Ramni Gupta, “Scaling behaviour of charged particle density fluctuations at LHC energies using EPOS4”, *DAE Symp.Nucl.Phys.* 67 1033-1034 ([2024](#)).
- Sheetal Sharma, Salman Khurshid Malik, Zarina Banoo, Ramni Gupta, “Normalized factorial moments of spatial distributions of particles in high multiplicity events: A Toy model study”, *Nucl. Phys. A* 1053 122963 ([2024](#)).

ALICE Internal Note:

- “A study of local multiplicity fluctuations in Pb-Pb collisions at 5.02 TeV”, ([Analysis note](#)).

ALICE publications co-authored:

- ALICE Collaboration, “The ALICE experiment: a journey through QCD”, *Eur.Phys.J.C* 84 8, 813, (2024).
- ALICE Collaboration, “First study of the two-body scattering involving charm hadrons”, *Phys.Rev.D* 106 5, 052010, (2022).
- ALICE Collaboration, “ALICE luminosity determination for Pb–Pb collisions at $\sqrt{s_{\text{NN}}} = 5.02$ TeV”, *JINST* 19 02, P02039, (2024).

- ALICE Collaboration, “Anisotropic flow and flow fluctuations of identified hadrons in Pb–Pb collisions at $\sqrt{s_{\text{NN}}} = 5.02$ TeV”, JHEP 05 243, (2023).
- ALICE Collaboration, “First Measurement of Antideuteron Number Fluctuations at Energies Available at the Large Hadron Collider”, Phys.Rev.Lett. 131 4, 041901, (2023).
- ALICE Collaboration, “Measurements of the groomed jet radius and momentum splitting fraction with the soft drop and dynamical grooming algorithms in pp collisions at $\sqrt{s_{\text{NN}}} = 5.02$ TeV”, JHEP 05 244, (2023).
- ALICE Collaboration, “System-size dependence of the charged-particle pseudorapidity density at $\sqrt{s_{\text{NN}}} = 5.02$ TeV for pp, pPb, and PbPb collisions”, Phys.Lett.B 845 137730, (2023).
- ALICE Collaboration, “Emergence of Long-Range Angular Correlations in Low-Multiplicity Proton-Proton Collisions”, Phys.Rev.Lett. 132, (2024).
- ALICE Collaboration, “Multiplicity dependence of charged-particle jet production in pp collisions at $\sqrt{s_{\text{NN}}} = 13$ TeV”, Eur.Phys.J.C 82, (2022) .
- ALICE Collaboration, “Closing in on critical net-baryon fluctuations at LHC energies: Cumulants up to third order in Pb–Pb collisions”, Phys.Lett.B 844 137545, (2023).

Data taking shifts:

During my visit to CERN (May–August, 2023), I took part in data taking shifts for the ALICE experiment.

- Shift role was ECS (Experiment Control System).
- Training shift dates: 16-18 May (2023).
- Shift dates: 23-28 May (2023), 14-19 June (2023).

NO. BLT/24/2996
Dy: 7-12-24

Submission Information

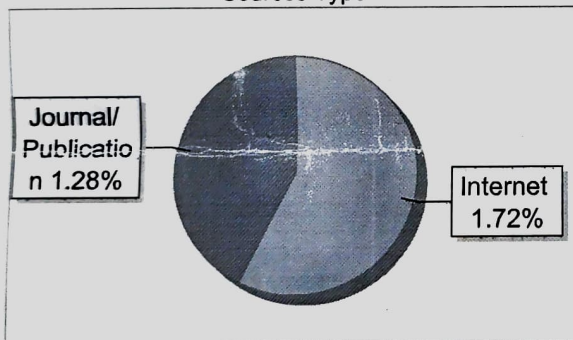
Author Name Salman Khurshid Malik
Title Ph.D
Paper/Submission ID 2722255
Submitted by sahi_vikram@yahoo.com
Submission Date 2024-12-07 12:26:04
Total Pages, Total Words 122, 39504
Document type Thesis

Result Information

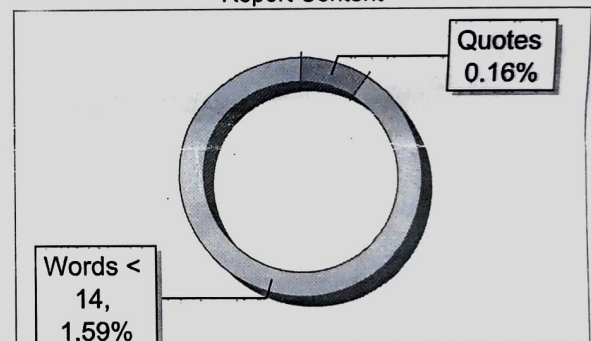
Similarity 3 %

Susan

Sources Type



Report Content



Exclude Information

Quotes	Excluded
References/Bibliography	Excluded
Source: Excluded < 14 Words	Excluded
Excluded Source	0 %
Excluded Phrases	Not Excluded

Database Selection

Language	English
Student Papers	Yes
Journals & publishers	Yes
Internet or Web	Yes
Institution Repository	Yes

A Unique QR Code use to View Download Share Pdf File



Vikram
In-charge Librarian
University Library
University of Jammu, Jammu

Intermittency analysis of charged hadrons generated in Pb-Pb collisions at $\sqrt{s_{NN}} = 2.76$ TeV and 5.02 TeV using PYTHIA8/Angantyr

Salman Khurshid Malik^{*} and Ramni Gupta

Department of Physics, University of Jammu, India

^{*} salman.khurshid.malik@cern.ch



51st International Symposium on Multiparticle Dynamics (ISMD2022)

Pitlochry, Scottish Highlands, 1-5 August 2022

doi:[10.21468/SciPostPhysProc.15](https://doi.org/10.21468/SciPostPhysProc.15)

Abstract

Local density fluctuations are expected to scale as a universal power-law when the system approaches critical point. Such power-law fluctuations are studied within the framework of intermittency through the measurement of normalized factorial moments in (η, ϕ) phase space. Observations and results from the intermittency analysis performed for charged particles in Pb-Pb collisions using PYTHIA8/Angantyr at 2.76 TeV and 5.02 TeV are reported. We observe no scaling behaviour in the particle generation for any of the centrality studied in narrow p_T bins. The scaling exponent ν shows no dependence on the centrality ranges.



Copyright S. K. Malik and R. Gupta.

This work is licensed under the Creative Commons

[Attribution 4.0 International License](https://creativecommons.org/licenses/by/4.0/).

Published by the SciPost Foundation.

Received 17-10-2022

Accepted 04-07-2023

Published 02-04-2024

doi:[10.21468/SciPostPhysProc.15.012](https://doi.org/10.21468/SciPostPhysProc.15.012)



Check for updates

1 Introduction

Critical point and phase transition are being continuously explored in heavy-ion collisions to understand quantum chromodynamics (QCD) phase structure. Lattice QCD predicts a crossover from hadronic matter to quark gluon phase (QGP) at $\mu_B = 0$ [1]. The first-order phase transition at large μ_B , if exists, will end at a critical point [2]. However, the location of critical point and the nature of phase transition is highly uncertain. The rapid increase in the correlation length as the system approaches critical point gives rise to a system which is scale-invariant and fractal [3]. Additionally, the large density fluctuations form a self-similar structure in final state particles which can be studied within the framework of intermittency, which reveals itself as a power-law behaviour of Normalized Factorial Moments (NFM). An advantage of NFM is that they remove the associated statistical fluctuations and characterize non-statistical fluctuations connected with the dynamics of particle production [5]. In this paper, we report intermittency measurements in Angantyr/PYTHIA8 at $\sqrt{s_{NN}} = 2.76$ TeV and 5.02 TeV.

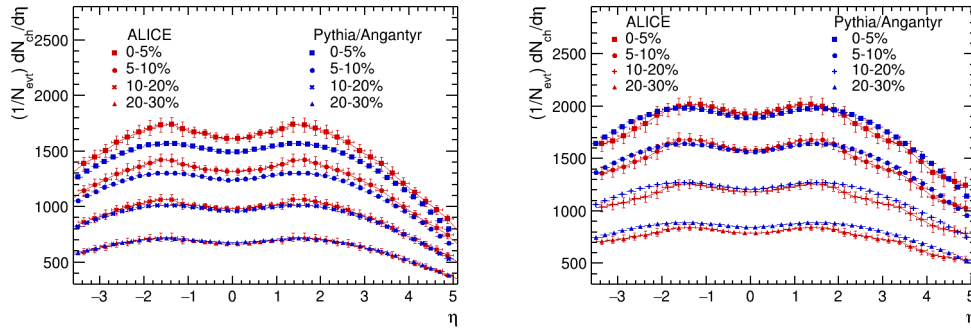


Figure 1: Charged particle pseudorapidity distribution for different centralities from Pb-Pb collisions using PYTHIA/Angantyr compared with that from ALICE at $\sqrt{s_{NN}} = 2.76$ TeV and 5.02 TeV [6, 7].

2 Methodology

Intermittency [3, 8] analysis has been performed in a two-dimensional (η, ϕ) phase space divided into $M \times M$ bins. The q -th order NFM are defined as:

$$F_q(M) = \frac{\frac{1}{N} \sum_{e=1}^N \frac{1}{M} \sum_{m=1}^M f_q(n_{me})}{\left(\frac{1}{N} \sum_{e=1}^N \frac{1}{M} \sum_{m=1}^M f_1(n_{me}) \right)^q}, \quad (1)$$

where n_{me} is the number of particles in m^{th} bin and e^{th} event with q being the order of the moment is an integer and is ≥ 2 . $f_q(n_{me}) = \prod_{j=0}^{q-1} (n_{me} - j)$.

For the systems approaching phase transition, multiplicities within the phase space are such that NFM exhibit power-law with decreasing bin size as:

$$F_q(M) \propto (M^D)^{\phi_q}, \quad (2)$$

where D ($= 2$ in this analysis) is the dimensionality of the phase space. This power-law scaling of NFM with the number of bins (M^D) is called *intermittency*. ϕ_q are intermittency indices. Intermittency studied within the realm of Ginzburg-Landau (GL) formalism [9]:

$$F_q(M) \propto F_2(M)^{\beta_q}, \quad (3)$$

where $\beta_q = \phi_q / \phi_2$. Equation 3 is called *F-scaling*. Intermittency index, ϕ_q and β_q are different in that they depend on different critical parameters of the system. This implies that even if Equation 2 dependence (M-scaling) is absent in a system, F-scaling can still be independently analyzed. β_q is described by *scaling exponent*, ν :

$$\beta_q \propto (q-1)^\nu. \quad (4)$$

The scaling exponent (ν) is independent of the parameters of the system. Its value is predicted to be 1.304 in Ginzburg-Landau theory for second-order phase transition and 1.0 from the 2D Ising model calculations [9] for critical fluctuations.

Angantyr is the heavy-ion generator of PYTHIA8 [10]. It doesn't assume a hot thermalised medium but it rather extrapolates pp dynamics to heavy-ion collisions. Angantyr gives a good description of final state particles in pA and AA collisions [10]. Figure 1 shows the charged particles pseudorapidity distribution for the events used in this analysis compared with ALICE data [6, 7].

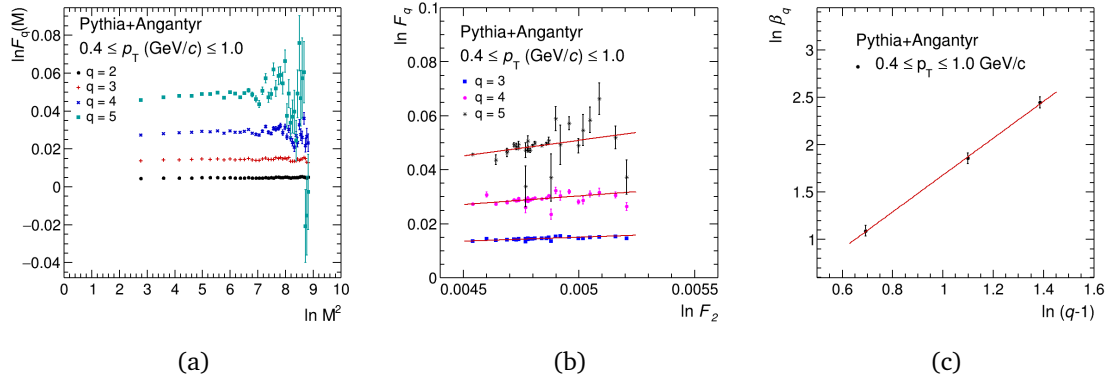


Figure 2: $\ln F_q$ dependence on (a) $\ln M^2$ and (b) $\ln F_2$, (c) $\ln \beta_q$ vs $\ln(q-1)$ plot to obtain scaling exponent (ν) for the p_T bin $0.4 \leq p_T \text{ (GeV/c)} \leq 1.0$.

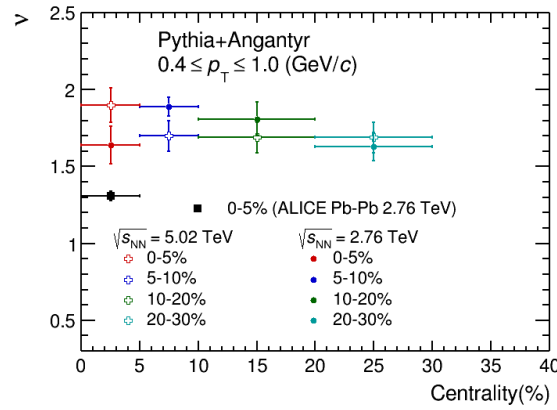


Figure 3: Centrality dependence of ν for Pb-Pb collisions at $\sqrt{s_{NN}} = 2.76 \text{ TeV}$ and 5.02 TeV . Scaling exponent for same p_T bin from ALICE experiment at 2.76 TeV also shown [11].

3 Observations

Two million events generated using PYTHIA+Angantyr for Pb-Pb collisions at $\sqrt{s_{NN}} = 2.76 \text{ TeV}$ and 1M at 5.02 TeV have been analyzed in the midrapidity region ($|\eta| \leq 0.8$) with centralities (the centrality is defined by $\sum E_t$ of the events) 0-5%, 5-10%, 10-20%, 20-30% for many differing width p_T bins out of which the results for $0.4 \leq p_T \text{ (GeV/c)} \leq 1.0$ are shown. NFM are calculated for $q = 2, 3, 4$ and 5. Number of phase space bins, M is taken from 4 to 84 in the intervals of 2.

Behaviour of NFM (F'_q 's) with number of bins M (M -scaling) is given in Figure 2a, and Figure 2b shows F'_q 's ($q = 3, 4, 5$) dependence on second-order NFM (F_2). It is observed that F'_q 's are independent of M , and thus M -scaling is absent. However, a weak dependence of F'_q 's on F_2 is observed and with scaling exponent (ν) = 1.945 ± 0.112 (Figure 2c). But ' ν ' gives quantitative characterization of spatial fluctuations of particles generated in Angantyr. Figure 3 gives the scaling exponent for $0.4 \leq p_T \text{ (GeV/c)} \leq 1.0$ bin studied for different centrality bins and $\gg 1.304$ value predicted by GL formalism for second order phase transition.

4 Conclusions

Investigations on the intermittency analysis for Pb-Pb collisions at 2.76 and 5.02 TeV within PYTHIA+Angantyr have been reported. It is concluded that no M-scaling is present in the particle generation particularly in narrow p_T bins is absent and no self-similarity in fluctuations. Hence, scale-invariant fluctuations are completely absent. In case of wide p_T bins, F-scaling is observed and the value of ν is 1.7-1.9 for different centralities. In Angantyr, the value of ν is greater than the value put forward in GL theory. Within statistical errors, ν is independent of the centrality ranges.

Acknowledgements

We are thankful to the Angantyr developers and particularly to Harsh Shah for his help regarding compatibility with ROOT and centrality calculations.

Funding information The authors are also thankful to RUSA2.0 to University of Jammu by Ministry of Education, India for partial support for computing resources.

References

- [1] Y. Aoki, G. Endrődi, Z. Fodor, S. D. Katz and K. K. Szabó, *The order of the quantum chromodynamics transition predicted by the Standard Model of particle physics*, Nature **443**, 675 (2006), doi:[10.1038/nature05120](https://doi.org/10.1038/nature05120).
- [2] P. Braun-Munzinger, V. Koch, T. Schäfer and J. Stachel, *Properties of hot and dense matter from relativistic heavy ion collisions*, Phys. Rep. **621**, 76 (2016), doi:[10.1016/j.physrep.2015.12.003](https://doi.org/10.1016/j.physrep.2015.12.003).
- [3] E. A. De Wolf, I. M. Dremin and W. Kittel, *Scaling laws for density correlations and fluctuations in multiparticle dynamics*, Phys. Rep. **270**, 1 (1996), doi:[10.1016/0370-1573\(95\)00069-0](https://doi.org/10.1016/0370-1573(95)00069-0).
- [4] S. Sharma and R. Gupta, *Intermittency analysis of toy Monte Carlo events*, SciPost Phys. Proc. **10**, 024 (2022), doi:[10.21468/SciPostPhysProc.10.024](https://doi.org/10.21468/SciPostPhysProc.10.024).
- [5] R. Gupta and S. K. Malik, *Intermittency study of charged particles generated in Pb-Pb collisions at $\sqrt{s_{NN}} = 2.76$ TeV using EPOS3*, Adv. High Energy Phys. **1** (2020), doi:[10.1155/2020/5073042](https://doi.org/10.1155/2020/5073042).
- [6] J. Adam et al., *Centrality evolution of the charged-particle pseudorapidity density over a broad pseudorapidity range in Pb-Pb collisions at $\sqrt{s_{NN}} = 2.76$ TeV*, Phys. Lett. B **754**, 373 (2016), doi:[10.1016/j.physletb.2015.12.082](https://doi.org/10.1016/j.physletb.2015.12.082).
- [7] J. Adam et al., *Centrality dependence of the pseudorapidity density distribution for charged particles in Pb-Pb collisions at $\sqrt{s_{NN}} = 5.02$ TeV*, Phys. Lett. B **772**, 567 (2017), doi:[10.1016/j.physletb.2017.07.017](https://doi.org/10.1016/j.physletb.2017.07.017).
- [8] R. C. Hwa and C. B. Yang, *Local multiplicity fluctuations as a signature of critical hadronization in heavy-ion collisions at TeV energies*, Phys. Rev. C **85**, 044914 (2012), doi:[10.1103/PhysRevC.85.044914](https://doi.org/10.1103/PhysRevC.85.044914).

- [9] R. C. Hwa and M. T. Nazirov, *Intermittency in second-order phase transitions*, Phys. Rev. Lett. **69**, 741 (1992), doi:[10.1103/PhysRevLett.69.741](https://doi.org/10.1103/PhysRevLett.69.741).
- [10] C. Bierlich, G. Gustafson, L. Lönnblad and H. Shah, *The Angantyr model for heavy-ion collisions in Pythia8*, J. High Energy Phys. **10**, 134 (2018), doi:[10.1007/JHEP10\(2018\)134](https://doi.org/10.1007/JHEP10(2018)134).
- [11] R. Gupta and S. Sharma, *Local multiplicity fluctuations in Pb-Pb collisions at $\sqrt{s_{NN}} = 2.76$ TeV with ALICE at LHC*, https://indico.cern.ch/event/895086/contributions/4723639/attachments/2421215/4147342/QM2022_IntermittencyAtLHCposterF11.pdf



Prof Andy Buckley
School of Physics & Astronomy
University of Glasgow
GLASGOW, G12 8QQ, UK
andy.buckley@cern.ch

May 30, 2023

Contribution to ISMD2022

I confirm that Mr Salman Malik of the University of Jammu is an author of the poster and remote flash-talk “Intermittency analysis of charged hadrons generated in Pb-Pb collisions at $\sqrt{s_{NN}} = 2.76$ TeV and 5.02 TeV using PYTHIA8 / Angantyr” shown at the ISMD2022 conference in Pitlochry, Scotland from 31 July to 5 August 2022. Mr Malik was registered to attend the conference virtual sessions held on Zoom and Gather.

Best regards,

A handwritten signature in black ink, appearing to read "A. Buckley", written in a cursive style.

Prof Andy Buckley
Co-chair, ISMD2022

67th DAE Symposium on Nuclear Physics, SNP-2023

December 9 - 13, 2023

Indian Institute of Technology Indore

Certificate of Participation

This is to certify that **Mr. Salman Malik** from University of Jammu has participated in the 67th DAE Symposium on Nuclear Physics, sponsored by Board of Research in Nuclear Sciences, held at IIT Indore, Indore, Madhya Pradesh, during December 09-13, 2023. **Mr. Salman Malik** has also made an Oral presentation for the contribution titled

"Event-by-event local multiplicity fluctuations in charged particle production at the LHC energies with ALICE"

Pandit

Dr. S. K. Pandit

Secretary, SNP-2023

Aradhana

Dr. A. Shrivastava

Convener, SNP-2023